UNIVERSITY OF BELGRADE
FACULTY OF PHYSICS

Veljko Maksimović

W Boson Physics and Luminosity Calibration at the ATLAS Experiment

Doctoral Dissertation

Belgrade, 2025

УНИВЕРЗИТЕТ У БЕОГРАДУ
ФИЗИЧКИ ФАКУЛТЕТ

Вељко Максимовић

Физика W бозона и калибрација луминозности на експерименту АТЛАС

докторска дисертација

Београд, 2025. година

Thesis Defense Committee

Thesis advisor:

Dr. Nenad Vranješ
Research Professor
Institute of Physics Belgrade
University of Belgrade

Committee member:

Dr. Maja Burić
Full Professor
Faculty of Physics Belgrade
University of Belgrade

Committee member:

Dr. Duško Latas
Associate Professor
Faculty of Physics Belgrade
University of Belgrade

Committee member:

Dr. Marija Vranješ Milosavljević
Research Professor
Institute of Physics Belgrade
University of Belgrade

Acknowledgements

...

Abstract

This thesis presents two complementary studies performed using data collected with the ATLAS detector at the Large Hadron Collider at CERN.

The first part documents the absolute calibration of the luminosity scale for pp collisions at $\sqrt{s} = 900$ GeV with high-β^*, based on van der Meer (vdM) beam-separation scans performed in 2018. The visible cross-sections (σ_{vis}) associated with several luminosity algorithms are determined, with systematic uncertainties evaluated in detail, including the impact of non-factorization effects. An overall calibration precision of 1.85% is achieved, with reference specific luminosity variations and non-factorization effects as the dominant contributors to the total uncertainty. Consistency across luminosity algorithms is assessed using the Inner Detector track counting data together with LUCID inclusive, coincidence, and hit-counting algorithms. The delivered integrated luminosity values derived for the given dataset are evaluated for two configurations of β^* to be used for the elastic scattering study:

$$\mathcal{L}_{\mathrm{int}} = 925.4 \pm 0.5_{\mathrm{stat}} \pm 20.0_{\mathrm{sys}}\ \mu\mathrm{b}^{-1}, \quad (\beta^* = 50/100\ \mathrm{m}), \tag{1}$$

$$\mathcal{L}_{\mathrm{int}} = 501.0 \pm 0.4_{\mathrm{stat}} \pm 10.6_{\mathrm{sys}}\ \mu\mathrm{b}^{-1}, \quad (\beta^* = 11\ \mathrm{m}). \tag{2}$$

The resulting total systematic uncertainty on the integrated luminosity amounts to 2.1% and includes contributions from the calibration procedure, stability of detector response, and consistency cross-checks.

The second part reports measurements of the total and fiducial $W^{\pm}$-boson production cross-sections and the corresponding ratio of the fiducial cross-sections for W^+ and W^-. The measurement is performed using proton–proton collision data collected at a centre-of-mass energy of $\sqrt{s} = 13.6$ TeV, corresponding to an integrated luminosity of 29 fb^{-1} recorded by ATLAS in 2022. For this study $W \to \ell\nu$ events are used, where ℓ corresponds to an electron or a muon. Fiducial region, defined by $p_{\mathrm{T}}^{\ell} > 27$ GeV, $|\eta_\ell| < 2.5$, $p_{\mathrm{T}}^{\mathrm{miss}} > 25$ GeV , and $m_{\mathrm{T}}^{W} > 50$ GeV, is determined by detector and trigger acceptance. Signal acceptance and correction factors are estimated using the SHERPA 2.2.12 model. The background levels for electroweak and top processes are estimated using a Monte Carlo simulation, while the multijet background is estimated using a data-driven technique. Experimental and modeling uncertainties are propagated to the measurement, with dominant uncertainties arising from the luminosity and jet reconstruction (for the muon channel), and multijet level and luminosity (for the electron channel). Results are obtained using the Profile-likelihood method. The measured fiducial cross-sections for W^+- and W^--boson production and corresponding ratio are:

$$\sigma_{\mathrm{fid}}^{W^+} = 4250 \pm 150\ \mathrm{pb}, \tag{3}$$

$$\sigma_{\mathrm{fid}}^{W^-} = 3310 \pm 120\ \mathrm{pb}, \tag{4}$$

$$R_{W^+/W^-} = 1.286 \pm 0.022. \tag{5}$$

The quoted uncertainty corresponds to the total uncertainty, including that arising from the luminosity for the fiducial cross-section, which amounts to about 2.2%. The dominant uncertainty for the charge ratio arises from uncorrelated multijet background level uncertainties. The measured W-boson cross-sections are in good agreement with the Standard Model predictions, based on Next-to-Next-to-Leading Order in α_s (plus NLO in α_{EW}) calculation. Predictions based on the most advanced PDFs are compared to the fiducial cross-sections as well as the charge ratio. All predictions are compatible with the measurements within the quoted uncertainties.

Keywords: ATLAS, Standard Model, luminosity calibration, van der Meer, vdM, electroweak boson, W boson, cross-section measurement, fiducial cross-section
Research field: Physics
Research subfield: High energy physics
UDC number:

Сажетак

У овој докторској дисертацији су представљене две комплементарне студије урађене коришћењем података прикупљених помоћу детектора АТЛАС на Великом сударачу хадрона у ЦЕРН-у.

У првом делу дисертације приказани су резултати калибрације апсолутне скале луминозности за протон-протон сударе у систему центра-масе $\sqrt{s} = 900$ GeV са *high*-β^* конфигурацијом, засноване на *van der Meer* (*vdM*) скенирањима спроведеним 2018. године. Одређени су мерљиви (видљиви) ефикасни пресеци (σ_{vis}) за различите алгоритме луминозности, уз детаљну евалуацију систематских неодређености, укључујући и ефекат нарушења факторизације. Постигнута укупна прецизност калибрације износи 1.85%, при чему су варијације референтне специфичне луминозности и ефекат нарушења факторизације доминантни доприноси укупној неодређености. Конзистентност резултата међу различитим алгоритмима луминозности потврђена је методом која користи трагове реконструисане у Унутрашњем детектору, као и коришћењем *LUCID* инклузивних, коинцидентних и *hit-counting* алгоритама. За дати скуп података, процењене су вредности испоручене интегралне луминозности за две β^*-конфигурације, са крајњом наменом коришћења истих у студији еластичног расејања:

$$\mathcal{L}_{\text{int}} = 925.4 \pm 0.5_{\text{stat}} \pm 20.0_{\text{sys}}\ \mu\text{b}^{-1}, \quad (\beta^* = 50/100\ \text{m}), \tag{6}$$

$$\mathcal{L}_{\text{int}} = 501.0 \pm 0.4_{\text{stat}} \pm 10.6_{\text{sys}}\ \mu\text{b}^{-1}, \quad (\beta^* = 11\ \text{m}). \tag{7}$$

Процењена укупна систематска неодређеност за интегралну луминозност износи 2.1% и укључује доприносе од процедуре калибрације, стабилности одзива детектора и провере конзистентности резултата међу различитим методама.

У другом делу дисертације приказани су резултати мерења тоталних и фидуцијалних ефикасних пресека продукције $W^{\pm}$ бозона и количника фидуцијалних ефикасних пресека за W^{+} и W^{-}. Мерење је изведено коришћењем података из протон–протон судара на енергији у систему центра-масе $\sqrt{s} = 13.6$ TeV, са подацима прикупљеним детектором АТЛАС током 2022. године који одговарају интегралној луминозности 29 fb^{-1}. За ово мерење коришћени су догађаји $W \to \ell\nu$, где ℓ означава електрон или мион. Фидуцијални фазни простор, дефинисан условима $p_{\text{T}}^{\ell} > 27$ GeV, $|\eta_{\ell}| < 2.5$, $p_{\text{T}}^{\text{miss}} > 25$ GeV и $m_{\text{T}}^{W} > 50$ GeV, одређен је тако да прати покривеност детектора и тригера. Аксептансе и корекциони фактори су процењени коришћењем модела *Sherpa* 2.2.12. Нивои фона за електрослабе процесе и процесе продукције топ кваркова процењени су коришћењем Монте Карло симулација, док је ниво фона који потиче од продукције џетова процењен директно из података. Експерименталне и теоријске неодређености пропагиране су у коначне резултате мерења. Доминантни доприноси укупној неодређености потичу од: мерења луминозности и реконструкције џетова за мионски канал распада, као и мерења луминозности и процене мултицет фона за електронски канал распада. Резултати су добијени употребом *Profile-likelihood* методе. Измерене вредности фидуцијалних ефикасних пресека продукције W^+ и W^- бозона, као и њиховог количника износе:

$$\sigma_{\mathrm{fid}}^{W^+} = 4250 \pm 150 \text{ pb}, \tag{8}$$

$$\sigma_{\mathrm{fid}}^{W^-} = 3310 \pm 120 \text{ pb}, \tag{9}$$

$$R_{W^+/W^-} = 1.286 \pm 0.022. \tag{10}$$

Изнад наведене неодређености представљају укупне процењене неодређеноси, у које је урачуната и неодређеност која потиче од мерења луминозности, а износи 2.2%. Доминантна неодређеност за количник фидуцијалних пресека потиче од неодређености процене мултиџета која је некорелисана између неистоимено наелектрисаних канала распада. Измерени пресеци продукције W бозона у сагласности су са предвиђањима Стандардног модела, заснованим на пертурбативном рачуну до *Next-to-Next-to-Leading* реда по α_s (уз *NLO* по α_{EW}). Теоријска предвиђања заснована на најсавременијим *PDF* скуповима упоређена су са измереним фидуцијалним ефикасним пресецима као и са фидуцијалним количником, показујући компатибилне резултате у оквирима наведених неодређености.

Кључне речи: АТЛАС, Стандардни модел, калибрација луминозности, van der Meer, vdM, електрослаби бозон, W бозон, мерење ефикасног пресека, фидуцијални ефикасни пресек
Научна област: Физика
Ужа научна област: Физика високих енергија
УДК број:

Contents

List of figures

List of Tables

Introduction

Understanding of the fundamental laws of Nature has progressed over time, turning independent theoretical ideas and experimental discoveries in particle physics into the remarkably coherent framework of the Standard Model. Pieces that once appeared separately - theory of electromagnetism, the weak nuclear interaction, and the strong force - have gradually merged into a single, unified theory. However, even with its remarkable success, the Standard Model remains incomplete. This recognition has motivated the continued development of increasingly sophisticated particle accelerators and complex detector systems used as experimental tools for studying the laws of Nature. The most powerful experimental setup to date, where the foundations of the Standard Model can be further strengthened and new concepts beyond explored, is the Large Hadron Collider (LHC) at CERN. One of its general-purpose detectors, ATLAS, is designed to test the Standard Model with high precision and to search for possible signs of phenomena beyond it.

The results presented in this thesis cover two major components of the ATLAS physics programme: the absolute calibration of the luminosity in proton–proton collisions and the measurement of W-boson production cross-sections at the LHC. Although these two studies serve different physics objectives, together they demonstrate the complete workflow of an ATLAS measurement - from establishing the absolute luminosity scale to extracting physics observables.

The performance of any accelerator ultimately depends on its ability to produce interactions. This capability is quantified through the luminosity, which is roughly proportional to the number of interactions produced per unit time. Almost every precision measurement at the LHC relies directly on the accuracy of the measured luminosity: it sets the overall normalization of all event yields, and its uncertainty often limits the achievable precision of the measurement. The first part of this thesis describes the luminosity calibration using the van der Meer formalism. The calibration is carried out using data collected during dedicated data-taking periods under controlled beam conditions, with the sole purpose of determining the calibration constant with high precision and transferring it to the physics data used in subsequent measurements. In particular, calibration is performed using special ATLAS data at a centre-of-mass energy of $\sqrt{s} = 900$ GeV, conducted in 2018 during Run 2. The luminosity calibration obtained in this thesis serves as a crucial input to the elastic-scattering analysis performed at the same energy. The energy point of $\sqrt{s} = 900$ GeV lies in the transition region where the rise of the total pp cross-section becomes pronounced. Measurements at $\sqrt{s} = 900$ GeV, therefore, provide an anchor for understanding how key elastic-scattering parameters evolve with energy. A precise determination at this intermediate energy helps to constrain soft-QCD models and test dispersion-relation expectations, while offering sensitivity to signatures of the Odderon, the color-singlet three-gluon exchange state predicted by QCD.

The W-boson is a cornerstone of the electroweak sector. Precise measurements of its production cross-sections, charge asymmetries, and decay properties provide stringent tests of perturbative QCD and electroweak theory. They also constrain parton distribution functions (PDFs), especially the u/d ratio at low Björken-x, which has wide implications for LHC phenomenology. With the increased centre-of-mass energy and luminosity in Run 3, ATLAS can achieve a new level of precision in W-boson measurements. The second part of this thesis focuses on the measurement of the inclusive total and fiducial production cross-sections of the $W^{\pm} \to \ell^{\pm}\nu$ processes, as well as their ratio. Here ℓ denotes an electron or a muon, representing two experimentally clean signatures. These measurements are performed using proton–proton collision data collected by the ATLAS experiment during 2022 at the increased centre-of-mass energy of $\sqrt{s} = 13.6$ TeV, corresponding to an integrated luminosity of 29 fb^{-1}. The analysis is based on profile-likelihood (PLH) fits to the inclusive event yields in the four single-lepton channels: $W^+ \to e^+\nu$, $W^+ \to \mu^+\nu$, $W^- \to e^-\bar{\nu}$, and $W^- \to \mu^-\bar{\nu}$. From these, the individual cross-sections and the ratio of W^+/W^- fiducial cross-sections are extracted with high precision. An alternative event-counting extraction of the cross-section quantities listed above is also performed.

The chapters that follow are organized as described below:

- **Chapter 1** introduces the fundamental concepts of circular accelerators, including beam dynamics, focusing, and collision schemes relevant for luminosity studies. It also provides a concise overview of the Standard Model, highlighting the theoretical foundations needed to understand the physics processes discussed later in the thesis.
- **Chapter 2** describes the experimental environment of the ATLAS detector, outlining the key subsystems involved in event reconstruction and luminosity determination. Particular attention is given to the luminosity detectors and the components most relevant for the studies presented in this thesis.
- **Chapter 3** presents a detailed description of the determination of the absolute luminosity scale using the van der Meer scan formalism. This chapter places special emphasis on the calibration of the visible cross-section, which represents the primary contribution of the author.
- **Chapter 4** focuses on the measurement of the fiducial W-boson production cross-section at $\sqrt{s} = 13.6$ TeV. The event selection, background estimation, and the extraction of the final physics results are discussed, illustrating the application of the calibrated luminosity scale in a high precision electroweak analysis. This chapter contains the author's contribution to the gauge boson physics at ATLAS.

Author‘s publications related to this thesis:

- G. Aad, ..., **V. Maksimovic**, *et al.*, "Measurement of vector boson production cross sections and their ratios using pp collisions at $\sqrt{s}$ =13.6 TeV with the ATLAS detector", *Physics Letters B* **854** (2024) 138725.
- G. Aad, ..., **V. Maksimovic**, *et al.*, "Measurement of the $t\bar{t}$ cross section and its ration to the Z production cross section using pp collisions at $\sqrt{s} = 13.6$ TeV with ATLAS detector", *Physics Letters B* **848** (2024) 138376.
- R. Hawkings, W. Kozanecki, J. Kuechler, **V. Maksimovic**, K. Monig, N. Vranjes, "Absolute luminosity calibration for the 900 GeV 2018 pp dataset with the ATLAS detector", ATL-COM-DAPR-2024-020 (2024).
- G. Aad, ..., **V. Maksimovic**, *et al.*, "Determination of the luminosity in pp collisions for elastic scattering measurements at $\sqrt{s} = 900$ GeV using the ATLAS detector at the LHC", Target journal: *European Physical Journal C (EPJC)*. Manuscript in preparation.

Chapter 1

An Overview of the Theoretical and Experimental Concepts

Particle accelerators are regarded as essential instruments in the exploration of the fundamental laws of nature. By colliding particles at high energies, access is provided to very small distance scales where new phenomena can be observed and existing theoretical predictions tested. The advancement of accelerator technology and the development of particle physics theory have been closely connected. Each new generation of accelerators has enabled deeper insights into the structure of matter and the forces that govern it. Circular accelerators, in which charged particles are guided along closed orbits by magnetic fields and gain energy by accelerating, are particularly well-suited for reaching very high collision energies. This chapter first introduces the fundamental principles of circular accelerators essential for understanding luminosity, followed by a brief overview of the Standard Model.

1.1 Principles of circular accelerators

The design and operation of modern high-energy circular accelerators are based on fundamental principles of accelerator physics that determine the transverse and longitudinal dynamics of charged particles. These concepts provide the basis for understanding the performance of large-scale machines, including the LHC introduced later in Section 2.2. In this section, the main ingredients are reviewed: transverse dynamics and focusing, longitudinal dynamics, and *Radio Frequency* (RF) acceleration. While the RF system is used for accelerating, dipole magnets bend the beam to keep it on a closed path, quadrupole magnets provide linear focusing in the horizontal and vertical planes, and sextupole magnets are used to correct chromatic effects [1] [1]. These elements are typically arranged in repeating units called *cells*; their pattern governs how the beam is transported and focused around the accelerator ring. The term *lattice* refers to the ordered sequence of magnets and accelerating elements that make up the ring [2]. A simple example for a lattice element is the FODO cell, which consists of a focusing quadrupole (F), a drift space (O), and a defocusing quadrupole (D), all of which are repeated periodically. In the LHC, the arc regions are constructed from long sequences of FODO cells. At

---

[1] This effect arises because particles with momenta different from the reference momentum are bent and focused with slightly different strengths by the quadrupole fields. If left uncorrected, this momentum dependence would lead to a spread in the particle trajectories and ultimately result in beam destabilization.

the same time, the insertions surrounding the detectors are specifically designed to provide a focused beam at the *interaction point* (IP) of the colliding beams.

1.1.1 Acceleration and beam steering

A fundamental component of any synchrotron and circular accelerator in general is the system used to accelerate particles. A magnetic field can only change particles' trajectories but cannot change the kinetic energy of the beam; acceleration must therefore be provided by an electric field parallel to the direction of motion of the particles. In the LHC, this is achieved with superconducting RF cavities operating at a frequency of $f_{RF} = 400.8$ MHz [3]. An RF cavity is a metallic resonator constructed to uphold an oscillating electromagnetic field at a well-defined frequency. The geometry of these cavities is designed to establish a strong longitudinal electric field along the beam axis. RF cavities operate at a harmonic h of the revolution frequency f_{rev} (≈11.245 kHz in the LHC [4]). An oscillating electric field defined as:

$$V(t) = V_{\text{RF}} \sin(\omega_{\text{RF}} t + \phi) \tag{1.1}$$

is applied along the beam path, where $\omega_{\text{RF}} = 2\pi h f_{\text{rev}}$. The oscillating RF field alternates between accelerating and decelerating. When a charged particle travels the cavity at the correct phase of the oscillation ϕ_s, it receives the energy increment $\Delta E = qV_{\text{RF}} \sin\phi_s$ needed to reach and maintain the desired momentum, where q is the particle charge, V_{RF} the cavity voltage. Particles with such a phase are called synchronous particles. In reality, beams consist of a vast number of particles with the energies spread around the nominal (synchronous) value. For example, a particle with a slightly smaller energy than the synchronous one, has, of course, lower momentum and arrives later in phase at the RF cavity. Because of the sinusoidal voltage, a late particle sees a larger accelerating field and therefore gains more energy than the synchronous particle. On the other hand, if a particle with slightly higher energy arrives earlier, it experiences a weaker accelerating field and gains less energy. In both cases, these particles are driven back to the synchronous energy on the next turn around the ring. This restoring-to-the-nominal-value mechanism does not return particles exactly to the synchronous phase. It instead causes particles to oscillate in phase and energy at the frequency [5]:

$$\omega_s = \sqrt{\frac{hqV_{\text{RF}} |\cos\phi_s| \, \zeta}{2\pi\tilde{\beta}^2 E}}, \tag{1.2}$$

where ζ is the slip factor, which tells how the revolution frequency shifts with momentum, $\tilde{\beta}$ is the relativistic velocity factor, and E is the total energy of the particle. In longitudinal phase space (ΔE versus ϕ), the trajectories of particles undergoing these oscillations are closed ellipses around the synchronous particle. The limit between stable and unstable motion is described by a curve in the longitudinal phase space, the *RF separatrix*. Particles within the RF separatrix remain confined and oscillate around the synchronous phase, whereas particles outside slip in phase until they are lost from the machine. An *RF bucket* is the stable region in longitudinal phase space created by the RF voltage, defined by the separatrix. Buckets exist independently of whether particles are present. A *bunch*, in contrast, is the actual collection of protons confined within a given bucket. The number of buckets around the ring in the LHC is determined by the machine's properties. Harmonic number gives the $h = f_{RF}/f_{rev} \approx 35640$ possible number of buckets with a $1/f_{RF} = 2.5$ ns time-length, but only every tenth bucket is filled. This produces a pattern of 3564 possible bunches per beam with 25 ns spacing [2]. The number of possible bunches is additionally reduced due to the machine protection and operational reasons, including the abort gap for beam dumping, injection kicker gaps, and reserved slots for synchronization [6]. As a result, the maximum number of filled bunches per beam is 2808, each populated with $\approx 10^{11}$ protons and identified by its unique *Bunch Crossing ID* (BCID). Such high bunch populations are required, given the extremely small probability that individual protons will collide within the tiny interaction region.

For charged particles to follow the circular path, dipole magnets are employed. Their field is used to bend the beams around the ring. The magnetic part of the Lorentz force acts like the centripetal acceleration:

$$\frac{p}{q} = B\rho, \tag{1.3}$$

where p is the particle momentum, q its charge, B the dipole magnetic field, and ρ the bending radius. The quantity $B\rho$ is called the *magnetic rigidity*, and it is a parameter very important in synchrotron design. For the LHC, dipoles of $8.3\,\mathrm{T}$ bend protons of $7\,\mathrm{TeV}$ momentum around a radius of $\rho \approx 2.8\,\mathrm{km}$. A charged particle undergoing acceleration emits electromagnetic radiation. In circular accelerators, the bending of particle trajectories by dipole fields provides a continuous centripetal acceleration, resulting in energy loss per revolution, known as synchrotron radiation. The energy loss is proportional to $E^4/(m^4\rho)$, which implies that synchrotron radiation is stronger for light particles such as electrons, but negligible for heavy particles such as protons. Taking into account, for example, electron and proton masses ($m_e = 0.511$ MeV, $m_p = 938$ MeV) at the exact bending radius, the ratio of the radiated power is proportional to $(m_p/m_e)^4 \sim 10^{13}$.

1.1.2 Transverse beam motion

The interplay of dipole and quadrupole fields controls the transverse motion of particles in a synchrotron. While dipoles bend the trajectory onto the reference orbit, quadrupoles provide linear restoring forces that localize deviations from it. The resulting equation of motion in the horizontal plane is (and analogous for a vertical plane):

$$\frac{d^2x}{ds^2} + K(s)\,x = 0, \tag{1.4}$$

where $x(s)$ is the horizontal displacement, s is the *longitudinal coordinate*, defined as the path length along the reference orbit, and $K(s)$ is the focusing function of the lattice. Longitudinal coordinate s increases continuously as one moves around the ring, with $s = 0$ typically chosen at a reference point such as an IP. After one revolution, $s = C$ corresponds to the circumference of the machine. Since the accelerator lattice is periodic, $K(s + C) = K(s)$. A quadrupole focuses in one plane while defocusing in the other. By arranging alternating gradients in a lattice cell (FODO structure), overall focusing is achieved in both planes. Form shown in Eq. (1.4) is known as Hill's equation [7]. This equation is directly analogous to the paraxial equation for light rays in a periodic lens system. Just as a sequence of lenses defines how a light beam is focused, a sequence of quadrupole magnets defines how a particle beam is focused. According to Floquet's theorem [1, 8], the solution of Hill's equation can be written as:

$$x(s) = \sqrt{\varepsilon\,\beta(s)}\,\cos\big(\psi(s) + \phi_0\big), \tag{1.5}$$

where ε is the *transverse emittance*, $\beta(s)$ the *betatron function* (envelope), and $\psi(s)$ the phase advance. Emittance quantifies the phase-space area occupied by the beam. In one transverse plane, it is defined as:

$$\varepsilon = \frac{1}{\pi}\,\mathrm{Area}(x, x'), \tag{1.6}$$

where x is the transverse position and $x' = dx/ds$ the angle with respect to the reference orbit. In practice, the often quoted variable is rather a *normalized emittance* defined as:

$$\varepsilon_N = \gamma\tilde{\beta}\,\varepsilon, \tag{1.7}$$

with γ being the Lorentz factor, and $\tilde{\beta} = \sqrt{1 - (1/\gamma)^2}$ the mean velocity of a beam particle in $c-$units. Normalized emittance is invariant under acceleration. For the LHC, a typical normalized transverse emittance at injection is $\varepsilon_N \approx 3.5\ \mu\mathrm{m}$. *Transverse beam size* $\sigma(s)$ at a position s along the beam pipe is given by:

$$\sigma(s) = \sqrt{\varepsilon\,\beta(s)}. \tag{1.8}$$

Thus, the beam envelope is determined by both the optical lattice (through $\beta(s)$) and the emittance ε. At the IP, beams are focused to maximize luminosity. The value of the betatron function at the IP is denoted as β^*. A smaller β^* corresponds to a tighter focus and smaller transverse beam size. Reducing β^* therefore increases luminosity, but also increases angular divergence, which can affect detector acceptance and pile-up conditions.

The *betatron tune* Q is defined as the number of transverse oscillations a particle performs per revolution around the ring:

$$Q = \frac{1}{2\pi}\oint \frac{ds}{\beta(s)}.$$

If the tune is close to a rational value $Q = m/n$, with small integers m and n, the betatron phase advance aligns with the periodic lattice after n turns. In this situation, small perturbations from magnet imperfections or nonlinear fields are reinforced coherently on every turn, leading to large oscillation amplitudes. Integer tunes are driven by dipole errors, half-integer tunes by quadrupole errors, and higher-order resonances by sextupoles and other nonlinearities. The strength of a resonance generally decreases with its order, so low-order rational tunes (e.g. $Q = 1/2, 1/3, 1/4$) are the most dangerous. To ensure beam stability, the operational tune values (Q_x, Q_y) are chosen to lie between resonance lines in tune space.

Owing to the close analogy between magnet configurations in a circular accelerator and optical lens systems, the transverse beam-dynamics parameters—such as the Q_x, Q_y, β^*—are collectively referred to as the *beam optics* configurations.

1.2 Luminosity

The term "luminosity" (from the Latin "lumen") was borrowed from optics/astronomy and was probably first used in the late 1950s, when storage rings and colliders were first being developed. To compare interaction rates at different energies and beam intensities, the physicists needed a normalized quantity. Hence, "luminosity" was adopted to quantify how "bright" the beams are in terms of producing interactions. If the two beams have equal intensities, the number of interactions N observed in a given time interval is proportional to the *instantaneous* luminosity $\mathcal{L}(t)$. The proportionality factor is the interaction cross-section σ, which represents the probability for a given process to occur:

$$R(t) = \frac{dN}{dt} = \mathcal{L}(t)\,\sigma, \tag{1.9}$$

where $R(t)$ is the interaction rate (events per unit time), with luminosity having a dimension of $\mathrm{cm}^{-2}\mathrm{s}^{-1}$. This relation is valid for any chosen reference process; it is convenient to select one with a well-defined and precisely measurable cross-section, such as the *inelastic proton–proton cross-section* σ_{inel}. Under this choice, the instantaneous luminosity per *bunch crossing* (BC) can be expressed as:

$$\mathcal{L}_b = \frac{\mu \cdot f_{\text{rev}}}{\sigma_{\text{inel}}}, \tag{1.10}$$

where f_{rev} denotes the bunch revolution frequency and μ is the number of inelastic interactions per BC. Instantaneous luminosity in a collider is not constant in time, but instead, it gradually decreases. This decay is primarily driven by reductions in beam intensity and increases in transverse beam size. Under nominal operating conditions, the dominant contribution to this degradation arises from the loss of accelerated particles due to collisions themselves. Other mechanisms, such as intrabeam scattering, residual-gas interactions, and various collective effects, play secondary roles but may become significant at very high luminosities. An example of the observed decay of the instantaneous luminosity during a typical Fill[2] is shown on the left side of Figure 1.1 as read by one of the luminosity monitoring systems (see Section 2.4). In most cases, this decrease can be well described by an exponential parameterization:

$$\mathcal{L}(t) = \mathcal{L}_0 \, e^{-t/\tau_T}, \tag{1.11}$$

where τ_T represents the *effective luminosity lifetime*. This single-parameter model provides a good approximation of the observed behavior during most physics fills. Although the exact functional form of $\mathcal{L}(t)$ is not essential for luminosity monitoring, since measurements are summed numerically, it becomes important for optimizing collider performance. Because the recorded luminosity decreases with time, there exists an optimal duration for each physics Fill ($\simeq 7h$).

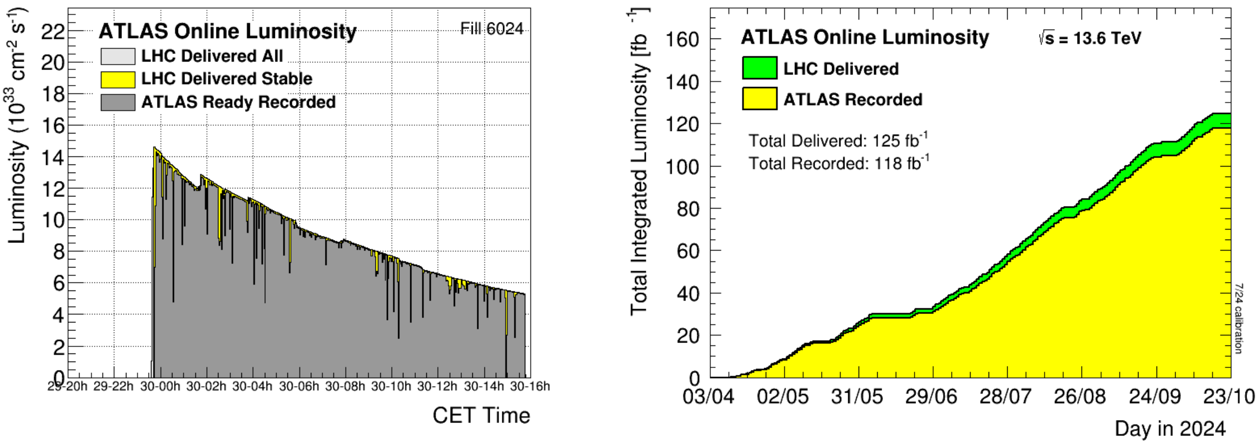

Figure 1.1: Left: Instantaneous luminosity as a function of time for LHC Fill 6024 in Run 2 during 2017 at $\sqrt{s} = 13$ TeV [9]. Luminosity decay is clearly visible. Right: Total integrated luminosity delivered by the LHC and recorded by the ATLAS detector in 2024 during Run 3, shown as a function of day [10].

The integrated luminosity refers to the luminosity collected over some period (e.g., the data-taking time period), and is obtained as:

$$\mathcal{L}_{\text{int}} = \int \mathcal{L}(t)\, dt. \tag{1.12}$$

Unit of integrated luminosity is the inverse barn (b^{-1}), where one barn equals $1\ \text{b} = 10^{-24}\ \text{cm}^2$. However, at collider experiments is more convenient to express $\mathcal{L}_{\text{int}}$ in inverse picobarns (pb^{-1}) or inverse femtobarns (fb^{-1}), reflecting the very small cross-sections typical for high-energy processes. There are several related definitions of luminosity. The *delivered* luminosity represents the total luminosity provided by the accelerator to the detectors built at the IPs (such as ATLAS, used in this thesis) during data-taking, encompassing the full beam conditions, regardless of whether the detector recorded all interactions. The *recorded* luminosity is the portion of the delivered luminosity that was actually collected by a detector and written to permanent storage, meaning $L_{\text{recorded}} \leq L_{\text{delivered}}$. Losses primarily result from detector downtime, data acquisition dead-time, trigger properties, and other factors. An example of the evolution of the total integrated luminosity at the LHC experiment ATLAS in 2024 is shown on the right side of Figure 1.1. Luminosity determined in experiments can be distinguished as *absolute* or *relative*. The absolute, or true physical, luminosity is obtained

---

[2] Fill denotes one complete beam cycle, in the case of LHC starting with beam injection, followed by the operational period in which collisions are delivered, and ending with beam dump.

from dedicated calibration procedures that directly measure the beam parameters and determine the physical luminosity scale. The relative luminosity quantifies the time-dependent variation of the interaction rate during normal operation, determined from the detector‘s counting rates normalized to the previously established calibrated luminosity.

1.2.1 Colliding bunches luminosity

The luminosity of a collider can be expressed in terms of the properties of the colliding bunches. Considering two particle bunches with normalized densities $\rho_1(x,y,z,t)$ and $\rho_2(x,y,z,t)$, the general expression reads:

$$\mathcal{L}_b = K\, n_1 n_2\, f_{\text{rev}} \int\!\!\int\!\!\int\!\!\int \rho_1(x,y,z,t)\, \rho_2(x,y,z,t)\, dx\, dy\, dz\, dt, \tag{1.13}$$

where $n_{1,2}$ denotes the number of particles per bunch in the two beams, f_{rev} the revolution frequency of the machine. The prefactor K is a kinematic term that accounts for the relative motion of the beams and is defined as:

$$K \;=\; \sqrt{(\vec{v}_1 - \vec{v}_2)^2 - \frac{(\vec{v}_1 \times \vec{v}_2)^2}{c^2}}, \tag{1.14}$$

where $\vec{v}_{1,2}$ are the beam velocities and c is the speed of light. For collinear beams traveling at relativistic speed, $K = 2c$. The *total instantaneous luminosity* is defined as the sum of the instantaneous luminosities over n_b colliding bunch-pairs at the IP:

$$\mathcal{L} = \sum_{b}^{n_b} \mathcal{L}_b = n_b \cdot \langle \mathcal{L}_b \rangle = n_b \cdot \frac{\langle \mu \rangle \cdot f_{\text{rev}}}{\sigma_{\text{inel}}}, \tag{1.15}$$

with $\langle \mathcal{L}_b \rangle$ being the mean per-bunch instantaneous luminosity, and $\langle \mu \rangle$ the interaction rate averaged over all colliding bunches—commonly referred to as the *pile-up*[3]. If the particle densities can be factorized into independent transverse and longitudinal components, the normalized density becomes:

$$\rho_i(x,y,z,t) = \rho_{ix}(x)\, \rho_{iy}(y)\, \rho_{iz}(z \pm ct). \tag{1.16}$$

The longitudinal part cancels in the overlap integral for head-on collisions (beams are collided along the z-axis), yielding:

$$\mathcal{L}_b = n_1 n_2\, f_{\text{rev}} \int \rho_{1x}(x) \rho_{2x}(x)\, dx \int \rho_{1y}(y) \rho_{2y}(y)\, dy. \tag{1.17}$$

Bunch densities are often well approximated by Gaussian distributions. For beam i with transverse widths σ_{ix} and σ_{iy}, the normalized densities are:

$$\rho_{ix}(x) = \frac{1}{\sqrt{2\pi}\,\sigma_{ix}} \exp\left(-\frac{x^2}{2\sigma_{ix}^2}\right), \tag{1.18}$$

$$\rho_{iy}(y) = \frac{1}{\sqrt{2\pi}\,\sigma_{iy}} \exp\left(-\frac{y^2}{2\sigma_{iy}^2}\right). \tag{1.19}$$

Substituting these profiles into Eq. (1.17), one obtains:

$$\mathcal{L}_b = \frac{n_1 n_2\, f_{\text{rev}}}{2\pi \sqrt{\sigma_{1x}^2 + \sigma_{2x}^2}\, \sqrt{\sigma_{1y}^2 + \sigma_{2y}^2}}. \tag{1.20}$$

---

[3] *In-time pile-up* refers to multiple *pp* interactions occurring within the same BC as the hard-scattering event of interest. *Out-of-time pile-up* refers to signals from interactions in earlier or later BC, recorded due to finite signal integration time.

For the special case of equal beam sizes, $\sigma_{1x} = \sigma_{2x} = \sigma_x$ and $\sigma_{1y} = \sigma_{2y} = \sigma_y$, this reduces to:

$$\mathcal{L}_b = \frac{n_1 n_2 f_{\text{rev}}}{4\pi\sigma_x\sigma_y}. \tag{1.21}$$

Eq. (1.21) makes explicit the parameters that drive luminosity: a large bunch population product $n_1 n_2$, a high revolution frequency, and small transverse beam sizes σ_x, σ_y at the IP. This expression can be further rewritten by expressing the transverse beam sizes in terms of the emittances $\varepsilon_{x,y}$ and the corresponding betatron functions $\beta_{x,y}$ (whose definitions are given in Section 1.1.2). Using the definition of the normalized emittances, $\varepsilon_N^{x,y} = \gamma\tilde{\beta}\varepsilon_{x,y}$, given in Eq. (1.7) and assuming the round-beam approximation ($\sigma_x = \sigma_y = \sigma$), the luminosity per bunch pair becomes:

$$\mathcal{L}_b = \frac{n_1 n_2\, f_{\text{rev}}}{4\pi\sigma^2} = \frac{n_1 n_2\, f_{\text{rev}}\, \gamma}{4\pi\, \varepsilon_N\, \beta^*}, \tag{1.22}$$

where $\varepsilon_N^x = \varepsilon_N^y = \varepsilon_N$ and $\beta_x = \beta_y$ due to the round-beams. This further illustrates that luminosity can be actively controlled through the lattice configuration (see Sections 2.1 and 1.1.2 for a definition and discussion), in particular by adjusting the value of the betatron function β^* at the IPs, which determines the transverse beam size and focusing strength at the collision region. In addition to these parameters, the total instantaneous luminosity from Eq. (1.15) can be further increased by increasing the number of colliding bunch pairs n_b. For the most general case, the luminosity expression can be extended to include reduction factors that account for realistic beam configurations.

1.2.2 Luminosity reduction effects

Several factors can reduce the achievable luminosity compared to the idealized case of perfectly head-on collisions with static Gaussian bunches summed by Eq. (1.21) and Eq. (1.22). Most relevant effects arise from the finite crossing angle, transverse offsets between the beams, their combination, and the so-called *hourglass effect* due to the variation of the β-function along the longitudinal direction [4, 11].

At colliders, beams are often brought into collision under a small crossing angle θ_c. For two Gaussian bunches with longitudinal beam size σ_z and transverse beam size σ_i in the plane of the crossing i, where $i = x, y$, the reduction factor $S(\theta_c)$ is approximetely given by:

$$S(\theta_c) \approx \left(1 + \left(\frac{\theta_c\sigma_z}{2\sigma_i}\right)^2\right)^{-1/2}, \tag{1.23}$$

which multiplies the nominal luminosity in Eq. (1.21). The reduction increases with both the crossing angle and the bunch length. The transverse offset between the beam at the IP, for instance, due to imperfect orbit steering, also reduces the overlap integral. Assuming a static Gaussian displacement δ_x^0 and δ_y^0 between the two beams, the reduction factor reads:

$$W(\delta_x^0, \delta_y^0) = \exp\left(-\frac{(\delta_x^0)^2}{4\sigma_x^2} - \frac{(\delta_y^0)^2}{4\sigma_y^2}\right). \tag{1.24}$$

Even small offsets of order $\sim 0.1\sigma$ can cause measurable luminosity loss, which motivates the use of continuous beam–beam centering during runs. When both a crossing angle and a transverse offset are present in the same plane (e.g, horizontal), the two effects no longer factorize exactly. The resulting overlap integral leads to a correction term of the form [11]:

$$e^{B_A^2} = \exp\left[\frac{1}{2}\left(\frac{\theta_c\sigma_z\delta_x^0}{2\sigma_x^2}\right)^2\right], \tag{1.25}$$

which partially compensates the luminosity reduction from S and W. This term appears in the general luminosity expression as an exponential enhancement factor, relevant when both effects coexist. The hourglass effect arises from the transverse focusing of the beams near the IP, where the β-function reaches its minimum value β^*. If the assumption of factorization (from Eq. (1.16)) between transverse and longitudinal bunch densities no longer holds, the transverse beam sizes become dependent on the longitudinal position z along the bunch. This breaks the simple picture described by Eq. (1.21) and Eq. (1.22). An additional factor, due to the $\sigma_i \to \sigma_i(z)$ transition, now arises and must be integrated numerically due to its complexity. Because the beam is continuously focused by alternating focusing and defocusing quadrupole magnets, the β-function increment can be approximated quadratically with distance from the IP as:

$$\beta(z) = \beta^* \left(1 + \frac{z^2}{\beta^{*2}}\right) , \tag{1.26}$$

resulting in a corresponding growth of the transverse beam size, $\sigma(z) = \sigma^* \sqrt{1 + (z/\beta^*)^2}$, with $\sigma^* = \sigma(z = 0)$. This leads to a reduction of the effective overlap of the colliding bunches, and consequently of the instantaneous luminosity. Hourglass effect becomes significant when the bunch length σ_z is comparable to β^*, and is negligible when $\beta^* \gg \sigma_z$. This effect is smaller compared to the effect caused by the crossing angle when assuming nominal LHC parameters. As shown in Figure 1.2, the transverse beam envelope widens more rapidly with z for smaller β^*, producing the hourglass-shaped (if taken both positive and negative solutions) focusing profile around the IP.

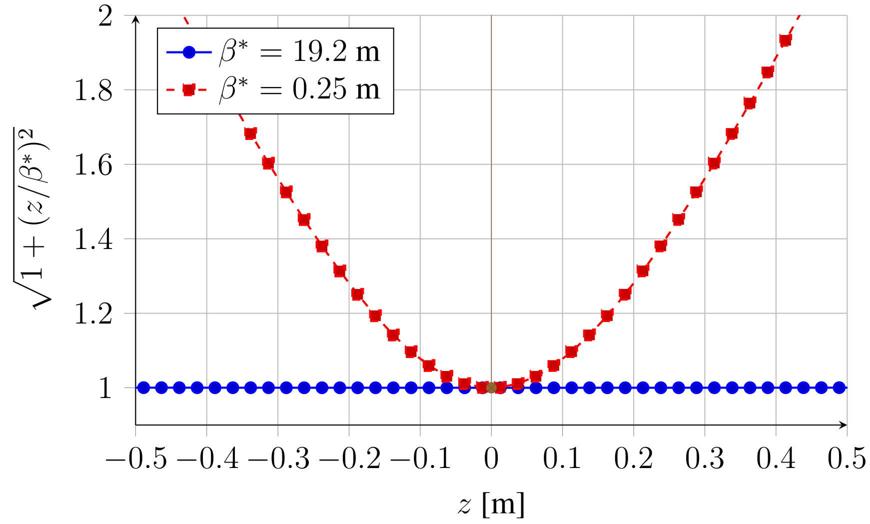

Figure 1.2: Dependence of the factor $\sqrt{1 + (z/\beta^*)^2}$ on the longitudinal position z for two optics configurations at ATLAS [12]. The large value $\beta^* = 19.2$ m corresponds to the high-β^* optics used during calibration runs while the small $\beta^* = 0.25$ m represents the low-β^* optics used in standard high-luminosity physics operation.

1.2.3 Importance of luminosity

Precision of any measurement in collider physics ultimately depends on the delivered luminosity, which determines both the achievable statistical accuracy and the sensitivity to rare processes with small production probabilities. The total number of events observed for a given process can be written as:

$$N_{\text{events}}^{\text{observed}} = \sigma \times \text{efficiency} \times \mathcal{L}_{int} . \tag{1.27}$$

Here, efficiency is the overall detection efficiency, accounting for the detector acceptance and event-selection performance, and $\mathcal{L}_{int}$ represents the integrated luminosity accumulated by the collider.

While the cross-section is a quantity fixed by the underlying physics and the efficiency is determined by the experimental apparatus, the integrated luminosity is a property of the accelerator and directly governs the statistical power of all measurements. The instantaneous luminosity is determined in experiments [13–15] using dedicated detector systems, and its absolute calibration is obtained through dedicated *van der Meer* (vdM) [16] beam-separation scans, explained in detail in Section 3.1.

The importance of achieving high luminosity precision becomes especially pronounced when potential signatures of new physics cannot be accessed through the direct (on-shell) production of heavy states. In such cases, new interactions may manifest indirectly through subtle modifications of existing observables.

An illustrative example is the measurement of the inclusive W-boson production cross-section multiplied by the leptonic branching ratio from Eq. (4.1). In this expression, any uncertainty in $\mathcal{L}_{\text{int}}$ propagates linearly to the extracted cross-section, making luminosity calibration one of the dominant systematic components in precision electroweak measurements. The same applies to a wide range of processes, including Z-boson, top-quark, and Higgs-boson production. The impact of luminosity precision on physics measurements can be illustrated using representative examples from Run 1 analyses. Figure 1.3 presents the comparison between measured and predicted differential cross-sections for Z boson production, evaluated with various theoretical predictions. This figure clearly shows that the luminosity uncertainty constitutes a significant fraction of the total error, and that reducing it directly improves the precision of measurements in constraining theoretical models.

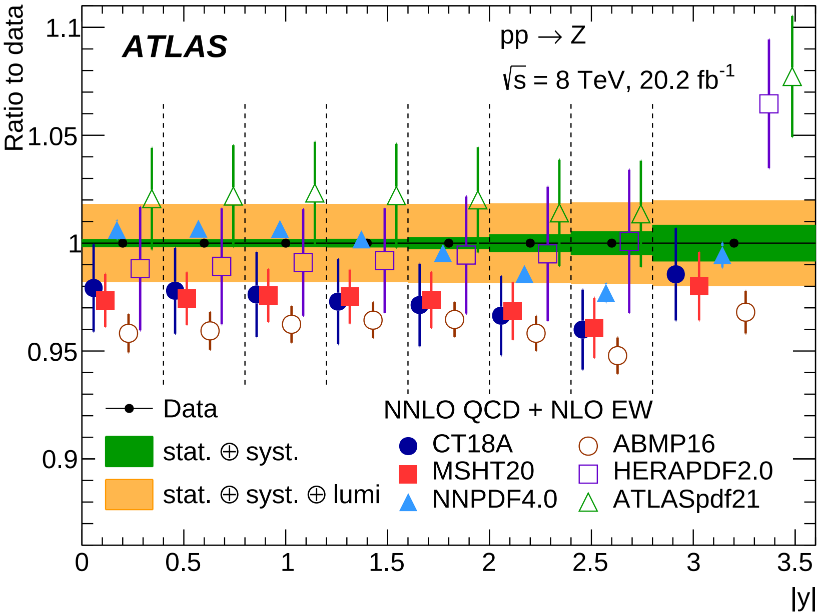

Figure 1.3: Ratio of the measured Z-boson differential cross-section to the several theoretical predictions as a function of the boson rapidity [17].

A similar conclusion can be drawn from measurements of the inclusive top-quark pair production cross-section, where the luminosity calibration remains one of the leading sources of systematic uncertainty. Figure 1.4 illustrates ATLAS results for the inclusive $t\bar{t}$ cross-section at $\sqrt{s} = 13$ TeV compared with the most precise theoretical predictions available. Even in these high-statistics datasets, the luminosity term contributes a substantial fraction of the total systematic uncertainty. Improvements in luminosity determination are directly reflected in the overall precision of top-quark cross-section measurements.

Beyond its role in physics analyses, continuous luminosity monitoring is also crucial for machine operation. Because the luminosity decreases exponentially, as described by Eq. (1.11), with time during

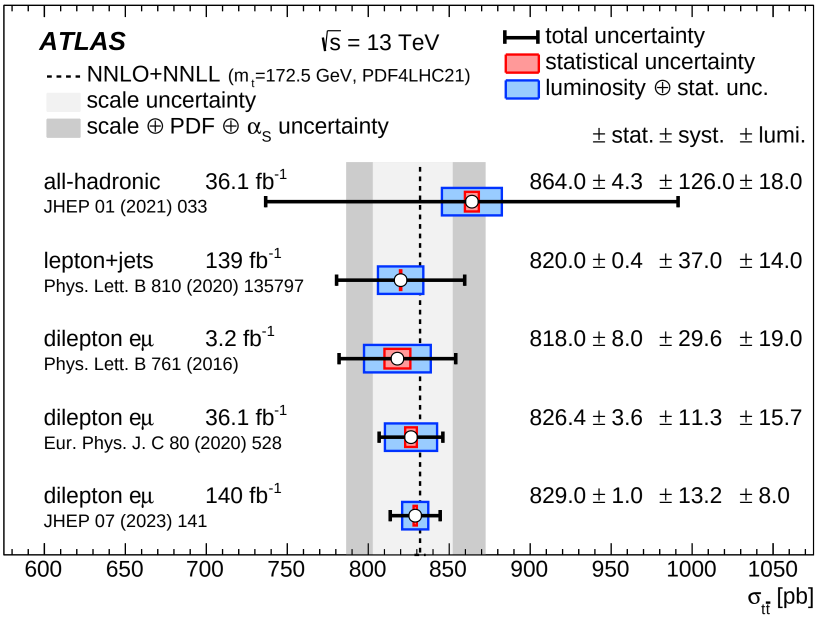

Figure 1.4: Comparison of measurements of the inclusive top-quark pair production cross-section at $\sqrt{s}$ =13 TeV with theoretical predictions. The experimental uncertainties are separated into statistical and systematic components, with the latter including the contribution from luminosity calibration. Adapted from Ref. [18].

a fill, real-time monitoring enables optimized decisions regarding beam dumps, injection cycles, and fill durations, maximizing the delivered and recorded integrated luminosity over a run.

Table 1.1 summarizes the evolution of collected integrated luminosity and corresponding uncertainty across different data-taking periods of the ATLAS experiment.

Table 1.1: Integrated luminosities with corresponding uncertainties recorded with the ATLAS detector at the LHC. Only proton-proton datasets are shown.

Dataset	$\sqrt{s}$ (TeV)	$\mathcal{L}_{int}$ [fb^{-1}]	$\delta\mathcal{L}_{int}/\mathcal{L}_{int}$	Ref.
Run 1 (2010)	7	0.05	3.4 %	[19]
Run 1 (2011)	7	5.5	1.8 %	[20]
Run 1 (2012)	8	22.7	1.9 %	[21]
Run 2 (2015)	13	3.24	1.13 %	[22]
Run 2 (2016)	13	33.40	0.89 %	[22]
Run 2 (2017)	13	44.63	1.13 %	[22]
Run 2 (2018)	13	58.79	1.10 %	[22]
Run 2 (2015–18 combined)	13	140.07	0.83 %	[22]
Run 2 (Low pile-up 2017)	5.02	0.257	1.6 %	[23]
Run 2 (Low pile-up 2017–18)	13	0.335	1.5 %	[23]
Run 3 (2022)	13.6	31.4	2.2 %	[24]
Run 3 (2023)	13.6	27.6	2.04 %	[25]
Run 3 (2024)	13.6	107.9	2.00 %	[26]
Run 3 (2022-24 combined)	13.6	166.9	1.90 %	[26]

1.3 A brief overview of the Standard Model

Over the past 130 years, particle physics has evolved from the discovery of the electron to the formulation of a unified theory that describes nearly all the known forces of nature. The culmination of this effort is the Standard Model (SM), a Quantum Field Theory (QFT) [27, 28] that combines Quantum Electrodynamics (QED) [29–31], the Electroweak (EW) theory [32–34], and Quantum Chromodynamics (QCD) [35–37] into a single coherent framework. It provides a remarkably successful description of the behavior and interactions of all known elementary particles, except gravity, whose effects become relevant only near the Planck scale, $M_{\mathrm{Pl}} \sim 10^{19}$ GeV [38–40]. A more comprehensive discussion of the SM and its historical development can be found in Refs. [41–45].

Within the SM, all matter and radiation arise from a small set of quantum fields. These include spin$-\frac{1}{2}$ fermions, which constitute matter; spin-1 gauge bosons, which mediate interactions; and a single spin-0 scalar field, the Higgs boson, responsible for generating masses of the elementary particles. Fermions are grouped according to their electric charge into two groups: *leptons* (ℓ) and *quarks* (q). For every matter particle, a corresponding antiparticle exists with identical mass and spin and opposite additive quantum numbers, except for neutrinos (ν), for which it remains unresolved whether they are distinct (Dirac) or identical (Majorana) to their antiparticles [46]. More precisely, within the set of elementary particles, all charged leptons and all quarks have their respective antiparticles. Leptons carry integer charge, while quarks possess fractional electric charge $\pm\frac{1}{3}$ or $\pm\frac{2}{3}$. Quarks also carry an additional quantum number, the *color charge*, which can take three values conventionally labeled red (r), green (g), and blue (b). They combine into color-neutral bound states known as hadrons: mesons ($q\bar{q}$) and baryons (qqq or $\bar{q}\bar{q}\bar{q}$). Gauge bosons mediate the fundamental interactions: eight gluons (g) transmit the strong force between quarks, the weak interaction is carried by the massive bosons W^+, W^-[4], and Z, while the photon γ mediates the electromagnetic force. Leptons interact through the weak interaction, and if charged, also through electromagnetism. Quarks, on the other hand, participate in all three interactions. Fermions occur in three generations of increasing mass. The first generation forms the stable matter of the visible Universe, whereas the second and third consist of unstable particles that decay rapidly into lighter states. The pattern of replicated generations remains one of the open questions in the SM. The complete set of elementary particles, together with their main quantum numbers, is summarized in Figure 1.5.

In QFT, particles are described as quantized excitations of fields $\phi_i(x)$ that depend on the space–time coordinates x. Fermions are represented by spinor fields $\psi(x)$, while gauge bosons are described by vector fields $A_\mu(x)$. The dynamics of a system are determined by the *Lagrangian density* $\mathcal{L}$, a function of the fields and their space–time derivatives $\partial_\mu \phi_i(x)$. The principle of least action requires the action integral $S = \int \mathcal{L}\, d^4x$ to be stationary, leading to the Euler–Lagrange equations of motion:

$$\partial_\mu \left(\frac{\partial \mathcal{L}}{\partial(\partial_\mu \phi)} \right) - \frac{\partial \mathcal{L}}{\partial \phi} = 0, \tag{1.28}$$

for each field ϕ in the theory.

Defining feature of the SM is its high degree of symmetry. According to Noether's theorem [48], each continuous symmetry of the Lagrangian corresponds to a conserved quantity: invariance under translations implies conservation of momentum, invariance in time leads to energy conservation, and rotational invariance yields angular momentum conservation. A generic field $\phi(x)$ transforms under a symmetry operation U as:

$$\phi(x) \to \phi'(x) = U\phi(x). \tag{1.29}$$

---

[4] In the following text, $W^\pm$ bosons are generally referred to as W unless the charge needs to be specified explicitly.

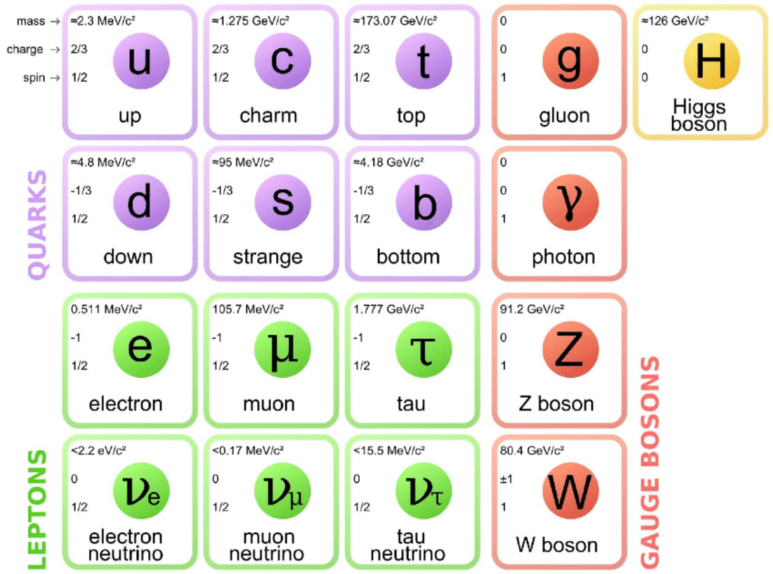

Figure 1.5: Standard Model particles [47].

If the equations of motion remain unchanged under this transformation, U represents a true symmetry of the theory. When U is constant, the symmetry is *global*; if U depends on space–time, $U(x)$, it is a *local* or *gauge* symmetry. The set of such unitary transformations forms a Lie group [49]. Abelian groups describe commuting transformations, while non-Abelian groups correspond to non-commuting ones. The Poincaré group, which contains translations, rotations, and Lorentz boosts, governs the space–time symmetries of all relativistic field theories. Additional internal symmetries describe charge, color, and weak isospin. Electromagnetic interactions preserve parity (P) and charge conjugation (C), whereas the weak interaction violates both P and C and even the combined CP symmetry. However, the overall CPT symmetry, where T denotes time inversion, is conserved in all Lorentz-invariant QFTs [50].

A *gauge theory* is a QFT whose Lagrangian remains invariant under local transformations of a given Lie group. The Standard Model is a non-Abelian gauge theory based on the symmetry group:

$$SU(3)_C \otimes SU(2)_L \otimes U(1)_Y, \tag{1.30}$$

where the indices C, L, and Y refer to color, left-handed chirality, and weak hypercharge, respectively. Each subgroup governs one sector of the interactions:

- $SU(3)_C$: Quantum Chromodynamics — the strong interaction between quarks and gluons;
- $SU(2)_L \otimes U(1)_Y$: Electroweak theory — unifying the weak and electromagnetic forces;
- Yukawa sector: interactions between the Higgs field and fermions that generate fermion masses;
- Higgs sector: dynamics of the scalar field responsible for electroweak symmetry breaking.

The complete SM Lagrangian density can therefore be expressed in the form of the following relation:

$$\mathcal{L}_{\text{SM}} = \mathcal{L}_{\text{EW}} + \mathcal{L}_{\text{QCD}} + \mathcal{L}_{\text{Yukawa}} + \mathcal{L}_{\text{Higgs}}. \tag{1.31}$$

Here $\mathcal{L}_{\text{EW}}$ and $\mathcal{L}_{\text{QCD}}$ refer to the gauge interactions of leptons and quarks, $\mathcal{L}_{\text{Yukawa}}$ is related to the couplings to the Higgs field, and $\mathcal{L}_{\text{Higgs}}$ describes the potential and self-interactions of the scalar field. This structure ensures that all known fundamental forces, except gravity, are embedded within a single renormalizable quantum field theory. The renormalizability of the SM guarantees that infinities appearing in perturbative calculations can be absorbed into a finite number of measurable parameters, ensuring that all physical predictions remain finite and testable. This property underlies the extraordinary precision with which quantities such as magnetic moments and decay rates can be calculated and compared to experiment.

In its minimal form, the SM contains 18 independent parameters: six quark masses, three charged-lepton masses, four Cabibbo–Kobayashi–Maskawa (CKM) parameters [51, 52], three gauge couplings, the Higgs boson mass, and the vacuum expectation value of the Higgs field. The CKM parameters describe the mixing between different quark generations and introduce complex phases responsible for CP violation in weak decays — an essential ingredient in explaining the observed matter–antimatter asymmetry in the Universe. Some of these parameters—such as the gauge couplings—are not directly observable but are related to precisely measured quantities, including the Fermi constant G_F, the strong coupling α_s, and the Z-boson mass m_Z. Once these quantities are experimentally determined, the SM enables the systematic calculation of scattering amplitudes, decay rates, and cross-sections using perturbation theory.

Finally, the Higgs sector plays a central role in reconciling gauge symmetry with particle masses. The mechanism of spontaneous symmetry breaking, discussed later in this chapter, generates nonzero masses for the W and Z bosons and for fermions through their Yukawa couplings to the scalar field, while leaving the photon massless.

1.4 The Standard Model Lagrangian

The EW sector of the Standard Model unifies the electromagnetic and weak interactions under a common theoretical framework. Historically, the electromagnetic interaction was described by QED [53, 54], the first successful quantum field theory. QED is an Abelian gauge theory based on the $U(1)$ symmetry group and remains the most precisely tested part of the SM, predicting phenomena such as the electron's anomalous magnetic moment with remarkable accuracy [55].

A free fermion of mass m satisfies the Dirac equation:

$$(i\gamma^\mu\partial_\mu - m)\psi(x) = 0 \tag{1.32}$$

which is derived from the Lagrangian density:

$$\mathcal{L} = \overline{\psi}(x)(i\gamma^\mu\partial_\mu - m)\psi(x). \tag{1.33}$$

The first term describes the kinetic energy of the fermion field, while the second represents its mass. To make the theory invariant under local phase transformations of the form:

$$\psi(x) \to \psi^{'}(x) = e^{i\alpha(x)}\psi(x), \tag{1.34}$$

a gauge field $A_\mu(x)$ is introduced, and the ordinary derivative is replaced by a *covariant derivative*:

$$\partial_\mu \;\to\; D_\mu \;=\; \partial_\mu - i\,e\,A_\mu(x)\,, \tag{1.35}$$

where e is the electric charge of the fermion. The transformation of the gauge field:

$$A_\mu(x) \;\to\; A'_\mu(x) \;=\; A_\mu(x) - \partial_\mu\alpha(x), \tag{1.36}$$

preserves local gauge invariance. The complete QED Lagrangian, including the photon kinetic term defined by the field-strength tensor, $F_{\mu\nu} = \partial_\mu A_\nu - \partial_\nu A_\mu$, becomes:

$$\mathcal{L}_\mathrm{QED} \;=\; \bar{\psi}(x)\left(i\,\gamma^\mu\partial_\mu - m\right)\psi(x) \;-\; e\,\bar{\psi}(x)\,\gamma^\mu A_\mu(x)\,\psi(x) \;-\; \frac{1}{4}\,F_{\mu\nu}F^{\mu\nu}\,. \tag{1.37}$$

Any explicit photon mass term would break local gauge invariance, explaining why the photon must remain massless. The small value of the fine-structure constant, $\alpha = e^2/4\pi \approx 1/137$, allows for highly accurate perturbative calculations.

Weak interaction is more complex because it involves both charged and neutral currents and acts only on left-handed fermions and right-handed antifermions. Following the success of QED, the weak force was modeled by extending gauge invariance to a non-Abelian $SU(2)$ symmetry [56]. The chiral components of a fermion field are defined as:

$$\psi_L = \frac{1}{2}(1-\gamma^5)\,\psi \qquad \text{and} \qquad \psi_R = \frac{1}{2}(1+\gamma^5)\,\psi\,, \tag{1.38}$$

where ψ_L and ψ_R represent left- and right-handed projections, respectively. Left-handed fermions appear in weak isospin doublets with $I = 1/2$ and $I_3 = \pm 1/2$, while right-handed fermions are isospin singlets ($I_3 = 0$):

$$\begin{pmatrix} u \\ d \end{pmatrix}_L, \quad \begin{pmatrix} c \\ s \end{pmatrix}_L, \quad \begin{pmatrix} t \\ b \end{pmatrix}_L, \quad \begin{pmatrix} \nu_e \\ e \end{pmatrix}_L, \quad \begin{pmatrix} \nu_\mu \\ \mu \end{pmatrix}_L, \quad \begin{pmatrix} \nu_\tau \\ \tau \end{pmatrix}_L. \tag{1.39}$$

This chiral structure explains why weak interactions violate parity symmetry.

The Electroweak theory, developed by Glashow, Weinberg, and Salam [32–34, 57], unifies electromagnetic and weak forces under the symmetry group $SU(2)_L \otimes U(1)_Y$. Below the electroweak scale (~ 246 GeV), this symmetry is spontaneously broken. A new quantum number, the weak hypercharge Y, is introduced through the relation:

$$Q = I_3 + \frac{Y}{2}\,, \tag{1.40}$$

where Q is the electric charge and I_3 the third component of weak isospin. The $SU(2)_L$ group provides three gauge fields W^a_μ ($a = 1, 2, 3$), while $U(1)_Y$ contributes one gauge field B_μ. The electroweak Lagrangian for massless fermions and gauge fields is:

$$\mathcal{L} = i\,\bar{\psi}(x)\,\gamma^\mu D_\mu\,\psi(x) - \frac{1}{4}W^a_{\mu\nu}\,W^{a\,\mu\nu} - \frac{1}{4}B_{\mu\nu}\,B^{\mu\nu}\,, \tag{1.41}$$

where

$$W^a_{\mu\nu} = \partial_\mu W^a_\nu - \partial_\nu W^a_\mu + g\,\epsilon^{abc}\,W^b_\mu W^c_\nu\,, \qquad B_{\mu\nu} = \partial_\mu B_\nu - \partial_\nu B_\mu\,, \tag{1.42}$$

and

$$D_\mu = \partial_\mu - i\,g\,\frac{\tau^a}{2}\,W^a_\mu - i\,g'\,\frac{Y}{2}\,B_\mu\,, \tag{1.43}$$

with τ^a being the Pauli matrices and g, g' the weak and hypercharge coupling constants. Because explicit mass terms would violate gauge invariance, all fields remain massless at this stage. The generation of particle masses happens through the mechanism of spontaneous symmetry breaking, explained later in this section.

Strong interaction is described by a non-Abelian gauge theory based on the $SU(3)_C$ symmetry group [36, 58–60]. Quarks appear in three colors—red, green, and blue—represented by the color triplet field:

$$\psi_f(x) = \begin{pmatrix} q_r \\ q_g \\ q_b \end{pmatrix}, \tag{1.44}$$

where f denotes the quark flavor. The QCD Lagrangian density is given by:

$$\mathcal{L}_{\text{QCD}} = \sum_f \bar{\psi}^{(f)}_j \left(i\,\gamma^\mu D^{jk}_\mu - m_f\right)\psi^{(f)}_k - \frac{1}{4}G^a_{\mu\nu}\,G^{a\,\mu\nu}\,, \tag{1.45}$$

where

$$D_\mu \;=\; \partial_\mu \;-\; i\, g_s\, G^a_\mu(x)\, \frac{\lambda^a}{2}\,, \tag{1.46}$$

and the field-strength tensor is

$$G^a_{\mu\nu} \;=\; \partial_\mu G^a_\nu \;-\; \partial_\nu G^a_\mu \;-\; g_s\, f^{abc}\, G^b_\mu G^c_\nu\,. \tag{1.47}$$

Here λ^a are the Gell-Mann matrices (generators of $SU(3)$), f^{abc} the structure constants, and g_s the strong coupling constant. The first term describes quark–gluon interactions and kinetic energy of quarks, while the second represents gluon dynamics and their self-interaction—an intrinsic property of non-Abelian gauge theories. Since no gauge-invariant mass term can be written, gluons are massless.

Strength of the strong coupling $\alpha_s = g_s^2/2\pi$ depends on the momentum scale Q of the process. The coupling decreases with increasing energy, a property known as *asymptotic freedom*, while at low energies quarks are confined into color-neutral bound states, or hadrons. At short distances, quarks and gluons behave as almost free particles, whereas at larger scales confinement prevents them from existing as free. When produced at high momentum in hard scatterings, they hadronize into jets of color-neutral particles observed in detectors.

The electroweak theory in its symmetric form predicts massless vector bosons and fermions, contradicting experimental observations. The resolution lies in the mechanism of *spontaneous symmetry breaking* (SSB), independently proposed by Brout, Englert, Higgs, Guralnik, Hagen, and Kibble in the 1960s [34, 49, 61–65]. SSB occurs when the ground state of a system does not share the symmetry of its governing equations, leading to the appearance of massive fields while preserving gauge invariance. For a complex scalar doublet field:

$$\Phi(x) \;=\; \begin{pmatrix} \Phi^+ \\ \Phi^0 \end{pmatrix} \;=\; \frac{1}{\sqrt{2}} \begin{pmatrix} \Phi_1 + i\,\Phi_2 \\ \Phi_3 + i\,\Phi_4 \end{pmatrix}, \tag{1.48}$$

the potential takes the form:

$$V\big(\Phi^\dagger\Phi\big) \;=\; \mu^2\, \Phi^\dagger\Phi \;+\; \lambda\, \big(\Phi^\dagger\Phi\big)^2\,, \tag{1.49}$$

where $\lambda > 0$. For $\mu^2 > 0$ the potential has a single minimum at $\Phi = 0$, but for $\mu^2 < 0$ it acquires a degenerate ring of minima, as shown in Figure 1.6. Choosing one vacuum configuration spontaneously breaks the symmetry and provides gauge bosons and fermions with mass.

The electroweak Lagrangian containing the scalar field is

$$\mathcal{L} \;=\; \big(D_\mu\Phi\big)^\dagger \big(D^\mu\Phi\big) \;-\; V\big(\Phi^\dagger\Phi\big)\,, \tag{1.50}$$

where the covariant derivative D_μ is defined as in Eq. (1.46). The vacuum expectation value (VEV) $v = \sqrt{-\mu^2/\lambda}$ defines the minimum of the potential,

$$\Phi_0 \;=\; \frac{1}{\sqrt{2}} \begin{pmatrix} 0 \\ v \end{pmatrix}\,, \tag{1.51}$$

which spontaneously breaks $SU(2)_L \otimes U(1)_Y$ to the electromagnetic $U(1)_{\text{em}}$. Expanding around this vacuum leads to three massive gauge bosons ($W^\pm$, Z) and one massless photon (A), given by:

$$W^\pm_\mu \;=\; \frac{1}{\sqrt{2}}\big(W^1_\mu \mp i\, W^2_\mu\big), \tag{1.52}$$

$$Z_\mu \;=\; -\sin\theta_W\, B_\mu + \cos\theta_W\, W^3_\mu, \tag{1.53}$$

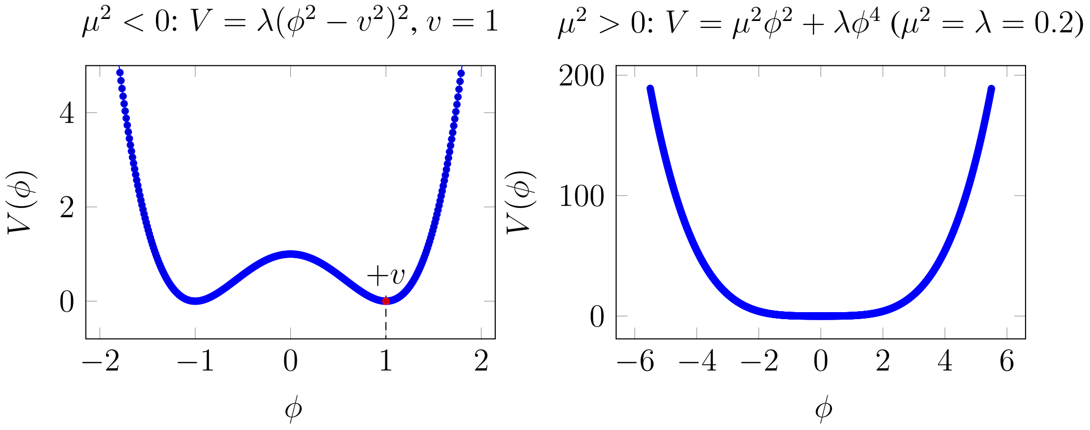

Figure 1.6: Higgs potential (2D view) with the $+v$ minimum indicated on the left panel. The left panel corresponds to $\mu^2 < 0$, producing a symmetry-breaking vacuum at $\phi = \pm v$, while the right panel shows the symmetric case $\mu^2 > 0$ with a single minimum at $\phi = 0$. For illustrative purposes, dimensionless parameters are set to $v = 1$ and $\mu^2 = \lambda = 0.2$.

$$A_\mu \;=\; \cos\theta_W\, B_\mu + \sin\theta_W\, W^3_\mu, \tag{1.54}$$

where θ_W is Weinberg's angle, and $\tan\theta_W = g'/g$ and $e = g'\cos\theta_W = g\sin\theta_W$. Substituting Φ_0 into the kinetic term gives the gauge-boson mass expressions:

$$\left(D_\mu\Phi_0\right)^\dagger\left(D^\mu\Phi_0\right) \;=\; \frac{g^2v^2}{4}\,W^+_\mu W^{-\mu} \;+\; \frac{(g^2+g'^2)\,v^2}{8}\,Z_\mu Z^\mu \;+\; \cdots\,, \tag{1.55}$$

leading to

$$m_f \;=\; \frac{y_f\,v}{\sqrt{2}}, \qquad m_W \;=\; \frac{g\,v}{2}, \qquad m_Z \;=\; \frac{v}{2}\sqrt{g^2+g'^2}\,. \tag{1.56}$$

Photon remains massless, while fermion masses arise through Yukawa couplings y_f between the Higgs and fermion fields. The Higgs boson mass is $m_H = \sqrt{2\lambda v^2}$. After nearly five decades of experimental searches, the discovery of the Higgs boson was announced at CERN by ATLAS and CMS experiments [66, 67].

1.5 Tests and limitations of the Standard Model

Over the past four decades, the Standard Model has been extensively tested at electron–positron colliders (LEP, SLC) [68, 69], lepton–hadron colliders (HERA) [70, 71], and hadron colliders (Tevatron, LHC) [72, 73]. Its predictions have been confirmed to extraordinary precision, often at the per-mille level. The model successfully accounts for a vast range of cross-section measurements across more than ten orders of magnitude, as illustrated in Figure 1.7, demonstrating its robustness and internal consistency. Despite its success, the SM is believed to be incomplete [74]. Several open issues motivate the search for physics beyond it:

- **Gravity:** The SM does not incorporate gravitational interactions and is valid only up to the Planck scale, $M_{\mathrm{Pl}} \sim 10^{19}$ GeV.
- **Dark matter and dark energy:** Observations show that ordinary matter accounts for less than 5% of the Universe, while dark matter and dark energy dominate the cosmic energy density. No SM particle fits the role of a dark matter candidate.

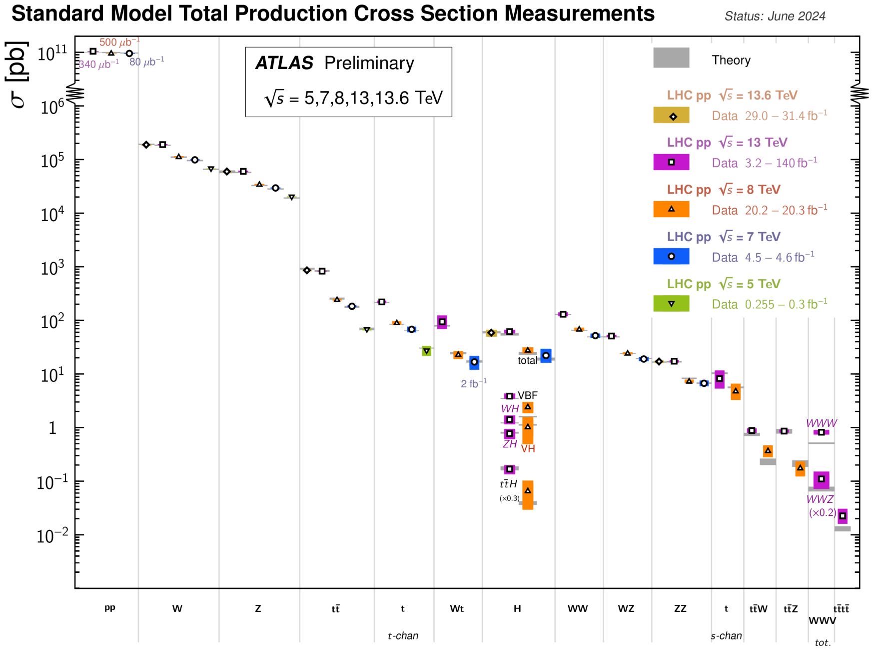

Figure 1.7: Summary of several SM total production cross-section measurements performed by the ATLAS experiment, compared to the corresponding theoretical expectations [76].

- **Hierarchy problem:** The large gap between the electroweak and Planck scales requires fine-tuning of the Higgs mass corrections, hinting at new dynamics at the TeV scale.
- **Neutrino masses:** The SM neutrinos are massless, contrary to experimental evidence from neutrino oscillations.
- **Matter–antimatter asymmetry:** The observed baryon asymmetry of the Universe cannot be explained by the small CP violation in the SM.

Among possible extensions, Supersymmetry (SUSY) [75] provides elegant solutions to several of these issues by postulating a symmetry between bosons and fermions. Each SM particle would have a heavier supersymmetric partner, stabilizing the Higgs mass and providing a natural dark matter candidate. The minimal realization of this framework, the Minimal Supersymmetric Standard Model (MSSM), remains one of the most studied alternatives, although no superpartners have been observes so far.

1.6 Electroweak bosons at hadron colliders

Hadron colliders offer a compelling environment for studying electroweak physics. In such machines, the production of W- and Z-bosons occurs abundantly through the Drell–Yan (DY) mechanism [77], offering clean experimental signatures and a means to probe partonic dynamics inside the proton. The complexity of these processes arises from the fact that hadrons are composite bound states: the hard interaction is not between the protons themselves, but among their underlying constituents. The proton is a strongly bound system composed of three valence quarks — two of type u and one of type d — which are held together by the exchange of gluons, the mediators of the strong interaction. The continual emission and reabsorption of gluons gives rise to short-lived quark–antiquark pairs that fill the proton with a dense background of low-momentum partons, often referred to as the *partonic* *sea*. The balance between valence quarks, sea quarks, and gluons determines the internal momentum structure of the proton and hence the probability for a given parton to participate in a hard scattering.

The conceptual framework used to describe these high-energy interactions is the *parton model*, first formulated by Feynman [78]. In this model, the proton is treated as an ensemble of point-like constituents — quarks and gluons — each carrying a fraction of the proton momentum and interacting incoherently in short-distance collisions. This perspective proved remarkably successful in explaining the results of deep inelastic scattering (DIS) experiments, which provided the first experimental evidence that nucleons possess an internal quark structure [79]. Within the parton model, these constituents are collectively referred to as *partons*, a term encompassing both valence and sea quarks as well as the gluons that mediate their interactions. At sufficiently high energies, these constituents interact as nearly free particles, allowing QCD to describe the dynamics of hadronic collisions in terms of parton-level scattering processes.

1.6.1 Phenomenology of proton–proton collisions

Collisions between protons can proceed through several qualitatively different mechanisms, depending on the nature of the interaction and the momentum transfer involved. From a phenomenological point of view, these processes can be grouped into two broad classes: *elastic* and *inelastic* scattering.

In elastic scattering, the incident protons interact without internal excitation or particle production, and the total kinetic energy of the system is conserved. The protons remain intact, and only a small amount of momentum is exchanged. Inelastic interactions, in contrast, involve the dissociation of one or both protons and the production of secondary particles. Depending on the characteristic momentum of these products, inelastic processes are further subdivided into *soft* and *hard* scattering regimes.

Soft inelastic events, such as diffractive and non-diffractive (minimum-bias) interactions, are dominated by non-perturbative QCD effects. They typically produce large numbers of low-momentum charged particles, and their theoretical description relies heavily on phenomenological modeling and event generators tuned to data. Hard scattering events, on the other hand, involve partons that exchange large transverse momentum. In this regime, the strong coupling constant α_s becomes small due to asymptotic freedom, and perturbative QCD can be applied to calculate parton-level cross-sections with good precision.

A schematic illustration of a typical hard scattering process is shown in Figure 1.8. In such events, the short-distance interaction occurs between two partons, while the remaining components of the incoming hadrons form so-called beam remnants. The outgoing partons radiate soft and collinear gluons (and occasionally photons), producing cascades of initial- and final-state radiation (ISR and FSR), collectively referred to as a *parton shower*. As the process evolves toward lower energy scales, confinement sets in and coloured partons recombine into colour-neutral hadrons — a process referred to as *hadronization*. These hadrons may subsequently decay into other hadrons or leptons, giving rise to a complex final state observed in the detector. Soft interactions among the proton remnants and secondary particles lead to additional low-energy activity in the event, collectively known as the *underlying event* (UE).

In a hard proton–proton (pp) interaction, the total momentum of the proton P is shared among its constituent partons. Each parton i carries a fraction x_i of the proton momentum, defined by $p_i = x_i P$. The momentum transfer Q^2 associated with the hard scattering sets the relevant energy scale of the process. Because the longitudinal momenta of the colliding partons are not directly measurable, quantities such as the partonic centre-of-mass energy $\hat{s}$ depend on the momentum fractions x_1 and x_2 of the two interacting partons.

The probability of finding a parton of flavour i with a given momentum fraction x_i at scale Q^2 is en-

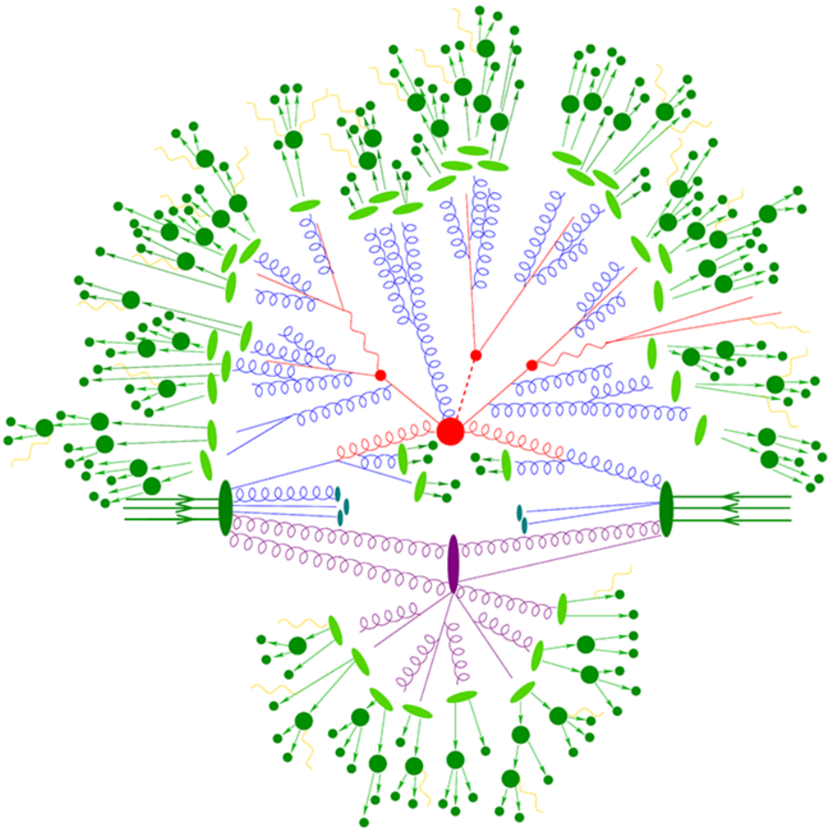

Figure 1.8: Schematic representation of a proton–proton collision. The hard scattering, indicated by the red circles, corresponds to the short-distance parton–parton interaction producing the primary high-energy system. Additional QCD radiation, illustrated by the light green circles, arises from initial- and final-state parton showers that precede hadronization. The produced partons subsequently hadronize, and the resulting hadrons may undergo secondary decays, represented by the dark green circles. Soft interactions between beam remnants and multiple parton interactions form the underlying event, shown in purple. Adopted from [80].

coded in the *parton distribution functions* (PDFs) $f_i(x_i, Q^2)$. Their evolution with Q^2 is described by the Dokshitzer–Gribov–Lipatov–Altarelli–Parisi (DGLAP) equations, while the x-dependence must be determined empirically from fits to data across a wide range of experiments [81]. Figure 1.9 illustrates the regions of the (x, Q^2) phase space probed by various measurements, highlighting the coverage achieved for W and Z production at the LHC.

Determination of PDFs involves global analyses of experimental data using parametrized functional forms at an initial scale. The fits incorporate results from fixed-target deep inelastic scattering, Drell–Yan production, inclusive jet measurements, and electroweak boson production at both the Tevatron and the LHC. An example from the CTEQ analysis is shown in Figure 1.10, where the parton densities for various flavours are compared at two characteristic energy scales. At low x, the gluon and sea-quark densities dominate, while at higher x the proton momentum is largely carried by the valence quarks.

To quantify the interaction rate between the two hadrons, it is common to use a hadronic cross-section. The relation between the hadronic and partonic cross-sections is given by:

$$\sigma_{A+B\to X}(\mu_f, \mu_r) = \sum_{a\in A,\, b\in B} \int dx_a\, dx_b\, f_{a/A}(x_a, \mu_f)\, f_{b/B}(x_b, \mu_f)\, \hat{\sigma}_{ab\to X}(\mu_f, \mu_r), \tag{1.57}$$

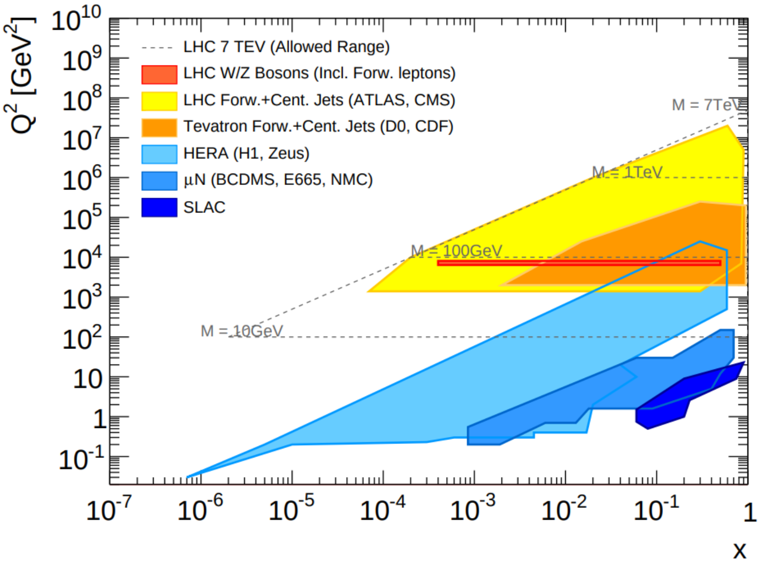

Figure 1.9: Kinematic coverage in the (x, Q^2) plane probed by different experiments. The shaded regions indicate areas explored by DIS and collider measurements, with the LHC region for W/Z production marked explicitly [82].

where a and b represent partons within protons A and B with momentum fractions x_a and x_b, respectively, and $\hat{\sigma}_{ab\to X}$ is the hard-scattering cross-section for those partons. The sum runs over all parton flavours contributing to the process.

Interacting quarks can radiate off gluons, where the probability of emitting a (collinear) gluon increases for decreasing momentum of the radiated gluon, resulting in divergent integrals in the cross-section calculation. Divergent integrals can be managed by separating the divergent part from the finite terms at a factorization scale μ_f. The divergent terms are absorbed into the PDFs using the factorization theorem [83, 84], leading to an infrared-safe expression of the partonic cross-section, which can still be calculated perturbatively. The μ_f is usually taken as the mass of the outgoing system of particles ($\mu_F \approx m_X$). The μ_r is the renormalization scale, which defines the QCD running coupling and the renormalization constant α_s. In the computation of observables such as cross-sections, only a finite number of terms can be calculated, which all depend on μ_r. The renormalization scale is usually chosen to be equal to the energy scale of the interaction, as this choice eliminates large logarithms in the loop diagrams and therefore optimizes the convergence of the perturbative expansion. However, the choice of μ_r represents a source of uncertainty in the calculation. It is also common to choose the factorization scale to be the same as the renormalization scale ($\mu_f = \mu_r$).

The parton-level hard-scattering cross-section is calculated using perturbative QCD as a power-series expansion in α_s:

$$\hat{\sigma}_{ab\to X} = \hat{\sigma}_0 + \alpha_s(\mu_R^2)\hat{\sigma}_1 + \alpha_s^2(\mu_R^2)\hat{\sigma}_2 + \mathcal{O}(\alpha_s^3), \tag{1.58}$$

where the first term represents the cross-section calculated at leading order (LO), and each subsequent term adds higher-order corrections: the second term adds next-to-leading order (NLO), and the third term adds next-to-next-to-leading order (NNLO). For processes calculated at LO, no radiative corrections are added to the initial or final states and only the matrix-element computation is present. In NLO calculations, real emissions (extra partons) or virtual corrections are included, each carrying a proportionality to α_s[5]. When the perturbative series does not converge because of the presence

---

[5] Alongside higher order corrections (NLO, NNLO, etc.) in QCD, higher order electroweak corrections can be introduced. Generic size $\mathcal{O}(\alpha) \sim \mathcal{O}(\alpha_s^2)$ suggests NLO EW ≈ NNLO QCD..

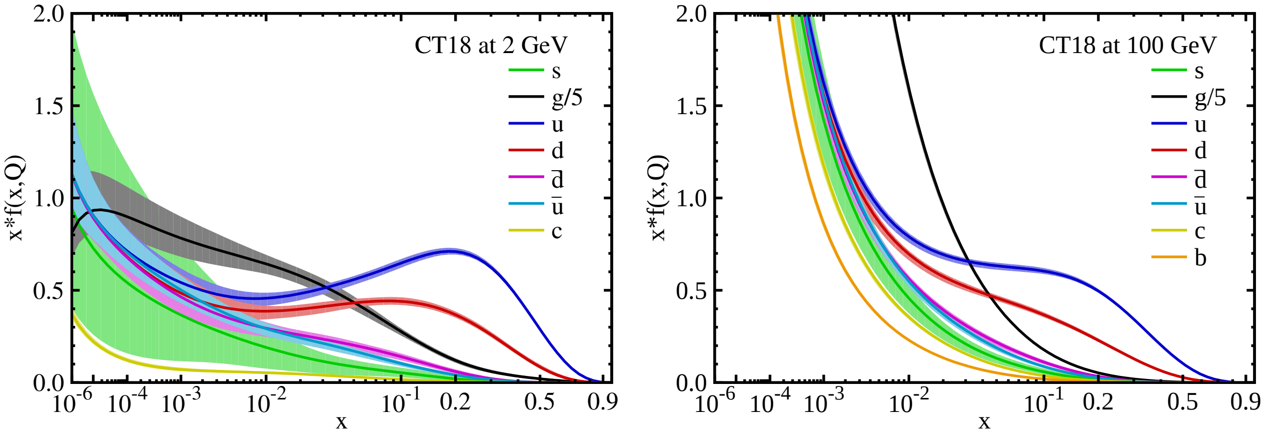

Figure 1.10: Parton distribution functions obtained by the CTEQ collaboration corresponding to the PDF set CT18 [85]. Left panel shows the PDFs evaluated at $Q = 2$ GeV, while the right one shows PDFs evaluated at $Q = 100$ GeV for the parton flavours u, $\bar{u}$, d, $\bar{d}$, $s = \bar{s}$, and g. The gluon distribution has been scaled as $g(x, Q)/5$ for visual clarity.

of large logarithms from the phase-space integration of soft and collinear gluon singularities, the so-called logarithmic resummation technique is used. This technique defines a convergent function in which the individual terms of the original function are rescaled and summed to the fixed-order contribution to restore convergence. The first term of the series represents the leading-log (LL) contribution, the second one the next-to-leading-log (NLL), and so on. The production cross-sections of main Standard Model processes in proton–proton collisions at the LHC and proton–antiproton collisions at other experiments as a function of centre-of-mass energy $\sqrt{s}$ are shown in Figure 1.11.

1.6.2 W-boson production and decay

In proton–proton collisions, the W bosons at LO are produced in the Drell–Yan process of quark–antiquark annihilation:

$$u\bar{d} \to W^+, \; d\bar{u} \to W^-.$$

At the LHC, W^+ bosons are produced with valence u and sea $\bar{d}$ quarks, and W^- bosons from valence d and sea $\bar{u}$ quarks. Since protons consist of two u and one d valence quark, the total number of produced W^+ bosons is larger. The next largest contribution to W-boson production is from sea c and s quarks, contributing about 17% for W^+ and 23% for W^- bosons. Although these are sea–sea processes, they dominate the Cabibbo-suppressed process from u and s valence–sea contributions [86]. The flavour decomposition for W production at LO is presented in Figure 1.12. Table 1.2 summarizes the contributing processes to W-boson production at LO, NLO, and NNLO in QCD. Besides these, higher order corrections include electroweak contributions, as well as mixed QCD–EW terms of order $\mathcal{O}(\alpha\alpha_s)$ [87]. The dominant source of electroweak corrections to W- and Z-boson production originates from QED final-state radiation, interference between ISR and FSR QED, purely weak corrections due to virtual-loop and box diagrams, and final-state emission of lepton pairs. Complete $\mathcal{O}(\alpha)$ electroweak corrections to the $pp \to W + X$, $W \to l\nu$ process were initially calculated in Refs. [88, 89].

The four-momenta of the interacting partons for the W-boson production at LO (Born level) are given by:

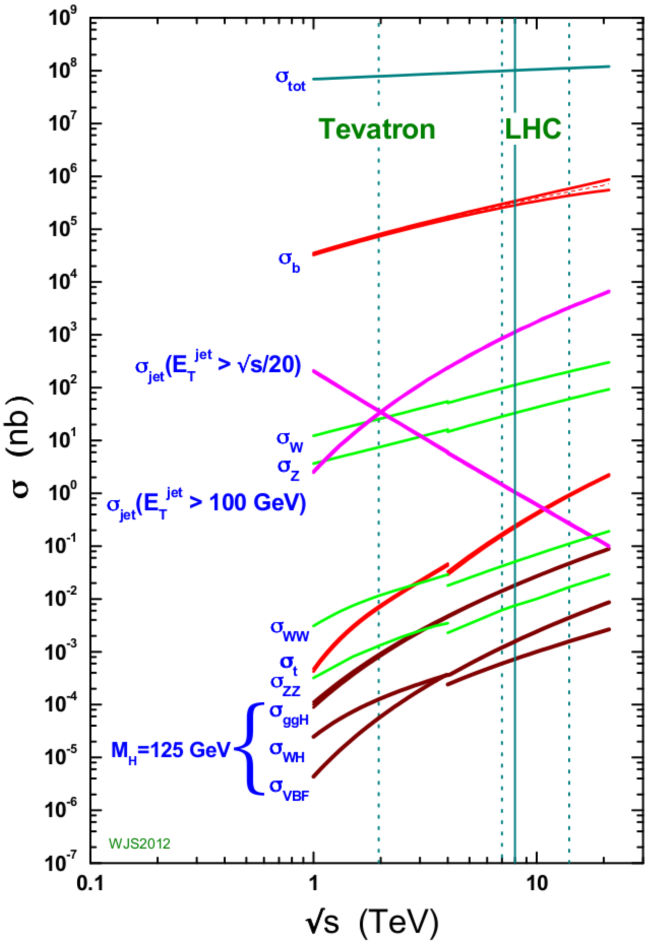

Figure 1.11: Cross-sections of selected $p\bar{p}$ and pp collisions processes versus centre-of-mass energy $\sqrt{s}$ [86].

$$p_1^\mu = \frac{\sqrt{s}}{2}(x_1,\, 0,\, 0,\, x_1), \tag{1.59}$$

$$p_2^\mu = \frac{\sqrt{s}}{2}(x_2,\, 0,\, 0,\, -x_2), \tag{1.60}$$

where the parton masses are neglected, assuming that the partons are exactly collinear with the colliding protons. The sum of the four-momenta of the W-boson decay products is defined as

$$\hat{s} = (p_1^\mu + p_2^\mu)^2 = s\, x_1 x_2. \tag{1.61}$$

Then the mass of the W boson is

$$\hat{s} = m_W^2. \tag{1.62}$$

The total partonic cross-section from Eq. (1.58) is calculated from the matrix element of the process [86]:

$$\hat{\sigma}(\hat{s}) \propto \left(\frac{G_F m_W^2}{\sqrt{2}}\right)^2 \frac{\hat{s}}{(\hat{s} - m_W^2)^2 - m_W^2 \Gamma_W^2}, \tag{1.63}$$

where the last fraction corresponds to the relativistic Breit–Wigner resonance distribution, which depends on $\hat{s}$. The Breit–Wigner resonance is a peak distribution at m_W with width Γ_W.

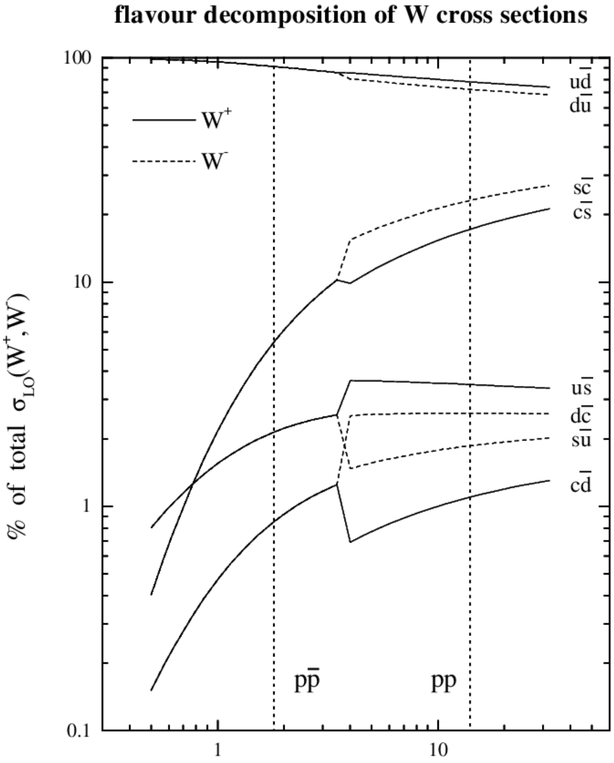

Figure 1.12: Parton decomposition of the W^+ (solid) and W^- (dashed) total cross-sections in proton–proton and proton–antiproton collisions as a function of $\sqrt{s}$ at LO. Individual contributions are shown as a percentage of the total cross-section in each case [86].

Table 1.2: The different contributing processes to W-boson production at LO, NLO, and NNLO in QCD [86].

Order	**Process**
α_s^0 (LO)	$q + \bar{q} \to W$
α_s^1 (NLO)	$q + \bar{q} \to W$ (one-loop corrections);
	$q(\bar{q}) + g \to W + q(\bar{q})$
α_s^2 (NNLO)	$q + \bar{q} \to W$ (two-loop corrections);
	$q + \bar{q} \to W + g$ (one-loop corrections);
	$q + \bar{q} \to W + g + g$;
	$q(\bar{q}) + g \to W + q(\bar{q})$ (one-loop corrections);
	$q(\bar{q}) + g \to W + q(\bar{q}) + g$;
	$q + \bar{q} \to W + q + \bar{q}$;
	$q(\bar{q}) + \bar{q}(q) \to W + q(\bar{q}) + \bar{q}(q)$;
	$g + g \to W + q + \bar{q}$

The W-boson decay modes are shown in Table 1.3. The decays are distributed nearly equally between the three lepton flavours. Since the jet production cross-section at hadron colliders is several orders of magnitude larger than the W-boson production cross-section (see Figure 1.11), the hadronic decay modes of the W boson are not suitable for precision measurements, even though their branching ratio is significantly higher than that of the leptonic decays. Consequently, precision W-boson measurements rely on the leptonic decay channels, where leptons refer primarily to electrons and muons, as these particles can be directly reconstructed in the detector. Due to its short lifetime, only the decay products of the τ lepton can be observed. Nevertheless, ATLAS has performed a cross-section measurement involving τ leptons, which was found to be consistent with the $e\nu$ and $\mu\nu$ results [90]. It should be noted that the branching ratio for $W \to \tau\nu$ in Table 1.3 does not include the most precise ATLAS measurement to date [91], shown in Figure 1.13.

Table 1.3: W-boson decay modes [92].

Decay mode	**Branching ratio [%]**
$W \to e\nu$	10.71 ± 0.16
$W \to \mu\nu$	10.63 ± 0.15
$W \to \tau\nu$	11.38 ± 0.21
$W \to$ hadrons	67.41 ± 0.27

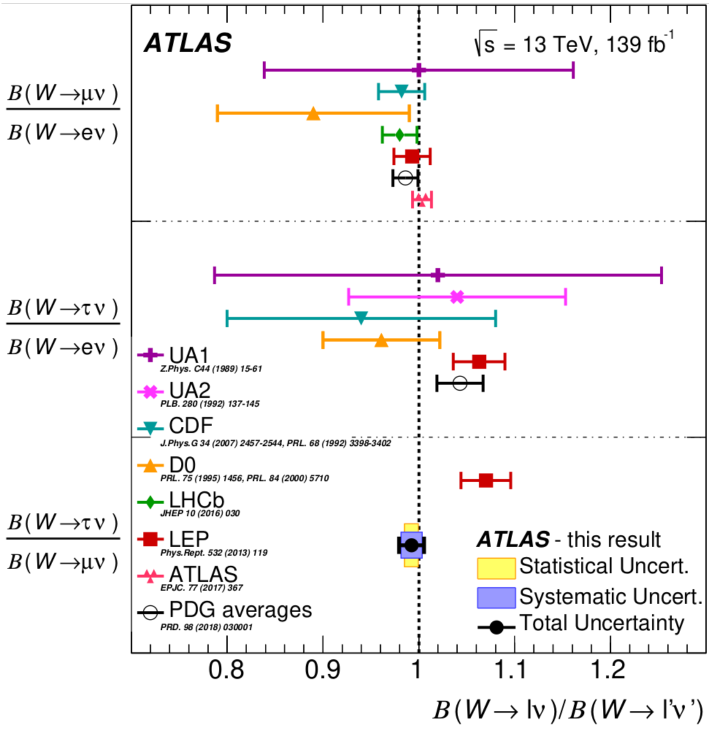

Figure 1.13: Comparison of the measured branching-ratio ratios of other leptonic W decays with respect to the τ channel, showing the ATLAS result alongside those from other experiments. The vertical dashed line indicates the SM expectation of lepton-flavour universality [91].

Chapter 2

The Experimental Setup

2.1 Nomenclature

Before discussing the detector device, it is helpful to introduce the terminology used throughout this thesis. The conventions described below are standard in accelerator and collider physics.

Centre-of-mass energy: Total energy available in the rest frame of the two colliding protons is expressed by the centre-of-mass energy $\sqrt{s}$, where s is defined as:

$$s = (p_1 + p_2)^2 = (p_1^\mu + p_2^\mu)(p_{1\mu} + p_{2\mu}), \tag{2.1}$$

with p_1^μ and p_2^μ denoting the four-momenta of the colliding particles and the Einstein summation convention used over the Lorentz index $\mu = 0, 1, 2, 3$. In the laboratory frame, it can be written as:

$$s = 2m_p^2 + 2\left(E_1 E_2 - \vec{p}_1 \cdot \vec{p}_2\right), \tag{2.2}$$

where E_i and $\vec{p}_i$ are the particle energies and three-momenta, respectively, and m_p is the proton mass. For symmetric proton–proton collisions with equal beam energies E_{beam} and opposite momenta, this simplifies to $\sqrt{s} = 2E_{\text{beam}}$ in the ultra-relativistic limit ($E_{\text{beam}} \gg m_p$).

Coordinate system: Standard right-handed coordinate system for the LHC is defined as follows: – the z-axis is taken along the nominal beam direction; – the x-axis points horizontally towards the center of the LHC ring; – the y-axis points vertically upwards. The x–y plane is called the transverse plane, while the z-direction defines the longitudinal axis. Angles are defined in the usual spherical coordinates: Polar angle θ is measured with respect to the beam (z) axis, while the azimuthal angle ϕ is defined in the transverse plane. The *A-side* of the detector corresponds to the positive-z direction, while the *C-side* corresponds to the negative-z direction.

Pseudorapidity: A natural variable to describe particle production in high-energy physics is the rapidity:

$$y = \frac{1}{2} \ln \frac{E + p_z}{E - p_z}, \tag{2.3}$$

where E is the particle energy and p_z is the component of its momentum along the beam axis. Rapidity is invariant under Lorentz boosts along the beam axis, which makes it particularly useful for comparing particle production at different collision energies. Since the full energy E of a particle is often not directly accessible, it is common to use the pseudorapidity, defined in terms of the polar angle θ as:

$$\eta = -\ln \tan \frac{\theta}{2}. \tag{2.4}$$

In the ultra-relativistic limit, where $E \gg m$, pseudorapidity η coincides with the rapidity y, which transforms additively under z-axis boosts. Moreover, collider detectors are designed with approximately cylindrical geometry around the beam axis, such that surfaces of constant η correspond to nearly uniform segmentation of the detector elements. For these reasons, detector acceptance and many physics distributions are conventionally expressed in terms of η rather than the polar angle θ, whose transformation law under z-boosts is non-linear and depends on both E and p_z.

Angular distances: Scattering angles of particles produced in hadron collisions are often very small, so it is convenient to describe angular separations in terms of the variable ΔR, defined as:

$$\Delta R = \sqrt{(\Delta\eta)^2 + (\Delta\phi)^2}, \tag{2.5}$$

where $\Delta\eta$ is the difference in pseudorapidity and $\Delta\phi$ is the difference in azimuthal angle between two particles. This definition provides a natural metric in the (η, ϕ) space, which directly reflects the cylindrical geometry of the detector. The variable ΔR is approximately invariant under boosts along the beam axis and is therefore widely used to quantify angular separations between particles. It plays a central role in jet reconstruction, in defining isolation criteria for leptons and photons, and in the cone sizes used by clustering algorithms [93].

2.2 The Large Hadron Collider

Large Hadron Collider (LHC) [2] is the largest circular collider built to date, with a circumference of 27 km. LHC is built and maintained by the European Organization for Nuclear Research (*Conseil Européen pour la Recherche Nucléaire*, CERN) and is situated on the French–Swiss border, near the city of Geneva. The LHC is the most powerful collider ever constructed, as demonstrated by two of its achievements. LHC design was driven by the objective of maximizing the delivered luminosity within the practical limits of accelerator technology. With a nominal proton beam energy of 7 TeV per beam and 2808 bunches circulating in each direction, the design instantaneous luminosity was set to $\mathcal{L}_{\text{design}} = 10^{34}\,\text{cm}^{-2}\text{s}^{-1}$. This corresponds to approximately $1\ \text{nb}^{-1}$ of delivered luminosity per second at full performance, enabling the accumulation of tens of inverse femtobarns per year. During high-performance operation in 2017, LHC produced up to 1.5×10^9 proton–proton collisions per second [94], with the peak luminosity of about $2.05 \times 10^{34}\,\text{cm}^{-2}\text{s}^{-1}$. Moreover, it has accelerated beams to energies of 6.8 TeV each (leading to $\sqrt{s} = 13.6$ TeV), the highest ever reached at a hadron collider. These two milestones confirm that the LHC fully realizes its design goal of delivering unprecedented interaction rates and particle energies. To achieve such performance, the accelerator must operate under conditions more extreme than those found in outer space. To bend the high-energy particle beams along the circular trajectory, 1232 superconducting dipole and quadropole magnets made of niobium-titanium (NbTi), each about 15 m long, are installed along the ring. These magnets must be cooled to 1.9 K ($-271.3\,^\circ$C) using superfluid helium at atmospheric pressure in the cryogenic system, ensuring the superconducting state necessary to sustain fields of up to 8.3 T. Beam pipes at the same time must be evacuated to ultrahigh vacuum levels of 10^{-10}–10^{-11} mbar. This prevents collisions between circulating protons and residual gas molecules, ensuring that the experiments record only

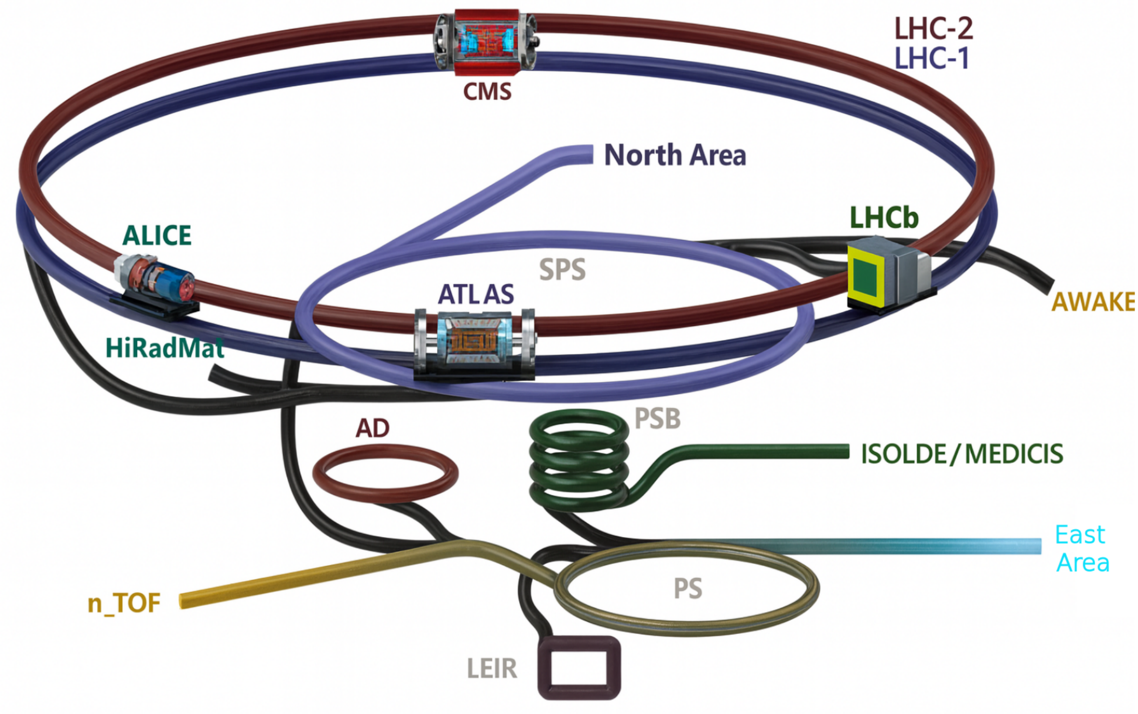

Figure 2.1: Schematic view of the CERN accelerator complex showing the injector chain that feeds protons into the LHC.

the intended proton–proton interactions. It is worth noting that the LHC physics programme is not limited to proton–proton operation: it also includes lead–lead, proton–lead, xenon–xenon, and neon–neon collisions, which provide complementary insights into the properties of strongly interacting matter. Most recently, the LHC has also collided protons with oxygen nuclei, as well as oxygen–oxygen beams [95], in dedicated short runs.

Operation of the LHC is organized into long data-taking periods, known as *Runs*, separated by extended *Long Shutdowns* during which major upgrades and maintenance are carried out. Run 1 (2010–2012) delivered proton–proton collisions at centre-of-mass energies of 7 and 8 TeV, culminating in the discovery of the Higgs boson in 2012 [96]. Following the Long Shutdown 1 (LS1), Run 2 (2015–2018) continued increasing the beam energy to 6.5 TeV, and luminosities above $2 \times 10^{34}\,\mathrm{cm}^{-2}\mathrm{s}^{-1}$ at $\sqrt{s} = 13$ TeV were achieved, corresponding to more than 150 fb^{-1} of integrated luminosity delivered to ATLAS and CMS. Following the second Long Shutdown (LS2, 2019–2021), Run 3 began in 2022, operating at 6.8 TeV per beam with higher luminosity and improved machine stability. The ongoing Run 3 (2022–2025) is expected to deliver approximately 250–300 fb^{-1}, paving the way for the High-Luminosity LHC (HL–LHC) upgrade. The HL-LHC stage is scheduled to start in the late 2020s, which aims to deliver an order of magnitude more integrated luminosity than all previous Runs combined. Instantaneous luminosity will be increased by a factor of five to seven, targeting a design value of $\mathcal{L}_{\mathrm{HL}} \approx 7.5 \times 10^{34}\,\mathrm{cm}^{-2}\mathrm{s}^{-1}$ and an ultimate integrated luminosity of $3\,\mathrm{ab}^{-1}$ over its lifetime. Such performance will enable precision measurements of SM processes and rare-decay studies, and will significantly extend the discovery reach for new physics phenomena.

Proton beams originate from a hydrogen gas, where protons are extracted, and are subsequently accelerated through a chain of smaller accelerators before injection into the main LHC ring. Figure 2.1 shows a schematic view of the CERN accelerator complex. The first acceleration stage is provided by a linear accelerator (LINAC). Until 2018, this role was fulfilled by LINAC2, which accelerated protons to 50 MeV. It has since been replaced by LINAC4, a modern accelerator that produces negative hydrogen ions (H^-) and accelerates them to 160 MeV. Before injection into the next machine, these ions pass through a thin carbon foil that strips away their two electrons. Resulting protons are injected into the Proton Synchrotron Booster (PSB), which accelerates them to 2 GeV. The next stage is the Proton Synchrotron (PS), a circular accelerator that increases the energy to 25 GeV. Protons are then transferred to the Super Proton Synchrotron (SPS), which accelerates them up to 450 GeV and serves as the final injector step. Beams are then injected into the LHC and accelerated to several TeV using eight superconducting RF cavities per beam, providing a total accelerating voltage of about 16 MV. In addition to increasing the beam energy, the RF cavities compensate for the small but continuous energy losses arising from synchrotron radiation and interactions with residual gas. For comparison, in the former LEP collider (with the same 27 km circumference), electrons at 100 GeV lost approximately 3 GeV per turn due to synchrotron radiation, requiring substantial RF power to sustain acceleration. In the LHC, protons at 7 TeV lose about 6.7 keV per turn. Thus, the RF system both compensates these losses while maintaining longitudinal confinement of the proton bunches. Finally, strong quadrupole focusing magnets focus these bunches from the two counter-rotating beams into collisions at the interaction points. At four of these points (IP1, IP2, IP5, IP8), large detectors — ATLAS (A Toroidal LHC ApparatuS) [13], CMS (Compact Muon Solenoid) [14], ALICE (A Large Ion Collider Experiment) [97], and LHCb (Large Hadron Collider beauty) [15] — have been constructed to record the products of the particle collisions. The remaining regions comprise machine elements, including the collimation system (IP3 and IP7), the RF cavities (IP4), and the beam dump (IP6). The LHC tunnel also hosts several smaller, specialised experiments located close to the main interaction points. These include TOTEM (TOTal cross-section, Elastic scattering and diffraction dissociation Measurement at the LHC) [98] and LHCf (Large Hadron Collider forward [99], with “f” denoting the forward region) near CMS and ATLAS, MoEDAL (Monopole and Exotics Detector at the LHC) [100] near LHCb, and the more recently installed FASER (ForwArd Search ExpeRiment) [101] and SND@LHC (Scattering and Neutrino Detector at the LHC) [102] in the forward region downstream of ATLAS.

2.3 General layout of ATLAS

ATLAS is the largest in volume detector at the LHC, measuring 44 m in length, 25 m in height, and weighing about 7000 t. It is built in a cylindrical geometry around the interaction point, with concentric layers of subdetectors specialized for the reconstruction of different particle types or different properties. Figure 2.2 illustrates the overall layout of the ATLAS detector. From the inside outward, the major components are the Inner Detector, the calorimeter systems, and the Muon Spectrometer, all of which are placed within a system of powerful magnets. ATLAS is designed to reconstruct and identify a wide range of final–state particles produced in proton–proton, ion–ion and ion–proton collisions. It is capable for identifying electrons, photons, muons, hadronically decaying τ–leptons, and jets, including those originating from b– and c–quarks. In addition, it reconstructs charged–particle tracks and interaction vertices with high precision, and measures the missing transverse energy ($E_{\mathrm{T}}^{\mathrm{miss}}$) as a signature of neutrinos and other hypothetical weakly interacting particles.

The physics programme of the LHC spans both precision tests of the SM and the exploration of new physics beyond it. ATLAS was therefore developed as a multipurpose detector, capable of addressing a wide variety of processes [13]. The central objective is the study of the Higgs boson, whose discovery and characterization formed one of the primary design benchmarks. Different decay modes highlight different experimental needs. The rare $H \to \gamma\gamma$ channel requires an electromagnetic calorimeter with excellent energy and angular resolution, while the $H \to ZZ^{(*)} \to 4\ell$ channel relies on precise reconstruction of electrons and muons. Other signatures, such as $H \to WW^{(*)} \to \ell\nu\ell\nu$, demand accurate lepton identification and reliable reconstruction of missing transverse energy. Equally important are precision studies of electroweak processes. The production of W and Z bosons at very high

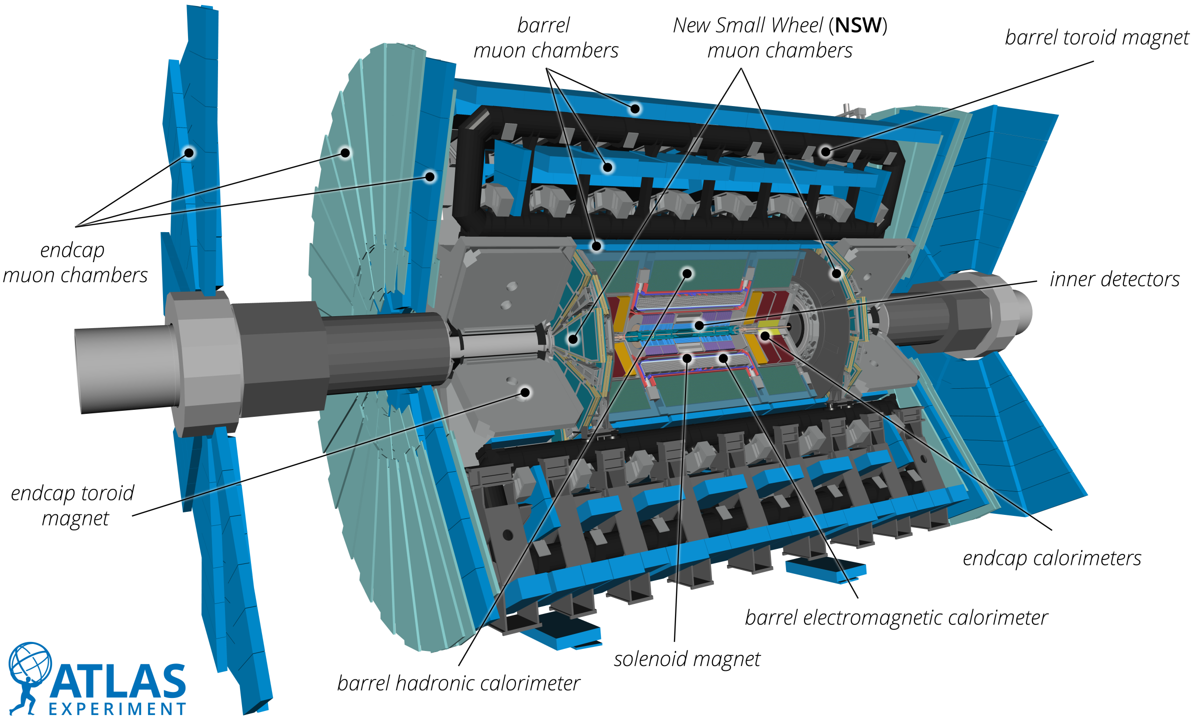

Figure 2.2: Schematic layout of the ATLAS detector showing the concentric subdetector systems and magnet configuration. For the official Run 3 configuration and details, see Ref. [103].

rates provides stringent tests of the SM and essential calibration channels for detector performance. Their leptonic decays demand broad acceptance and high reconstruction efficiency for electrons and muons. The LHC also provides a copious source of top quarks, enabling precise measurements of its mass, couplings and production properties. Another fundamental part of the ATLAS programme is the investigation of QCD and proton structure. Since jet cross-sections are very large, they provide an opportunity to probe PDFs, but they also dominate the background in most searches, requiring excellent jet energy calibration. Beyond the SM, ATLAS is expected to be sensitive to a wide variety of new phenomena. Searches for supersymmetry target final states with multiple jets, leptons, and large missing transverse energy. Heavy resonances such as hypothetical W' or Z' bosons would manifest as high-momentum leptons, requiring accurate momentum resolution. Additionally, there are forward and diffractive physics programmes, which extend the reach of QCD studies into the very low-x[1]

The range of physics goals can be expressed as a set of design requirements for the ATLAS detector. The inner tracking system must combine high granularity with excellent spatial resolution to provide precise momentum measurements, efficient reconstruction, and the ability to resolve secondary vertices. A finely segmented electromagnetic calorimeter is essential for the measurement of photons and electrons, while a hermetic hadronic calorimeter ensures reliable jet reconstruction and the determination of missing transverse energy. The muon spectrometer must be capable of measuring muon momenta over a wide range, including the multi-TeV domain, with precise charge identification. To achieve this performance, the entire detector must be highly segmented, radiation-hard, and capable of withstanding the 40 MHz bunch crossing frequency of the LHC. It must provide nearly complete coverage in pseudorapidity and azimuth, so that no significant component of an event escapes detection. A flexible multi-level trigger system is necessary to reduce the raw interaction rate while retaining efficiency for rare physics channels. Table 2.1 summarizes the key performance goals that guided the design of the ATLAS detector. The subsequent sections summarize the main ATLAS sub-

---

[1] The internal structure of the proton is commonly described in terms of the Björken scaling variable x

systems and their respective functions.

Table 2.1: Summary of the general performance goals of the ATLAS detector.

Subsystem	**Resolution goal**	**Measurement** $\lvert\eta\rvert$ **range**	**Trigger** $\lvert\eta\rvert$ **range**
Tracking	$\frac{\sigma_{p_\mathrm{T}}}{p_\mathrm{T}} = 0.05\% \, p_\mathrm{T} \oplus 1\%$	≤ 2.5	≤ 2.5
Electromagnetic calorimeter	$\frac{\sigma_E}{E} = \frac{10\%}{\sqrt{E}} \oplus 0.7\%$	≤ 3.2	≤ 2.5
Hadronic calorimeter (barrel/end-cap)	$\frac{\sigma_E}{E} = \frac{50\%}{\sqrt{E}} \oplus 3\%$	≤ 3.2	≤ 3.2
Hadronic calorimeter (forward)	$\frac{\sigma_E}{E} = \frac{100\%}{\sqrt{E}} \oplus 10\%$	$3.1 < \lvert\eta\rvert < 4.9$	$3.1 < \lvert\eta\rvert < 4.9$
Muon spectrometer	$\frac{\sigma_{p_\mathrm{T}}}{p_\mathrm{T}} = 10\%$ at $p_\mathrm{T} = 1$ TeV	≤ 2.7	≤ 2.4

Inner Detector

Closest to the colliding beams is the Inner Detector (ID) [104], which provides the reconstruction of trajectories of electrically charged particles (tracks). It covers the pseudorapidity range $|\eta| < 2.5$ and is immersed in a 2 T solenoidal magnetic field, which bends the paths of charged particles, allowing their momentum and charge sign to be determined from the curvature. Charged particles such as electrons, protons, pions, and kaons ionize the detector material, producing signals that are converted into hits. Reconstruction algorithms then process these hits to build complete particle tracks. A further role of the ID is vertex reconstruction. Charged-particle tracks are combined to determine common points of origin. Primary vertex corresponds to the proton–proton collision point, while secondary vertices arise from the decay of long-lived particles. Accurate vertexing is important for separating multiple interactions within the same bunch crossing (pile-up). In ATLAS, the transverse position of the primary vertex can typically be determined with a precision of 10–20 μm. ID consists of three subsystems:

Pixel Detector [105] consists of several cylindrical barrel layers surrounding the beam pipe, complemented by endcap disks at each end. The original detector included only three barrel layers. In 2014, an additional innermost layer, the **Insertable B-Layer** (IBL), was installed at a radius of 3.3 cm, becoming part of the detector from Run 2 onward. The detector is constructed of silicon pixel sensors, in which each pixel is a small (50×250 μm^2) silicon element that produces an electrical signal when intersected by a charged particle. This fine segmentation offers spatial resolutions of a few micrometers, enabling excellent separation of nearby tracks. Pixel Detector is used to determine the impact parameter, which is the distance of closest approach of a track to the primary vertex. This measurement is essential for vertexing and for identifying displaced vertices from decays of long-lived particles such as b-hadrons.

While the Pixel Detector provides measurements with very fine spatial granularity, the **Semiconductor Tracker (SCT)** [106] offers coarser resolution but covers a substantially larger active area. Based on silicon microstrip technology, the SCT provides multiple precision space points for each track, ensuring robust momentum reconstruction.

Transition Radiation Tracker (TRT) [107] forms the outermost part of the ID, and it acts as an extended lever arm, supplying many additional measurements of a track over a large radius. It consists of nearly 300,000 thin straw tubes, arranged to cover the $|\eta| < 2.0$ region. TRT also provides electron identification using the detection of photons, which are emitted when relativistic particles cross the interfaces between materials of different dielectric constants. This makes TRT capable of distinguishing electrons from other charged hadrons.

Calorimeters

Calorimeters [108–110] surround the ID and measure the energies of electrons, photons, hadrons, and jets, as well as contributing to the measurement of missing transverse momentum. They provide nearly full solid-angle coverage up to $|\eta| < 4.9$ and are divided into electromagnetic and hadronic sections:

Electromagnetic Calorimeter (ECal) is a sampling calorimeter, in which dense absorber plates and active material are arranged in alternating layers. In ATLAS, thin lead plates act as absorbers that initiate electromagnetic showers, while liquid argon (LAr) is used as the active medium in which the ionization charge is collected. The electrodes are folded in a "zig-zag" shape, which guarantees full coverage in azimuth without cracks between modules. It is designed for the precise measurement of electrons and photons. The barrel region covers $|\eta| < 1.475$, while the endcap sections extend coverage to $|\eta| < 3.2$.

Hadronic Calorimeter is designed to measure energies of hadrons, jets, and the hadronic component of tau decays. It consists of three main parts. Tile Calorimeter (TileCal) is a steel/scintillator-tile sampling calorimeter covering the central region ($|\eta| < 1.7$). Hadronic Endcap Calorimeter (HEC) is located behind the EM endcaps, consisting of copper/LAr modules covering $1.5 < |\eta| < 3.2$. It measures hadronic showers in the forward region. Forward Calorimeter (FCal) is a compact LAr calorimeter with copper and tungsten absorbers covering $3.1 < |\eta| < 4.9$.

Muon Spectrometer

Muon Spectrometer (MS) [111] is the outermost tracking system designed to identify and precisely measure the momentum of muons that escape the calorimeters. It combines two types of chambers with complementary functions. Precision tracking chambers (Monitored Drift Tubes [112] and Cathode Strip Chambers [113]) provide high spatial resolution, measuring track positions with 80 μm resolution. Fast trigger chambers (Resistive Plate Chambers in the barrel and Thin Gap Chambers in the endcaps) deliver coarse position and excellent timing information within nanoseconds, enabling the online trigger system to rapidly decide whether to record an event.

Magnet system

This system consists of three main components: a central solenoid and large superconducting air-core toroidal magnets in both the barrel and endcap regions. The solenoid surrounds the ID and provides the 2 T field for charged-particle momentum measurement at small radius. The barrel and endcap toroids generate a strong bending power for muons traversing the spectrometer, enabling precise measurement of their trajectories while leaving most of the detector volume free of material. Together, these magnet systems provide the necessary bending power to ensure good momentum resolution for both inner tracking and outer muon measurements.

Trigger and Data Acquisition systems

The LHC delivers proton–proton collisions at a bunch crossing rate of 40 MHz, corresponding to about 10^9 interactions per second. Since it is impossible to record and store all events at this rate, the ATLAS Trigger and Data Acquisition (TDAQ) [114] system reduces the data flow to a manageable rate of around 1 kHz, selecting the most interesting events for permanent storage and offline analysis. This is achieved in multiple stages of event selection, combining fast hardware-based decisions with more sophisticated software algorithms.

Quality Control and Simulation Infrastructure

The ATLAS experiment must reliably record collision events, ensure high data quality, and build a trustworthy simulation framework to allow meaningful comparisons between theoretical predictions and observations. During LHC beam operation, all ATLAS subsystems are coordinated by a central run-control framework, which ensures that each component transitions through detector states coherently. A data-taking run can begin only when every detector element is confirmed to be ready, and LHC beam conditions are declared stable. Each run is assigned a unique identifier and typically spans a single LHC fill. Runs are subdivided into *luminosity blocks* (LBs) of order one minute, within which the instantaneous luminosity, detector conditions, and trigger settings are considered constant. If a subsystem experiences a transient problem, only the affected LBs may be excluded from analysis rather than discarding the entire run. The collection of LBs certified for physics usage is called the Good Run List (GRL). Events passing the trigger are forwarded to the Data Acquisition (DAQ) [114–117] system and recorded in raw format at CERN's Tier-0. Events are organized into separate streams based on signature type: e.g., EGamma (electrons, photons), Muon, JetTauEtMiss (hadronic energy or missing energy), CosmicCalo (events originating outside LHC-induced collisions), debugging streams, and others. As data are recorded, they are cataloged, transferred, and processed through the Worldwide LHC Computing Grid (WLCG) [118]. During active beam collisions, each subdetector is monitored at both the hardware and software levels; reconstructed quantities are checked in near real-time to detect anomalies. Shifter experts in the control room review and flag possible issues for further inspection.

In parallel with the data, Monte Carlo (MC) simulation samples are generated for both signal and background processes. These simulations are crucial for calibration, efficiency estimation, acceptance corrections, and the evaluation of systematic uncertainties. The MC simulation workflow typically encompasses: (i) Hard-scatter / parton-level generation using matrix-element tools such as POWHEG [119, 120], MADGRAPH5 AMC@NLO [121], or SHERPA [122], often interfaced with parton-shower and hadronization models implemented in PYTHIA8 [123]. (ii) GEANT4 [124], a detector-based simulation toolkit, where generated stable particles are propagated through the full ATLAS geometry, simulating interactions (e.g. energy loss, scattering, hadronic and electromagnetic showers).

Derivation of the real physics object is obtained for both real and simulated objects. Analysis-level formats are produced, containing only the relevant reconstructed quantities for physics analyses, Analysis Object Data (AOD), or reduced data volume focused on variables of interest, Derived Analysis Object Data (DAOD). The ATLAS software framework Athena holds up virtually all offline and many online processing tasks: event generation, detector simulation, reconstruction, derivation, and even portions of the trigger chain. Since data and simulated events traverse essentially identical reconstruction and calibration pipelines, the same selection criteria, object definitions, and corrections can be applied consistently in analyses.

2.4 Luminosity detectors

A precise determination of the luminosity at ATLAS requires multiple dedicated and complementary detectors. Each system covers different pseudorapidity regions, operates with distinct technologies, and contributes to the overall precision of the luminosity calibration.

2.4.1 LUCID

The LUminosity measurement using a Cherenkov Integrating Detector (LUCID) is the primary ATLAS luminosity monitor, and one of the dedicated luminosity detectors that are collectively termed luminometers. LUCID-1, used during Run 1, employed aluminium tubes filled with C_4F_{10} gas as Cherenkov radiators, each coupled to a photomultiplier tube (PMT), for a total of 20 PMTs per side at ±17 m from the interaction point [125, 126]. Although it provided the reference luminosity for ATLAS during 2010–2013, the detector suffered from radiation damage to its materials, resulting in limited long-term stability. LUCID-2 [127] was rebuilt entirely for Run 2, replacing the gas tubes with quartz radiators. It is designed to provide reliable bunch-by-bunch luminosity measurements over the full range of beam conditions, from dedicated special scans at low pile-up to high-luminosity pp and heavy ion physics running. LUCID-2 consists of two identical modules, located symmetrically at ±17 m from the IP, just as LUCID-1. Each module is constructed as a ring of 16 PMTs arranged around the beam pipe with a radius of 12 cm. Charged particles emerging at very small polar angles generate Cherenkov light directly in the quartz windows of the PMTs, which is then collected and read out with nanosecond timing resolution. On the quartz window of each PMT, a ^{207}Bi radioactive source is deposited. The decay of ^{207}Bi through internal conversion produces $\sim$ 1 MeV electrons. The activity of this source is low enough not to interfere with luminosity measurements, even in the low-luminosity regime, but sufficiently strong to be exploited for continuous PMT gain monitoring. This feature ensures stable and calibrated detector response throughout LHC operation. For redundancy and cross-checks, the PMTs are grouped into two independent sub-groups called Bi and Bi2. These groups are defined symmetrically around the beam pipe, each with similar characteristics, but read out and analyzed separately, as shown in Figure 2.3. By combining fast timing, high radiation hardness, and redundant readout, LUCID has established itself as the reference luminometer of ATLAS since Run 2. It is worth noting that for Run 3, LUCID has been upgraded to the LUCID-3 [128] detector, which retains the same basic operating principle as LUCID-2 but features improved radiation hardness and upgraded photomultiplier technology.

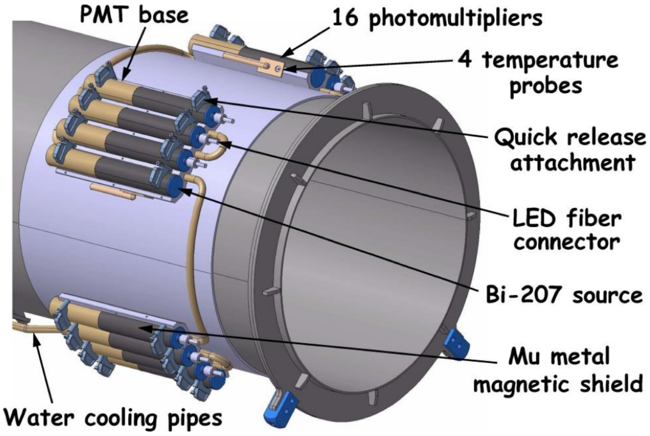

Figure 2.3: Schematic illustration of the LUCID detector, showing the PMTs arranged cylindrically around the beam pipe. Adopted from [129].

2.4.2 BCM

The Beam Conditions Monitor (BCM) [130] is another central detector for luminosity measurements, originally designed for machine protection. Its primary role is to provide ultra-fast abort signals to the LHC in case of abnormal beam losses. In addition, BCM has been used extensively as a reference luminometer, particularly during the high-luminosity operation of 2011–2013, and continues to provide powerful bunch-by-bunch luminosity data. The BCM is installed at $z = \pm 1.84$ m from the IP, with two sets of four modules mounted symmetrically around the beam pipe at a radial distance of 55 mm. Each module contains 500 μm-thick radiation-hard polycrystalline chemical-vapor-deposited diamond sensors, oriented at 45° with respect to the beam axis. This tilt maximizes the signal yield from minimum ionizing particles. The sensors are coupled to very fast front-end electronics, providing a time resolution of about 0.7 ns. This excellent timing allows the separation of signals originating from pp collisions from those due to incoming single-beam backgrounds. BCM measures the hit rate in individual sensors at the level of every single bunch crossing.

2.4.3 Other luminosity measurement systems

In addition to the primary luminometers (LUCID and BCM), ATLAS utilizes additional systems and methods that contribute to luminosity determination under specific running conditions or serve as valuable cross-checks.

Minimum Bias Trigger Scintillators (MBTS) [13] are mounted on the inner face of the electromagnetic endcap calorimeter cryostats, at $z = \pm 3.6$ m from the IP. Each MBTS station consists of a 2 cm thick polystyrene scintillator disk segmented into 16 counters, arranged in two pseudorapidity rings with eight azimuthal sectors. The inner ring covers $2.08 \leq |\eta| \leq 2.76$, while the outer ring covers $2.76 \leq |\eta| \leq 3.86$. The MBTS was initially designed as a trigger system, and although it can be exploited for luminosity estimates at low pile-up, its readout does not resolve individual bunch crossings.

Track Counting (TC)[2]: An alternative approach to luminosity determination is provided by track counting, which relies on the central tracking detectors (IBL, Pixel, and SCT). The track counting method depends on the offline reconstruction of charged-particle tracks in the ID. It therefore yields average luminosity values over longer intervals, LBs, rather than on a bunch-by-bunch basis.

As briefly introduced in Section 2.3, the calorimeter systems, in addition to their primary role in measuring particle energies, have also been used for luminosity monitoring through their average signal readout. In the Tile Calorimeter, a dedicated integrator circuit records the mean photomultiplier currents from minimum-bias events, providing a signal proportional to the instantaneous luminosity [131]. Similarly, in the LAr calorimeter, the average ionization current readout in the electrodes offers an independent measure of the luminosity, based on the continuous flux of particles traversing the detector [132]. However, both methods integrate signals over long timescales and therefore cannot resolve luminosity on a bunch-by-bunch basis.

Zero Degree Calorimeters (ZDC) [133] are located at ± 140 m from the IP within the TAN absorbers, massive shielding blocks that stop neutral particles. ZDC detects neutral particles, primarily neutrons and photons, emitted at very small polar angles. ZDC plays a prominent role in heavy-ion running and contributes to specific runs requiring very forward coverage, making it unsuitable for precise bunch-resolved measurements.

Absolute Luminosity For ATLAS (ALFA) [134] detectors are Roman Pot stations at ± 240 m from

---

[2] The *Z-counting* technique estimates luminosity from the observed yield of $Z \to \ell\ell$ decays, using the theoretically well-known Z production cross-section as a reference.

the IP. They contain scintillating-fibre trackers designed to detect elastically scattered protons at very small angles. ALFA is used in dedicated high-β^* runs to determine the total pp cross-section via the optical theorem as detailed in Sec 3.2, thereby anchoring the absolute luminosity scale. This technique inherently delivers only integrated luminosity values over dedicated runs.

Timepix (TPX) [135, 136] detectors have also been deployed in monitoring bunch-integrated luminosity using hit-counting and cluster methods. TPX is a hybrid silicon pixel device installed in several locations around the ATLAS cavern outside the main detector volume. It operates as a standalone monitor of the radiation field intensity and the instantaneous and integrated luminosity. More recent efforts explore Timepix3 [137] devices and the use of thermal neutron counting modes for improved stability and accuracy.

Figure 2.4 illustrates schematically the relative locations and pseudorapidity coverage of the detectors discussed in this section, which are close to the IP. Unlike LUCID and BCM, which are capable of delivering accurate bunch-by-bunch luminosity information, the other methods available in ATLAS do not provide such time granularity. These methods, therefore, play a complementary role in providing important cross-checks. The advantage of having several independent luminosity measurements is that their mutual consistency provides an important validation of the long-term stability and linearity of each detector's response (see Figure 2.5).

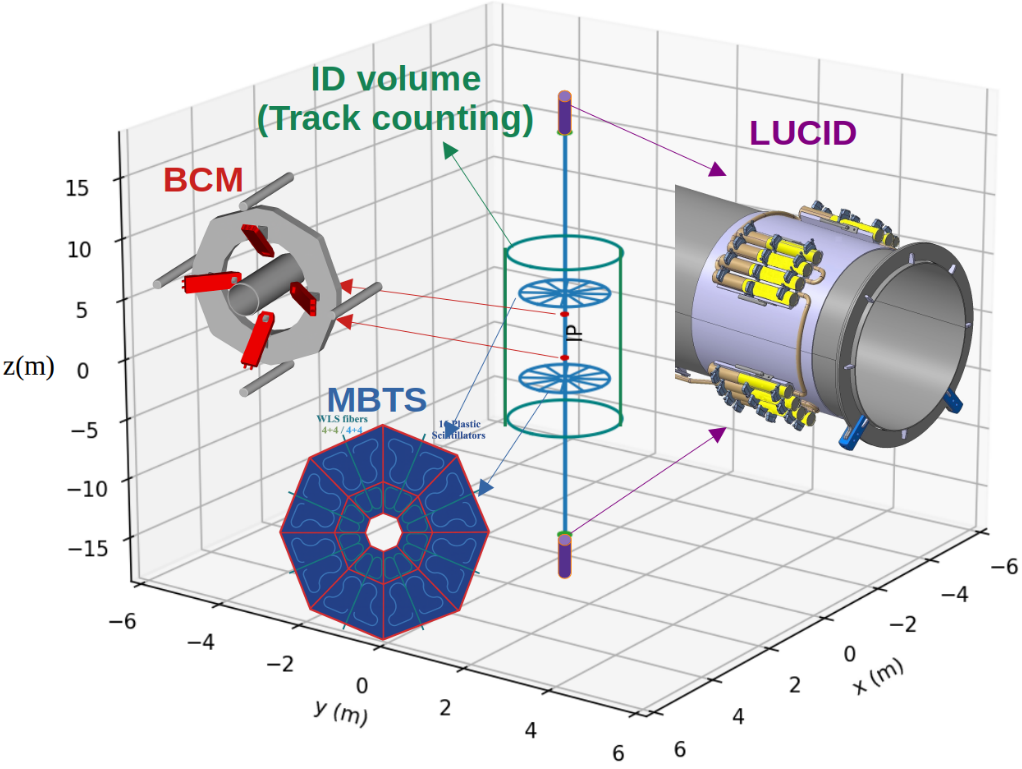

Figure 2.4: ATLAS luminosity detectors LUCID, BCM, and MBTS are shown at their respective longitudinal positions z relative to the IP, together with their pseudorapidity coverage.

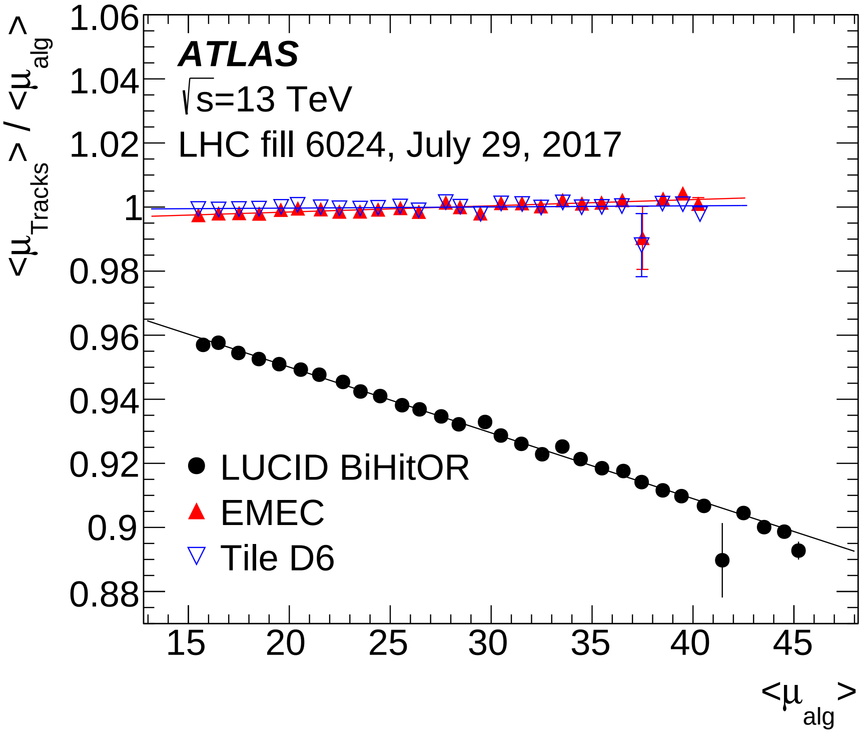

Figure 2.5: Ratios of instantaneous luminosity measured by track counting to that measured by LUCID (black points), EMEC (red filled triangles), and Tile (blue open inverted triangles) as a function of the mean number of interactions per bunch crossing $\langle\mu\rangle$ measured by the latter algorithms in long LHC physics fill during 2017 [22]. The lines show linear fits through each set of points. Time progresses from right to left.

Chapter 3

Absolute Luminosity Calibration in ATLAS

3.1 Methodology

The interaction rate per-bunch crossing μ, inelastic pp cross-section σ_{inel} and per-bunch instantaneous luminosity $\mathcal{L}_b$ are related via Eq. (1.10). Detector measures (with efficiency ϵ) the mean number of *visible interaction rates* per bunch crossing, $\mu_{\text{vis}} = \epsilon\,\mu$. Corresponding *visible cross-section* is defined as $\sigma_{\text{vis}} = \epsilon\,\sigma_{\text{inel}}$. Instantaneous luminosity per-bunch is then related to detector observables by:

$$\mathcal{L}_b = \frac{\mu_{\text{vis}} f_{\text{rev}}}{\sigma_{\text{vis}}}, \tag{3.1}$$

where the visible cross-section σ_{vis} is a calibration constant that links the detector response, through the measured μ_{vis} in Eq. (3.1), to the absolute per-bunch luminosity $\mathcal{L}_b$. Since f_{rev} is known with extremely high precision from the accelerator parameters, the accuracy of the luminosity determination is therefore driven by the precision of σ_{vis}. The measured μ_{vis}, obtained continuously from dedicated luminometer signals, is directly proportional to the instantaneous luminosity, while σ_{vis} provides the proportionality factor established through dedicated vdM calibration scans. Both the detection efficiency ϵ and, consequently, the visible cross-section σ_{vis} depend on the type of colliding particles, collision energy, and angular and transverse-momentum distributions of the final-state particles. Because these properties differ for each luminometer and for each specific luminosity algorithm (as explained in Section 3.4), the corresponding values of σ_{vis} are detector- and algorithm-dependent.

The determination of the absolute luminosity at LHC follows a sequence of well-defined steps:

1. **Measurement with luminometers:** The first requirement is a dedicated detector system, the luminometer, which measures event rates.
2. **Absolute calibration from vdM scans:** Dedicated low-intensity calibration runs are performed, from which the visible cross-section σ_{vis} is determined.
3. **Calibration transfer:** Since vdM scans are carried out under special beam conditions (low μ, low luminosity, few isolated bunches, zero crossing angle), the calibration must be transferred to regular physics conditions. This includes corrections for the change to high-intensity bunch trains, non-zero crossing angles, etc.

4. **Long-term stability:** vdM runs at a given $\sqrt{s}$ typically occur once per year, with occasional additional sessions under special operating conditions[1] or when the calibration quality needs to be re-validated, e.g. due to unexpected detector behavior. Over extended data-taking periods, additional corrections account for detector aging, time-dependent efficiency variations, and possible drifts in beam instrumentation. These corrections ensure consistency of the luminosity scale throughout a long period ($\sim$1 year).

In this thesis, the focus is on the determination of σ_{vis} from vdM scans performed in pp collisions at $\sqrt{s} = 900$ GeV during Run 2 in 2018. The subsequent steps of calibration transfer and long-term stability are beyond the present scope. A detailed description of the vdM calibration procedure is provided in Section 3.6.

3.2 Alternative methods for luminosity determination

Several approaches exist for absolute luminosity calibration in hadron colliders. They differ in the observables they rely on, the achievable precision, and the experimental conditions required. The most relevant approaches are the beam-parameter-based method, luminosity determination from elastic scattering (and the pp total cross-section), and luminosity extraction from well-measured Standard Model processes. We summarize briefly these approaches for completeness.

First, luminosity can be expressed directly in terms of beam parameters. A simpler approach expresses the luminosity directly in terms of beam parameters, assuming Gaussian profiles with rms widths σ_x, σ_y, as derived in Eq. (1.21). This provides fast, online estimates of luminosity without dedicated scans, but it depends a lot on the accurate determination of beam sizes and optics. In addition to the vdM scan technique introduced in Section 3.1, several other beam–parameter–based methods are employed to determine the transverse beam sizes:

- Profile monitors: Both invasive and non-invasive devices, such as wire scanners [138, 139] and synchrotron light monitors [140, 141], can provide direct measurements of the transverse beam profiles at specific locations along the accelerator.
- Beam–gas imaging (BGI): This method, first used at LHCb experiment [142], reconstructs the transverse beam shapes from the spatial distribution of vertices originating from beam–gas interactions near the IP. This way, beam sizes can be determined without the need for dedicated scans.

Although such techniques can offer valuable cross-checks and independent information on beam parameters, their achievable precision and control of systematics are not competitive with the vdM scan method.

Other approach exploits the connection between elastic scattering, luminosity $\mathcal{L}$, and the total cross-section σ_{tot} provided by the optical theorem, a general result of scattering theory which follows from unitarity [27]. It states that:

$$\sigma_{\text{tot}} = 4\pi\, Im[f_{\text{el}}(t=0)], \tag{3.2}$$

where f_{el} is the elastic scattering amplitude and $t = -p^2\theta^2$ is the momentum transfer squared at small scattering angles. The differential elastic cross-section is related to the amplitude by $\frac{d\sigma_{\text{el}}}{dt} = \pi\,|f_{\text{el}}(t)|^2$.

---

[1] During low-energy runs, major machine or detector configurations can change. There is also an early vdM run performed to establish the scale (commissioning period) after long shutdowns.

Applying the optical theorem leads to the relations:

$$\sigma_{\text{tot}} = \frac{16\pi}{1+\rho^2}\,\frac{(dR_{\text{el}}/dt)|_{t=0}}{R_{\text{tot}}}, \qquad \mathcal{L} = \frac{1+\rho^2}{16\pi}\,\frac{R_{\text{tot}}^2}{(dR_{\text{el}}/dt)|_{t=0}}, \tag{3.3}$$

where ρ is ratio between real and imaginary parts amplitudes of the f_{el} for a small $t \to 0$, and R_{el}, R_{tot} are elastic and total interaction rates respectively. This method is independent of beam instrumentation, provides both σ_{tot} and $\mathcal{L}$ simultaneously, and yields the ρ parameter. Disadvantages are that it requires measurements at very small t with high-β^* optics, and precise forward detectors in a harsh radiation environment.

Another method is based on processes whose cross-sections are theoretically well known, such as W or Z boson production [20, 143–145]. The integrated luminosity $\mathcal{L}_{int}$ can be extracted from the expression of the total production cross-section of weak bosons σ_{tot} (see Section 4.1). This method is applicable during regular physics runs without special optics, and can achieve precisions of 2–3% when efficiencies and acceptances are well controlled. The absolute accuracy of this approach is limited by the theoretical knowledge of the cross-section, dominated by uncertainties in parton distribution functions. Acceptance corrections add 1.5–2% uncertainty, and efficiencies require careful data-driven calibrations. Thus, SM processes are mainly used for relative-luminosity monitoring or as a cross-check against the vdM calibrations.

3.3 vdM scan formalism

A fundamental beam-parameter-based method for absolute luminosity calibration at colliders is the *van der Meer* (vdM) method, introduced by Simon van der Meer in 1968 in the context of the CERN Intersecting Storage Rings [16].

This technique relates the observed interaction rate from dedicated calibration runs, referred to as vdM scans, to the geometric overlap of the colliding beams. During these scans, the two beams are transversely displaced with respect to each other in small, well-controlled steps, either in the horizontal (x) or vertical (y) plane—referred to as *X* and *Y* scans, respectively. By varying the beam separation in each plane, the overlap of the bunch-density profiles is mapped, allowing the effective beam widths and corresponding interaction rates to be extracted for each scan step. The visible cross-section σ_{vis} is then determined from these measured quantities, which relates the observed interaction rate to the absolute luminosity calculated from the beam parameters. These so-called *on-axis* scans, performed around the nominal interaction point ($\delta_x^0 = 0,\ \delta_y^0 = 0$), are often complemented by *off-axis* scans (see Figure 3.1), in which one coordinate in the non-scanning plane is held at a non-zero offset. Off-axis scans are used to probe possible transverse correlations between the beams and to study the non-factorization effect explained later in this chapter.

The procedure is based on the following formalism. If one considers two bunches populated with n_1 and n_2 protons colliding with no crossing angle, within two beams (beam 1 and beam 2) with normalized transverse density distributions $\rho_1(x,y)$ and $\rho_2(x,y)$ of beam 1 and beam 2, respectively, that satisfy:

$$\int \rho_i(x,y)\,dx\,dy = 1, \qquad i = 1,2, \tag{3.4}$$

then particle density in each beam is $n_i\rho_i(x,y)$. Instantaneous luminosity for a single colliding bunch pair is proportional to the overlap of the two distributions:

$$\mathcal{L}_b \;=\; f_{\text{rev}}\, n_1 n_2 \iint \rho_1(x,y)\,\rho_2(x,y)\,dx\,dy. \tag{3.5}$$

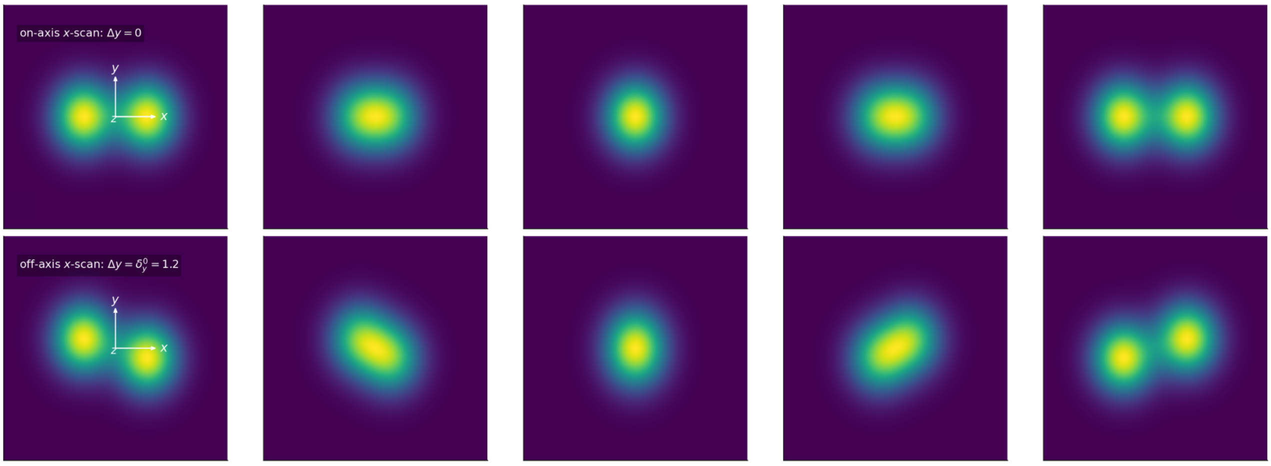

Figure 3.1: Illustration of van der Meer scans in the horizontal plane. The top row shows an on-axis x-scan, where the vertical separation is zero ($\delta_y^0 = 0$). The bottom row shows an off-axis x-scan with a finite vertical offset ($\delta_y^0 \neq 0$). Each panel corresponds to a different five horizontal separations δ_x, ranging from the maximum negative offset on the left to the maximum positive offset on the right.

A key assumption of the vdM formalism is that the transverse bunch density distributions can be factorized into independent horizontal and vertical components:

$$\rho_i(x, y) \;=\; \rho_{ix}(x)\, \rho_{iy}(y), \quad i = 1, 2. \tag{3.6}$$

With the factorization assumption in place, Eq. (3.5) becomes:

$$\mathcal{L}_b \;=\; f_{\text{rev}}\, n_1 n_2 \left[\int \rho_{1x}(x)\, \rho_{2x}(x)\, dx \right] \left[\int \rho_{1y}(y)\, \rho_{2y}(y)\, dy \right]. \tag{3.7}$$

During a vdM scan, the beams are transversely displaced by controlled offsets (δ_x, δ_y), so the overlap integral becomes:

$$\mathcal{L}_b(\delta_x, \delta_y) \;=\; f_{\text{rev}}\, n_1 n_2 \left[\int \rho_{1x}(x)\, \rho_{2x}(x + \delta_x)\, dx \right] \left[\int \rho_{1y}(y)\, \rho_{2y}(y + \delta_y)\, dy \right]. \tag{3.8}$$

In Eq. (3.8), the offset δ_x is applied only to ρ_{2x} by convention (similarly for δ_y), since it is defined as the relative displacement of beam 2 with respect to beam 1. This is mathematically equivalent to shifting beam 1 instead, as only the relative separation matters. A symmetric form can also be written as $\int \rho_{1x}(x - \delta_x/2)\, \rho_{2x}(x + \delta_x/2)\, dx$, which is identical after a change of variables. Let $R(\delta_x, \delta_y)$ denote the interaction rate for a process with a visible cross-section σ_{vis} measured by the luminosity detector. It will be then:

$$R(\delta_x, \delta_y) \;=\; \sigma_{\text{vis}}\, \mathcal{L}_b(\delta_x, \delta_y). \tag{3.9}$$

By fixing $\delta_y = \delta_y^0$ (a vertical working point) and displacing beams along the x-axis by δ_x, Eq. (3.8) implies:

$$R(\delta_x, \delta_y^0) \;=\; \sigma_{\text{vis}}\, \Omega_y \int \rho_{1x}(x)\, \rho_{2x}(x + \delta_x)\, dx, \tag{3.10}$$

with Ω_y being the vertical overlap factor that remains constant during the displacement along the x-axis, and it is defined as:

$$\Omega_y \;\equiv\; f_{\text{rev}}\, n_1 n_2 \int \rho_{1y}(y)\, \rho_{2y}(y + \delta_y^0)\, dy. \tag{3.11}$$

Integration of Eq. (3.10) over the horizontal separation δ_x gives:

$$\begin{aligned}\int_{-\infty}^{\infty} R(\delta_x,\delta_y^0)\,d(\delta_x) &= \sigma_{\text{vis}}\,\Omega_y \int_{-\infty}^{\infty}\left[\int_{-\infty}^{\infty} \rho_{1x}(x)\,\rho_{2x}(x+\delta_x)\,dx\right] d(\delta_x)\\ &= \sigma_{\text{vis}}\,\Omega_y \int_{-\infty}^{\infty} \rho_{1x}(x)\left[\int_{-\infty}^{\infty} \rho_{2x}(x+\delta_x)\,d(\delta_x)\right] dx,\end{aligned} \tag{3.12}$$

where the order of integration has been swapped. Using the substitution $u = x+\delta_x$, and the fact that ρ_{2x} is normalized ($\int_{-\infty}^{\infty} \rho_{2x}(u)\,du = 1$):

$$\int_{-\infty}^{\infty} R(\delta_x,\delta_y^0)\,d(\delta_x) \;=\; \sigma_{\text{vis}}\,\Omega_y \int_{-\infty}^{\infty} \rho_{1x}(x)\,dx \;=\; \sigma_{\text{vis}}\,\Omega_y. \tag{3.13}$$

Eq. (3.13) means that the area under the horizontal scan curve equals σ_{vis} times the vertical overlap factor Ω_y. Dividing Eq. (3.10) by Eq. (3.13) gives an expression in terms of measurable quantities:

$$\frac{R(\delta_x^0,\delta_y^0)}{\displaystyle\int_{-\infty}^{\infty} R(\delta_x,\delta_y^0)\,d(\delta_x)} \;=\; \int_{-\infty}^{\infty} \rho_{1x}(x)\,\rho_{2x}(x+\delta_x^0)\,dx. \tag{3.14}$$

Doing an analogous derivation for a vertical scan at fixed $\delta_x = \delta_x^0$ yields:

$$\frac{R(\delta_x^0,\delta_y^0)}{\displaystyle\int_{-\infty}^{\infty} R(\delta_y,\delta_x^0)\,d(\delta_y)} \;=\; \int_{-\infty}^{\infty} \rho_{1y}(y)\,\rho_{2y}(y+\delta_y^0)\,dy. \tag{3.15}$$

After substituting derived Eqs. (3.14) and (3.15) into Eq. (3.8):

$$\mathcal{L}_b(\delta_x^0,\delta_y^0) \;=\; n_1 n_2\, f_{\text{rev}}\, \frac{R(\delta_x^0,\delta_y^0)}{\displaystyle\int_{-\infty}^{\infty} R(\delta_x,\delta_y^0)\,d(\delta_x)} \cdot \frac{R(\delta_x^0,\delta_y^0)}{\displaystyle\int_{-\infty}^{\infty} R(\delta_y,\delta_x^0)\,d(\delta_y)}. \tag{3.16}$$

This expression summarizes the main feature of vdM scans: the luminosity at any transverse working point (δ_x^0,δ_y^0) is expressed in terms of bunch parameters n_1, n_2, f_{rev} and measured scan integrals and rates. Horizontal and vertical convolved beam sizes are defined as:

$$\Sigma_x \;\equiv\; \frac{1}{\sqrt{2\pi}}\,\frac{\displaystyle\int_{-\infty}^{\infty} R(\delta_x,\delta_y^0)\,d(\delta_x)}{R(0,\delta_y^0)}, \qquad \Sigma_y \;\equiv\; \frac{1}{\sqrt{2\pi}}\,\frac{\displaystyle\int_{-\infty}^{\infty} R(\delta_y,\delta_x^0)\,d(\delta_y)}{R(\delta_x^0,0)}. \tag{3.17}$$

Eq. (3.16) can be simplified by evaluating it at the point $(\delta_x^0,\delta_y^0) = (0,0)$ where beams are colliding head-on, and using Eq. (3.17) definitions yields the standard head-on formulae:

$$\boxed{\mathcal{L}_b(0,0) \;=\; \frac{n_1 n_2\, f_{\text{rev}}}{2\pi\,\Sigma_x\,\Sigma_y}}, \qquad \boxed{\sigma_{\text{vis}} \;=\; \frac{2\pi\,\Sigma_x\,\Sigma_y}{n_1 n_2}\,R(0,0)}. \tag{3.18}$$

Once σ_{vis} is determined from a dedicated vdM session, the luminosity monitor can provide $\mathcal{L}$ at any time via Eq. (3.1). A useful quantity that can be directly extracted from the vdM scan data is the *specific luminosity*, defined as:

$$\mathcal{L}_{\text{spec}} \;=\; \frac{\mathcal{L}_b}{n_1 n_2} \;=\; \frac{f_{\text{rev}}}{2\pi\,\Sigma_x\,\Sigma_y}. \tag{3.19}$$

This quantity depends only on the convolved beam sizes and is independent of the bunch intensities or the number of colliding pairs. Comparing the values of $\mathcal{L}_{\text{spec}}$ obtained from different luminometers and reconstruction algorithms during the same vdM scan, therefore, provide a sensitive cross-check of the consistency of the fitted beam-size parameters and the overall scan quality.

3.4 ATLAS luminosity algorithms

One can distinguish the possible outcomes of a single bunch crossing as seen by a luminometer with two symmetric arms on each side of the interaction point, denoted A and C. Three mutually inclusive cases can occur: In the first case, a hit is registered on the A side but not on the C side. In the second case, a hit is registered on the C side but not on the A side. In the third case, hits are registered simultaneously on both the A and C sides. And let $\epsilon_{\mathrm{ORA}}, \epsilon_{\mathrm{ORC}}, \epsilon_{\mathrm{AND}}$ denote efficiencies of these conditions respectively. Based on these outcomes, the commonly used counting algorithms are defined as follows:

- EventOR: The event is accepted if at least one hit is observed on either side. This corresponds to the logical union of cases (1), (2), and (3).
- EventORA (EventORC): The event is accepted if at least one hit is observed on side A (or side C). This corresponds to case (1) for side A and case (2) for side C.
- EventAND: The event is accepted only if both sides register a hit in the same bunch crossing, i.e. case (3).

The Event counting rate can be converted to μ_{vis} under the assumptions that the number of proton–proton interactions per bunch crossing follows a Poisson distribution, and that the probability of detecting a single interaction is independent of the number of interactions that occur in the same bunch crossing. According to the Poisson distribution, the probability of observing n proton-proton interactions in a single bunch crossing is:

$$P(n;\mu) = \frac{\mu^n e^{-\mu}}{n!},$$

where μ is the average number of interactions per bunch crossing. The use of the Poisson distribution is justified because each bunch contains a vast number of protons, while the probability for any individual proton pair to interact is very small. Under these conditions, the total number of interactions in a bunch crossing can be modeled as a sequence of many independent Bernoulli trials [146] with low probability, which converges to the Poisson distribution in the limit. It is convenient to also define one-interaction exlusive probabilities $P_{00}(1), P_{10}(1), P_{01}(1), P_{11}(1)$, meaning, respectively: no hit on A or C; A only; C only; A and C. These relate to the inclusive efficiencies as:

$$P_{00}(1) = 1 - \epsilon_{\mathrm{OR}}, \tag{3.20}$$

$$P_{10}(1) = \epsilon_{\mathrm{ORA}} - \epsilon_{\mathrm{AND}}, \tag{3.21}$$

$$P_{01}(1) = \epsilon_{\mathrm{ORC}} - \epsilon_{\mathrm{AND}}, \tag{3.22}$$

$$P_{11}(1) = \epsilon_{\mathrm{AND}}. \tag{3.23}$$

It can be shown that combining relations from Eqs. (3.20)-(3.23) for one interaction with expression $P_{10}(1) + P_{01}(1) + P_{11}(1) = 1 - P_{00}(1)$ gives the relation between efficiencies:

$$\epsilon_{\mathrm{OR}} \;=\; \epsilon_{\mathrm{ORA}} + \epsilon_{\mathrm{ORC}} - \epsilon_{\mathrm{AND}}. \tag{3.24}$$

3.4.1 Inclusive algorithm

Let n be the number of inelastic interactions in a bunch crossing. For a fixed n, EventOR fails only if none of the n interactions produces a hit on A or C. Since each interaction fails with probability $P_{00}(1)$, independence gives:

$$P_{00}(n) \;=\; \left[P_{00}(1)\right]^n \;=\; \left(1 - \epsilon_{\mathrm{OR}}\right)^n. \tag{3.25}$$

Since the number of interactions n in a bunch crossing follows a Poisson distribution with mean μ, the probability of observing no hit is given by the expectation value of $P_{00}(n)$ with respect to that distribution:

$$P_{00}(\mu) = \sum_{n=0}^{\infty} P_{00}(n)\,\frac{\mu^n e^{-\mu}}{n!}, \tag{3.26}$$

which with Eq. (3.25) gives:

$$P_{00}(\mu) = \sum_{n=0}^{\infty} e^{-\mu}\,\frac{\mu^n}{n!}\,\big(1-\epsilon_{\mathrm{OR}}\big)^n \;=\; e^{-\mu}\sum_{n=0}^{\infty}\frac{\big[\mu(1-\epsilon_{\mathrm{OR}})\big]^n}{n!} \;=\; e^{-\mu\,\epsilon_{\mathrm{OR}}}, \tag{3.27}$$

here Taylor series $e^x = \sum_{n\geq 0} x^n/n!$ have been used. If the visible interaction rate is defined like $\mu_{\mathrm{vis}}^{\mathrm{OR}} = \mu\,\epsilon_{\mathrm{OR}}$, this yields:

$$P_{00}(\mu) \;=\; e^{-\mu_{\mathrm{vis}}^{\mathrm{OR}}} \qquad \Longrightarrow \qquad \mu_{\mathrm{vis}}^{\mathrm{OR}} \;=\; -\ln\!\big(P_{00}(\mu)\big). \tag{3.28}$$

Experimentally, if N_{EventOR} number of bunch crossings pass the OR condition out of the total N_{BC} number, then $P_{00}(\mu) = 1 - N_{\mathrm{EventOR}}/N_{\mathrm{BC}}$ gives finally:

$$\boxed{\mu_{\mathrm{vis}}^{\mathrm{OR}} = -\ln\!\left(1-\frac{N_{\mathrm{EventOR}}}{N_{\mathrm{BC}}}\right),} \tag{3.29}$$

with analogous formulae for $\mu_{\mathrm{vis}}^{\mathrm{ORA}}$ and $\mu_{\mathrm{vis}}^{\mathrm{ORC}}$ after replacing OR with ORA/ORC.

3.4.2 Coincidence algorithm

EventAND condition fails if a bunch crossing produces no coincidence. Equivalently, all n interactions result in configurations that are not 11, i.e., they are in $\{00, 10, 01\}$. For a fixed n, the probability of failure is the sum of three mutually exclusive composite cases:

$$P_{00,10,01}(n) \;=\; P_{00}(n) + P_{10}(n) + P_{01}(n). \tag{3.30}$$

Since $P_{00}(n) = [P_{00}(1)]^n$ is already known, $P_{10}(n)$ and $P_{01}(n)$ remain to be calculated. The probability $P_{10}(n)$ corresponds to the situation where, in a bunch crossing with n interactions, exactly k of them produce a hit on the A side while the remaining $n-k$ interactions produce no hits at all. In this way, the A side registers activity, but the C side remains silent. So, all permutations with this case should be calculated like:

$$P_{10}(n) = \sum_{k=1}^{n}\binom{n}{k}\big[P_{10}(1)\big]^k\big[P_{00}(1)\big]^{n-k} \;=\; \big[P_{10}(1)+P_{00}(1)\big]^n - \big[P_{00}(1)\big]^n, \tag{3.31}$$

where the Binomial expansion[2] formulae have been used. Similarly:

$$P_{01}(n) \;=\; \big[P_{01}(1)+P_{00}(1)\big]^n - \big[P_{00}(1)\big]^n. \tag{3.32}$$

Summing Eqs. (3.25), (3.31), (3.32) gives:

$$P_{00,10,01}(n) = \big[P_{10}(1)+P_{00}(1)\big]^n + \big[P_{01}(1)+P_{00}(1)\big]^n - \big[P_{00}(1)\big]^n. \tag{3.33}$$

---

[2] $\big[P_{10}(1)+P_{00}(1)\big]^n = \sum_{k=0}^{n}\binom{n}{k}\,\big[P_{10}(1)\big]^k\,\big[P_{00}(1)\big]^{n-k}$

Calculating expected values of $P_{00,10,01}(n)$ now yields:

$$P_{00,10,01}(\mu) = \sum_{n=0}^{\infty} e^{-\mu} \frac{\mu^n}{n!} \Big(A^n + B^n - C^n \Big) \;=\; e^{-\mu} \Big(e^{\mu A} + e^{\mu B} - e^{\mu C} \Big), \tag{3.34}$$

with $A = P_{10}(1) + P_{00}(1)$, $B = P_{01}(1) + P_{00}(1)$, $C = P_{00}(1)$. Using (3.20)–(3.22) and (3.24),

$$A = 1 - \epsilon_{\text{ORC}}, \qquad B = 1 - \epsilon_{\text{ORA}}, \qquad C = 1 - \epsilon_{\text{OR}},$$

so Eq. (3.34) becomes the compact form:

$$P_{00,10,01}(\mu) = e^{-\mu\,\epsilon_{\text{ORC}}} + e^{-\mu\,\epsilon_{\text{ORA}}} - e^{-\mu\,\epsilon_{\text{OR}}}, \tag{3.35}$$

which is the probability that a bunch crossing does not satisfy EventAND condition. The measured value is

$$P_{00,10,01}(\mu) \;=\; 1 - \frac{N_{\text{EventAND}}}{N_{\text{BC}}}. \tag{3.36}$$

For a $\epsilon_{\text{AND}} << \epsilon_{\text{ORA(C)}}$ and equal A-side and C-side efficiencies $\epsilon_{\text{ORA}} \simeq \epsilon_{\text{ORC}}$, simplified Eq. (3.35) combined with Eq. (3.36) gives [147]:

$$\boxed{\frac{N_{\text{AND}}}{N_{\text{BC}}} \;=\; 1 - 2e^{-(1+\sigma_{\text{vis}}^{\text{OR}}/\sigma_{\text{vis}}^{\text{AND}})\mu_{\text{vis}}^{\text{AND}}/2} + e^{-(\sigma_{\text{vis}}^{\text{OR}}/\sigma_{\text{vis}}^{\text{AND}})\mu_{\text{vis}}^{\text{AND}}}.} \tag{3.37}$$

Here, visible cross-sections defined like $\epsilon^{\text{AND}} = \sigma_{\text{vis}}^{\text{AND}}/\sigma_{\text{inel}}$ and $\epsilon^{\text{OR}} = \sigma_{\text{vis}}^{\text{OR}}/\sigma_{\text{inel}}$ are used, where σ_{inel} represents the inelastic cross-section for a given process. There is no closed-form analytic inversion of (3.37) for $\mu_{\text{vis}}^{\text{AND}}$; in practice, a numerical inversion is used, given the simultaneously measured $\mu_{\text{vis}}^{\text{ORA}}$ and $\mu_{\text{vis}}^{\text{ORC}}$ or $\mu_{\text{vis}}^{\text{OR}}$ for a simplified case.

3.4.3 Hit-counting algorithms

HitOR algorithms count the number of detector modules that generate a hit in a BC. The summed number of hits during N_{BC} bunch crossings is denoted N_{HIT}, and the number of modules used for the hit counting is denoted N_{Modules}. Under the assumption that the efficiency to register a hit in a given module is independent of the number of hits in other modules, the conversion of event rates to $\mu_{\text{vis}}^{\text{HIT}}$ can be done via a formula:

$$\boxed{\mu_{\text{vis}}^{\text{HIT}} = -ln\left(1 - \frac{N_{\text{HIT}}}{N_{\text{BC}}N_{\text{Modules}}}\right).} \tag{3.38}$$

(the special case $N_{\text{Modules}} = 1$ reduces to EventOR).

3.5 The 2018 900 GeV vdM run

This particular vdM scan session at $\sqrt{s} = 900$ GeV forms the central dataset for the present thesis. In the following, the session overview and the physics motivation are summarized, setting the stage for the detailed calibration studies that follow.

3.5.1 Motivation

The primary physics goal for measuring elastic scattering using pp data at $\sqrt{s} = 900$ GeV is to determine parameters such as the total pp cross-section, ρ-parameter defined as in Section 3.2, B-slope parameter, which is at small $|t|$-region related to the differential cross-section as $d\sigma_{\mathrm{el}}/dt \propto e^{-B|t|}$, and the shape of the t-spectrum. In order to calculate the ρ parameter, special optics are required to enable access to very small t-values. The imaginary part of the amplitude is directly related to the total cross-section via the optical theorem Eq. (3.2). There is also a relation between the ρ-parameter and the integral of the total cross-section via dispersion relations shown in Eq. (3.3). A study of energy evolution of total cross-section and ρ-parameters might point to possible new phenomena: the existence of the three-gluon compound that can be exchanged in elastic scattering (allowed in QCD), and there are strong indications from 8 TeV [148] and 13 TeV [149] elastic data for that. In this case, there will be a difference at 900 GeV between the pre-LHC prediction of ρ and the data. Another possible conclusion that might be obtained from this analysis is a slowing down in the energy of the rise of the total cross-section. The slower rise does not influence the ρ-value around 900 GeV; therefore, there will be no differences at 900 GeV between the pre-LHC prediction of ρ and the data. Energy evolution of the elastic–scattering observables (ρ, σ_{tot}) is shown in Figure 3.2, where experimental results at higher energies are compared between ATLAS [150] and TOTEM [149], together with other measurements and theoretical predictions. The region between 100 GeV and 7 TeV exhibits a lack of experimental data, highlighting the importance of the $\sqrt{s} = 900\ \mathrm{GeV}$ measurement for improving the understanding of the energy dependence of these quantities. Available datasets with a center-of-mass energy of 900 GeV from special runs in 2018, using β^{*} = 100 m and β^{*} = 11 m optics, will be used for these purposes. The first one is sensitive to the low-t Coulomb Nuclear Interference (CNI) region [151, 152], and the second one is sensitive to the high-t slope region. The ultimate goal for the best precision is the analysis and combination of these two datasets. One of the necessary steps before any further analysis is luminosity determination. In this purpose, luminosity calibration for the 900 GeV pp collisions, consisting of the vdM beam separation scans in 2018 with β^{*} = 11 m will be used.

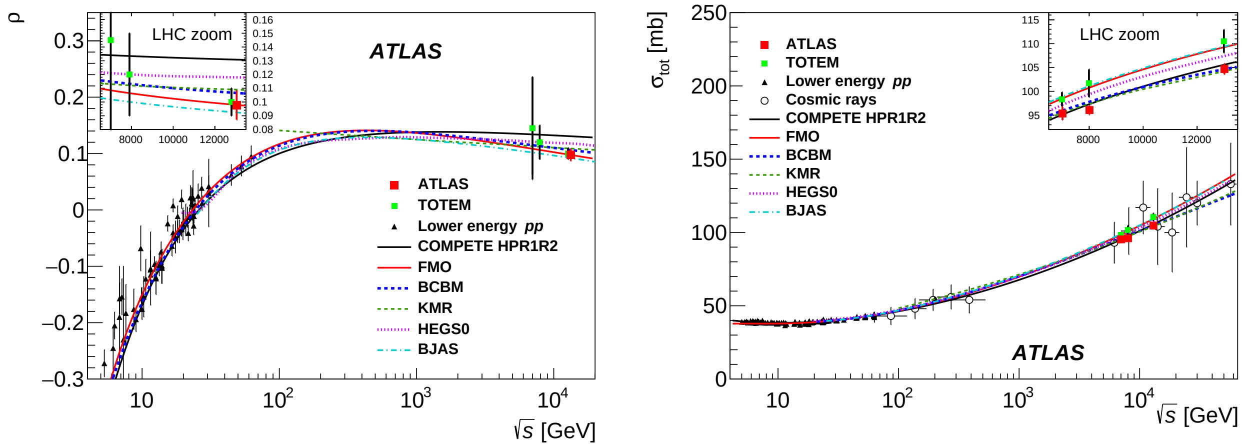

Figure 3.2: Dependence of key elastic scattering observables (left ρ parameter, right total pp cross-section) on collision energy. Adopted from [150].

3.5.2 Session overview

The beam-separation scans that were retained for determining the absolute luminosity scale and its uncertainty are illustrated in Figure 3.3 and summarized in Table 3.1. Initial van der Meer scans

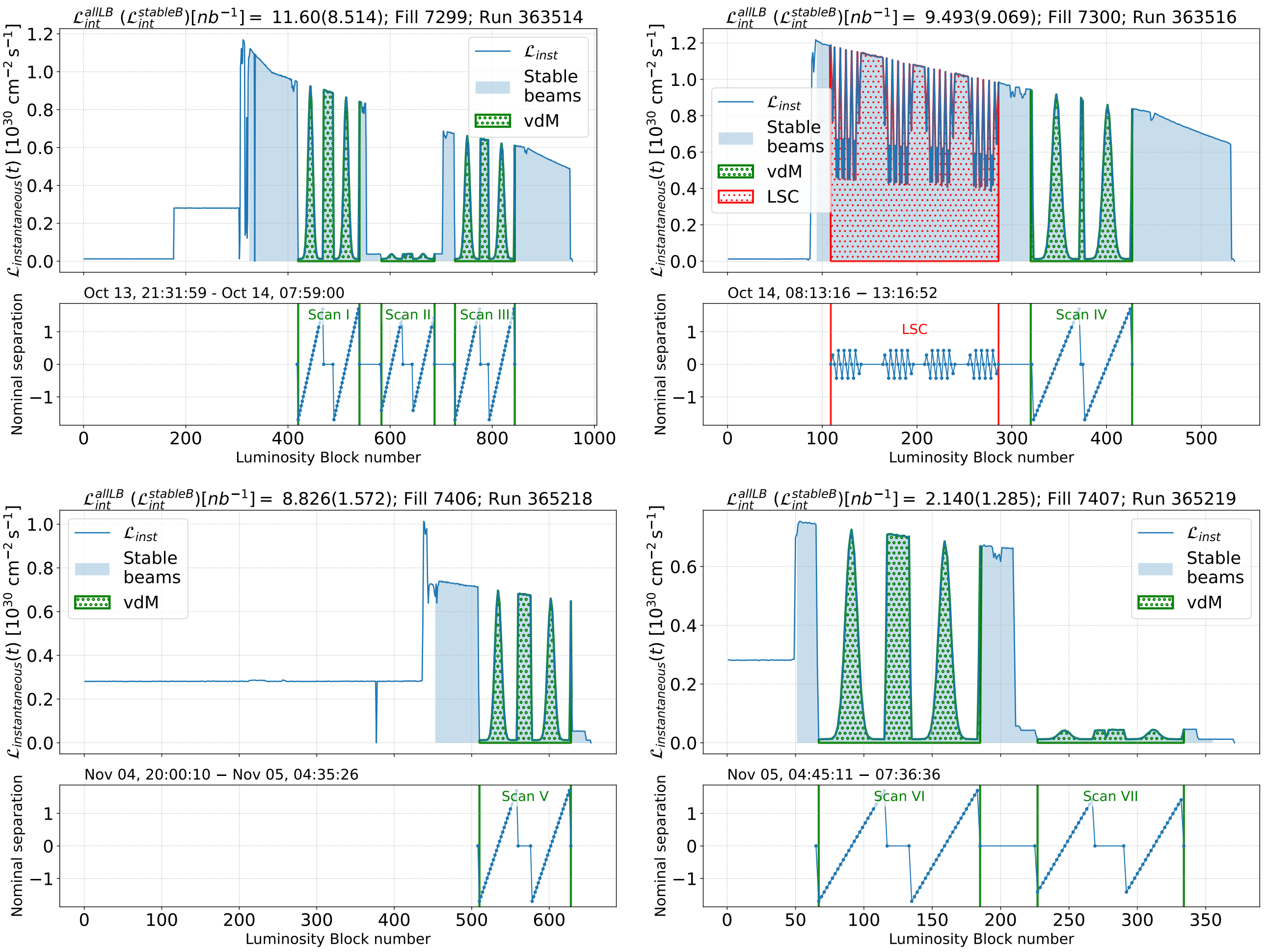

Figure 3.3: Instantaneous luminosity as a function of the luminosity block (LB) number for Fills 7299, 7300, 7406, and 7407. Periods of stable beams are indicated by pale blue shading. The ranges in which vdM scans were performed are shown as green hatched regions, while the Length Scale Calibration (LSC) intervals are indicated in red hatching. The lower panels display the nominal beam separation corresponding to the vdM and LSC periods, illustrating the programmed beam-separation pattern with each vdM scan number indicated on the plot. Integrated luminosity indicated on the plots is based on preliminary calibration.

were conducted during October 2018 in pp collisions at $\sqrt{s} = 900$ GeV, using the highest possible bunch intensity for best statistical precision to offset the reduced specific luminosity, $\mathcal{L}_{\text{spec}}$, σ_{vis}, and inelastic interaction rate. However, the October scans were impacted by extremely unfavourable beam conditions that were eventually traced to a combination of the low beam energy (dictated by the physics goals), a statistically motivated but excessively large bunch charge, and a too low RF voltage. These factors led to excessive bunch length, protons drifting to the edges of the RF buckets, and an anomalously high rate of debunching [153]. The consequences were very large and uncertain corrections to the bunch-population measurements that will be detailed in Sec. 3.6.2.1, as well as poorly understood backgrounds to the luminosity signal during the scans (Sec. 3.6.3). A second vdM session was therefore carried out in November 2018. At that time, reducing the bunch charge by 25% and significantly raising the RF voltage brought the bunch length within nominal tolerances, almost completely eliminated debunching, and resulted in significantly more favourable beam conditions for luminosity-calibration purposes. The vdM scans labeled I, III, IV, V, and VI are used for the calibration with 150 colliding bunches and 2 unpaired bunch-pairs per beam for estimating beam-gas. The remaining scans, Scan II from Fill 7299 and Scan VII from Fill 7407, were off-axis. Due to the issues observed in the October scans, and unless stated otherwise, the November scans (V and VI) are used throughout this thesis for correction steps and for the evaluation of systematic uncertainties. Typical number of protons per bunch for scans I, III, and IV was 1.2×10^{11} (1.8×10^{13} per beam) and for scans V and VI was 0.96×10^{11} (1.4×10^{13} per beam). All scans were performed using dedicated vdM-scan optics with $\beta^* = 11$ m in order to increase the transverse beam sizes. The total number of scan steps per plane is 25 across all scans. The requested transverse emittance was $1.8 - 2.5\mu m$ with the actual transverse emittance on the lower limits. Maximum beam separation was $\pm 6\sigma_b$ ($\sigma_b = 283.3$ μm) for all on-axis scans. On the detector side, the LUCID system operated with a reduced set of PMTs during these runs. A total of nine PMTs were active: four from the Bi subgroup (A9, A13, C7, C15) and five from the Bi2 subgroup (A8, A16, C4, C12, C13). This configuration enabled the definition of nine independent single-PMT algorithms, each identified by its subgroup (Bi/Bi2) and by detector side (A/C). These algorithms provided additional handles for internal cross-checks of stability and consistency in the luminosity calibration procedure. Given this configuration, it is worth noting that the Bi2-based hit-counting algorithms benefited from having more active PMTs and, therefore, achieved slightly better statistical precision compared to the Bi subgroup.

Table 3.1: Summary of the October and November 2018 900 GeV vdM session.

Scan label	I	III	IV	V	VI
Date of run	Oct 13	Oct 13	Oct 14	Nov 5	Nov 5
Time of run	03:50–04:29	05:45–06:23	11:04–11:44	03:17–03:56	05:41–06:18
LHC Fill number	7299	7299	7300	7406	7407
ATLAS run number	363514	363514	363516	365218	365219

3.6 Visible cross-section (σ_{vis}) calibration

Visible cross-section, obtained on a per-bunch basis from Eq. (3.18) using the vdM formalism and the dedicated special runs described in Sec. 3.2, must be calibrated to provide an absolute luminosity scale. The calibration of the visible cross-section σ_{vis} is a central step in the vdM analysis, and requires the application of several corrections and the evaluation of systematic uncertainties in order to properly determine all variables involved. Calibration procedure can be structured as follows:

- $n_1 n_2$: The product of the bunch intensities is determined using the fast beam-current transformer (FBCT) or BPTX, normalized to the DC current transformer (DCCT) (see Sec. 3.6.2). Corrections must account for ghost-charge and satellite bunches, as detailed in Sec. 3.6.2.1.

- $\mathcal{L}$: The raw interaction rates used to compute the luminosity must be corrected for background contributions, such as noise, beam–gas (Sec. 3.6.3), and for beam-beam optical distortions (Sec. 3.6.4).

- δ_x, δ_y : Nominal displacements used during vdM scans must be corrected for the actual beam–beam separation. This involves correction for beam–beam deflections that modify the effective separation during the scans (Sec. 3.6.4), correction for orbit drifts between scan steps (Sec. 3.6.5), and a length-scale calibration to translate magnet settings into physical displacements (see Sec. 3.6.8).

- Σ_x, Σ_y : Convolved beam sizes extracted from the scan curves must be corrected for non-factorization effects if the beam densities cannot be expressed as simple products of independent x and y components (Sec. 3.6.7).

These aspects will be discussed in detail in this section.

3.6.1 Scan curve fitting

The expression for $R(0,0)$ on the right-hand side of Eq. (3.18) corresponds to the special case $\delta_x^0 = \delta_x^0 = 0$. More general expression for a non-zero working point ($\delta_x^0 \neq 0$, $\delta_x^0 \neq 0$) is $\big(R(0,\delta_y^0) \cdot R(\delta_x^0,0)\big) \;/\; R(\delta_x^0,\delta_y^0)$. For a Gaussian-like density profiles $R(0,\delta_y^0)$ and $R(\delta_x^0,0)$ correspond to the horizontal and vertical peak interaction rates ($\mu_{\text{vis,x}}^{\text{max}}$ and $\mu_{\text{vis,y}}^{\text{max}}$) respectively, while $R(\delta_x^0,\delta_y^0)$ is interpreted as the average of these peaks. The resulting formula for σ_{vis} is then written as:

$$\sigma_{\text{vis}} \;=\; \frac{2\pi\,\Sigma_x\,\Sigma_y}{n_1 n_2}\,\frac{\mu_{\text{vis},x}^{\text{max}} \cdot \mu_{\text{vis},y}^{\text{max}}}{0.5\cdot\big(\mu_{\text{vis},x}^{\text{max}} + \mu_{\text{vis},y}^{\text{max}}\big)}. \tag{3.39}$$

It is evident from the formula above that an accurate determination of both the peak interaction rates and the convolved beam sizes is crucial in the accurate estimation of the σ_{vis}. These quantities are extracted from the bell-shaped functions that describe the interaction rate as a function of beam separation during the vdM scans. Different models of functions have been used for these purposes. To eliminate variations in the bunch current during the scan, the *specific visible interaction rate*, $\mu_{\text{vis}}^{\text{spec}} = \mu_{\text{vis}}/(n_1 n_2)$, is fitted instead of μ_{vis} itself. For a simple Gaussian model, the convolved beam sizes Σ_u ($u \in \{x,y\}$) can be obtained from the peak and area of the scan curve:

$$\mu_u(u) \;\propto\; \exp\Big[-\tfrac{(u-\nu_u)^2}{2\,\Sigma_u^2}\Big] \quad\Rightarrow\quad \int \mu_u\,du \;=\; \mu_u(\nu_u)\,\sqrt{2\pi}\,\Sigma_u, \tag{3.40}$$

with $\mu_u(\nu_u)$ being the peak obtained at the mean ν_u of the Gaussian curve, hence:

$$\Sigma_u \;=\; \frac{1}{\sqrt{2\pi}}\,\frac{\displaystyle\int \mu_u(u)\,du}{\mu_u(\nu_u)}, \tag{3.41}$$

meaning that the width of the Gaussian curve is exactly the convolved beam size by definition Eq. (3.17). Real scan curves deviate from a perfect Gaussian (non-Gaussian beam tails, small non-linearities, and other conditions that break assumptions of the vdM formalism). Fit must therefore (i) capture the peak accurately and (ii) describe the tails. This is done by multiplying a Gaussian core by a polynomial in the normalized coordinate:

$$\xi \;\equiv\; \frac{u-\nu}{\Sigma_u^{\text{eff}}}, \tag{3.42}$$

where effective width Σ_u^{eff} is related to the convolved beam size Σ_u such that the Gaussian peak–area identity (3.41) holds by construction, and is for a n^{th}-order polynomial defined as:

$$\Sigma_u^{\text{eff}} \;=\; \Sigma_u \;-\; \sum_{k\geq 2}(k-1)!!\;c_k, \tag{3.43}$$

where c_k are polynomial coefficients. General case of the Gaussian × n^{th}-polynomial fit function is then:

$$\mu_u^{\text{GPn}}(u) = \mu_u(\nu_u)\,\exp\left[-0.5\cdot\left(\frac{u-\nu_u}{\Sigma_u^{\text{eff}}}\right)^2\right]\left[1+\sum_{k\geq 2}^{n}\frac{c_k}{\Sigma_u^{\text{eff}}}\left(\frac{u-\nu_u}{\Sigma_u^{\text{eff}}}\right)^k\right]. \tag{3.44}$$

After substituting with normalized coordintas and analytically integrating Eq. (3.44) term by term using $\int e^{-\xi^2/2}\xi^{2n}\,d\xi = \sqrt{2\pi}\,(2n-1)!!$, one obtains:

$$\int \mu_u^{\text{GPn}}(u)du \;=\; \mu_u(\nu_u)\,\sqrt{2\pi}\,\Sigma_u.$$

Most commonly used GPn function for fitting vdM scan curves is GP6, with effective width defined as:

$$\Sigma_u^{\text{eff}} = \Sigma_x - c_2 - 3 \cdot c_4 - 15 \cdot c_6. \tag{3.45}$$

Although GP6 provides additional freedom by including sixth-order terms, this very flexibility can make the fits unstable, especially when scan points fluctuate around the peak or in low-statistics cases such as the one in the presented study. Such instabilities may bias the extracted peak position and width, or even lead to non-physical results. For this reason, many analyses switch to the simpler GP4 model, which sacrifices some descriptive power in the tails but offers greater stability and robustness in estimating the key parameters needed for the luminosity calibration.

GP4+G extends GP4 by adding an extra simple Gaussian term, specifically to better reproduce the narrow peak region of the scan curve. This improves the description of the central points but at the cost of introducing more parameters and, in some cases, less stability of the fits. In addition to Gaussian-polynomial models, another class of functions often used in luminosity calibration is the double Gaussian. This type of function provides more flexibility in describing the scan curves, especially when the beam profiles deviate from a single Gaussian shape. The double Gaussian can be written as:

$$\mu_u^{\text{DblG}}(u) \;=\; \mu_u(\nu_u)\left[f\ \exp\left(-\frac{(u-\nu_u)^2}{2\sigma_1^2}\right) + (1-f)\ \exp\left(-\frac{(u-\nu_u)^2}{2\sigma_2^2}\right)\right], \tag{3.46}$$

where $\mu_u(\nu_u)$ denotes the peak value at the mean position $u = \nu_u$, f is the relative weight of the first Gaussian component ($0 \leq f \leq 1$), and σ_1, σ_2 are the widths of the two Gaussian components. This functional form is normalized such that $\mu_u^{\text{DblG}}(\nu_u) = \mu_u(\nu_u)$. Ultimately, for the analyzed dataset, the GP4 model with the odd polynomial parameter set to zero was selected as the baseline fit function. The associated fit-model uncertainty was evaluated by comparing the baseline results to those obtained with the GP6 model. Figure 3.4 illustrates this comparison on a logarithmic scale for two different algorithms, highlighting the differences between the two functional forms across the scan range.

3.6.2 Beam current measurement

An important part of the absolute luminosity determination in vdM scans is the knowledge of the number of protons per bunch, n_1 and n_2, for the two colliding beams. Since the observed visible interaction rate is normalized by the product $n_1 n_2$, any uncertainty in the bunch populations directly translates into an uncertainty on σ_{vis}. Beam currents are measured using different kinds of *Beam current transformers* (BCT) [4].

The total beam intensity per beam is measured by a high-precision device called *Direct Current Current Transformers* (DCCT) [154, 155]. The DCCT provides an absolute measurement of the integrated beam current by sensing the magnetic field generated by the circulating protons. While the DCCT measures the total current in a beam, bunch-resolved measurements are required for vdM scans, because luminosity is evaluated per colliding bunch crossing. These are provided by the *Fast Beam Current Transformers* (FBCT) [156, 157], which sample the beam current at the 25 ns bunch spacing, and the ATLAS *Beam Pickup and Timing System* (BPTX) [158], which also provides timing and phase information for the bunches. Unlike the DCCT, both FBCT and BPTX can distinguish between individual bunch slots but are less precise in their absolute calibration. Nominal bunch populations at the head-on luminosity block for the two beams are shown in Figure 3.5 as a function of BCID. A gradual loss of protons from the beam, primarily driven by intra-beam scattering and other beam–beam effects, is visible when comparing the early (Ix) and later (IIIy) scans of the October session. The DCCT is considered the reference device due to its improved accuracy. To obtain reliable

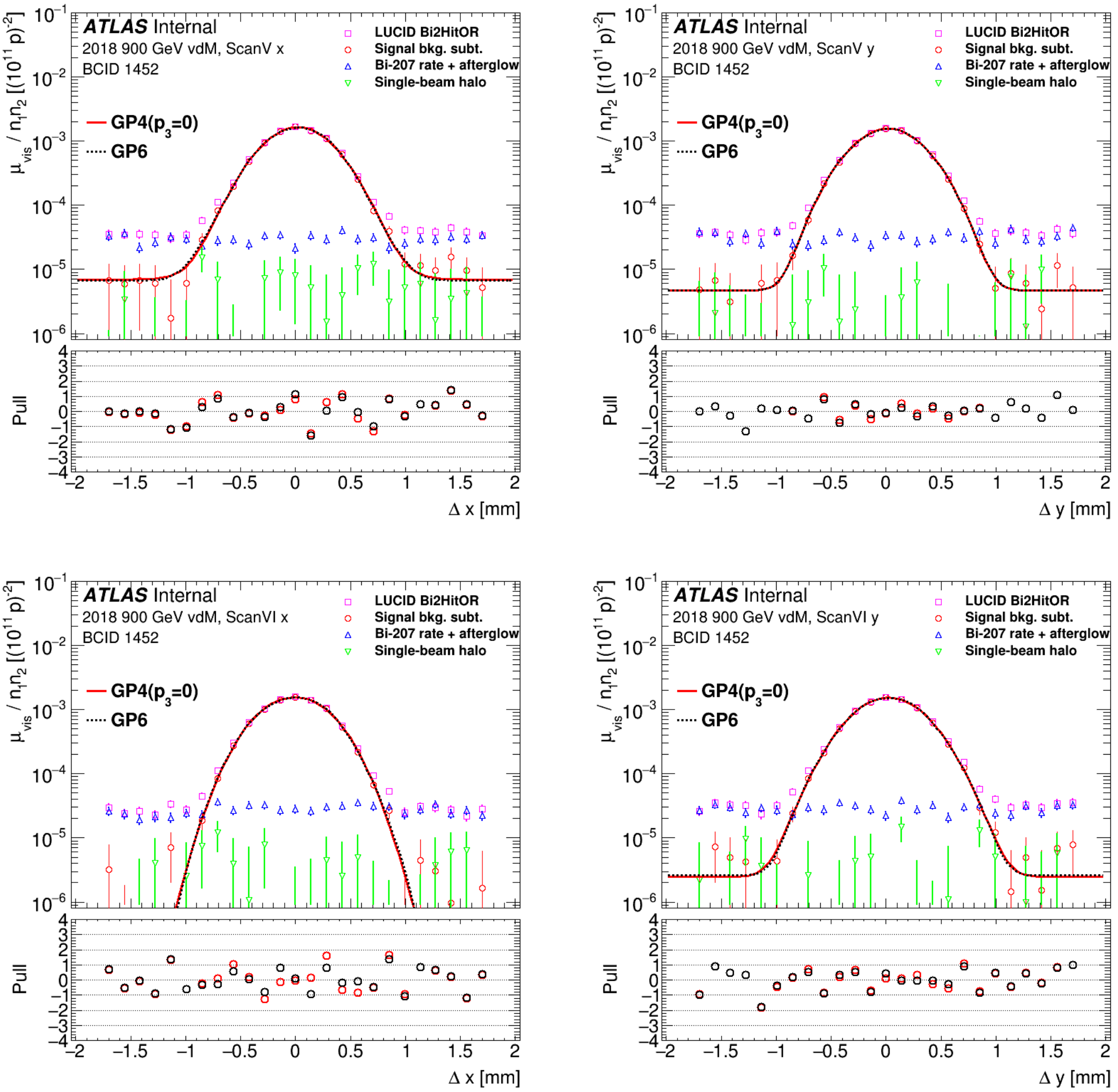

Figure 3.4: Specific visible interaction rate, $\mu_{\text{vis}}/(n_1 n_2)$, vs. beam separation for the LUCID Bi2HitOR algorithm. Each plot contains an upper panel with data before (magenta squares) and after (red circles) background subtraction, together with fits using different model functions; estimated noise and beam–gas contributions are indicated per scan step. Lower panels show the pull distributions, i.e., (data−fit) normalized to the statistical uncertainties. Results are shown for the GP4 (red open circles) and GP6 (black open circles) fit functions. Top row: Scan V in x (left) and y (right). Bottom row: Scan VI in x (left) and y (right). Results are presented for the same BCID (number 1452).

per-bunch intensities, the FBCT (or BPTX) measurements are normalized to the DCCT value: the sum of the measured intensities of the nominally filled bunches is rescaled such that it matches the total beam intensity measured by the DCCT. Differences between the calibrated FBCT and BPTX values are taken as a source of systematic uncertainty. The raw beam current measurements require corrections for effects not associated with the nominal colliding bunches:

- Ghost-charge: protons circulating in nominally empty bunch slots, i.e. in RF buckets where no bunch should have been injected.

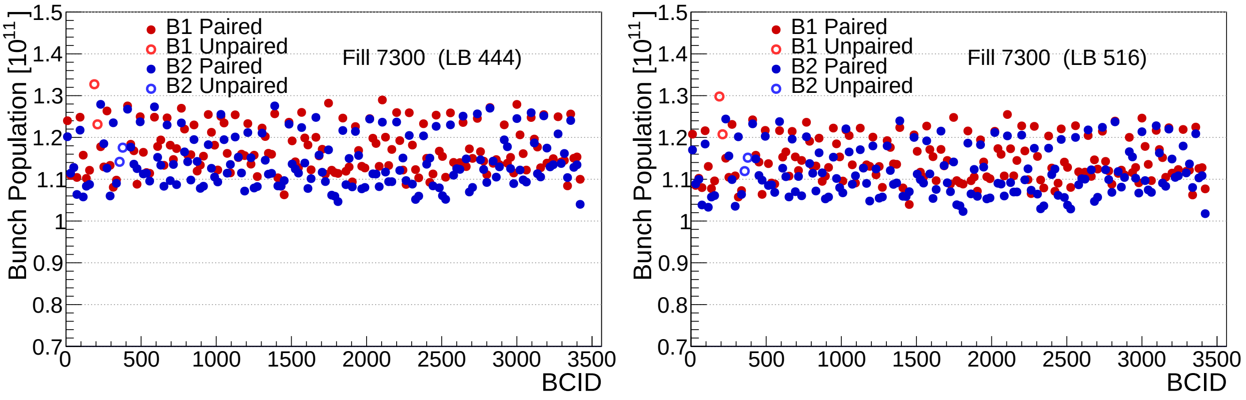

Scan Ix

Scan Iy

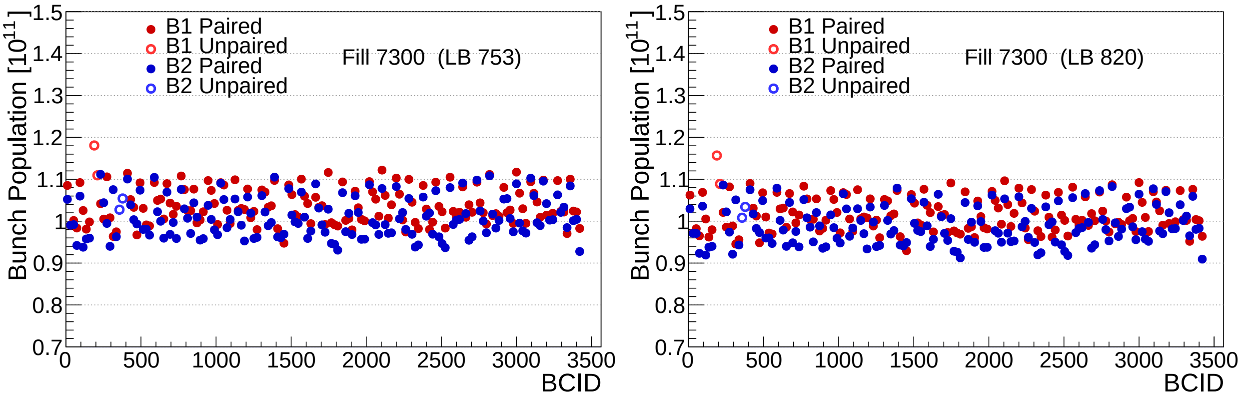

Scan IIIx

Scan IIIy

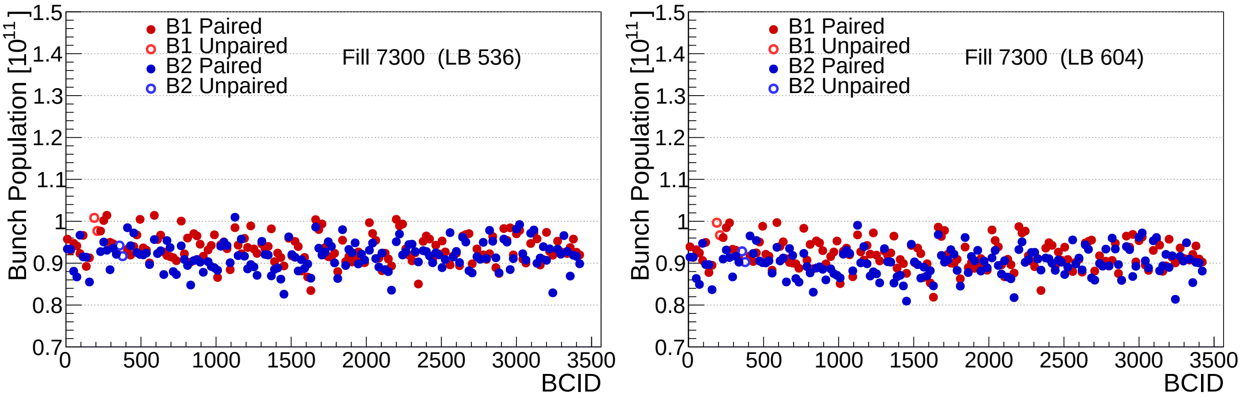

Scan Vx

Scan Vy

Figure 3.5: Bunch population per BCID measured using FBCT device, with paired bunches indicated by filled circles and unpaired ones by open circles. Beam 1 is shown in red and Beam 2 in blue. Only the on-axis vdM scans are shown here, drawn from two distinct fills, and for each scan, the head-on luminosity block is used. Scans Ix, Iy, IIIx, IIIy originate from Fill 7299 of the October vdM session, while Scans Vx and Vy correspond to Fill 7406 from the November session. A gradual decrease in bunch population is observed from Scan Ix to Scan IIIy, as well as a noticeable difference in the overall bunch populations between the two sessions.

- Satellite bunches: protons within the same nominal bunch slot, but captured in neighboring RF buckets around the central filled one.

Corrections for these effects, as well as their associated uncertainties, are discussed in the following subsections.

3.6.2.1 Correction for ghost-charge and satellite bunches

The DCCT current includes contributions from both ghost-charge and satellite bunches. Both populations dilute the effective normalization of the FBCT/BPTX to DCCT, leading to a bias in the derived number of protons per nominally colliding bunch. During the October fills, the elevated levels of ghost-charge and satellite contamination introduced significant challenges. This is clearly illustrated in the time evolution of the per-beam ghost-charge fractions measured by the LHC Longitudinal Density Monitor (LDM) [159, 160], shown in Figure 3.6. The LDM is an optical device based on avalanche photodiodes (APDs) [161], which detect visible synchrotron-radiation photons emitted by beam particles as they exit an LHC magnet. These photon counts, accumulated in 50-ps time bins, provide a relative measurement of the charge contained in each of the 35640 RF buckets, each 2.5 ns wide, around the ring circumference. However, the determination of ghost-charge and satellite content is affected by a fundamental ambiguity: distinguishing light originating from a coasting beam (which lacks the strong time structure of a bunched beam) from random hits caused by electronic noise, ambient light, dark counts[3], or afterpulses[4] is intrinsically challenging. The blue markers in Figure 3.6 show the effect of the simplest baseline correction, which assumes that no particles are present at the edges of each RF bucket.[5] In the absence of significant debunching (right side of the Figure 3.6), this procedure yields a lower limit on the ghost-charge and satellite fractions; in the presence of a significant coasting-beam fraction, the apparent ghost-charge fraction can become negative (left side of the Figure 3.6), and therefore nonphysical. A refined analysis, which corrects only for the dark counts measured in the absence of any circulating beam and for afterpulses, gives the data shown by the red markers. These represent the best estimate of the ghost-charge fraction, and the same procedure is applied to measure the satellite fraction. Since the background and afterpulse correction either may not account for all the sources of parasitic counts or may overestimate the magnitude of the subtraction, this correction is assigned, somewhat arbitrarily, a systematic uncertainty equal to half of the shaded area between red and blue markers, where red is the best estimate.

The calibration of bunch-resolved current measurements requires a consistent normalization between the DCCT (which measures the total beam current with high accuracy) and the FBCT/BPTX (which provide bunch-by-bunch resolution but are less precise in absolute scale). This normalization is complicated by the presence of ghost-charge and satellite bunches, which affect the DCCT measurement but are distributed differently across the FBCT and BPTX readouts. For each luminosity block i, a normalization factor is defined as:

$$\mathcal{N}_i = \frac{I_i^{\mathrm{DCCT}}}{I_i^{\mathrm{device}}}, \tag{3.47}$$

where I_i^{DCCT} is the total beam current measured by the DCCT, and I_i^{device} is the corresponding total current measured by either the FBCT or BPTX, which is a sum over nominally filled bunch currents. This factor rescales the bunch-resolved intensities measured by either the FBCT or BPTX device to match the absolute scale of the DCCT.

---

[3] Dark counts are believed to originate primarily from thermal noise in the light sensors.

[4] Afterpulses originate from charge carriers that become trapped in the semiconductor band gap and are subsequently released, generating secondary avalanches that are indistinguishable from true photon-induced counts.

[5] No particles are expected to remain at the separatrix since this is a line of unstable equilibrium.

3.6.2.2 Ghost-charge and satellite correction methods

Two approaches are employed: the first is referred to as the "classical method", suitable for low contamination levels, and the second is referred to as the "alternative method", developed to address the high ghost-charge observed in the October scans.

Classical method. In the classical procedure, the DCCT measurement is first corrected for ghost and satellite fractions:

$$I_i^{\text{DCCT,corr}} = (1 - g_i - s_i) \cdot I_i^{\text{DCCT}}, \tag{3.48}$$

where g_i and s_i are the ghost and satellite fractions of the beam in luminosity block i. The corrected DCCT current is then used to renormalize the FBCT measurement:

$$I_{i,k}^{\text{FBCT,corr}} = \frac{I_i^{\text{DCCT,corr}}}{I_i^{\text{FBCT,raw}}} \cdot I_{i,k}^{\text{FBCT,raw}}, \tag{3.49}$$

where $I_i^{\text{FBCT,raw}} = \sum_k I_{i,k}^{\text{FBCT,raw}}$ is the total raw FBCT current for filled bunches, and $I_{i,k}^{\text{FBCT,raw}}$ is the raw current for bunch k. An analogous procedure applies for BPTX. This method ensures that, after correcting for ghost and satellites, the bunch-resolved FBCT/BPTX currents are consistent with the DCCT absolute scale. However, in the October session, ghost fractions reached up to $\sim 13\%$ and varied significantly in time, making this procedure unstable and introducing large biases in σ_{vis}.

Table 3.2 summarizes the scan-average ghost-charge and satellite fractions per beam, together with their net impact on the visible cross-section obtained using the classical method described in this section. The large effect observed in the October scan session highlights the need for an alternative procedure, which was therefore developed for this purpose.

Table 3.2: Scan-averaged correction factors for ghost-charge and satellite bunches per beam, and their impact on σ_{vis}. These values were computed using the classical method.

	Ghost		Satellite		Effect on
Scan	B1	B2	B1	B2	σ_{vis}
I	7.5%	7%	0.35%	0.36%	16.00%
III	13.5%	13%	0.6%	0.6%	34.00%
IV	7.5%	8%	0.3%	0.4%	19.00%
V	0.3%	0.25%	0.05%	0.05%	0.60%
VI	0.3%	0.26%	0.05%	0.05%	0.60%

Alternative method. To mitigate the instability of the classical method under high contamination, an alternative normalization scheme was developed. The key idea is to determine the DCCT-to-FBCT normalization factor early in the fill, when ghost and satellite fractions are still negligible, and to reuse this factor for the entire scan. For example, in Fill 7299, the reference normalization was determined at luminosity block $i_0 = 302$, yielding

$$\mathcal{A}_{i_0} = \frac{(1 - g_{i_0} - s_{i_0}) \cdot I_{i_0}^{\text{DCCT}}}{I_{i_0}^{\text{FBCT,raw}}}. \tag{3.50}$$

For a later luminosity block i, the corrected per-bunch currents are then obtained as:

$$I_{i,k}^{\text{FBCT,alt}} = \frac{I_{i,k}^{\text{FBCT,raw}}}{I_i^{\text{FBCT,raw}}} \cdot I_i^{\text{FBCT,raw}} \cdot [1 - (s_i - s_{i_0})] \cdot \mathcal{A}_{i_0}. \tag{3.51}$$

Here, only the relative change in the satellite fraction $(s_i - s_{i_0})$ is applied on top of the initial calibration factor $\mathcal{A}_{i_0}$, while the ghost-charge correction is effectively frozen at its early-fill value. For BPTX, which is less sensitive to satellites, only the fixed normalization factor $\mathcal{A}_{i_0}$ is applied without an explicit correction for satellite evolution. The justification for treating FBCT and BPTX corrections differently for the October session stems from the fact that satellites are "picked up" by FBCT and are partially or totally invisible to BPTX.

Uncertainties. The systematic uncertainty on these corrections is evaluated by varying the ghost and satellite fractions within the half-range of the shaded uncertainty bands in Figure 3.6. The November scans, with stable and low contamination, are used to define the uncertainty estimate, while the October scans are considered unreliable for direct evaluation due to the dominance of ghost-charge.

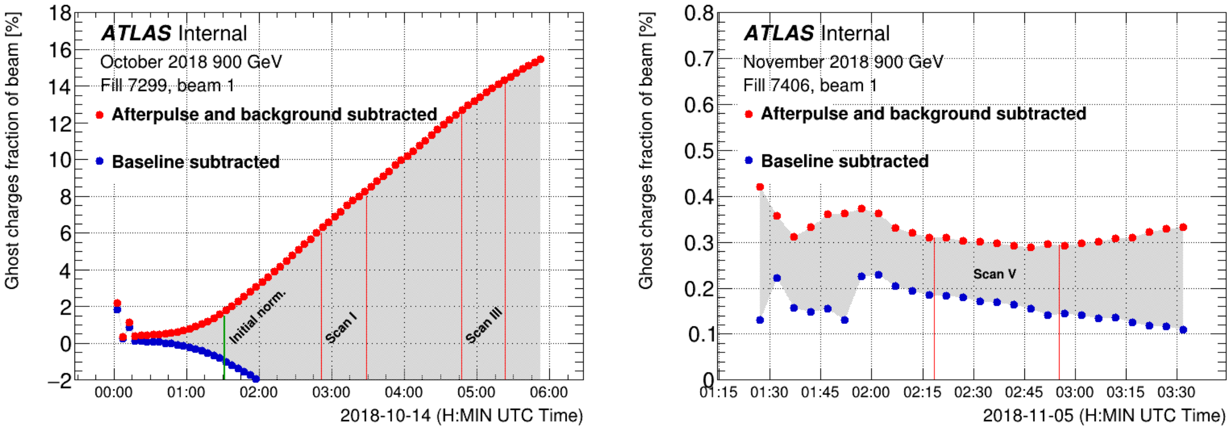

Figure 3.6: Left: Time evolution of ghost-charge fraction for beam 1 during Fill 7299 in the October session. The green vertical line marks the LB used to determine the initial normalization factor. Red vertical lines delimit the vdM scan intervals. Blue points show the total fraction of the beam in nominally empty bunch slots with baseline subtraction (overestimated). Red points represent the same total fraction of the beam but with both afterpulse and background corrections incorporated.

3.6.2.3 FBCT bunch–current offset correction

Even after applying DCCT→FBCT/BPTX normalization and the ghost/satellite corrections of Sections 3.6.2.1–3.6.2.2, a residual device non-linearity in the FBCT response can bias the per-bunch luminosity. This manifests as a dependence of the per-BCID visible cross-section, σ_{vis}, on the bunch-current product $n_1 n_2$. Ideally, σ_{vis} is a detector constant, hence $\mathrm{d}\sigma_{\text{vis}}/\mathrm{d}(n_1 n_2) = 0$ is the expected behaviour. A non-zero slope indicates a remaining intensity-dependent bias in the measurement of the bunch current (see the left plots in Figure 3.7).

To remove this effect, the procedure outlined in Ref. [22] was used. One can introduce per-beam offset parameters that absorb the residual FBCT non-linearity around the mean bunch intensities. Use n_k^i to denote (already DCCT-normalized and ghost/satellite–corrected) bunch population for beam $k \in \{1, 2\}$ and BCID i, and let $\bar{n}_k$ be the average bunch population in beam k over the BCIDs used in the fit. A common visible cross-section is fitted $\bar{\sigma}_{\text{vis}}$ together with two offset parameters b_k $(k = 1, 2)$, by minimizing the following χ^2 distribution:

$$\chi^2(\bar{\sigma}_{\text{vis}}, b_1, b_2) = \sum_{i \in \text{BCIDs}} \left(\frac{S(\bar{\sigma}_{\text{vis}}, b_1, b_2, n_1^i, n_2^i) - \sigma_{\text{vis}}^{\text{no offs},i}}{\Delta\sigma_{\text{vis}}^{\text{no offs},i}} \right)^2 , \tag{3.52}$$

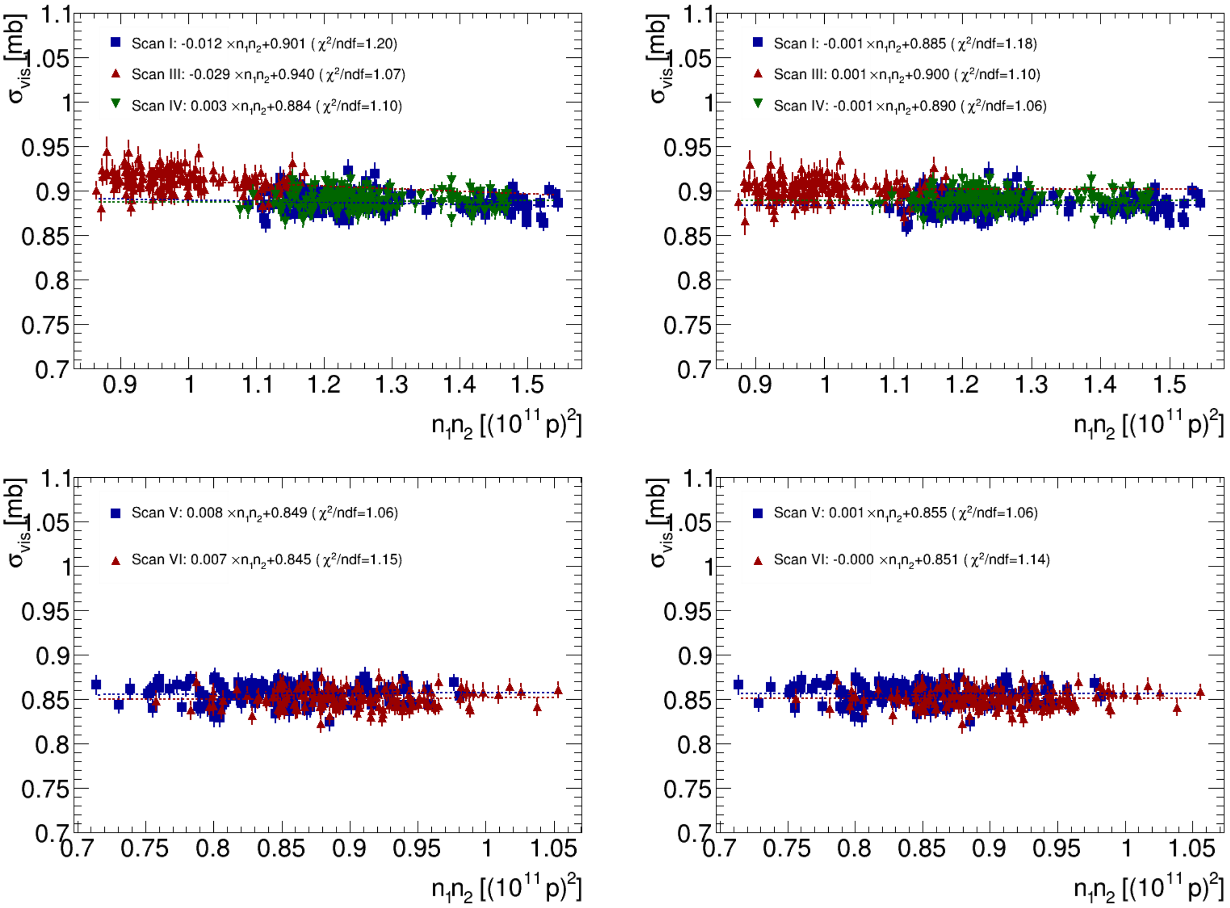

Figure 3.7: Comparison of the σ_{vis} dependence on the bunch current product $n_1 n_2$ for the October–November sessions (top to bottom) without (left) and with (right) the FBCT offset-fit correction applied.

where S is:

$$S(\bar{\sigma}_{\text{vis}}, b_1, b_2, n_1^i, n_2^i) = \bar{\sigma}_{\text{vis}} \frac{n_1^i + b_1 \cdot (n_1^i - \bar{n}_1)}{n_1^i} \frac{n_2^i + b_2 \cdot (n_2^i - \bar{n}_2)}{n_2^i} . \tag{3.53}$$

Here $\sigma_{\text{vis}}^{\text{no offs},i}$ is the per-BCID visible cross-section prior to the offset correction, and $\Delta\sigma_{\text{vis}}^{\text{no offs},i}$ its statistical uncertainty. Eq. (3.52) parametrizes the leading non-linearity as a linear correction in the deviation of each bunch current from its beam average; the fitted b_k capture a small, beam-dependent re-scaling that flattens the σ_{vis} versus $n_1 n_2$ trend.

Fitted offsets b_1 and b_2 are applied multiplicatively through S to all BCIDs, yielding a corrected, current-independent estimate of $\bar{\sigma}_{\text{vis}}$. Computed bunch current offsets per beam and each scan are shown in Table 3.3. Stability of the procedure is validated by comparing the *slope* of σ_{vis} versus $n_1 n_2$ before and after applying the offset correction: a reduction of the slope towards zero indicates a successful removal of the residual FBCT non-linearity, which can be clearly observed in the right-hand plot of Figure 3.7.

Table 3.3: FBCT bunch current offsets computed for the 900 GeV vdM scans.

2018	Scan I	Scan III	Scan IV	Scan V	Scan VI
Beam 1	-0.062 ± 0.028	-0.062 ± 0.035	0.06 ± 0.028	-0.009 ± 0.028	-0.025 ± 0.027
Beam 2	0.021 ± 0.025	-0.007 ± 0.030	-0.05 ± 0.027	0.023 ± 0.028	0.037 ± 0.028

3.6.3 Beam background subtraction

A precise determination of luminosity during vdM scans requires careful treatment of background levels, since even small contributions can bias the extracted calibration constants. The primary sources of background are electronic noise, calibration source signals, and beam-related processes.

Bismuth-source noise. For the LUCID algorithms, the dominant background arises from the embedded Bismuth-207 calibration source. This isotope undergoes radioactive decay, emitting electrons that pass through the quartz windows of the PMTs and produce Cherenkov radiation, thereby mimicking real collision signals. Secondary background contribution comes from so-called afterglow: these are delayed photons generated from the de-excitation of nuclei created in hadronic showers following pp collisions. Unlike the Bismuth decay, which is independent of beam conditions, the afterglow contribution scales with the instantaneous luminosity at each scan point. The combined effect of these processes is estimated by measuring the rate in the empty bunch slot preceding a colliding bunch, where no pp collisions are present. Subtracting this rate ensures that only beam-induced activity remains. This method relies on the fact that the detector response in consecutive bunch slots is identical, apart from the presence of collisions.

Beam–gas interactions. Another important background originates from collisions between beam particles and residual gas molecules in the beam pipe, leading to signals in the luminometer. These so-called beam-gas interactions are estimated using unpaired bunches, i.e., bunch crossings where only one beam carries a particle bunch. Since no actual collisions occur in such bunch crossings, any recorded signal can be attributed to beam–gas processes (after correcting for the Bismuth and afterglow noise using the preceding empty slot). By averaging over all unpaired bunches in a fill, an estimate of the beam–gas background rate for each beam is obtained, which can then be subtracted from the measured visible interaction rate.

Background-subtracted interaction rate. After accounting for both effects, the background-subtracted specific visible interaction rate for bunch i is expressed as:

$$\mu^{i}_{\text{vis, spec}} = \frac{\mu^{i}_{\text{vis}}}{n_1 n_2} - \frac{\mu^{i-1}_{\text{vis}}}{n_1 n_2} - \frac{n_1 \cdot \mu^{\text{beam-gas}}_{\text{vis},B1} + n_2 \cdot \mu^{\text{beam-gas}}_{\text{vis},B2}}{n_1 n_2}, \tag{3.54}$$

where the second term subtracts the Bismuth-induced noise (from bunch slot $i-1$), and the third term accounts for the beam–gas backgrounds. The beam–gas contribution for beam $k = 1, 2$ is determined as:

$$\mu^{\text{beam-gas}}_{\text{vis},Bk} = \frac{1}{N_{\text{unpaired}}} \sum_{i \in \text{unpaired}} \left(\frac{\mu^{i}_{\text{vis}} - \mu^{i-1}_{\text{vis}}}{n_{i,k}} \right), \qquad k = 1, 2. \tag{3.55}$$

Ghost-charge contamination. In practice, the beam–gas estimate can be contaminated by ghost-charge, originating from collisions between the main bunch and ghost-charge protons. This effect was observed in the October scans, where the beam–gas estimate showed a dependence on the beam separation (Figure 3.8, left). The most prominent observed peak is correlated with the highest ghost-charge level during Scan III. In contrast, the November scans exhibited no such dependence, consistent with a negligible (or regular) level of ghost-charge (Figure 3.8, right). Consequently, only the November session scans were considered reliable for estimating the background-related uncertainty.

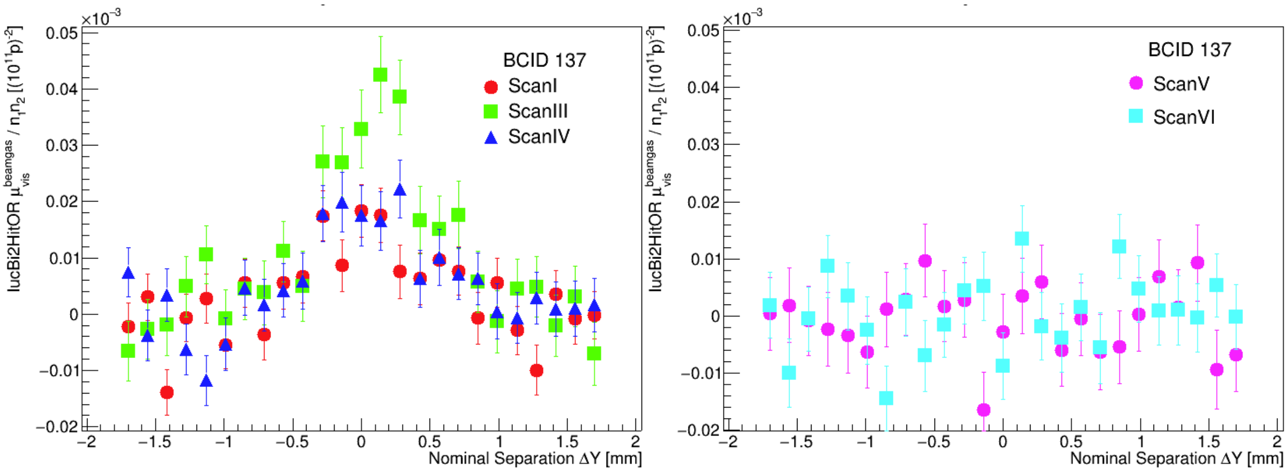

Figure 3.8: Example of beam–gas estimation for one BCID: Fills 7299–7300 (left) showing separation dependence due to ghost-charge; and Fills 7406–7407 (right) showing no such effect, consistent with a negligible ghost-charge.

Fluctuations in single-PMT algorithms. Single-PMT LUCID algorithms were found to be particularly sensitive to beam–gas subtraction due to large estimated fluctuations. As shown in Figure 3.9, these fluctuations are consistent with statistical noise and converge to zero under a constant-fit model, confirming their negligible physical impact. For consistency across all LUCID algorithms, beam–gas subtraction was therefore excluded from the final background estimation strategy. Instead, a constant fit for noise was adopted across all colliding bunch crossings (BCIDs), providing a more uniform background treatment.

Systematic uncertainty. An alternative approach is to model the background as a constant offset parameter in the fit of the vdM scan curve. This method does not require the explicit identification of the background origin, but instead assumes that the background level is independent of the transverse beam separation. The difference between this method and the direct subtraction approach is used to derive a systematic uncertainty on the background subtraction.

3.6.4 Beam-beam effects

When two high-intensity LHC beams cross each other at an interaction point, their strong electromagnetic fields lead to mutual perturbations [162]. These beam–beam interactions manifest in two ways:

- Beam-beam deflection: A transverse electromagnetic deflection of each bunch by the other when separated. This deflection acts like a small dipole “kick”, leading to an orbit shift at the interaction point, which changes the nominal separation.
- Optical distortions: Whereby the non-linear focusing of one beam by the other modifies the local optics. This changes both the effective beam sizes and the shape of the transverse density profiles, in particular when the separation changes.

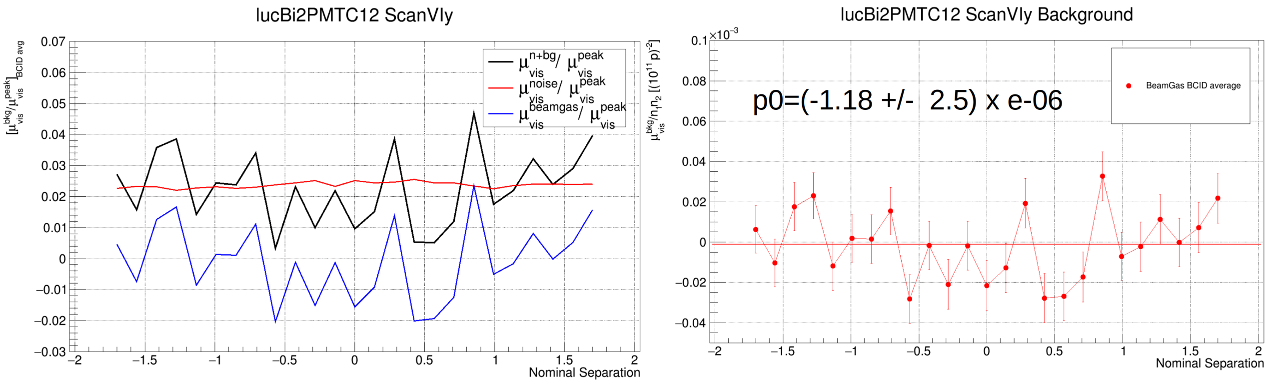

Figure 3.9: Estimated bunch-averaged background fraction of $\mu_{\rm vis}$ at near-zero separation for the single PMT LUCID Bi2PMTC12 algorithm. Left: fluctuations dominated by beam–gas contributions (blue) compared with stable noise (red). Right: constant fit shows fluctuations consistent with zero, validating their negligible impact.

Both effects change the apparent overlap integral of the beams and must be corrected to ensure an unbiased determination of the visible cross-section.

The size of the beam–beam effect depends on the instantaneous bunch parameters, notably the bunch intensities, the transverse beam sizes, the optics at the interaction point through the β^* values, the fractional tunes (Q), and the beam energy E. A useful figure of merit to quantify the strength of these interactions is the round-beam equivalent beam–beam parameter ξ_R, defined as:

$$\xi_R = \frac{r_p N \beta^*}{4\pi\gamma\sigma_R^2}\ , \tag{3.56}$$

with $N = \frac{1}{2}(n_1 + n_2)$ the average number of protons per bunch, $\gamma = E/m_p$ the Lorentz factor, $\sigma_R^2 = \frac{1}{2}\Sigma_x\Sigma_y$ the effective transverse beam size, and $r_p = 1.534695 \times 10^{-18}\,m$ the classical proton radius. Figure 3.10 shows the distribution of ξ_R values for the analyzed bunches in all scans. The average beam–beam parameter ranges between 4.8×10^{-3} and 6.1×10^{-3}, with typical spreads of about 0.3×10^{-3}.

Analytical modelling of the beam–beam deflection:

For an on-axis horizontal scan (analogous arguments apply in the vertical plane), the deflection of one beam due to the other can be treated approximately in the round-beam limit by an angular kick, e.g. [162]:

$$\theta_{x,1} = \frac{2r_p n_2}{\gamma_1 \Sigma_x}\left[1 - \exp\left(-\frac{\Delta x^2}{2\,\Sigma_x^2}\right)\right], \tag{3.57}$$

where r_p is the classical proton radius, n_2 is the bunch intensity of the opposing beam, γ_1 is the relativistic gamma factor of beam 1, Δx the nominal transverse separation, and Σ_x the convolved transverse beam size in the x-direction. The induced displacement of beam 1 at the IP, $\delta x_{IP,bb,1}$, then scales approximately like:

$$\delta x_{IP,bb,1} \;=\; \theta_{x,1}\,\frac{\beta_x^*}{2}\,\tan(\pi Q_x), \tag{3.58}$$

where Q_x is the horizontal fractional tune of the machine. Beam 2 receives an opposite displacement of approximately equal magnitude.

Optical distortion ("dynamic-β") corrections:

The optical effect arises because one beam's electromagnetic field acts like an additional, separation-dependent "quadrupole" component, modifying the effective focusing seen by particles in the other

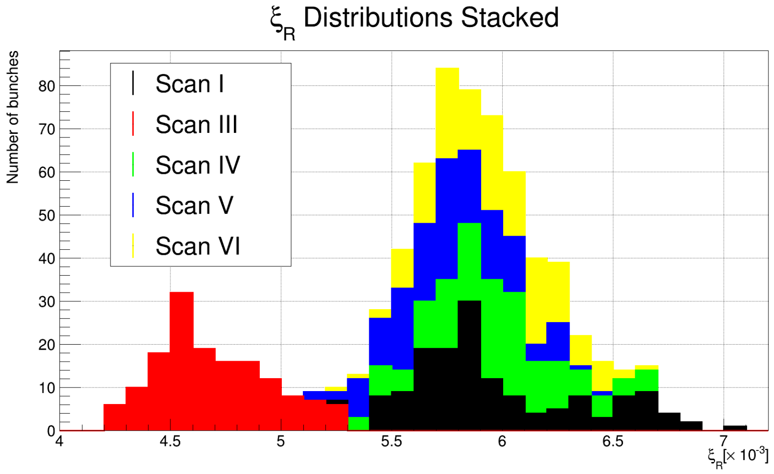

Figure 3.10: Distribution of the beam-beam parameter ξ_R for all bunches. The distributions of all scans are stacked.

Table 3.4: LHC beam parameters and uncertainties for 900 GeV.

Parameter name	Value and uncertainty	Correlations assumed
Beam energy	$E = 0.45$ TeV	No uncertainty assumed
Beam 1	$\beta^*_{B1} = 11.00\text{m} \pm 10\%$	Unc correlated between x and y
Beam 2	$\beta^*_{B2} = 11.00\text{m} \pm 10\%$	Unc correlated between x and y
Fractional tune	$Q_x = 0.314 \pm 0.002$	Unc correlated between x and y, as well as $B1$ and $B2$
Fractional tune	$Q_y = 0.322 \pm 0.002$	Unc correlated between x and y, as well as $B1$ and $B2$

beam. Because the overlap integral depends not only on the core but also on the tails of the bunch density, as the separation increases, particles at larger transverse amplitude contribute more; the force becomes more non-linear, and the simple linear approximation breaks down.

Simulations are used to model how both the effective β^* and the beam sizes change with separation (and with beam–beam parameter, beam energy, and tunes). These simulations also account for the fact that beam profiles may deviate from perfect Gaussians (or from factorization in x and y), and that collisions elsewhere (in “witness IPs”) produce additional tune shifts which feed back into the dynamic-β effect.

Combined impact and systematic considerations:

Because the deflection tends to increase the apparent separation (reducing overlap), and the optical distortion tends to change beam sizes and focusing, the two effects act in opposite directions on the determination of the visible cross-section.

Several sources of uncertainty are important in correcting for beam–beam effects:

- Uncertainties in the bunch currents and beam sizes, which enter into the beam–beam parameter and the analytical expressions for deflection and focusing.
- Uncertainty in β^* and its actual value at the IP.
- Uncertainty in the betatron tunes Q_x and Q_y, including shifts due to collisions in other IPs.
- Deviations from assumptions: non-Gaussian beam shapes; asymmetries between beams (in size or intensity); non-zero crossing angles; multiple collision points.

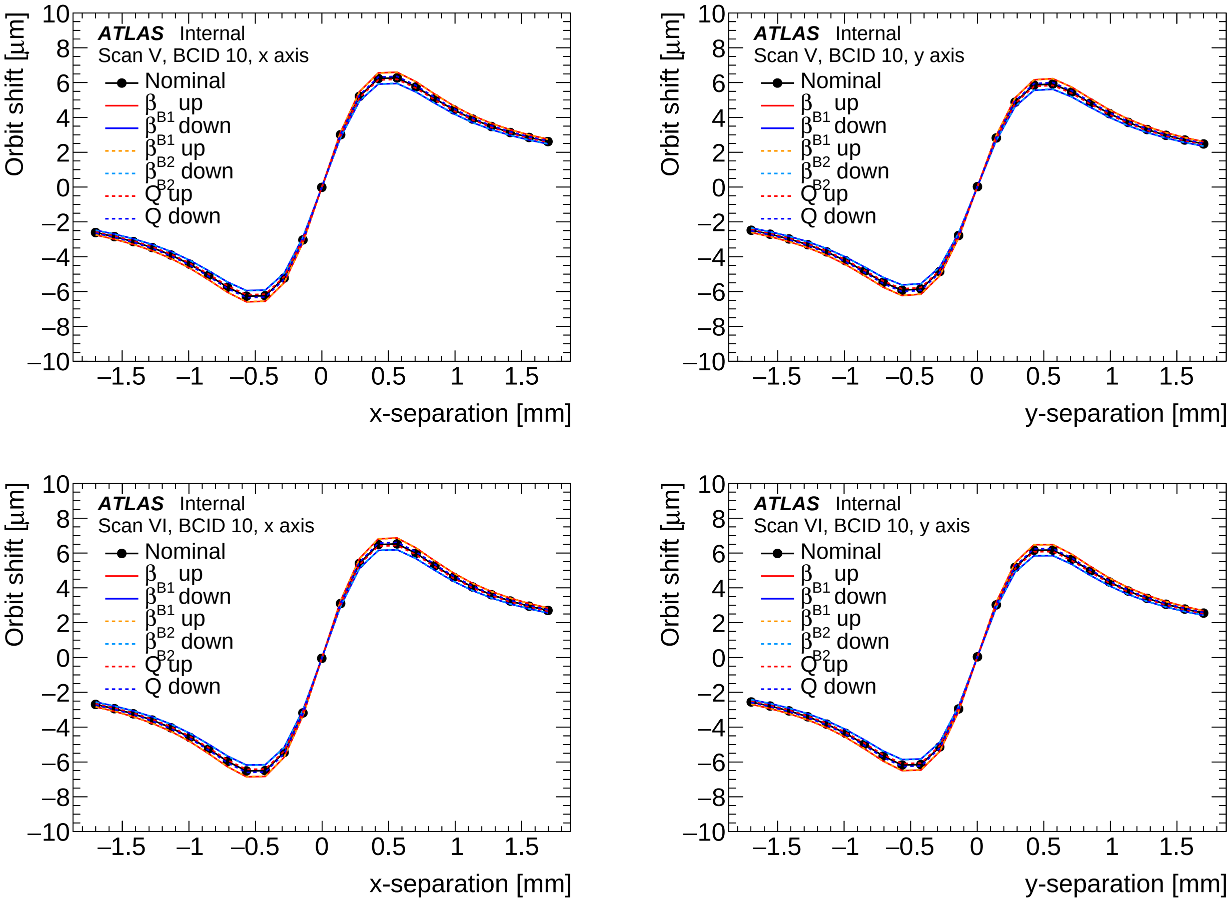

Figure 3.11: Change in beam separation due to the beam–beam deflection as a function of the separation for representative bunches. The black dots show the nominal orbit shift at the separation steps during the scans, while the coloured lines indicate the effect of varying the beam parameters by $\pm 1\sigma$ of their uncertainty. Top row: Scan V in x (left) and y (right). Bottom row: Scan VI in x (left) and y (right).

The relevant beam parameters, uncertainties, and assumed correlations are listed in Table 3.4. The systematic impact of these uncertainties is evaluated later in this section.

The beam–beam deflection shifts the effective orbit of the beams. The corresponding orbit offsets are evaluated from the Bassetti–Erskine formula [163] and applied to the separation during the vdM scan. Figure 3.11 illustrates the correction and its parameter dependence. After applying the correction, the visible cross-section σ_{vis} increases by $\mathcal{O}(3\%)$ relative to the value obtained after orbit drift corrections.

In addition to centroid shifts, the non-linear focusing from the electromagnetic interaction modifies the effective optics ("dynamic β" effect). The correction is evaluated with independent simulations using COMBI [164] and B*B [165], and parameterized in terms of ξ_R, Q_x, Q_y, and the separation. An example is shown in Figure 3.12. The dominant systematic sensitivity arises from uncertainties on the machine tunes. The correction reduces σ_{vis} by about 1.5–2%, partly compensating the increase due to the deflection correction.

Table 3.5 summarizes the cumulative effect of the beam–beam corrections. Starting from a baseline that already includes bunch current, orbit drift, and background corrections, the deflection correction increases σ_{vis} by 2.2–3.1%, while the optical distortion reduces it by 1.5–1.9%. The resulting net correction ranges from 0.39% to 1.30%, with a systematic uncertainty of about 0.4%. The bunch-by-bunch reproducibility values listed in the table correspond, from top to bottom, to the results obtained before corrections, after the deflection correction, and after the full beam–beam corrections.

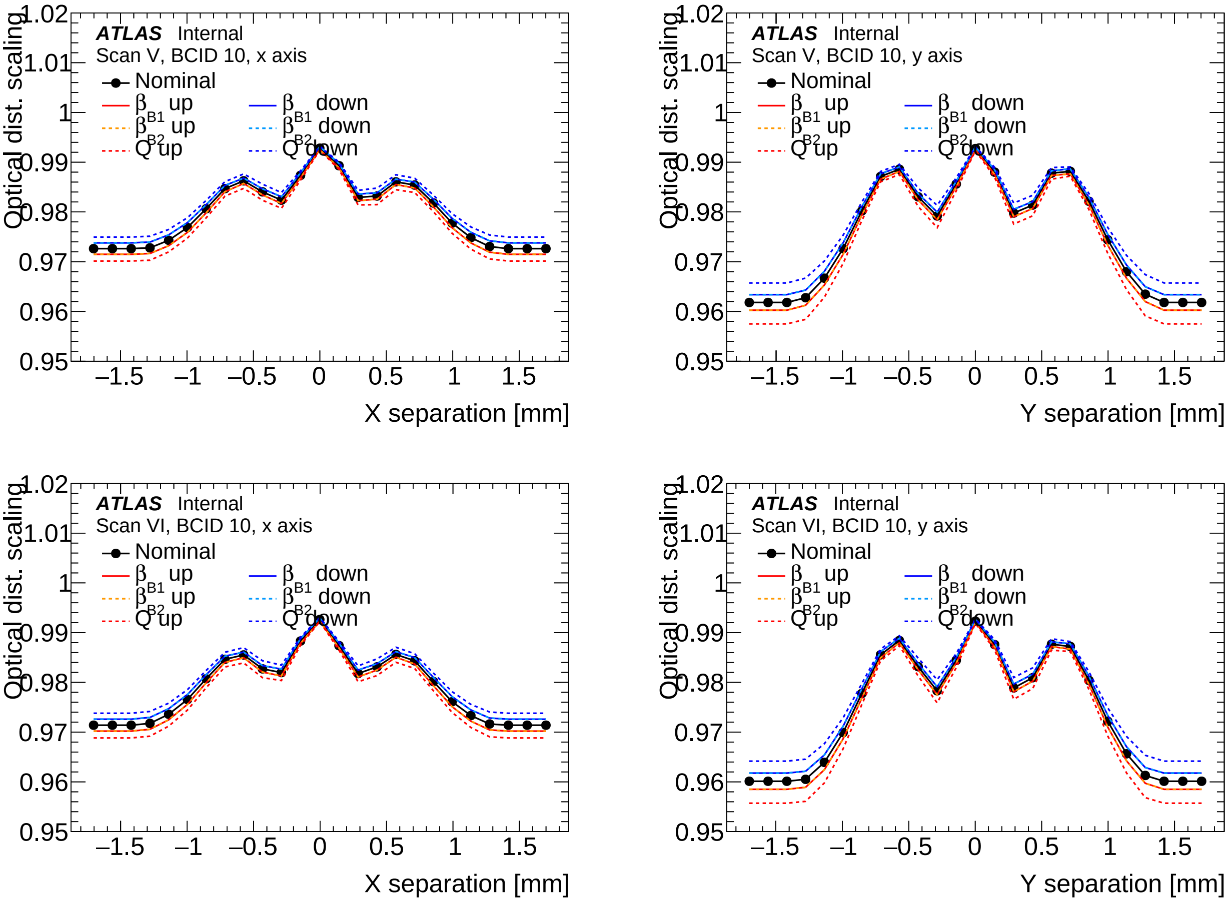

Figure 3.12: Luminosity scale factor due to the optical distortion as a function of the beam separation for representative bunches. The black dots show the nominal values at the separation steps during the scans. Top row: Scan V in x (left) and y (right). Bottom row: Scan VI in x (left) and y (right).

Table 3.5: Impact of the beam–beam corrections for the LUCID Bi2HitOR algorithm. The scan-to-scan (S-to-S) consistency is evaluated using the fractional difference between Scans V and VI, and amounts to 0.6%. S-to-S remains unchanged after applying the beam–beam corrections.

lucBi2HitOR	Scan I	Scan III	Scan IV	Scan V	Scan VI
Bunch-by-bunch	0.50%	0.37%	0.47%	0.29%	0.55%
Avg. ξ_R [$\times 10^{-3}$]	6.097	4.775	6.057	5.812	5.956
Bunch-by-bunch	0.48%	0.35%	0.44%	0.29%	0.48%
Δ BB defl.	+2.91%	+2.31%	+2.86%	+2.84%	+2.83%
Bunch-by-bunch	0.48%	0.35%	0.48%	0.28%	0.44%
Δ Dyn.-beta	-1.89%	-1.65%	-1.84%	-1.94%	-1.93%
Total BB	+0.96%	+0.62%	+0.96%	+0.85%	+0.85%
Total error	0.39%	0.37%	0.39%	0.39%	0.38%

3.6.5 Orbit drift corrections

Gradual orbit drifts of up to $\mathcal{O}(10\ \mu\mathrm{m})$ in the positions of one or both beams have been observed during vdM scans. Such drifts change the actual beam separation from the nominal values commanded by the LHC steering corrector magnets and, if sufficiently large, bias the determination of the overlap integrals and/or the peak interaction rate. The dominant effect arises from *in-plane drifts* (drifts within the scanning plane), which distort the beam-separation scale. These are corrected by adjusting the nominal beam separations at each scan step using interpolated orbit drift measurements. *Out-of-plane drifts* (drifts between horizontal and vertical scan peaks) are a subdominant effect, corrected using differences in orbit drifts at the peaks of the x and y scans. Orbit drift corrections rely on *beam position monitors* (BPMs) [166], in particular the DOROS (Diode Orbit and Oscillation System) [167] devices located inside the closed-orbit bumps used to generate the vdM separations, and the ArcBPM (BPMs in arcs) [168] devices situated in the LHC arcs outboard of the orbit-bump corrector magnets.

DOROS devices are directly sensitive to the nominal beam separation, while ArcBPMs are not. However, ArcBPMs can be affected by beam–beam induced displacements during the scans. In both cases, only points outside the scan are considered for the drift determination. Although the central scan point at zero nominal separation is theoretically unaffected by beam–beam or calibration effects, it is in practice influenced by magnetic non-linearities[6] and is therefore excluded.

For each device, measurements are averaged between "left" and "right" sides and further averaged over all points in a luminosity block. Beam positions are then plotted as a function of time, defined as the midpoint of each luminosity block relative to the start of the run. For display purposes, DOROS and ArcBPM series are anchored to one another at the first measurement point. This does not affect the drift determination, which depends only on relative changes.

Nominal orbit drift correction is obtained by fitting the DOROS measurements immediately before and after a scan with a linear function, as displayed on Figures 3.13 and 3.14. ArcBPM measurements, which show larger scatter, are treated with a two-stage procedure: a quadratic fit is first applied to points before and after the scan (together with the central point) to obtain a smoothed trend; this is then used to define the effective positions before and after the scan, which are linearly interpolated.

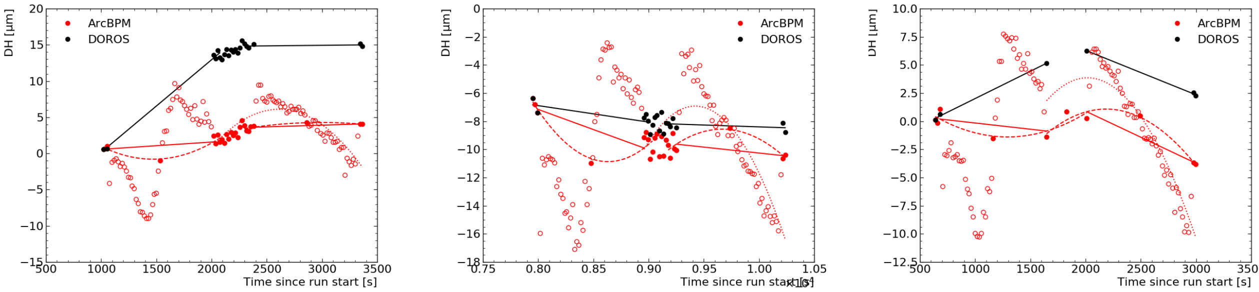

Scan I Scan III Scan IV

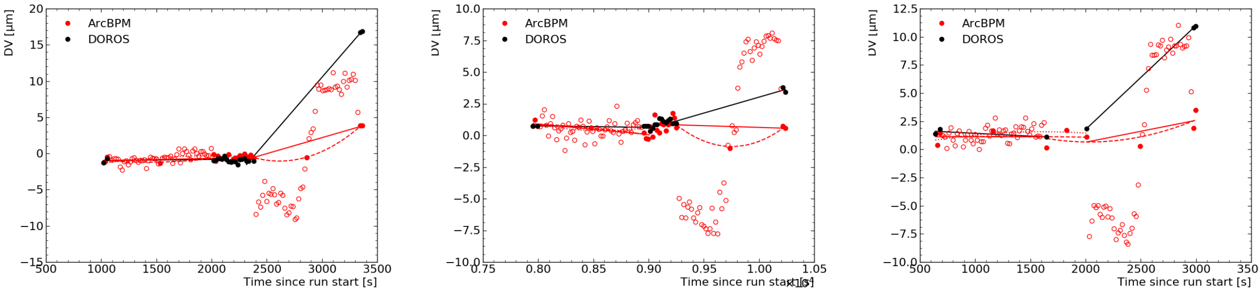

Figure 3.13: Orbit drifts for vdM Scans I, III, and IV. Top row: horizontal drifts (DH). Bottom row: vertical drifts (DV). Solid lines show the linear orbit drift fits for DOROS (black) and ArcBPM (red). The red dashed line corresponds to the ArcBPM 'guide' fit to the filled points, while the red dotted lines show the fit to ArcBPM data used to extract fast beam position jitter.

---

[6] Magnetic non-linearity refers here to the hysteresis effect of the magnetic field response from an ideal. Because the beams are displaced from the center to the maximum negative separation and then returned, hysteresis effects can prevent the beam from returning exactly to its original position. This makes the absolute orbit anchor potentially unreliable, particularly for DOROS, which are located closer to the IP than the corrector magnets.

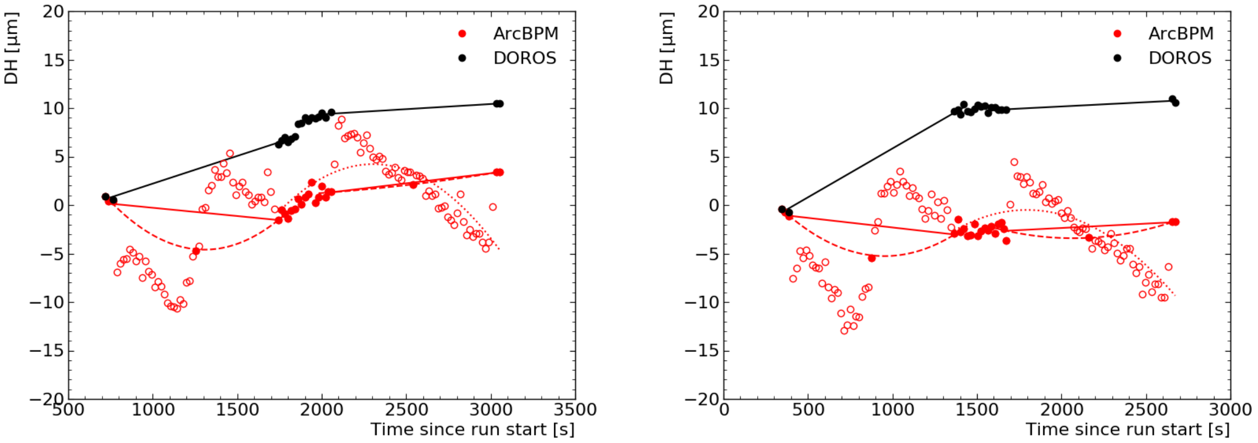

Scan V

Scan VI

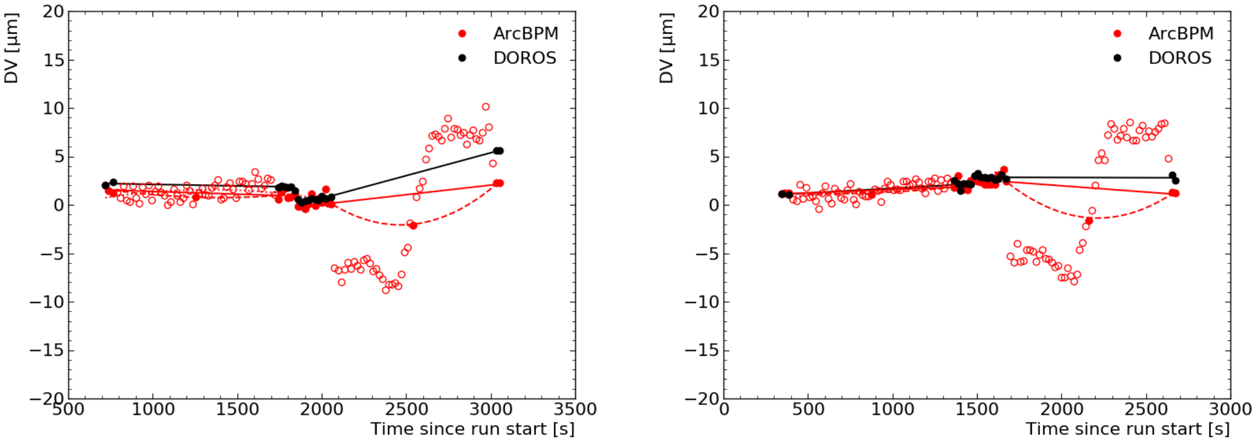

Figure 3.14: Orbit drifts for vdM Scans V and VI. Top row: horizontal drifts (DH). Bottom row: vertical drifts (DV). Solid lines show the linear orbit drift fits for DOROS (black) and ArcBPM (red). The red dashed line corresponds to the ArcBPM ‘guide’ fit to the filled points, while the red dotted lines show the fit to ArcBPM data used to extract fast beam position jitter.

In-plane deformation of the scan curves is corrected by adjusting the nominal beam separation $\Delta x(t)$ at the time t of each scan point according to:

$$\Delta x(t) \;\rightarrow\; \Delta x(t) + \delta_{H,B1}(t) - \delta_{H,B2}(t) \qquad \text{and analogously for } x, H \leftrightarrow y, V \;, \tag{3.59}$$

where $\delta_{H,Bk}(t)$ is the measured orbit drift of beam $k = 1, 2$. A smaller, but non-negligible, effect arises from drifts out of the scan plane, which shift the effective working point. This is approximately corrected by evaluating the relative differences of orbit drifts at the fitted scan-curve peaks t_x^0 and t_y^0:

$$\Delta V = \delta V(t_x^0) - \delta V(t_y^0), \qquad \Delta H = \delta H(t_y^0) - \delta H(t_x^0),$$

with $\delta V = \delta_{V,B1} - \delta_{V,B2}$ and similarly for δH. The visible cross-section is then given by:

$$\sigma_{\text{vis}} = 2\pi\Sigma_x\Sigma_y \frac{\mathcal{G}_x(\mu_x)\,\mathcal{G}_y(\mu_y)}{\frac{1}{2}\left(\mathcal{G}_x(\Delta H) + \mathcal{G}_y(\Delta V)\right)} \;, \tag{3.60}$$

where $\mathcal{G}_x$ ($\mathcal{G}_y$) denote the fitted horizontal (vertical) scan functions, and μ_x (μ_y) are the nominal separations at the scan peaks. In the absence of drift ($\Delta H = \Delta V = 0$), this expression reduces to the standard case with non-scanning-plane offsets.

Table 3.6: Fractional differences of visible cross-section for LUCID Bi2HitOR in vdM scans after applying ArcBPM- and DOROS-based orbit drift corrections.

Scan #	ArcBPM/No	DOROS/No	DOROS/ArcBPM
I	0.12%	0.83%	0.71%
III	-0.12%	0.02%	0.14%
IV	0.04%	0.46%	0.42%
V	-0.02%	0.29%	0.31%
VI	-0.07%	0.32%	0.38%

Large in-plane drifts were observed in Scan I of 2018, as shown on Figure 3.13. Their effect on the bunch-averaged visible cross-section is summarized in Table 3.6, along with other Scans. Table 3.6 reports the visible cross-section measured with the LUCID Bi2HitOR algorithm in the vdM scans, shown both without orbit drift correction and after applying corrections based on the ArcBPM and DOROS readings. The second to fourth columns list the absolute values of σ_{vis} for the uncorrected case and for the two correction schemes. The next two columns give the fractional deviations of the corrected values relative to the uncorrected result, while the final column shows the relative difference between the DOROS- and ArcBPM-corrected measurements. The ArcBPM value from the November session is taken as the nominal reference. All values are corrected for ghost-charge and satellite population, normalized using the DCCT beam-current measurement, and include background subtraction. In general, applying the orbit drift correction reduces the spread of σ_{vis} values among scans.

Orbit drifts during a scan are assessed by comparing BPM readings at zero nominal separation directly before and after the scan. Since the corrector-induced deflections vanish at these points, any observed difference is attributed to orbit drift. In the analyzed dataset, significantly larger drifts were observed by DOROS compared to ArcBPM (except in Scan III). After applying DOROS-based corrections to Scan I, σ_{vis} shifted by about 0.83%.

During a scan, DOROS BPMs are sensitive to both corrector-induced movements and beam–beam effects, while ArcBPMs can also be biased at the μm level by beam–beam deflections and possible knob leakage[7]. Midpoints of the scans could, in principle, be used as anchors, but magnetic hysteresis effects often prevent the beam from returning to the true initial position, particularly at 900 GeV, where the transverse beam sizes are about three times larger than at 13 TeV. This makes ArcBPM-based corrections more robust for the nominal determination. DOROS-based corrections, normalized to ArcBPM values, are instead used to evaluate the systematic uncertainty.

3.6.6 Beam position jitter

On short time scales, the beams do not remain perfectly stable but undergo small, random fluctuations around their nominal position. These fast variations, referred to as beam position jitter, can influence the calibration by distorting the measured scan curves. To quantify the effect, the beam positions recorded by the ArcBPM system at intervals of a few seconds are analyzed. In order to avoid contamination from beam–beam effects, the horizontal jitter is evaluated during vertical scans, while the vertical jitter is determined during horizontal scans. The time evolution of the measured positions is approximated with a quadratic function, and the residuals with respect to this fit provide an estimate of the instantaneous jitter amplitude, as illustrated in Figure 3.15 for Scans V and VI.

---

[7] A "knob" refers to a closed orbit-bump, i.e, a predefined combination of steering magnets (correctors) that are adjusted together to control a displacement of a beam in a correlated manner. Their effects cancel outside the bump region, so the orbit returns exactly to normal once the last corrector is passed. Correctors, however, never cancel perfectly, and the real optics deviate slightly from the ideal lattice. The bump is not fully confined and "leaks" outside the intended interval. This knob leakage appears as a small residual orbit oscillation around the entire ring.

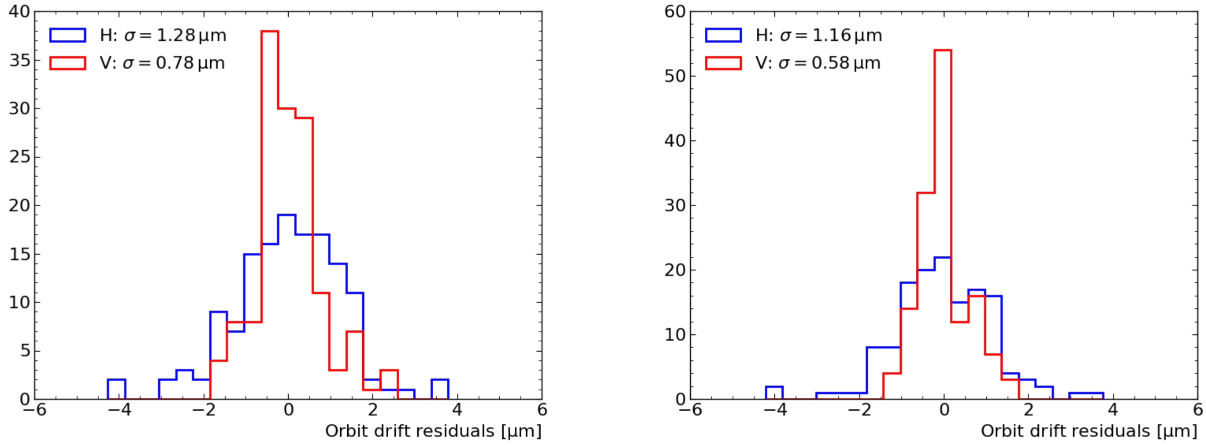

Scan V

Scan VI

Figure 3.15: Residuals of the ArcBPM measurements with respect to a second–degree polynomial fit, used to estimate the fast beam position jitter. Left Scan V, right Scan VI.

The associated uncertainty is assessed through dedicated simulations. Artificial scan curves are generated by shifting the nominal beam separation of each scan point by a random value drawn from a Gaussian distribution with a width equal to the measured jitter. The same random offset is applied coherently across all bunches in a scan to reflect the correlated nature of the fluctuations. By repeating this procedure for a large ensemble of simulated scans, a distribution of visible cross-sections is obtained. The width of this distribution defines the uncertainty contribution from beam position jitter.

To make these simulations computationally efficient, the scan curves are fitted with a simplified model that reproduces the main features of the full fit but requires an order of magnitude less computing time. Comparisons confirm that both approaches yield consistent results, ensuring that the choice of the faster model introduces no bias while allowing the uncertainty evaluation to be completed within practical limits.

3.6.7 Non-factorization effect

The fundamental assumption of the vdM formalism is that transverse bunch densities can be factorized into independent horizontal and vertical components. While this simplifies the overlap integral, it is only an approximation. If the true beam distributions are non-factorizable, this assumption introduces a potential bias in the determination of the visible cross-section σ_{vis}. Although the head-on expression in Eq. (3.18) remains formally valid, the convolved beam sizes must then be computed from the full two-dimensional distributions. In such cases, the effective convolve beam size is obtained as:

$$[\Sigma_x \Sigma_y] = \frac{1}{2} \frac{\iint R_{x,y}(\delta_x, \delta_y) \mathrm{d}\delta_x \mathrm{d}\delta_y}{R_{x,y}(0,0)}. \tag{3.61}$$

Evidence for non-factorization was clearly observed in Run 1 [147, 169, 170] and Run 2 [22], particularly in periods when dedicated beam-tailoring techniques in the LHC injector chain were not applied [171].

When two proton beams collide, the overlap of their spatial distributions defines a region in space where the majority of primary vertices are produced. This region, known as the *luminous region* [172], reflects the convolution of the transverse and longitudinal beam profiles. Its properties (centroid, widths, and possible x–y correlations) can be directly reconstructed from the distribution of collision vertices measured by the tracking detectors. The luminous region thus provides experimental access to the underlying beam parameters without relying solely on beam instrumentation. At $\sqrt{s} = 13$ TeV pp collisions during Run 2 [22], non-factorization effects were studied using reconstructed primary vertices from the ID. The goal was to go beyond the standard vdM assumption of factorizable beam densities $\rho_i(x, y, z) = \rho_{ix}(x)\,\rho_{iy}(y)\,\rho_{iz}(z)$, which neglects possible correlations between x and y. In reality, beam profiles may be tilted or rotated in the transverse plane, making $\rho_i(x, y)$ non-separable. In this procedure, the three-dimensional luminous region was measured from primary vertex distributions for each scan step. Only high-statistics BCIDs were used, since $\mathcal{O}(10^5)$ vertices per step are needed. Each single-beam profile was parametrized as a weighted sum of three 3D Gaussians,

$$\rho_i(x, y, z) \;\approx\; \sum_{j=1}^{3} w_j\, G_j(x, y, z),$$

where each Gaussian G_j had an independent covariance matrix. This allowed the model to capture tilts and x–y correlations, or longitudinal–transverse couplings. Three Gaussians were found to be the minimum needed to reproduce both the core and the tails of the luminous region. With these beam profiles, pseudo vdM scans were simulated by computing the overlap integral:

$$\mathcal{L}(\Delta x, \Delta y) \;=\; f_{\text{rev}} n_1 n_2 \int \rho_1(x, y)\, \rho_2(x + \Delta x, y + \Delta y)\, dx\, dy. \tag{3.62}$$

Ratio defined as:

$$R_{\text{NF}} \equiv \frac{\mathcal{L}_b}{\mathcal{L}_b^0}, \tag{3.63}$$

was calculated, where $\mathcal{L}_b^0$ is luminosity computed from the simulated vdM scan under the factorization assumption, and is derived without the factorization assumption and represents the true 3D overlap integral. This ratio directly quantifies the correction needed to apply to σ_{vis}. In the $\sqrt{s} = 13$ TeV vdM scans, residual non-factorization effects were found to be very small due to dedicated beam tailoring in the injector chain, yielding corrections of order $\mathcal{O}(10^{-3})$ [22]. The fitted scale ratios were $R_{\text{NF}} = 1.006 \pm 0.003$ (2016), 0.998 ± 0.001 (2017), and 1.003 ± 0.003 (2018), indicating sub-percent deviations from the factorized vdM formalism. The uncertainties were taken as the RMS spread of R_{NF} values across the subset of bunches with enhanced vertex readout used for detailed 3D beam–profile fits, while for 2015 a unity correction with a conservative ± 0.006 uncertainty was assigned to cover the range between alternative methods.

For the 2018 900 GeV vdM scans, the lower pp cross-section allowed the data acquisition system to record beamspot information for up to 75 BCIDs, much higher than at 13 TeV. However, the reduced event rates at 900 GeV limited the number of reconstructed vertices per BCID, preventing a reliable per-BCID luminous region measurement. To gain statistical power, beamspot data from many BCIDs were combined under the assumption of uniform beam profiles across bunches. Attempts to fit these combined distributions with a triple 3D Gaussian model, however, resulted in poor fit quality and large residuals [173].

To overcome these limitations, a dedicated two-dimensional fit model is developed, the so-called Coupled Model Fit (CMF). This approach parameterizes the interaction rate dependence on horizontal and vertical beam separations simultaneously, using a Gaussian modulated by the polynomial (analogous to the GP4 family of functions, but extended to two dimensions [174]). The form used for this study is:

$$\mu_{\text{vis,spec}}^{\text{GP4}}(x, y) = p_k \cdot \mathcal{G} \cdot \left[1 + \left(\sum_{i}^{2,4} c_{x^i} \left(\frac{x - \mu_x}{\sigma_x}\right)^i + c_{y^i} \left(\frac{y - \mu_y}{\sigma_y}\right)^i\right)\right]. \tag{3.64}$$

Here, $\mathcal{G} = \mathcal{G}(x, y, \mu_x, \mu_y, \sigma_x, \sigma_y)$ represents a Gaussian function defined in the $x - y$ plane, where μ_x and μ_y denote the nominal beam separation at the peak of the x and y scans respectively, and

σ_x and σ_y are the standard deviations of the corresponding one dimensional Gaussians. The term p_k corresponds to the peak amplitude of the function. For stability, all cross-terms are set to zero while odd-power polynomial parameters (c_{x3}, c_{y3}) were fixed to zero, since they do not contribute to the overlap integral. An example of such a fit for one BCID in the 900 GeV dataset is shown in Figure 3.16.

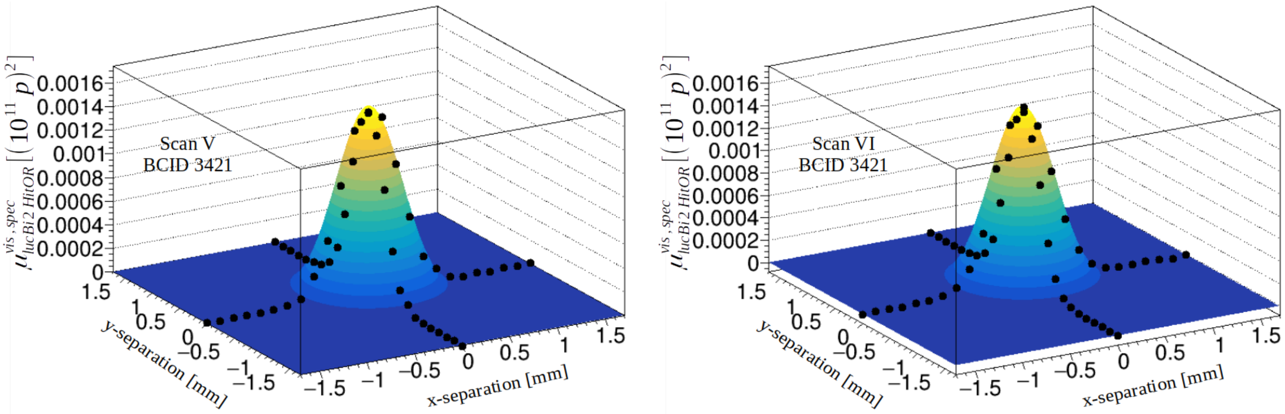

Scan V

Scan VI

Figure 3.16: Examples of Coupled Model Fits applied to the November vdM scans. Each fit simultaneously models the interaction rate as a function of horizontal and vertical beam separations. Left Scan V, right Scan VI. BCID is the same for both examples (number 3421).

Although the CMF provides a more realistic description of the scan curves, the increased number of free parameters led to strong correlations and, consequently, large uncertainties in the overlap integral. To handle these correlations, MINOS [175] error propagation was employed in the extraction of per-bunch convolved beam sizes. Even so, about 39 out of 150 BCIDs from the November scans had to be excluded due to non-convergent fits or large numerical instabilities.

The overlap integral from the CMF was used to determine the per-bunch non-factorizable beam size product $\left[\Sigma_x \Sigma_y\right]_b$. These were compared to the standard factorizable estimates $\Sigma_x(b) \cdot \Sigma_y(b)$. The non-factorization impact is evaluated by comparing the ratio between $[\Sigma_x \Sigma_y]$ and the product $\Sigma_x \cdot \Sigma_y$ obtained from the standard factorizable vdM formalism, both averaged over the same set of valid (i.e. successfully fitted) colliding-bunch pairs. Since an accurate estimation of the ratio R_{NF} proves challenging, the fractional difference is used as an uncertainty measure instead of a direct correction. Figure 3.17 shows the extracted $\left[\Sigma_x \Sigma_y\right]_b$ values and the corresponding R_{NF} distributions, while the average results are summarized in Table 3.7. To address the larger spread of R_{NF} values, conservative estimates derived from linear addition of the mean and its error are utilized as the final uncertainty, as shown in the last column. For the November session, the non-factorization uncertainty was estimated at the level of 1%.

Table 3.7: Fractional differences between convolved beam sizes obtained from the CMF and standard vdM formalism, for the November session.

Scan	$\langle \lvert R_{\text{NF}} - 1 \rvert \rangle$	± (stat.)	± (syst.)
V	0.69 %	0.46 %	1.15%
VI	0.44 %	0.51 %	0.95%

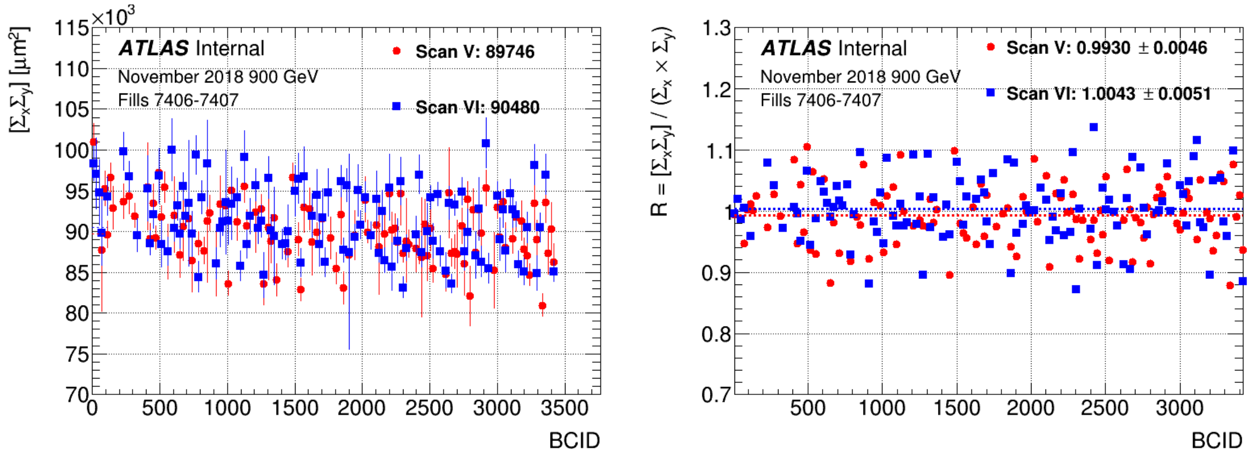

Figure 3.17: Per-BCID $[\Sigma_x\Sigma_y]$ obtained from the CMF using MINOS for scans V&VI (left) and per-BCID R_{NF} values (right).

3.6.8 Length scale determination

The calibration of the length scale, which converts nominal magnet settings into actual transverse beam separations, is essential for the determination of $\Sigma_{x,y}$. This procedure was not carried out within the scope of this thesis; instead, the corresponding uncertainty is taken from dedicated analyses performed by the ATLAS collaboration [22, 176, 177].

The method relies on special length scale calibration (LSC) scans, where one beam is displaced in a controlled manner to several predefined positions while the luminous centroid is reconstructed from primary collision vertices in the inner detector. By comparing the nominal magnet-induced displacements with the measured beamspot positions, a calibration factor is derived for each beam and scan plane. The procedure, together with corrections for magnetic non-linearities, is described in detail in Ref. [22]. The resulting contribution to the uncertainty on σ_{vis} amounts to 0.05%, which represents a marginal contribution to the overall uncertainty.

3.6.9 Emittance growth correction

The convolved beam widths Σ_x and Σ_y are measured during beam-separation scans, each lasting about 20 minutes, with a typical interval of 20–40 minutes between horizontal and vertical scans. Since the beam emittances can evolve differently in the two planes, this time dependence can affect the calibration in two ways. First, changes in the beam width during a scan may distort the scan curve and bias the determination of $\Sigma_{x,y}$. Second, the fact that the horizontal and vertical scans are not performed simultaneously means that differences in the evolution of Σ_x and Σ_y between the respective peak times can bias the extracted visible cross-section.

The beam widths and peak rates are fitted with linear functions, allowing the time dependence to be parameterized. The emittance growth correction factor is then defined as:

$$c_\varepsilon = \frac{\sigma_{\text{vis}}(t_{\text{mid}}, t_{\text{mid}})}{\sigma_{\text{vis}}(\hat{t}_x, \hat{t}_y)} - 1\,, \tag{3.65}$$

where $\sigma_{\text{vis}}(t_i, t_j)$ denotes the visible cross-section evaluated at times t_i and t_j, $\hat{t}_x$ and $\hat{t}_y$ are the peak times of the horizontal and vertical scans, and t_{mid} is the midpoint between them. This fraction quantifies the bias that occurs when combining quantities that are not measured simultaneously.

The evolution of the beam widths over consecutive scans within one fill is shown in Figure 3.18, while Figure 3.19 displays the corresponding change in peak rates. Both quantities increase with time, reflecting the gradual emittance growth in both planes. The mismatch between the observed and expected peak-rate evolution introduces a time dependence in the correction, which is treated as a systematic uncertainty.

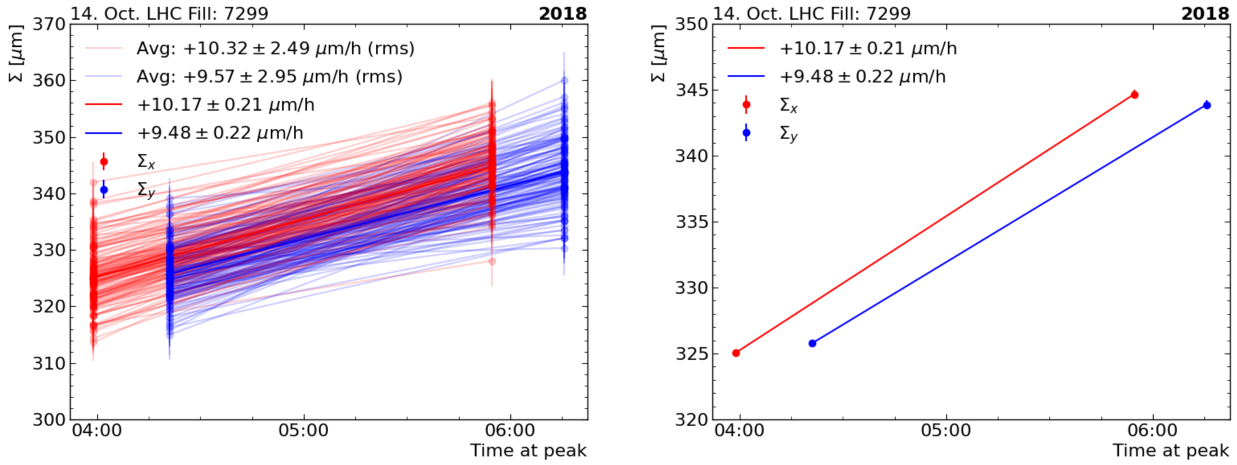

Figure 3.18: Measured convolved beam width as a function of time during consecutive scans in one Fill 7299. Linear fits are overlaid, with slopes given in the legend. Left per-bunch fits, right bunch-averaged fit.

Since only one Fill 7299 contained more than one on-axis scan, only Scans I and III are used for the emittance growth uncertainty estimate. The effect of the peak-rate mismatch is estimated by replacing the midpoint t_{mid} with either $\hat{t}_x$ or $\hat{t}_y$, yielding the uncertainty contribution:

$$\Delta c_{\varepsilon}(x/y) = \frac{1}{2}\left|\frac{\sigma_{\text{vis}}(\hat{t}_x) - \sigma_{\text{vis}}(\hat{t}_y)}{\sigma_{\text{vis}}^{ref}}\right|. \tag{3.66}$$

Statistical uncertainties from the linear fits are also propagated and reported as Δc_{ε} (fit). The corrections are found to be 0.037% for Scan I and 0.031% for Scan III.

Bunch-by-bunch fits give very similar corrections, as all bunches display comparable emittance growth, as seen in Figure 3.18 (left). Consequently, the correction does not alter the consistency between scans, nor does it reduce the bunch-to-bunch scatter of σ_{vis}. The emittance growth effect is therefore small and under control, with a maximum correction of order $\sim 0.04\%$.

3.6.10 Consistency checks

This section evaluates the stability of measurements across individual bunches, reproducibility across scans, and systematic uncertainty tied to the reference specific luminosity.

The bunch-by-bunch consistency uncertainty is assessed to account for variations in the visible cross-section, across individual colliding bunches. This uncertainty is quantified using the root mean square ($\sigma_{\text{bbb,stat}}$) corrected for the average statistical uncertainty of visible cross-section $\langle \delta\sigma_{\text{vis,stat}} \rangle$:

$$\sigma_{\text{bbb,cor}} = 1/\sigma_{\text{vis}} \cdot \sqrt{(\sigma_{\text{bbb,stat}})^2 - \langle \delta\sigma_{\text{vis,stat}} \rangle^2}. \tag{3.67}$$

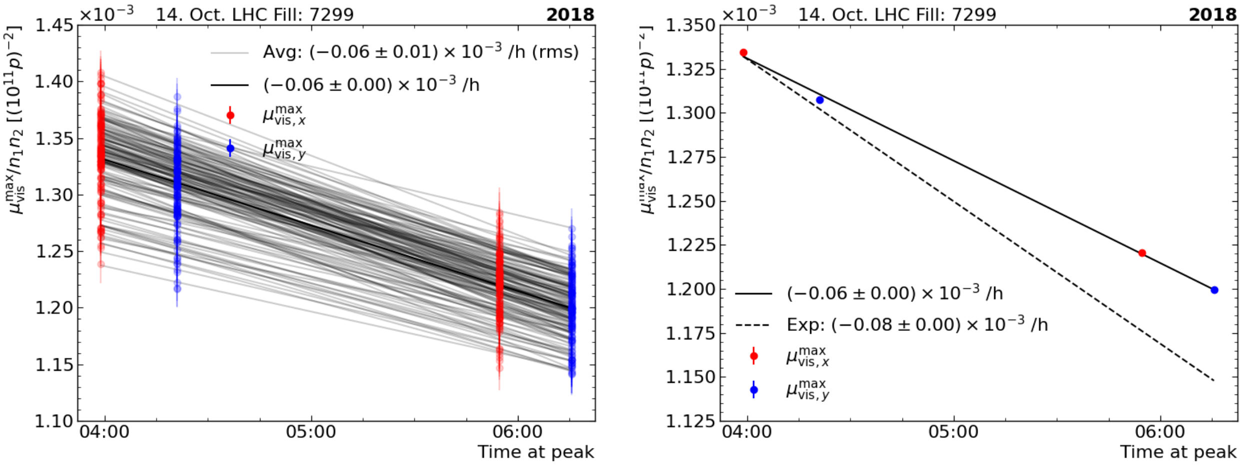

Figure 3.19: Measured peak rate as a function of time during consecutive scans in fill number 7299. The fitted (solid) and expected (dashed) rates of change are shown on the right. Semi-transparent lines on the left show per-bunch measurements.

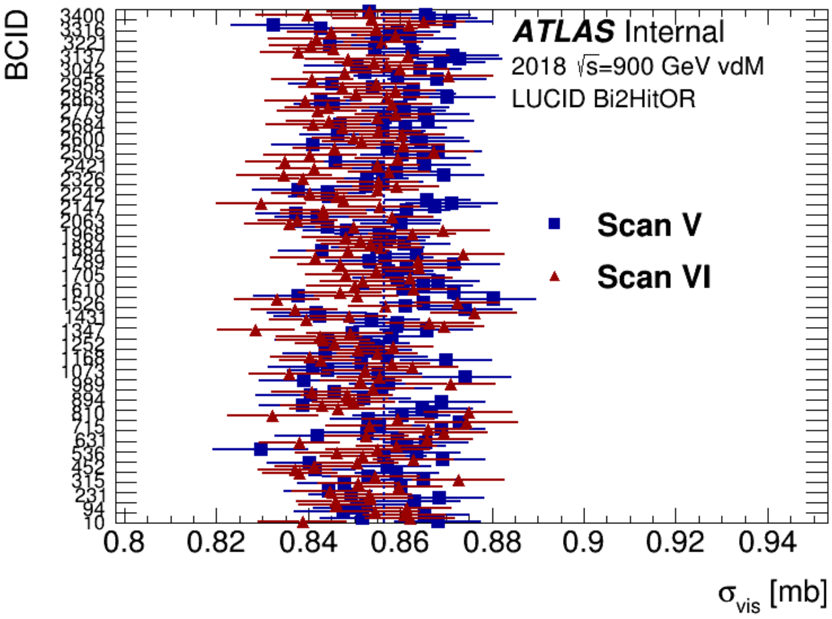

Figure 3.20: Per-bunch calibrated visible cross-section values for Scans V and VI, assessing bunch-by-bunch consistency.

If the RMS value is less than or equal to $\delta\sigma_{\text{vis}}$, bunch-by-bunch uncertainty is set to zero. For all scans I, III, IV, V, and VI, uncertainties are 0.48%, 0.35%, 0.48%, 0.28%, and 0.44%, respectively. The largest uncertainty from the November scan (0.44% from scan VI) is adopted as the final uncertainty.

The fractional difference in calibrated bunch-averaged σ_{vis} values between scans V and VI from November sessions provides the scan-to-scan consistency uncertainty, calculated as 0.61%. This difference, illustrated in Figure 3.20, emphasizes the reproducibility between successive scans. Figure 3.21 presents the bunch-averaged σ_{vis} values for all scans, alongside the session averages for October and November, revealing a distinct session difference and a deviation in scan III due to the large and difficult-to-assess uncertainty affecting the ghost-charge and satellite fractions, combined with the pathological single-beam background signal (Figure 3.8, left).

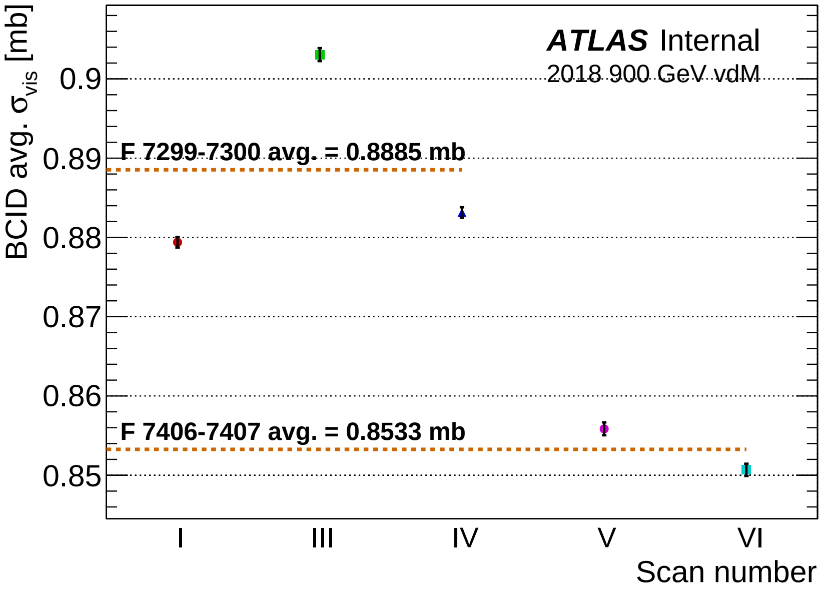

Figure 3.21: Bunch-averaged, calibrated visible cross-section values for all vdM scans at 900 GeV. The average values for the October and November sessions are highlighted with orange dashed lines, and their respective numerical values are indicated. The statistical error bars are smaller than the size of the markers.

The reference specific luminosity depends solely on beam parameters and serves as a metric for evaluating algorithmic stability. Here, deviations in specific luminosity are used to estimate the systematic uncertainty, which is derived by averaging the relative difference between $\mathcal{L}_{\text{spec}}$ for each algorithm and the mean across all algorithms over all bunches in each scan. This systematic deviation is calculated as:

$$\Delta^a(s,b) = \frac{\mathcal{L}^a_{\text{spec.}}(s,b) - \langle \mathcal{L}_{\text{spec.}}(s,b)\rangle}{\langle \mathcal{L}_{\text{spec.}}(s,b)\rangle}, \tag{3.68}$$

where $\Delta^a(s,b)$ represents the relative deviation for a given algorithm a, scan s, and bunch b, while $\langle \mathcal{L}_{\text{spec.}}(s,b)\rangle$ denotes the average across algorithms. The final deviation in $\mathcal{L}_{\text{spec}}$ is determined by averaging deviations across scans and bunches. The highest systematic deviation, 0.98%, arises from the LUCID BiC15 PMT algorithm, which has the largest pull. Figure 3.22 shows the bunch-averaged deviations in $\mathcal{L}_{\text{spec}}$ for two scans as well as their average. October scans are excluded due to high ghost-charge contamination.

3.7 Results and conclusions of Chapter 3

The determination of the integrated luminosity for the 2018 pp dataset at $\sqrt{s} = 900\,\text{GeV}$ with high-β^* optics constitutes a critical input to the elastic-scattering analysis and, more broadly, to the precision programme at low centre-of-mass energy. The evaluation required dedicated procedures tailored to the very low-μ regime of these runs, where noise, afterglow, and single-beam backgrounds are non-negligible. In addition, several LUCID algorithms had to be validated or cross-calibrated, since standard vdM methods were not directly applicable under such conditions.

Noise and background subtraction. At such low pile-up, the contributions from Bi-source noise and afterglow photons become significant compared to the collision signal. Using the “BCID-1”

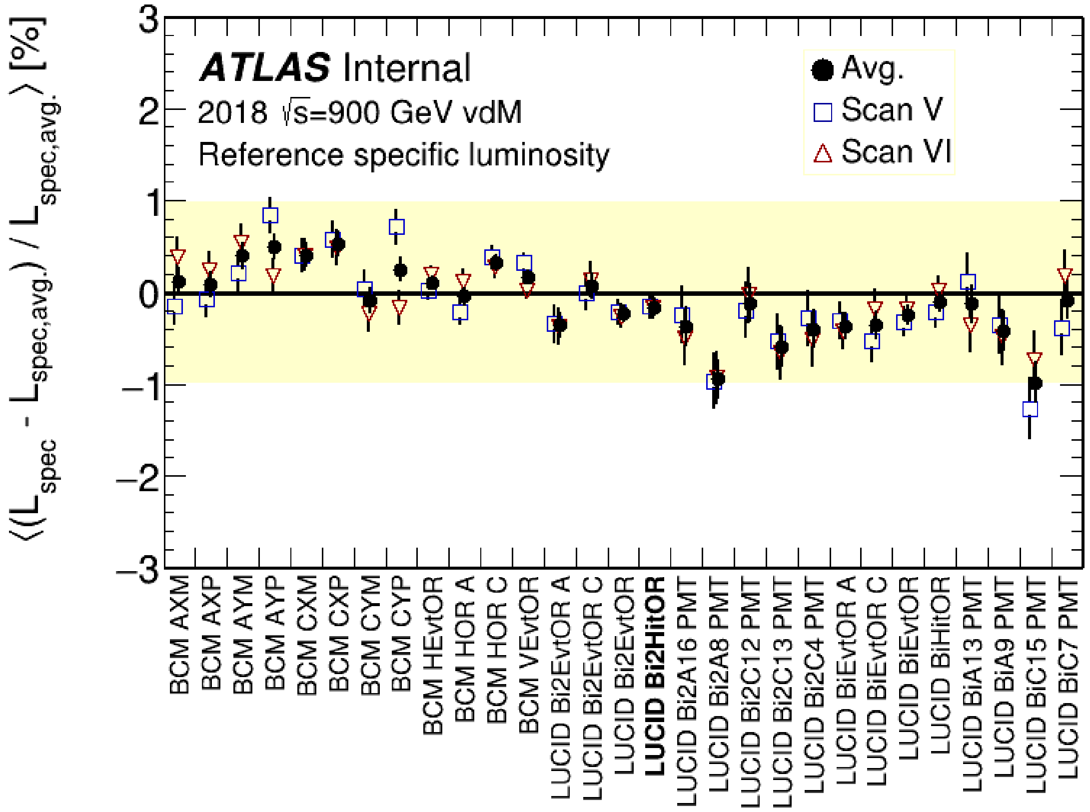

Figure 3.22: Bunch-averaged reference specific luminosity $\mathcal{L}_{\text{spec}}$ deviations are shown, capturing systematic differences in algorithm response.

method, these backgrounds were estimated to contribute $\sim 16.1\%$ in the $\beta^* = 50/100\,\text{m}$ runs and $\sim 1.3\%$ in the $\beta^* = 11\,\text{m}$ runs. The ratio between these two values matches well the ratio of the average μ values in the corresponding datasets, consistent with expectations. A systematic uncertainty of 0.001% was estimated from the difference between the BCID-1 and BCID-2 subtraction methods. Beam-induced background (BIB) was studied using unpaired bunches. For fills with a large difference in colliding versus unpaired bunch intensity ($n_{\text{coll}}/n_{\text{unp}} \sim 10$), the BIB subtraction produced unstable or even negative fractions, driven by statistical fluctuations amplified by the large intensity ratio. A dedicated pseudo-experiment confirmed that in these cases, the BIB estimate was unreliable. For this reason, only fills with $n_{\text{coll}}/n_{\text{unp}} \sim 1$ were retained, yielding a BIB contribution of $(0.77 \pm 0.22)\%$ for the LUCID Bi2HitOR algorithm. This value was subtracted from all HitOR and EvtOR algorithms.

vdM calibration Luminosity scale is anchored to vdM scans at $\sqrt{s} = 900\,\text{GeV}$. Table 3.8 summarizes fractional corrections applied to σ_{vis} per scan; Table 3.9 presents the overall uncertainty breakdown. The final σ_{vis} is taken from the **November 2018** session average using **LUCID Bi2HitOR** as preferred algorithm (all standard corrections applied). The **total vdM calibration uncertainty is 1.85%**. Dominant effects and inputs are:

- **Reference specific luminosity** and **Non-factorization** dominate the November-session uncertainty value.
- **Beam–beam effects** produce the largest correction on average, with relatively modest scan-to-scan spread.
- **Orbit drift** corrections vary substantially between scans.

In October, ghost-charge and satellite corrections could not be evaluated and were found to be overestimated by standard methods, and November is used for the final calibration. For emittance-growth uncertainty, the October session (Fill 7299) is retained because it is the only case with more than one on-axis scan; the corresponding uncertainty is propagated to the November-based result.

Table 3.8: Summary of the fractional corrections to σ_{vis} applied for all scans at $\sqrt{s} = 900$ GeV.

Correction [%]	I	III	IV	V	VI
FBCT offset	0.273	1.041	-0.082	0.003	0.002
Orbit-drift (arc BPM)	0.12	-0.12	0.04	-0.02	-0.07
Beam-Beam	1.30	0.71	1.04	0.39	0.38
Emittance growth	0.037	0.031	-	-	-
Ghost charge & satellite	16.00	34.00	19.00	0.60	0.60

Table 3.9: Overall summary of the nominal σ_{vis} and the systematic uncertainties for 900 GeV. With "*" indicating systematic uncertainties taken from the November session only, "**" indicates that the October session only was used, and cases without any "stars" indicator where a combination of uncertainties or the largest uncertainty was taken as the final uncertainty.

Algorithm	LUCID Bi2HitOR
Final σ_{vis} *	0.85326 mb
Statistical Uncertainty $\delta\sigma_{\text{vis}}$ *	0.07% (0.00056 mb)
Total Uncertainty	1.85% (0.01579 mb)
Fit model *	0.33%
DCCT normalisation	0.20%
Ghost-charge and satellites *	0.14%
FBCT offset *	0.02%
Background Subtraction *	0.13%
Orbit-Drift correction *	0.35%
Beam Position Jitter	0.14%
Non-Factorisation *	1.15%
Beam-Beam corrections *	0.39%
Emittance growth **	0.30%
Magnetic non-lin + LSC	0.05%
Bunch-by-Bunch σ_{vis} consistency *	0.44%
Scan-to-Scan reproducibility *	0.61%
Reference Specific Luminosity *	0.98%

Calibration of EvtAND algorithms. LUCID EvtAND algorithms, by construction insensitive to the dominant backgrounds, provide an important cross-check but lack a reliable vdM calibration. The visible cross-section for EvtAND was therefore obtained by cross-calibration to the vdM-calibrated LUCID Bi2HitOR algorithm, in a low-μ dataset ($\langle\mu\rangle \sim 0.008$). A simulation study quantified the bias introduced by the small-μ approximation, showing a relative difference of 0.78% between reconstructed and true μ. This was applied as a correction factor to the cross-calibrated $\sigma_{\text{vis}}^{AND}$, enabling EvtAND to be used consistently in the stability studies.

Stability and consistency checks. LUCID Bi2HitOR algorithm was chosen as the preferred reference, being well studied during vdM scans and statistically precise (five PMTs). Its results were compared to other LUCID algorithms and to track counting (where available) to assess systematic

Table 3.10: BIB-subtracted absolute integrated luminosity values and fractional difference with respect to LUCID Bi2HitOR algorithm for the main LUCID algorithms. In the last two columns, the same quantities are reported for the two LHC fills with Inner Detector available (7289, 7282).

	Full dataset		Dataset for Trk Count	
Algorithm	$\mathcal{L}_{tot}$ [μb^{-1}]	$\Delta\mathcal{L}/\mathcal{L}_{ref}$ [%]	$\mathcal{L}_{tot}$ [μb^{-1}]	$\Delta\mathcal{L}/\mathcal{L}_{ref}$ [%]
LUCID Bi2HitOR	1426.48 ± 0.65	/	153.57 ± 0.22	/
LUCID BiEvtOR A	1429.3 ± 1.0	0.199 ± 0.085	153.66 ± 0.35	0.06 ± 0.27
LUCID BiEvtOR C	1424.2 ± 1.1	-0.164 ± 0.089	153.53 ± 0.38	-0.02 ± 0.28
LUCID BiHitOR	1488.21 ± 0.74	0.121 ± 0.069	153.71 ± 0.26	0.10 ± 0.22
LUCID BiEvtAND	1416.5 ± 5.1	-0.70 ± 0.36	150.5 ± 1.7	-2.0 ± 1.1
LUCID Bi2EvtAND	1426.5 ± 4.2	0.00 ± 0.30	151.5 ± 1.4	-1.32 ± 0.92
Track counting			152.79 ± 0.20	-0.51 ± 0.19

consistency. BCM data were excluded due to known charge-pumping[8] effects in the low-μ regime. The agreement across algorithms was excellent: for example, track counting was found to be only 0.26% lower than Bi2HitOR in a representative fill, well within systematic expectations. Fractional differences between LUCID Bi2HitOR and BiEvtOR A/C, BiHitOR, BiEvtAND, and track counting showed flat, unbiased behaviour across luminosity blocks and runs. The largest deviation was observed for BiEvtAND, amounting to 0.70%, which was conservatively taken as the systematic uncertainty due to long-term consistency.

Integrated luminosity values. Table 3.10 reports the BIB-subtracted integrated luminosity values. For the full dataset, Bi2HitOR measured $\mathcal{L}_{int} = 1426.5 \pm 0.7$ μb^{-1}. The differences with respect to BiEvtOR A/C and BiHitOR are at the per-mille level. The track counting measurements used for comparison in Table 3.10 were obtained in an independent study that lies outside the scope of this thesis [178]. For the reduced dataset with Inner Detector availability, track counting gave $\mathcal{L}_{int} = 152.8 \pm 0.2$ μb^{-1}, differing by only -0.5% from Bi2HitOR. This demonstrates that independent methods, including one based on central tracking, converge within uncertainties. Integrated luminosity delivered by the LHC is quoted separately for the two optics configurations. With Bi2HitOR as reference, the results are:

$$\beta^* = 50/100 \text{ m}: \quad \mathcal{L} = 925.4 \pm 0.5_{\text{stat}} \pm 20.0_{\text{sys}}\ \mu\text{b}^{-1}, \tag{3.69}$$

$$\beta^* = 11 \text{ m}: \quad \mathcal{L} = 501.0 \pm 0.4_{\text{stat}} \pm 10.6_{\text{sys}}\ \mu\text{b}^{-1}. \tag{3.70}$$

Systematic uncertainties. Three dominant sources contribute to the total uncertainty:
– vdM calibration: 1.85%,
– Beam-induced background: 0.77%,
– Consistency/stability: 0.70%.
Adding these in quadrature gives a total systematic uncertainty of 2.1%, identical for both β^* datasets. The statistical component is negligible in comparison ($\sim$ 0.05–0.08%).

In summary, the integrated luminosity of the 2018 pp runs at $\sqrt{s} = 900$ GeV has been determined with a total uncertainty of 2.1% (vdM alone contributing 1.85%). The analysis required dedicated background subtractions and cross-calibration methods tailored to the low-μ environment. The LUCID Bi2HitOR algorithm, cross-checked with other LUCID algorithms and with track counting, was established as the baseline reference. When combined with the complementary studies presented

---

[8] Trapped charge carriers accumulated during previous irradiation are slowly released and generate spurious pulses unrelated to actual pp interactions. These fake signals become comparable to the true interaction rate in the low-μ regime.

in this thesis—most notably the detailed vdM calibration analysis and systematic studies of beam-beam, orbit drift, and non-factorization effects—a coherent and precise luminosity determination is achieved. This provides a strong foundation for the measurement of the total pp cross-section and related forward-physics observables at $\sqrt{s} = 900\,\text{GeV}$, where luminosity represents the leading source of systematic uncertainty.

Chapter 4

W-Boson Physics at the LHC

In this chapter, the measurement of the W-boson total and fiducial production cross-sections is presented. The results are obtained using proton-proton data collected with the ATLAS detector during the first year of the ongoing Run 3 at center-of-mass energy $\sqrt{s} = 13.6$ TeV. Presented results include the selection of signal events, evaluation of efficiencies and background contributions, and the assessment of experimental and theoretical uncertainties.

4.1 W-boson cross-section measurement

Measurements of W-boson (as well as Z-boson) production cross-sections at the LHC provide an important test of *perturbative Quantum Chromodynamics* (pQCD) [179] and offer constraints on the PDFs of the proton. These processes are among the cleanest signatures in proton–proton collisions and serve as standard candles for validating the performance of the detector, the reconstruction of leptons and missing transverse momentum, and – although not their primary objective – provide an additional cross-check of the luminosity calibration. The total inclusive production cross-section of the W boson multiplied by the branching ratio for the leptonic decay channels (where by lepton we refer to an electron or a muon) can be measured using the following equation:

$$\sigma_{\text{tot}} \times \text{BR}(W \to \ell\nu) = \frac{N - N_{\text{bg}}}{A \cdot C \cdot \mathcal{L}_{\text{int}}}, \tag{4.1}$$

where N is the total number of selected events in data, N_{bg} the estimated number of background events, A and C are the signal *acceptance* and *correction* factor respectively, and $\mathcal{L}_{\text{int}}$ the integrated luminosity of the sample used for the measurement. Product of C and A corresponds to the efficiency in Eq. (1.27). Acceptance A represents the fraction of generated W-boson decays that satisfy the fiducial requirements imposed by the detector geometry and the kinematic constraints of the trigger (for details, refer to Sections 4.3.1 and 4.4.2). The correction factor C is defined as the ratio of the number of generated signal events that pass all selection requirements after full reconstruction to the number of generated signal events that satisfy the fiducial criteria at particle level. The factor C thus accounts for the efficiencies of event reconstruction, particle identification, isolation, and trigger requirements. The acceptance is estimated using Monte Carlo simulations, while the correction factor is obtained from *in-situ* measurements, and the results are compared with Monte Carlo predictions.

The product of total cross-section, branching ratio, and acceptance is referred to as the *fiducial cross-section*:

$$\sigma_{\text{fid}} = \sigma_{\text{tot}} \times \text{BR}(W \to \ell\nu) \times A. \tag{4.2}$$

It is also useful to study ratios of fiducial cross-sections, such as:

$$R_{\text{fid}}^{W^+/W^-} = \frac{\sigma_{\text{fid}}^{W^+}}{\sigma_{\text{fid}}^{W^-}}. \tag{4.3}$$

By forming the W^+/W^- ratio of fiducial cross-sections, measured within the same dataset and under identical reconstruction conditions, many experimental uncertainties cancel to a large extent. From a physics perspective, this ratio is highly sensitive to the flavour composition of the proton. In particular, the W^+/W^- ratio probes the u/d structure of the valence quarks. At LHC energies, this sensitivity maps the ratio $u(x)/d(x)$ in the low Björken-x region, corresponding to the momentum fractions carried by the partons producing the bosons. Thus, the measurement of W-boson cross-section ratios provides stringent constraints on PDFs, particularly improving the knowledge of the up- and down-quark distributions.

Reconstruction of W-boson leptonic final states relies on several components of the ATLAS detector. Electrons are reconstructed from energy deposits in the ECal matched to tracks in the ID, while muons are reconstructed from combined tracks in the ID and MS, as detailed in Section 4.3.1. Undetected neutrino in W-boson decays is inferred from the *missing transverse momentum*, $E_{\text{T}}^{\text{miss}}$, reconstructed from all calibrated objects and soft activity in the event. The *fiducial phase-space* match these reconstruction capabilities and for W-boson production is defined by the following requirements:

- Lepton transverse momentum: $p_{\text{T}} > 27$ GeV,
- Lepton pseudorapidity: $|\eta| < 2.5$,
- Missing transverse momentum: $p_{\text{T}}^{\text{miss}} > 25$ GeV,
- Transverse mass: $m_{\text{T}}^{W} > 50$ GeV.

The transverse mass m_{T}^{W} is used instead of the invariant mass because the longitudinal momentum of the neutrino cannot be reconstructed experimentally. It is defined as:

$$m_{\text{T}}^{W} = \sqrt{2\, p_{\text{T}}^{\ell}\, p_{\text{T}}^{\nu}\, (1 - \cos(\phi_\ell - \phi_\nu))}\,, \tag{4.4}$$

where ϕ_ℓ and ϕ_ν denote the azimuthal angles of the charged lepton and the neutrino, respectively.

Background processes originate primarily from Z-boson decays ($Z \to \ell\ell$, where $\ell = e, \mu, \tau$), top-quark production ($t \to Wb,\ W \to \ell\nu$), the τ-lepton decay channel of the W boson ($W \to \tau\nu \to e\nu\nu,\ \mu\nu\nu$), and diboson or triboson production ($pp \to VV,\ VVV$, where $V = W^{\pm}, Z$). The contribution of these background processes can be estimated from Monte Carlo simulations. Events originating from semileptonic decays of heavy quarks or from misidentified hadrons reconstructed as leptons are collectively referred to as *multijet* processes. Because multijet backgrounds are not well modeled by MC simulations, they are estimated directly from data using so-called *data-driven techniques*. A typical approach involves inverting one or more selection criteria to obtain a data sample in which this background dominates. By extrapolating the observed distributions under variations of the selection requirements, the number of background events and the shapes of characteristic variables in the signal region can be determined.

Previous ATLAS measurements of W production have been performed at center-of-mass energies of 2.76 TeV [180], 5.02 TeV [181] , 7 TeV [182], 8 TeV [183, 184], and 13 TeV [185, 186]. CMS has provided corresponding results at the 7 TeV [187, 188], 8 TeV [189, 190], and 13 TeV [191] centre-of-mass energies, while LHCb has performed complementary measurements in the forward region (covering ranges within $2 < \eta < 5$) at the 5.02 TeV [192], 7 TeV [193], and 8 TeV [194]. Results presented in this thesis extends these measurements to $\sqrt{s} = 13.6$ TeV, representing the first determination of W-boson production cross-section including ratio of W^+ and W^- using Run 3 data collected in 2022 by the ATLAS, corresponding to an integrated luminosity of 29 fb^{-1} [24]. The analysis targets the inclusive production cross-section (total and fiducial) of $W^+ \to \ell^+\nu$ and $W^- \to \ell^-\bar{\nu}$ processes. Measured cross-sections and their ratios are compared to theoretical predictions calculated at next-to-next-to-leading order (NNLO) in QCD, supplemented by next-to-next-to-leading-logarithmic (NNLL) resummation and next-to-leading-order (NLO) electroweak corrections. Predictions are obtained using several state-of-the-art PDF sets. In addition, the dependence of the production cross-sections on the center-of-mass energy is examined to test the consistency of the pQCD framework across different collision energies.

4.2 Data and simulation

4.2.1 Data samples

This analysis is based on proton–proton collision data recorded in 2022 by the ATLAS detector at a center-of-mass energy of $\sqrt{s} = 13.6$ TeV, corresponding to an integrated luminosity of $29.0\pm0.6\,\text{fb}^{-1}$. Only events meeting all data-quality requirements are included. Data-quality selection ensures that only periods with optimal detector and trigger performance are used for physics analysis. Each data-taking run is certified through a detailed evaluation of the operative status of all relevant subsystems, including the ID, calorimeters, MS, and trigger. This guarantees that the data sample used in the analysis is free from detector or trigger inefficiencies that could bias the measurements.

4.2.2 Simulation samples

The production of W and Z bosons is simulated using the SHERPA, version 2.2.12 [195] generator. Matrix elements (MEs) are calculated at NLO in QCD for up to two additional partons and at LO for up to five partons, using the COMIX [195] and OPENLOOPS [196–198] libraries. The parton shower is modeled with SHERPA's internal algorithm [199] following the MEPS@NLO matching scheme [200]. The tune parameter settings[1] provided by the generator authors are applied. The NNPDF3.0NNLO PDF set [201] is used, and the samples are normalized to NNLO theoretical cross-section predictions [202]. SHERPA W and Z production samples are composed of three disjoint sets categorized by their associated jet flavor: $W{+}b$, $W{+}c$, and $W{+}$light, where "light" refers to jets originating from light quarks or gluons. This is implemented through three mutually exclusive generator-level filters, listed in decreasing values of $\sigma \times \mathrm{BR}$ for each signal channel as follows: defining (i) events containing no b- or c-hadrons ($W{+}$light), (ii) events containing at least one c-hadron while suppressing b-hadrons, and (iii) events containing at least one b-hadron. These samples are combined using the appropriate generator cross-sections and filter efficiencies weights to recover the inclusive W sample. Alternative samples of W and Z bosons are generated with the POWHEG BOX V2 framework [119, 120, 203], providing NLO accuracy for the hard-scattering process and the leptonic decays (e, μ, and τ channels). These samples are interfaced to PYTHIA 8.307 [123]

---

[1] Monte Carlo events with small transverse momentum transfer from initial to final state are generally described by phenomenological models in MC event generators. These models contain many parameters whose values are a priori unknown and thus need to be constrained by data. This optimization process is known as tuning, and the resulting parameter sets are referred to as tunes.

for parton showering, hadronization, and the modeling of the underlying event, using the AZNLO tune [204]. The CT10NLO PDF set [205] is employed for the matrix-element calculation, while the CTEQ6L1 set [206] is used for the parton shower. Final-state QED radiation is modeled with PHOTOS++ 3.64 [207, 208]. These POWHEG+PYTHIA samples are employed for the assessments of the systematic uncertainties and cross-checks.

Top-quark pair ($t\bar{t}$) and single-top production are modeled with POWHEG BOX v2 interfaced to PYTHIA 8.307, using the A14 parton-shower tune [209]. Matrix elements are computed at NLO precision in QCD with the NNPDF3.0NLO PDF set. The $t\bar{t}$ samples are normalized to the NNLO+NNLL cross-section prediction obtained with TOP++ 2.0 [210–216].

Diboson (WW, WZ, ZZ) processes are simulated using SHERPA 2.2.12, including off-shell effects and Higgs-boson contributions where applicable. Both fully leptonic and semileptonic (one boson decays leptonically and the other hadronically) final states are included, with matrix elements evaluated at NLO accuracy in QCD for up to one additional parton and at LO for up to three partons. Since a dedicated cross-section calculation for 13.6 TeV is not yet available, the same normalization K-factors[2] used in Run 2 analyses are applied, corresponding to $K = 0.91$.

The effect of multiple interactions in the pile-up (both in the same and the neighbouring bunch crossing) is modelled by overlaying [217] the original hard-scattering event with simulated inelastic pp events generated by EPOS 2.0.1.4 [218, 219] and PYTHIA 8.307. The events generated with EPOS used the EPOS LHC tune, while the PYTHIA8 events used the NNPDF 2.3 LO PDFset [220] and the A3 tune [221]. The ATLAS detector response is simulated by the GEANT4 [124] with the full simulation of the ATLAS detector [222]. The events in simulated samples are processed with the same reconstruction conditions as the ones in real data. The complete list of simulated samples employed in this study is given in Tables 4.1 and 4.2.

All Monte Carlo samples are produced prior to data-taking using the best available estimates of the expected pile-up conditions. To match the actual pile-up distribution observed in data, a reweighting procedure is applied to the simulated events. The pile-up weight for each MC event is derived using the nominal MC pile-up profile and the $\langle\mu\rangle$ distribution from data corresponding to the GRL. Figure 4.1 compares the pile-up distributions in data and simulation after reweighting.

4.3 Event selection

4.3.1 Object reconstruction

The reconstruction of physics objects in the ATLAS detector is a crucial step in the physics analyses. This section describes the procedure for transforming detector signals into reconstructed objects, including charged-particle tracks and primary vertices, electrons, muons, jets, and missing transverse momentum ($p_{\mathrm{T}}^{\mathrm{miss}}$). All algorithms are optimized for Run 3 conditions and follow the standard ATLAS prescriptions.

Reconstruction of tracks and vertices. When a charged particle passes through the ID, it leaves energy deposits in the silicon sensors — the Pixel and SCT detectors — and in the TRT. The tracking software reconstructs these signals into helical trajectories, described by a set of five parameters:

---

[2] The K-factor is defined as the ratio between the cross-section calculated at a given order (usually the highest possible available) and the cross-section obtained by the MC generator used for the simulation.

Table 4.1: Simulated W and Z samples used in this thesis, with SHERPA providing the nominal signal samples. For each sample, the table reports the production cross-section times branching ratio (σ·BR), the applied K-factor, the total number of generated events, and the generator used.

Channel	$\sigma\cdot$BR [pb]	K-factor	N_{events} [$\times 10^6$]	Generator
$W^{\pm} \to e\nu$	19290.2	0.9059	30.650	SHERPA 2.2.12
	3402.25	0.9059	7.450	
	220.132	0.9059	1.750	
$W^{\pm} \to \mu\nu$	19326.7	0.9059	30.730	SHERPA 2.2.12
	3411.47	0.9059	7.600	
	218.007	0.9059	1.750	
$W^{\pm} \to \tau\nu$	19337.6	0.9059	30.740	SHERPA 2.2.12
	3411.31	0.9059	7.600	
	220.519	0.9059	1.740	
$Z \to ee$	1974.0	0.9340	30.630	SHERPA 2.2.12
	303.25	0.9340	6.170	
	59.841	0.9340	3.520	
$Z \to \mu\mu$	1974.2	0.9340	30.690	SHERPA 2.2.12
	304.48	0.9340	6.140	
	58.688	0.9340	3.500	
$Z \to \tau\tau$	1971.0	0.9340	30.740	SHERPA 2.2.12
	302.53	0.9340	6.150	
	59.655	0.9340	3.510	
$W^{+} \to e^{+}\nu$	11912.0	1.0070	29.930	POWHEG BOX v2 +PYTHIA 8.307
$W^{+} \to \mu^{+}\nu$	11910.0	1.0070	29.790	
$W^{+} \to \tau^{+}\nu$	11902.0	1.0070	29.880	
$W^{-} \to e^{-}\bar{\nu}$	8766.4	0.9996	19.930	
$W^{-} \to \mu^{-}\bar{\nu}$	8765.3	0.9996	19.950	
$W^{-} \to \tau^{-}\bar{\nu}$	8757.2	0.9996	19.950	
$Z \to ee$	1998.8	1.0124	216.440	
$Z \to \mu\mu$	1998.8	1.0124	219.120	
$Z \to \tau\tau$	1996.7	1.0124	49.940	

- The transverse impact parameter, d_0, represents the distance of closest approach of the reconstructed track to the beam line in the x–y plane, while the longitudinal impact parameter, z_0, denotes the z-coordinate at that point.
- The azimuthal and polar angles, ϕ_0 and θ, describe the direction of the track.
- q/p is the charge divided by the momentum, which determines the curvature direction and radius of the helix.

The first stage of track reconstruction is the *clusters formation*. Clusters of adjacent Pixel or SCT hits are combined into two-dimensional space-points, from which *seeds*—typically triplets of space-points that define the initial curvature and direction of a particle trajectory consistent with a helix pointing to the beam line—are built and used as starting points for the track-finding algorithm. To identify full tracks, a *combinatorial Kalman filter* [223] is applied. This algorithm extrapolates each seed outward through the detector, searching for compatible hits in subsequent silicon layers. At this stage, many more track candidates exist than real tracks. Because several candidates can share the same hits, an *ambiguity solver* is employed to rank them according to a scoring function. Each candidate is evaluated based on the number of precision hits, missing (expected but unfound) hits, the

Table 4.2: Simulated electroweak and top background samples used in this thesis. Leptonic final states include τ leptons as well. For each channel, the table reports the production cross-section times branching ratio ($\sigma\cdot$BR), the applied K-factor, the total number of generated events, and the generator used.

Channel	$\sigma\cdot$BR [pb]	K-factor	N_{events} [$\times 10^6$]	Generator
$t\bar{t}$	355.63972	1.1381	49.970	Powheg Box v2 +Pythia 8.307
	85.482	1.1381	49.920	
$\bar{t}$ (t-chan)	24.203	1.0858	5.990	Powheg Box v2 +Pythia 8.307
t (t-chan)	39.936	1.1066	8.960	
$\bar{t}$ (s-chan)	1.3525	1.0872	2.990	
t (s-chan)	2.1455	1.0963	4.990	
$W\bar{t}$	39.839	1.10269	9.990	
Wt	39.876	1.10269	9.980	
$WW \to \ell\nu qq$	51.226	0.91	5.000	Sherpa 2.2.12
$WZ \to \ell\nu bb$	2.5961	0.91	5.000	
$WZ \to \ell\nu qq$	9.2309	0.91	5.000	
$WZ \to qq\ell\ell$	3.5549	0.91	5.000	
$ZZ \to bb\ell\ell$	0.4986	0.91	4.990	
$ZZ \to qq\ell\ell$	1.7741	0.91	5.000	
$ZZ \to \ell\ell\ell\ell$	1.3351	0.91	9.960	
$WZ \to \ell\ell\ell\nu$	4.8181	0.91	0.990	
$\ell\ell\nu\nu$ OS	12.618	0.91	0.800	
$\ell\ell\nu\nu$ SS	0.0241	0.91	0.080	
$WZ \to \ell\nu\nu\nu$	3.289	0.91	0.350	

track χ^2 [224] of the fit, and the estimated p_{T}, giving preference to higher-quality, higher-momentum tracks. When a new candidate shares too many hits with an already accepted track, it is rejected. In dense environments (e.g., for instance, in the core of a 1 TeV jet), multiple charged particles can strike the same pixel sensors, merging their charge deposits into a single cluster. A dedicated *neural-network (NN)* [225] algorithm analyzes the cluster shape, width, charge asymmetry, and incident angles of nearby tracks to determine whether a cluster originates from multiple particles. If identified as merged, the cluster may be shared between tracks without penalizing their reconstruction quality. After ambiguity resolution, the surviving track candidates are refitted precisely in a final smoothing step. Candidate tracks are required to satisfy quality criteria. Additional selection criteria include cuts on transverse momentum and pseudorapidity, $p_{\mathrm{T}} > 400$ MeV and $|\eta| < 2.5$, as well as on the track impact parameters: $|d_0| < 2.0$ mm and $|z_0 \sin\theta| < 3.0$ mm. Using these tracks, interaction *vertices* are reconstructed by clustering tracks in z (beam axis) and fitting them with adaptive vertex fitting algorithms. Due to high pile-up, several vertices may be reconstructed in an event. The *primary vertex* [226], corresponding to the hard-scatter interaction, is selected as the vertex with the largest scalar sum of squared transverse momenta of its associated tracks. Tracks used for vertex reconstruction must satisfy requirements on the transverse (d_0) and longitudinal (z_0) impact parameters.

Reconstruction and identification of electrons. A particle interacting with the ATLAS calorimeter deposits energy across multiple calorimeter cells, which must be grouped to reconstruct the full energy deposit. This is achieved using the *topological clustering (topo-cluster)* algorithm. For each calorimeter cell, a deposited energy to noise ratio $E_{\text{cell}}/\sigma_{\text{noise}}$ is calculated, where if ratio is larger then 4, a cluster seed is defined. Neighbouring cells with $E_{\text{cell}}/\sigma_{\text{noise}} > 2$ are then added, followed by all adjacent cells without any energy requirement. Finally, topo-clusters containing multiple local

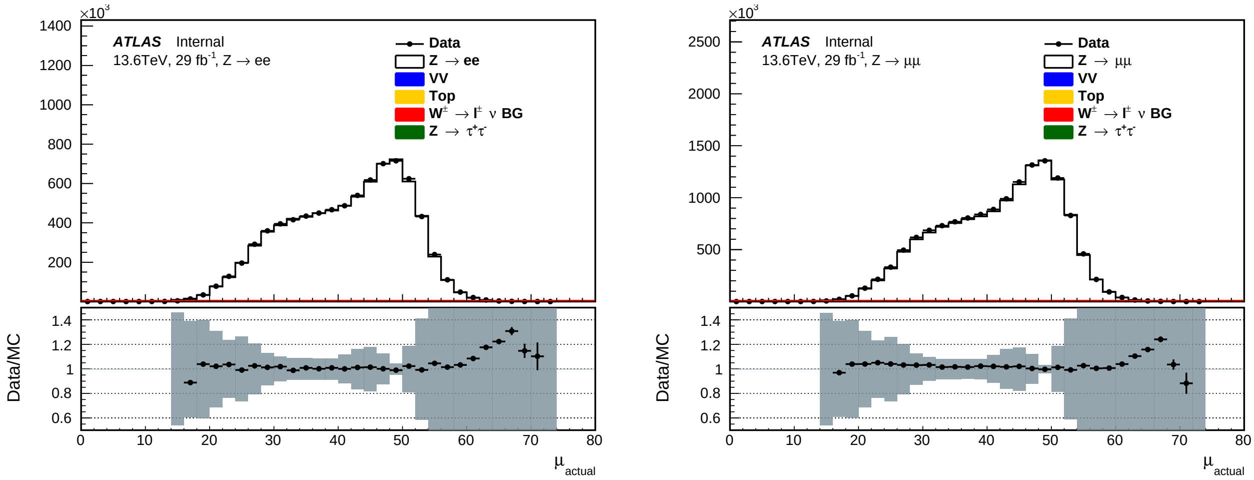

Figure 4.1: Comparison of the pile-up distributions $\langle\mu\rangle$ between data and simulation after applying pile-up reweighting in the $Z \to ee$ and $Z \to \mu\mu$ channels. The lower panels display the data-to-simulation ratios, and the shaded bands indicate the total systematic uncertainty from experimental, pile-up, and luminosity sources.

energy maxima are split into separate clusters to preserve substructure information.

Electrons are reconstructed by combining topo-clusters in the ECal with tracks in the ID. ECal topo-clusters are defined as calorimeter clusters with more than 50% of their energy deposited in the electromagnetic calorimeter, and one or several ID tracks are assigned. Since electrons can radiate bremsstrahlung photons in the ID, which may subsequently convert into e^+e^- pairs also leaving tracks, multiple tracks may be associated with the same topo-cluster. When combined, these matched tracks and clusters form a *supercluster*, which defines the reconstructed electron candidate. Topological clusters in the HCal are also used in this procedure, as true electrons are expected to deposit no energy in the HCal, therefore reducing number of selected objects. Electron energies are calibrated using a multivariate regression trained on simulation, with data–MC corrections derived from $Z \to e^+e^-$ events. To distinguish genuine electrons from hadronic backgrounds or calorimeter noise, a likelihood-based discriminant is built using calorimeter-shape, track-quality, and track–cluster-matching variables. Different working points (WPs) are defined by varying the discriminant threshold, `LooseLH`, `MediumLH`, and `TightLH` [227, 228], providing trade-offs between signal efficiency and background rejection. In this thesis, the `TightLH` identification (ID) WP is employed, corresponding to an average electron-identification efficiency of about 80%, as shown on Figure 4.2. Reconstructed electrons must satisfy $p_{\mathrm{T}} > 27$ GeV and $|\eta| < 2.47$, excluding the electromagnetic barrel–endcap transition region $1.37 < |\eta| < 1.52$. Additional impact-parameter selections are applied: $|z_0 \sin\theta| < 0.5$ mm and $|d_0/\sigma(d_0)| < 5$, with $\sigma(d_0)$ being estimated uncertainty. To further suppress *non-prompt* electrons – originating from heavy-flavour decays or photon conversions – from *prompt* electrons – originating from the primary vertices – isolation requirements are imposed. The calorimeter-based variable $E_{\mathrm{T}}^{\mathrm{cone20}}/p_{\mathrm{T}}$ and the track-based variable $p_{\mathrm{T}}^{\mathrm{varcone30}}/p_{\mathrm{T}}$ quantify the energy and momentum activity around the electron within cones of $\Delta R = 0.2$ and $\Delta R = \min\{10\ \mathrm{GeV}/p_{\mathrm{T}}^{e}, 0.3\}$, respectively. Electrons in this thesis are required to satisfy $E_{\mathrm{T}}^{\mathrm{cone20}}/p_{\mathrm{T}} < 0.06$ and $p_{\mathrm{T}}^{\mathrm{varcone30}}/p_{\mathrm{T}} < 0.06$. These isolation requirements define the `Tight_VarRad` WP used in this thesis. Additionally, data-driven methods are used to identify *fake electrons* — a calorimeter–track combinations misidentified as genuine electrons, most often originating from hadronic showers (e.g. charged pions), photon conversions, or overlapping energy deposits.

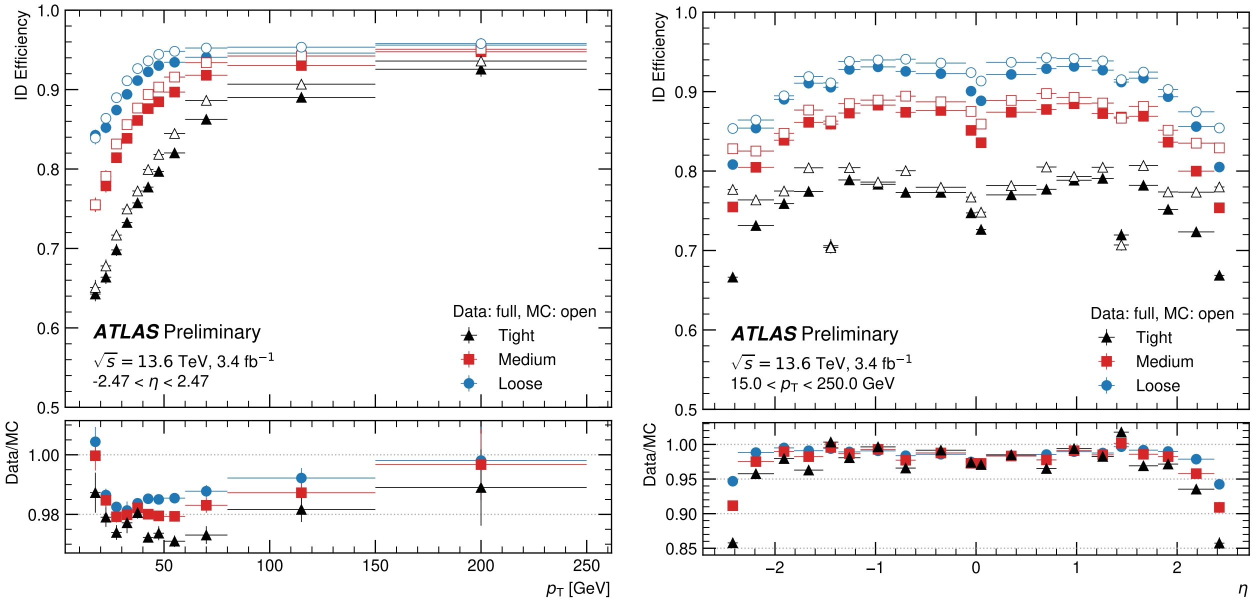

Figure 4.2: Electron identification efficiency as a function of the (left) p_T and (right) pseudorapidity η for electrons with p_T between 25 and 50 GeV. Efficiencies in data and simulation are shown for three likelihood-based working points (`Loose`, `Medium`, and `Tight`). The measurements are derived from 2022 pp collision data at $\sqrt{s} = 13.6$ TeV, corresponding to an integrated luminosity of 3.4 fb^{-1}, with total uncertainties indicated by the error bars [229].

Reconstruction of muons. Muons are leptons about 200 times heavier than electrons. Owing to their large mass, the bremsstrahlung radiation probability scales as $1/m_{\mu}^{2}$, making radiative energy losses negligible. Since muons do not undergo strong interactions, they traverse both the ECal and HCal with only minimal ionization energy loss of a few GeV, even across several meters of material. Consequently, muons might not be absorbed in the calorimeters and escape to the outermost detector layers. Escaping muons are measured in the MS. Several complementary reconstruction algorithms are used to identify muon candidates. In this thesis, the *Combined (CB)* [230] muon reconstruction is used. In this approach, independent tracks reconstructed in the ID and the MS are matched and refitted together in a global fit procedure. The fit can dynamically include or exclude individual MS hits to optimize the track quality. Most CB muons are reconstructed following an outside-in strategy, starting from the MS track and extrapolating it inward to find a compatible ID track. This method provides the best momentum resolution and the highest reconstruction purity across the full detector acceptance. Other algorithms are also used in ATLAS for specific geometrical or kinematic regions: *Segment-Tagged (ST)* muons are formed by matching ID tracks to one or more MS track segments; *Inside-Out (IO)* muons start from ID tracks and associate them with multiple MS hits; *Calorimeter-Tagged (CT)* muons rely on ID tracks linked to energy deposits in the calorimeter, mainly in regions not instrumented with MS chambers ($|\eta| < 0.1$); *Muon-Extrapolated (ME)* muons are reconstructed using only the MS track, with a loose requirement on compatibility with the interaction point ($2.5 < |\eta| < 2.7$); and finally, *Standalone (SA)* muons are built solely from MS information without requiring an ID track match. The reconstructed muon momentum is calibrated by applying corrections to both data and simulation, accounting for charge-dependent biases and mismodeling effects arising from detector geometry, magnetic field description, and multiple scattering. Muon identification is based on track-quality and hit multiplicity requirements in the ID and MS, with the `Medium` WP [231] used in this thesis, which provides an optimal balance between efficiency and purity while selecting only combined muons. Additional rejection of non-prompt muons is achieved through isolation criteria, with this thesis employing the `Tight_VarRad` working point defined for muons by $p_{\mathrm{T}}^{\mathrm{varcone30}}/p_{\mathrm{T}} < 0.04$ and $E_{\mathrm{T}}^{\mathrm{cone20}}/p_{\mathrm{T}} < 0.15$. Muons are further required to satisfy $p_{\mathrm{T}} > 27$ GeV and $|\eta| < 2.5$. The reconstruction, identification, and isolation efficiencies for these selections are derived using $Z \rightarrow \mu^{+}\mu^{-}$ events from pp collisions at $\sqrt{s} = 13.6$ TeV (see Figure 4.3).

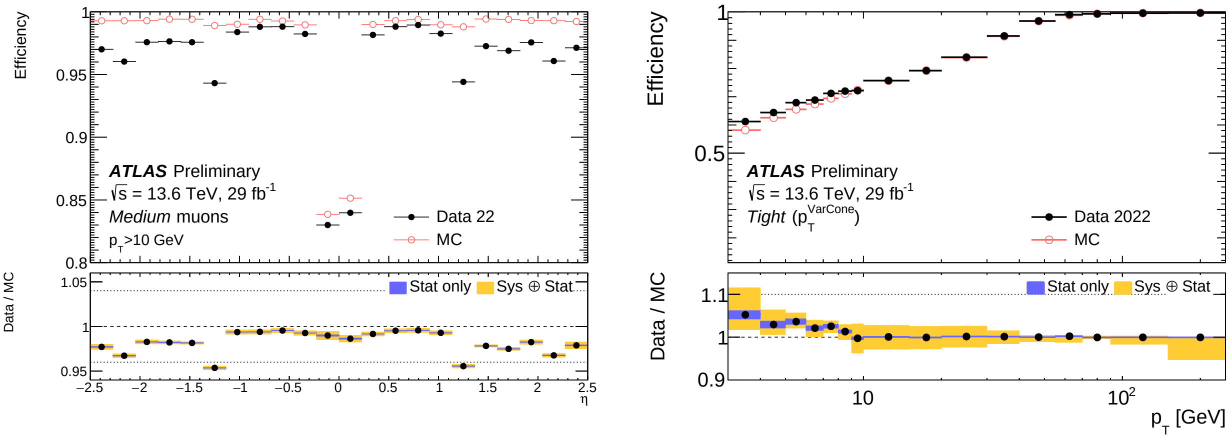

Figure 4.3: Muon reconstruction efficiency as function of η for `Medium` selection (left) [232] and isolation efficiency as functions of p_{T} for `Tight_VarRad` isolation criteria (right) [233], measured in $Z \rightarrow \mu^{+}\mu^{-}$ events from 2022 data. Black points indicate data, red circles indicate simulation, with statistical and total uncertainties shown. Lower panels show Data-to-MC ratios.

Jet reconstruction. Jets are reconstructed using the anti-k_t algorithm [234], a sequential clustering algorithm belonging to the generalized k_t family. It defines distance measures $d_{ij} = \min(p_{T,i}^{-2}, p_{T,j}^{-2})\,(\Delta_{ij}^{2}/R^{2})$ and $d_{iB} = p_{T,i}^{-2}$, where $\Delta_{ij} = \sqrt{(y_i - y_j)^2 + (\phi_i - \phi_j)^2}$ is angular distance in rapidity-azimuth $(y - \phi)$ space and R is the usual jet-radius parameter. Indices i and j run over all input objects (particles or topological clusters). The quantity d_{ij} measures the distance between two objects in (y, ϕ) space, while d_{iB} represents the distance of object i to the beam, determining whether it should be merged or declared as a final jet. In this scheme, hard particles are clustered first, resulting in jets that are circular in the (η, ϕ) plane. The anti-k_t algorithm is infrared safe and robust against soft radiation, meaning that the presence of additional low-p_{T} particles does not significantly modify the reconstructed jet boundaries or kinematics, as soft particles are naturally clustered into nearby hard jets. This property makes the anti-k_t algorithm the standard choice in ATLAS, implemented through the `FastJet` [235] package with $R = 0.4$. The *Jet Vertex Tagger* (Jvt) [236] is a discriminant tool used to distinguish jets originating from the primary interaction vertex from those produced by pile-up interactions. In this thesis, jets with transverse momentum below 60 GeV are required to satisfy the `Tight` working point of the *neural-network-based Jet Vertex Tagger* (NNJvt) [237], an advanced version of the standard Jvt algorithm.

Missing transverse momentum measurement. Neutrinos and other non-interacting particles escape detection but can be inferred from the missing transverse momentum $\vec{p}_{\mathrm{T}}^{\,\mathrm{miss}}$ [238]. Assuming momentum conservation in the transverse plane, $\sum \vec{p}_{\mathrm{T}} = 0$, the missing transverse momentum is defined as the negative vector sum of the calibrated momenta of all reconstructed physics objects (electrons e, photons γ, muons μ, τ leptons, and jets):

$$\vec{p}_{\mathrm{T}}^{\,\mathrm{miss}} = -\sum_{r}^{e,\gamma,\mu,\tau,\mathrm{jet}} \vec{p}_{\mathrm{T}}^{\,r} - \vec{p}_{\mathrm{T}}^{\,\mathrm{soft}}. \tag{4.5}$$

The soft term includes charged-particle tracks associated with the primary vertex but not linked to hard objects. An example of the distribution of the $p_{\mathrm{T}}^{\mathrm{miss}}$ is shown on Figure 4.4. Ambiguities between overlapping objects (e.g. electrons overlapping with jets) are resolved in a dedicated *overlap-removing* step. For this result, $p_{\mathrm{T}}^{\mathrm{miss}}$ is constructed from electrons, muons, and jets, while photons and τ-leptons are omitted as they are not part of the signal final state. The `Tight` [239, 240] working point of $p_{\mathrm{T}}^{\mathrm{miss}}$ reconstruction is used based on NNJvt, requiring forward jets ($2.5 < |\eta| < 4.5$) to have $p_{\mathrm{T}} > 30$ GeV to suppress pile-up contamination.

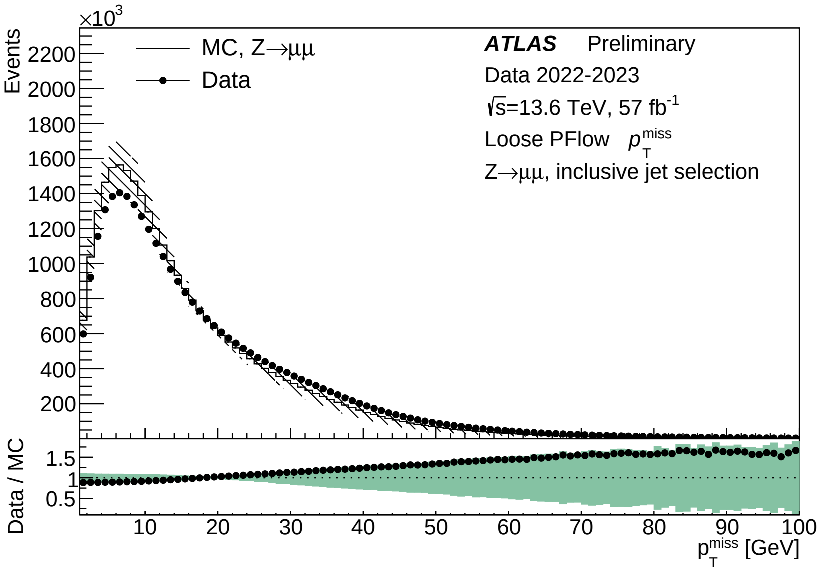

Figure 4.4: Distribution of missing transverse momentum reconstructed with the TST algorithm (Loose WP) in $Z \to \mu^+\mu^-$ events at $\sqrt{s} = 13.6$ TeV. Data from 2022-2023 is compared to simulated events generated with POWHEG and PYTHIA 8 [241].

Overlap removal ensures that electrons, muons, and jets reconstructed from the same detector activity are not double-counted. A dedicated procedure is applied after the baseline selection of the objects, including the isolation criteria, and an independent internal treatment is used in the missing transverse momentum reconstruction to handle lepton–jet sharing. In this study, the algorithm removes jets close to electrons, then electrons close to the surviving jets, followed by low-track-multiplicity jets close to the muons and finally muons close to the remaining jets, with typical angular requirements of $\Delta R < 0.2$ for the primary veto step and $\Delta R < 0.4$ for the secondary veto step.

4.3.2 W-boson physics candidates

Events used in this thesis are selected using single-lepton triggers for electrons and muons, as listed in Table 4.3. The different triggers are optimized for various kinematic regions by applying distinct requirements on lepton identification, isolation, and lepton p_{T}. Triggers with lower p_{T} thresholds enforce tighter quality and isolation criteria to suppress backgrounds, while those with higher thresholds rely on looser or no such requirements, ensuring high efficiency for energetic leptons. All triggers are combined using a logical OR to maximize signal efficiency. To guarantee operation in the plateau region of the trigger efficiency, only leptons with $p_{\mathrm{T}} > 27$ GeV are considered. The lepton that fired the trigger is required to be geometrically matched to the corresponding offline-reconstructed object in the η–ϕ plane, ensuring consistency between the online and offline selections.

Table 4.3: Single-electron and single-muon triggers used to select W-boson candidates.

Electron triggers	Muon triggers
HLT_e26_lhtight_ivarloose_L1EM22VHI	HLT_mu24_ivarmedium_L1MU14FCH
HLT_e60_lhmedium_L1EM22VHI	HLT_mu50_L1MU14FCH
HLT_e140_lhloose_L1EM22VHI	

Events must contain exactly one reconstructed and isolated lepton and significant missing transverse momentum, $p_{\mathrm{T}}^{\mathrm{miss}} > 25$ GeV, arising from the undetected neutrino. To further suppress multijet and background processes, the transverse mass of the W candidate is required to be greater than 50 GeV.

Electron and muon reconstruction, identification, isolation, p_{T}, and η requirements are detailed in Section 4.3.1. For W-boson candidates, the selections include the trigger requirements listed in Table 4.3, together with the additional $p_{\mathrm{T}}^{\mathrm{miss}}$ and m_{T} thresholds.

4.3.3 Background estimation

Background contributions to the W-boson final states can be grouped into two main categories: electroweak (EW) and top-quark processes, which are estimated using MC simulation, and the multijet background, which is derived from data.

EW category includes single-boson and diboson production processes that can mimic the W-boson signature, while the top background arises primarily from events containing real W bosons in top-quark decays. Dominant EW background originates from $W \to \tau\nu$ decays, where the τ subsequently decays leptonically and produces a final state with a lepton and missing transverse energy, closely resembling the signal topology. Additional EW contributions come from $Z \to \ell\ell$ and $Z \to \tau\tau$ events, in which one of the leptons either escapes reconstruction or fails the identification or isolation criteria, leading to an apparent imbalance in transverse momentum and hence a fake W-like signature. Such backgrounds are particularly relevant in regions of high missing transverse energy and are modeled using MC. Diboson processes, including WW, WZ, and ZZ production, can also contribute when one of the bosons decays hadronically or invisibly, or when a lepton from a leptonic decay fails the reconstruction or isolation criteria. Their overall contribution is small due to the lower production cross-sections compared to inclusive W production. Top-quark backgrounds arise mainly from $t\bar{t}$ pair and single-top (Wt) production, where at least one of the W bosons from the top decays leptonically. These events often contain additional jets from b-quark decays, which distinguish them from the inclusive W signal. They can enter the selection if these jets fail the b-tagging [242] or are not reconstructed. Their contribution is modeled using MC simulation and normalized to the theoretical NLO cross-sections.

The multijet (MJ) background originates from QCD jet production in which hadronic activity is misidentified as isolated prompt leptons. Its main sources include collimated charged and neutral pions and non-prompt real leptons from semi-leptonic heavy-flavour decays or in-flight pion decays. Although such events are largely suppressed by the lepton identification, isolation, and by the p_{T}, $p_{\mathrm{T}}^{\mathrm{miss}}$, and m_{T}^{W} requirements, they remain a significant background in W-boson analyses, particularly under high pile-up, due to their large production cross-section and artificial $p_{\mathrm{T}}^{\mathrm{miss}}$ arising from jet energy mis-measurements. Processes where a jet is misidentified as a lepton or a non-prompt lepton passes the selection depend on detailed detector effects, mis-reconstruction, and isolation behaviour that are difficult to reproduce in MC. Therefore, the MJ contribution is estimated directly from data using phase-space *control regions* (CRs) defined by modifying the lepton-isolation and kinematic requirements. These regions allow the separation of event samples dominated by MJ processes from those dominated by genuine electroweak W production. The strategy is to use a region rich in MJ events (anti-isolated leptons) to derive the MJ *template* shape, and to use leptons with looser kinematic requirements to fit the MJ *normalization* to data. Finally, the region with a signal-like kinematics is used to extrapolate this result to the signal selection. Although the control regions are designed to be dominated by MJ events, they are not completely free of signal contamination. A small fraction of genuine W-boson events can migrate into these regions due to detector resolution effects, imperfect reconstruction of $p_{\mathrm{T}}^{\mathrm{miss}}$ or m_T^W, or fluctuations in the lepton isolation caused by nearby jet activity and high pile-up. For this reason, the expected contributions from EW and top-quark processes, estimated from simulation, are subtracted from the data when building the MJ templates.

In this thesis, four mutually exclusive regions are defined to extract the MJ background, as illustrated in Figure 4.5. The *signal region* (SR) corresponds to isolated leptons with nominal $p_T > 27$ GeV, $p_{\mathrm{T}}^{\mathrm{miss}} > 25$ GeV and $m_T^W > 50$ GeV requirements, while the *fit region* (FR) and the two control regions (CR1 and CR2) are obtained by inverting isolation or relaxing kinematic selections to enrich MJ events and enable a data-driven extrapolation toward the SR.

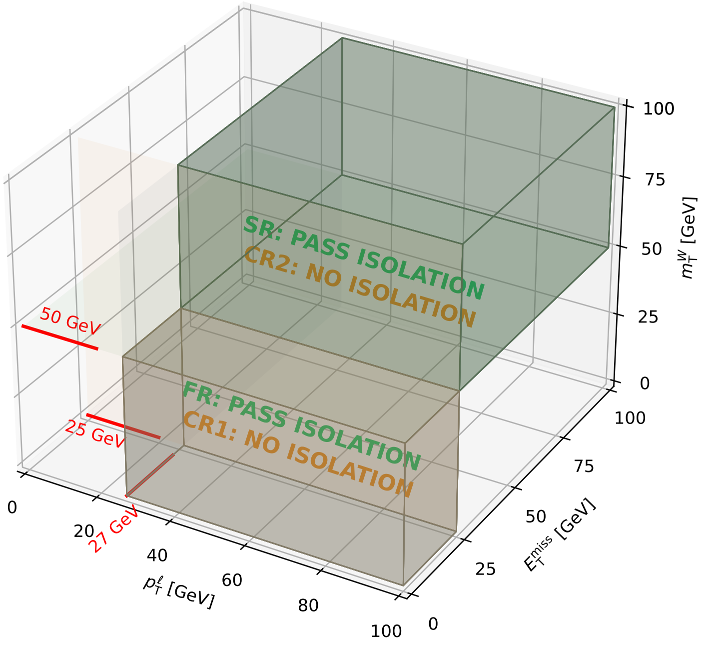

Figure 4.5: Schematic illustration of the regions used for the multijet background estimation in the $W \to \ell\nu$ analysis, defined in the $(p_{\mathrm{T}}^{\ell},\, E_{\mathrm{T}}^{\mathrm{miss}},\, m_T^W)$ space.

An example with relaxed kinematic requirements ($m_T^W > 0$ and $p_{\mathrm{T}}^{\mathrm{miss}} > 0$) is shown in Figure 4.6. The procedure starts from control region 1 (CR1), which is enriched in MJ events by inverting both the isolation and the kinematic requirements relative to the nominal selection. In this region, the data distribution of a given observable O is corrected for the small EW and top-quark contributions, estimated from simulation. The resulting distribution represents the MJ template and is defined as:

$$d_{\mathrm{MJ}}^{\mathrm{CR1}}(O) = d_{\mathrm{data}}^{\mathrm{CR1}}(O) - d_{\mathrm{EW}}^{\mathrm{CR1}}(O), \tag{4.6}$$

where $d(O)$ denotes the distribution of an observable O, such as m_{T}^W, $p_{\mathrm{T}}^{\mathrm{miss}}$ or p_{T}^{ℓ}. Next step uses these MJ templates in the FR, which has the same kinematic requirements as CR1 but with isolated leptons instead of anti-isolated ones. A template fit is performed on the data in FR according to:

$$d_{\mathrm{data}}^{\mathrm{FR}}(O) = T_{\mathrm{MJ}} \cdot d_{\mathrm{MJ}}^{\mathrm{CR1}}(O) + \alpha_{\mathrm{EW}} \cdot d_{\mathrm{EW}}^{\mathrm{FR}}(O), \tag{4.7}$$

where the fit parameters T_{MJ} and α_{EW} scale the MJ and EW contributions, respectively, to best reproduce the data in FR. Although $d_{\mathrm{MJ}}^{\mathrm{CR1}}$ is already corrected for EW contamination, the free parameter α_{EW} allows for small adjustments to the EW normalization to absorb residual MC uncertainties and prevent bias in the determination of T_{MJ}. In the final step, the extrapolation toward the signal-like phase space is performed. The relative change in the MJ yield between the two anti-isolated regions (CR1 and CR2) defines the *transfer factor*:

$$\varepsilon = \frac{N_{\mathrm{MJ}}^{\mathrm{CR2}}}{N_{\mathrm{MJ}}^{\mathrm{CR1}}}, \tag{4.8}$$

where both normalizations are corrected for EW and top-quark contributions by subtraction. This factor quantifies how the MJ yield changes as one moves from relaxed kinematic selections in CR1 to the tighter selections in CR2. Finally, the MJ yield in the SR is obtained by scaling the fitted MJ yield in the FR with this transfer factor:

$$N_{\mathrm{MJ}}^{\mathrm{SR}} = \varepsilon \cdot N_{\mathrm{MJ}}^{\mathrm{FR}}. \tag{4.9}$$

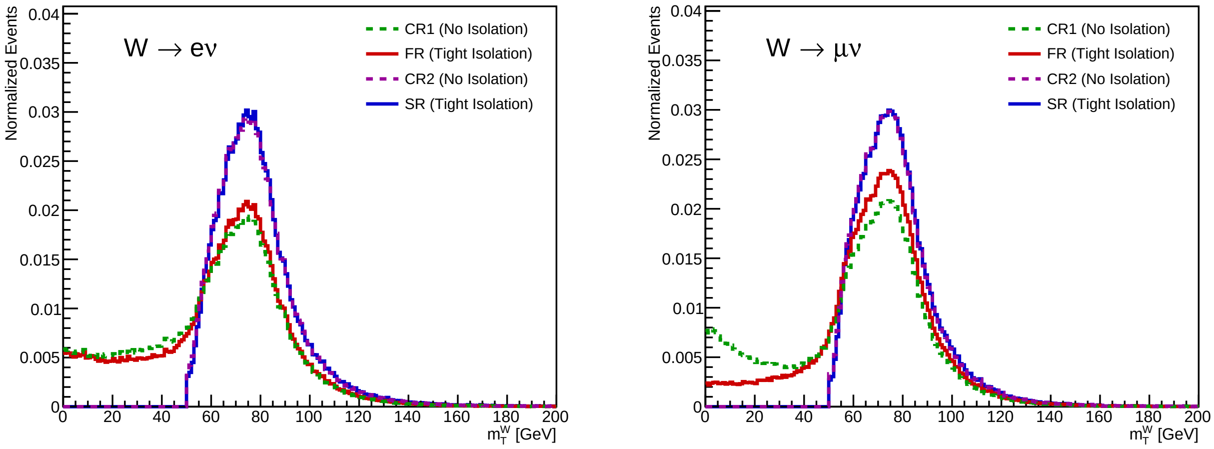

Figure 4.6: Comparison of the transverse mass m_T^W distributions in the four analysis regions used for the multijet estimation: The distributions are obtained with relaxed kinematic selections ($m_T^W > 0$, $p_{\mathrm{T}}^{\mathrm{miss}} > 0$) used in CR1 and FR.

Nominal single-lepton triggers used in the signal selection, listed in Table 4.3, include isolation requirements at the trigger level in order to suppress background from non-prompt or misidentified leptons. However, such isolation conditions would bias the composition of events in the multijet control regions, where the aim is to collect a sample enriched in non-isolated leptons. For this reason, dedicated *support triggers* without isolation requirements are used to select events in the control regions. In this thesis, the triggers `HLT_e20_lhvloose_L1EM15VH` and `HLT_e26_idperf_tight_nogsf_L1EM22VHI` are used for the electron channel, and `HLT_mu22_L1MU14FCH` for the muon channel. A change in trigger selection implies a different integrated luminosity, since these triggers are subject to different prescales and data-taking conditions. The corresponding luminosities are therefore recalculated using the Z-boson peak counting method (briefly introduced in Section 2.4.3), yielding $\mathcal{L}_{int} = 19.65 \pm 0.26\ \mathrm{pb}^{-1}$ for electrons and $\mathcal{L}_{int} = 19.69 \pm 0.19\ \mathrm{pb}^{-1}$ for muons. These luminosity values are used to normalize the simulated EW and top-quark background contributions that are subtracted from the data in the control regions. The effective luminosity of the control samples is much smaller than the full dataset (29 fb^{-1})

because the support triggers used in the MJ control regions are prescaled and only active for a subset of luminosity blocks; this luminosity is used solely to normalize the simulated EW/top contributions in CR1/CR2.

The previously described MJ estimation procedure assumes that the MJ kinematics (both shape and normalization) do not depend strongly on the tightness of the lepton-isolation requirement. To verify and, if necessary, correct for this assumption, an additional study is performed in which the isolation requirement is progressively varied from loose to tight isolation. The nominal `Tight_VarRad` WP used for electrons and muons is defined in Section 4.3.1. In this study, the track-based isolation variable (cuts on $p_{\mathrm{T}}^{\mathrm{varcone30}}/p_{\mathrm{T}}$) is scanned in several steps while the calorimeter-based isolation, $E_{\mathrm{T}}^{\mathrm{cone20}}/p_{\mathrm{T}}$, is kept fixed at 0.06 for electrons and 0.15 for muons. The track-isolation ranges are defined in four slices, moving from looser to tighter isolation, and are finally extrapolated to the nominal `Tight_VarRad` WP used in the SR:

$$\begin{aligned} \text{Electrons:} \quad & [0.24, 0.30] \rightarrow [0.18, 0.24] \rightarrow [0.12, 0.18] \rightarrow [0.06, 0.12] \rightarrow \texttt{Tight\_VarRad}, \\ \text{Muons:} \quad & [0.16, 0.20] \rightarrow [0.12, 0.16] \rightarrow [0.08, 0.12] \rightarrow [0.04, 0.08] \rightarrow \texttt{Tight\_VarRad}. \end{aligned}$$

For each isolation slice, the same template-fit procedure described previously is applied to data, yielding the multijet normalization $N_{\mathrm{MJ}}(I_i)$, where I_i represents the mean track-isolation value of slice i. These values are then fitted with a linear or quadratic function of the isolation variable:

$$N_{\mathrm{MJ}}(I) = a + bI \quad \text{or} \quad N_{\mathrm{MJ}}(I) = a + bI + cI^2, \tag{4.10}$$

and the result is extrapolated to the isolation value corresponding to the signal-region selection.

An illustrative example of the m_T^W and $E_{\mathrm{T}}^{\mathrm{miss}}$ in the CR1 , obtained for four different isolation slices, is shown in Figure 4.7, using nominal trigger selections.

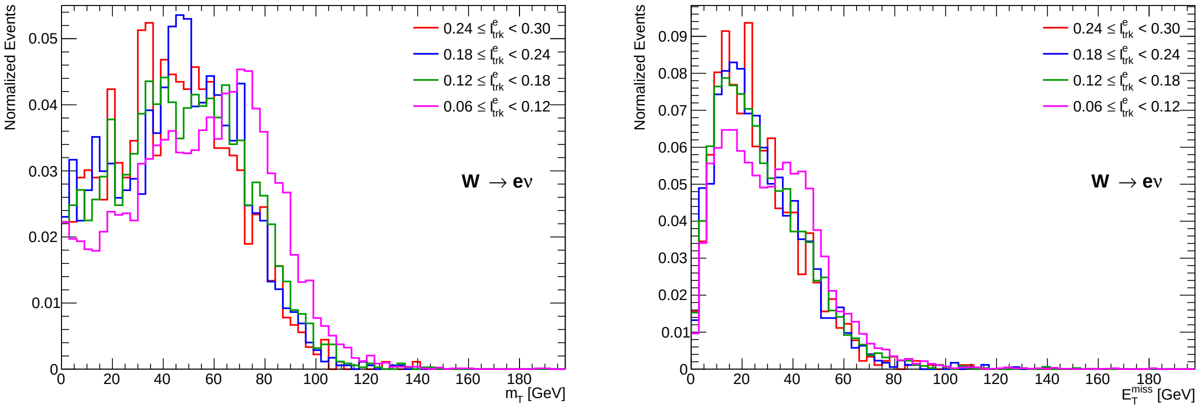

Figure 4.7: Distributions of (left) transverse mass m_T^W and (right) trasverse momentum $p_{\mathrm{T}}^{\mathrm{miss}}$ in CR1 for four isolation slices, shown for the $W \to e\nu$ channel.

This isolation-scan study thus bridges the gap between the anti-isolated control regions, used to obtain the MJ shape, and the tightly isolated signal region where the MJ contamination must be estimated. It quantifies the evolution of the MJ yield with isolation and provides both the extrapolation to the SR and an associated uncertainty. An example of the linear and quadratic fits is shown in Figure 4.8, while the multijet yields obtained from the latter are summarized in Table 4.4.

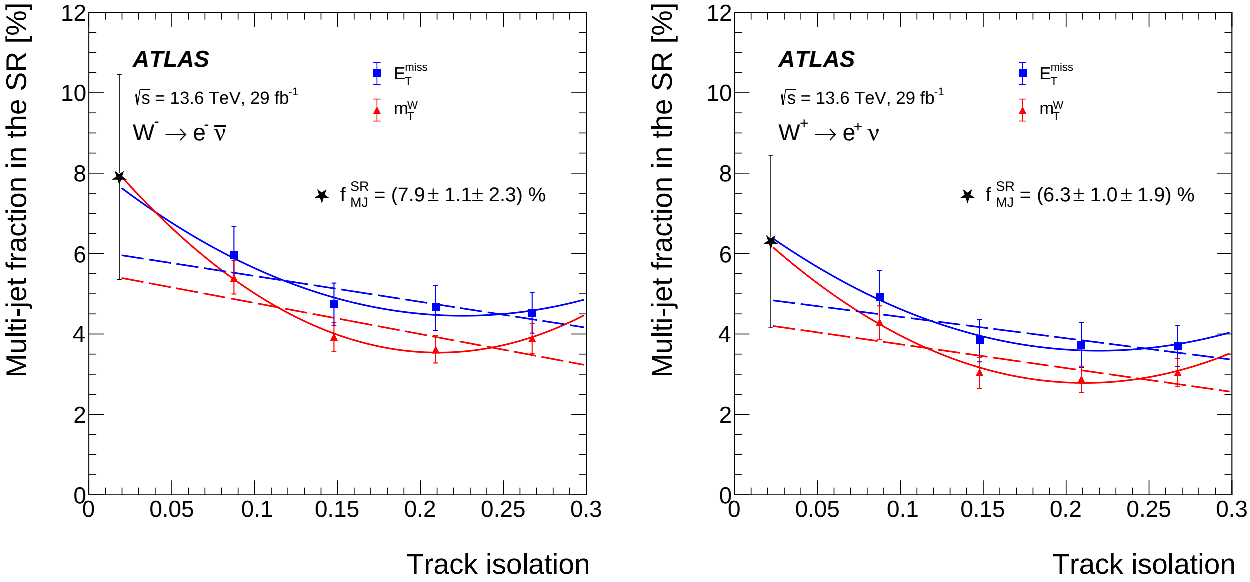

(a) $W^- \to e^-\bar{\nu}$ (b) $W^+ \to e^+\nu$

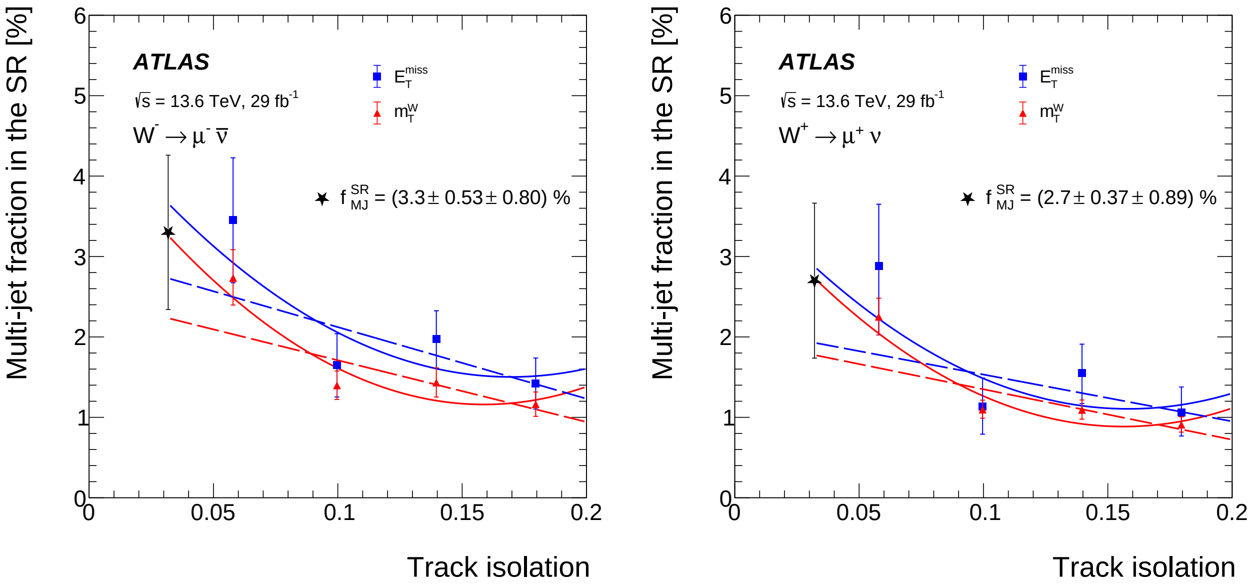

(c) $W^- \to \mu^-\bar{\nu}$ (d) $W^+ \to \mu^+\nu$

Figure 4.8: Determination of the MJ normalization in the SR using the nominal method. Each panel corresponds to one of the four W-boson decay channels: (a) $W^- \to e^-\bar{\nu}$, (b) $W^+ \to e^+\nu$, (c) $W^- \to \mu^-\bar{\nu}$, and (d) $W^+ \to \mu^+\nu$. Points show MJ yields obtained from quadratic (solid) and linear (dashed) fits in control regions defined by successive lepton-isolation slices, plotted versus the central isolation value of each slice. The quadratic fits describe the isolation dependence of the MJ yield, and their extrapolation to the tight-isolation WP provides the predicted MJ contribution in the SR. Results extracted from p_T^{miss} and m_T^W fits are shown in black and red, respectively, demonstrating their mutual consistency.

Channel	$m_{\mathrm{T}}^{\mathrm{W}}$	$p_{\mathrm{T}}^{\mathrm{miss}}$	Combined mean
$W^- \to e^- \bar{\nu}$	7.98 ± 1.21	7.67 ± 1.96	7.9 ± 1.03
$W^+ \to e^+ \nu$	6.2 ± 1.19	6.41 ± 1.89	6.26 ± 1.01
$W^- \to \mu^- \bar{\nu}$	3.26 ± 0.58	3.66 ± 1.32	3.33 ± 0.53
$W^+ \to \mu^+ \nu$	2.73 ± 0.39	2.87 ± 1.42	2.74 ± 0.37

Table 4.4: Relative event yields (in %) of the estimated multijet background, extracted from quadratic fits performed in the isolation–scan study described in the text.

4.3.4 Event yields

The evolution of the number of selected events after each successive requirement is summarized in the cutflow shown in Table 4.5, separately for the $W \to e\nu$ and $W \to \mu\nu$ channels. The expected and observed event yields after all selection criteria are summarized in Table 4.6. The predictions are derived from MC simulations based on the SHERPA generator, which serves as the nominal event generator for this thesis. SHERPA provides a consistent treatment of matrix elements and parton showers for both signal and background processes. The event yields reflect the normalization of these simulated samples to the integrated luminosity of the analyzed dataset after applying all reconstruction, identification, and kinematic selections described in Sections 4.3.1 and 4.3.2. For the multijet background, a data-driven estimation is employed, with its normalization constrained from control regions. Quoted uncertainties correspond to the statistical precision of the MC samples for the electroweak and top-quark processes, while the multijet contribution includes an overall normalization uncertainty. Comparison between the total predicted yields and those observed in data demonstrates good agreement within the quoted uncertainties, validating both the selection strategy and the modeling of the principal processes.

Table 4.5: Cutflow yields for $W \to e\nu$, $W \to \mu\nu$, and combined W channels.

Step	$W \to e\nu$	$W \to \mu\nu$	Total W
INITIAL	2.63e+09	2.62e+09	5.25e+09
GRL	2.59e+09	2.57e+09	5.15e+09
Primary Vertex cut	2.57e+09	2.56e+09	5.13e+09
At least 1 lepton p_T >27 GeV	1.78e+08	2.04e+08	3.82e+08
Exactly 1 lepton p_T >27 GeV	1.70e+08	1.89e+08	3.59e+08
$p_{\mathrm{T}}^{\mathrm{miss}} > 25$ GeV	1.24e+08	1.57e+08	2.81e+08
$m_{\mathrm{T}}^{W} > 50$ GeV	1.13e+08	1.47e+08	2.61e+08

4.4 Systematic uncertainties

4.4.1 Experimental systematic uncertainties

Luminosity. The uncertainty on the integrated luminosity is obtained from a dedicated calibration procedure, largely following the methodology described in Chapter 3, and based on the measurements performed with the LUCID-2 luminometer [24] at $\sqrt{s}$ =13.6 TeV. The resulting preliminary uncertainty on the integrated luminosity for the 2022 dataset is estimated to be 2.2%.

	$W^- \to e^-\bar{\nu}$	$W^+ \to e^+\nu$	$W^- \to \mu^-\bar{\nu}$	$W^+ \to \mu^+\nu$
$W \to \ell\nu$ $(\ell = e, \mu)$	$43,650,000 \pm 70,000$	$55,370,000 \pm 80,000$	$57,760,000 \pm 80,000$	$74,900,000 \pm 90,000$
$W \to \tau\nu$	$684\,000 \pm 8\,000$	$819\,000 \pm 9\,000$	$906\,000 \pm 10\,000$	$1\,120\,000 \pm 10\,000$
$Z \to ee$	$1\,416\,000 \pm 4\,000$	$1\,459\,000 \pm 4\,000$	0 ± 0	0 ± 3
$Z \to \mu\mu$	175 ± 42	180 ± 42	$4\,638\,000 \pm 8\,000$	$4\,903\,000 \pm 8\,000$
$Z \to \tau\tau$	$88\,000 \pm 1\,000$	$91\,000 \pm 1\,000$	$107\,000 \pm 1\,000$	$111\,000 \pm 1\,000$
Top	$863\,800 \pm 400$	$905\,400 \pm 500$	$802\,200 \pm 400$	$843\,400 \pm 400$
VV	$93\,500 \pm 300$	$97\,600 \pm 300$	$98\,500 \pm 300$	$102\,800 \pm 300$
Multijet	$4\,000\,000 \pm 1\,000\,000$	$4\,000\,000 \pm 1\,000\,000$	$2\,100\,000 \pm 700\,000$	$2\,200\,000 \pm 800\,000$
Total prediction	$51\,000\,000 \pm 1\,000\,000$	$63\,000\,000 \pm 1\,000\,000$	$66\,400\,000 \pm 700\,000$	$84\,200\,000 \pm 800\,000$
Data	50 748 537	62 610 338	65 053 470	82 360 980
Data/Prediction	0.99 ± 0.02	0.99 ± 0.02	0.98 ± 0.01	0.98 ± 0.01

Table 4.6: Event yields in data and predicted signal and background after all selection criteria. The statistical uncertainties are indicated for the electroweak and top-quark processes, while a normalization uncertainty is shown for the multijet contribution. Rounding rules from PDG are applied [243].

Lepton trigger. To determine the efficiency of the lepton triggers, clean and well-understood dilepton resonances, such as $Z \to \ell\ell$ and $J/\psi \to \ell\ell$ are used (with $\ell = e, \mu$). Method employed for this determination is known as the *tag-and-probe* technique [244, 245]. One of the leptons from these decays, referred to as the *tag*, serves as a reference object with a reliably known origin, as it satisfies strict identification, reconstruction, isolation, and trigger requirements. This ensures that the event is a genuine $Z \to \ell\ell$ (or $J/\psi \to \ell\ell$) decay and that it has been adequately recorded. The second lepton, called the *probe*, is subject only to data-quality and background-rejection criteria. Together with the tag, it forms a clean lepton-pair candidate. The probe is then used to test the trigger's performance [246]: depending on whether it matches a fired trigger object, it is counted as a *passing* or *failing* probe. The trigger efficiency is defined as the ratio of the number of passing probes to the total number of probes. This measurement is performed both in data and in MC samples, and the ratio of the two efficiencies:

$$\mathrm{SF}(p_\mathrm{T}, \eta) = \frac{\varepsilon_\mathrm{data}(p_\mathrm{T}, \eta)}{\varepsilon_\mathrm{MC}(p_\mathrm{T}, \eta)},$$

defines the *scale factor* (SF), which is applied to simulated events to correct for residual data–MC differences. Scale factors are derived in bins of lepton transverse momentum and pseudorapidity to account for variations across the detector acceptance. For the Run 3 dataset, the associated systematic uncertainties are evaluated by repeating the measurement with intentional variations of certain components in the procedure, such as the background subtraction method, tag selection, fitting model, and trigger-matching criteria. These variations result in alternative SF values, and deviations from the nominal SF define the upward and downward systematic shifts assigned as the trigger efficiency uncertainty.

Lepton efficiency. Data-to-MC efficiency SFs are also obtained in bins of electron p_T and η for reconstruction, identification, and isolation criteria. Associated uncertainties for these efficiencies follow the methodology established in the Run 2 performance study [227], with additional variations introduced by comparing simulations between Run 2 and Run 3 conditions. As this work was carried out at an early stage of the Run 3 performance evaluation, dedicated Run 3 systematic uncertainties for electron efficiency were not yet available at that time. Electron reconstruction efficiency uncertainty quantifies the precision with which tracks are correctly matched to electromagnetic clusters, a procedure explained in Section 4.3.1. It is estimated by varying the track–calorimeter cluster matching requirements and by comparing different tag-and-probe selections that study reconstruction from independent samples (e.g. $Z \to ee$ vs. $J/\psi \to ee$). The resulting change in the data-to-MC efficiency ratio defines the reconstruction uncertainty. Additional contributions arise from background estimation in the probe sample and from energy-scale and resolution effects that can shift the invariant-mass window used in the fit. Identification efficiency uncertainty is determined by repeating the tag-and-probe analysis with modified identification criteria and alternative background-subtraction and signal-extraction models. These variations test the likelihood-based discriminant used to separate electrons from the background. Possible dependencies on pile-up, charge, and event topology are also examined. Estimation of the systematic uncertainty in the electron isolation efficiency follows a similar procedure, using alternative background-subtraction methods, different invariant-mass fit models, and modifications of the underlying-event subtraction applied in the isolation calculation. The latter tests the stability of the isolation efficiency with respect to the correction for soft energy deposits from pile-up and underlying-event activity. Systematic uncertainties in the overall data-to-simulation correction factors are obtained by repeating the measurement under these alternative configurations of tag and probe selections, background treatments, fitting procedures, etc. The average value is taken as the nominal result, and the systematic uncertainty is assigned as the spread of the SFs obtained from the variations.

Electron calibration. The electron energy calibration in ATLAS is derived using a combination of simulation-based corrections and in-situ data-driven adjustments, following the procedure established in Ref. [227]. Initial energy reconstruction employs a multivariate regression algorithm that optimizes the calorimeter response using shower-shape and cluster-position information. The absolute energy scale is then determined from well-known resonant decays, primarily $Z \to ee$, by aligning the reconstructed invariant-mass peak between data and simulation. Additional cross-checks using $J/\psi \to ee$ and radiative Z-boson decays validate the calibration across different energy ranges and detector regions. Systematic uncertainties associated with the calibration originate from several sources. The dominant contributions arise from the material description in front of the calorimeter, the modeling of pile-up noise, and the determination of the energy scale and resolution corrections. The impact of the mismodeling of passive material is evaluated by varying the material distribution in the simulation within its measured uncertainty. Uncertainty due to pile-up is assessed by modifying the pile-up reweighting factors and the noise parametrization used in the energy reconstruction. Differences between the independent methods used to extract the calibration constants—template fits and Gaussian-sum fits—are taken as an additional systematic component. Energy-scale uncertainties are also assigned from variations of the pile-up rescaling factors, amounting to about 4×10^{-4} in the barrel and up to 2×10^{-3} in the endcap.

Muon efficiency. The determination of muon reconstruction and isolation efficiencies follows a methodology analogous to that used for electrons, relying on tag-and-probe techniques applied to samples of $Z \to \mu\mu$ and $J/\psi \to \mu\mu$ decays. The measurement procedure for Run 3 closely follows the approach established in Run 2 [230], with adjustments reflecting the updated muon reconstruction and trigger algorithms. Efficiency SFs are derived as a function of the muon transverse momentum and pseudorapidity to correct for residual data–simulation differences. Compared to electrons, additional variations test the dependence on pile-up conditions and detector-alignment configurations.

Muon calibration. The muon momentum calibration aligns the simulated transverse momenta of combined muons with those measured in data by applying detector-dependent scale and resolution corrections derived separately for the ID and the MS [231]. The calibration parameters are obtained from template fits to the invariant-mass distributions of $J/\psi \to \mu\mu$ and $Z \to \mu\mu$ decays, performed in dedicated (η, ϕ) detector regions to account for local variations in magnetic field, alignment, and material distribution. Additional constraints on the MS resolution are derived from special alignment runs with the magnetic field turned off. The dominant systematic uncertainties arise from the choice of the invariant-mass window, background parameterization in the J/ψ region, possible nonlinearities between the J/ψ- and Z-based scale corrections, and from the imperfect knowledge of the MS alignment.

Muon TTVA. *Track-To-Vertex Association* (TTVA) efficiency quantifies the probability of correctly associating a reconstructed muon to the primary vertex. It is measured using $Z \to \mu\mu$ events [230], where the tag muon ensures event purity and the probe tests the TTVA requirement. Corresponding uncertainty is derived by varying the association criteria and pile-up modeling in simulation, and it accounts for potential mismodeling of the vertex-association efficiency in dense event environments. Although typically small, this uncertainty is propagated independently in analyses involving prompt-muon selections.

Jet energy scale and resolution. Following reconstruction of the jets described in Section 4.3.1, jet energies are calibrated to correct the detector response and achieve a uniform energy scale across the calorimeter acceptance. Measured jet energies are corrected to the particle level through a multi-step calibration procedure [247]. Initial simulation-based calibration accounts for detector response, non-compensation effects, and out-of-cluster energy losses. Subsequent in-situ calibrations refine the *jet energy scale* (JES) using well-balanced events such as γ+jet, Z+jet, and multijet systems, where the reference object provides an accurate momentum scale. Systematic uncertainties in the JES originate from the modeling of the calorimeter response, pile-up corrections, flavor composition of the jet sample, and the in-situ calibration techniques themselves. Each source is evaluated by repeating the calibration under varied assumptions or alternative MC generators. *Jet energy resolution* (JER) is measured in data using dijet balance methods, which use the transverse momentum asymmetry of back-to-back jet pairs to estimate the detector response resolution. The difference between the JER obtained in data and simulation defines the JER uncertainty, which is propagated as a smearing correction to simulated jets. Further uncertainty, obtained from simulation comparisons between Run 2 and Run 3, accounts for changes in detector conditions [248]. A conservative 10% uncertainty per jet is included to cover possible mismodeling of the NNJvt efficiency in simulation.

Multijet and pile-up. Uncertainties in the missing transverse momentum reconstruction arise from the modeling of the track-based soft term in the $E_{\mathrm{T}}^{\mathrm{miss}}$ calculation (from Eq.(4.5)), evaluated by comparing data and simulation in events without genuine missing energy and by varying the soft-term scale and resolution components parallel and perpendicular to the hard-object direction [239]. Systematic uncertainties in the multijet background estimation are obtained from the data-driven normalization procedure (explained in Section 4.3.1), by varying the control-region definitions, fitting methods, and isolation templates used in the extraction. The uncertainty due to pile-up reweighting is evaluated by varying the average number of interactions per BC in the simulation by $\pm 3\%$, corresponding to the uncertainty in the inelastic cross-section measurement.

Table 4.7 summarizes all experimental systematic uncertainties discussed in this section.

4.4.2 Modelling uncertainties

Theoretical and modeling uncertainties influence the prediction and measurement of the W-boson production cross-section through several aspects of the event simulation chain. They originate from the description of the hard-scattering process, the choice of parton distribution functions, higher-order

Table 4.7: Summary of the relative experimental systematic uncertainties in percent.

$\delta\sigma/\sigma$	$W^- \to e^-\bar{\nu}$	$W^+ \to e^+\nu$	$W^- \to \mu^-\bar{\nu}$	$W^+ \to \mu^+\nu$
Luminosity	2.2	2.2	2.2	2.2
Electron trigger efficiency	1.2	1.2	–	–
Electron reconstruction efficiency	0.3	0.3	–	–
Electron identification efficiency	0.2	0.2	–	–
Electron isolation efficiency	0.6	0.6	–	–
Electron calibration	0.1	0.1	–	–
Muon trigger efficiency	–	–	1.1	1.1
Muon identification efficiency	–	–	0.2	0.2
Muon isolation efficiency	–	–	1.0	1.0
Muon TTVA efficiency	–	–	< 0.1	< 0.1
Muon calibration	–	–	0.2	0.2
Jet energy scale	1.7	1.6	1.6	1.6
Jet energy resolution	0.4	0.4	0.4	0.5
$E_{\mathrm{T}}^{\mathrm{miss}}$ soft term scale	< 0.1	< 0.1	< 0.1	< 0.1
$E_{\mathrm{T}}^{\mathrm{miss}}$ soft term resolution	0.2	0.2	0.2	0.3
Electroweak+top background	0.2	0.2	0.2	0.1
Multijet background	2.9	2.4	1.3	1.1
JVT	1.6	1.5	1.4	1.3
Pile-up modeling	1.1	1.2	0.4	0.4

QCD and electroweak corrections, and from the modeling of the parton shower, hadronization, and underlying event. These effects enter the analysis through two key quantities that link the observed signal yields to the fiducial and total phase-space cross-sections: the acceptance (A) and the correction factor (C) (briefly introduced in Section 4.1). Both are defined as:

$$A = \frac{N_{\text{fid}}}{N_{\text{total}}}, \qquad C = \frac{N_{\text{reco}}}{N_{\text{fid}}}, \tag{4.11}$$

where N_{fid}, N_{total}, and N_{reco} denote the numbers of events in the fiducial region, total phase space, and reconstructed level, respectively. The acceptance quantifies the fraction of generated signal events that satisfy the fiducial selection at particle level, while the correction factor accounts for detector effects and reconstruction efficiencies within that region. The determination of A and C is based on fully simulated signal samples whose event yields are normalized to the generator cross-section and integrated luminosity of the sample. In addition, simulation-to-data efficiency SFs are applied to reproduce the measured trigger, reconstruction, identification, and isolation efficiencies observed in data. While A reflects the extrapolation from the fiducial to the full phase space and depends primarily on theoretical and PDF modeling, C captures the detector response and reconstruction performance and is more sensitive to parton-shower and hadronization effects. Both quantities are treated as independent sources of uncertainty in the extraction of the final cross-sections. The fiducial phase space for the $W \to \ell\nu$ process is designed to match the experimental event selection applied at the reconstruction level, thereby minimizing dependence on theoretical extrapolations. These thresholds ensure high trigger efficiency and avoid regions of low p_{T} where theoretical predictions become less reliable. Main sources of theoretical and modeling uncertainties affecting A and C include variations of the PDFs and the associated strong coupling α_s, renormalization and factorization scale variations to account for missing higher-order QCD effects, EW corrections such as photon radiation and weak-loop contributions, and uncertainties related to the modeling of parton showers and hadronization. Additional uncertainties arise from the description of background processes, including top-quark and diboson production. Among these, the acceptance is most sensitive to PDF and QCD-scale variations, typically at the few-percent level, whereas the correction factor is affected at the sub-percent level. Together, these components define the overall theoretical uncertainty propagated to the measured fiducial and total W-boson cross-sections.

Parton distribution functions. Predictions of W-boson production depend on the PDFs used to describe the proton structure. Several NNLO sets are commonly employed, including PDF4LHC21 [249], CT18 [85], MSHT20 [250], NNPDF4.0 [251], ABMP16 [252], and ATLASpdf21[253]. PDF uncertainty is evaluated following the prescriptions of the respective sets: Hessian variations are used for PDF4LHC21, CT18, MSHT20, ABMP16, and ATLASpdf21, while a Monte Carlo replica method is used for NNPDF4.0. The typical PDF uncertainty in the acceptance is at the level of a few percent, while its effect on the correction factor is subdominant, below the percent level. To account for possible differences between global PDF fits, an additional envelope uncertainty from the choice of PDF set is included, considering differences between NNPDF3.0NNLO [201] and PDF4LHC21.

QCD scale and missing higher-order effects. Uncertainties due to missing higher orders are evaluated by varying the renormalization (μ_R) and factorization (μ_F) scales by factors of 0.5 and 2 using the standard 7-point prescription[3]. Variations are performed independently for the matrix-element ME and parton-shower PS components, and the largest deviation from the nominal prediction is assigned as the QCD scale uncertainty. The resulting effect on the C factor is small ($\lesssim 0.5\%$), while the acceptance A is typically affected at the level of $\sim$ 2–3%.

Electroweak corrections. Higher-order EW effects mainly arise from QED final-state radiation (FSR) off the leptons, which is modeled using `Photos` [207] and treated consistently in the unfolding procedure. The remaining NLO EW corrections include initial-state photon radiation, weak-loop contributions, and interference between initial- and final-state photons. Their combined effect on the W-boson fiducial cross-section is approximately -0.4%, consistent with previous LHC EW working group studies [254–258]. Higher-order (two-loop) EW terms are negligible, below 0.1%.

Strong coupling constant. The uncertainty related to the value of the strong coupling constant $\alpha_s(m_Z^2)$ is assessed using the PDF4LHC21 sets with $\alpha_s = 0.1180 \pm 0.0010$. The corresponding effect on the fiducial cross-section is evaluated as [249]:

$$\delta^{\alpha_s}\sigma = \frac{\sigma(\alpha_s = 0.119) - \sigma(\alpha_s = 0.117)}{2}\,, \tag{4.12}$$

which yields a sub-percent impact on both A and C.

Background modeling. The contribution of background processes is small but non-negligible. Following Refs. [248, 259], conservative uncertainties of 5% are assigned to W and Z background processes, and 10% to diboson (VV) production. For top-quark backgrounds, modeling uncertainties are taken as 5.1% for $t\bar{t}$ and 3.5% for single-top production. These variations are propagated through the analysis to the final measured cross-sections.

4.4.3 Isolation efficiency modeling

The `Tight_VarRad` isolation WP defined in Section 4.3.1 is used throughout this study to select isolated electrons and muons. This WP ensures high signal purity by rejecting leptons originating

---

[3] (μ_R, μ_F) pairs variations $(\mu_R/2, \mu_F/2), (2\mu_R, 2\mu_F), (\mu_R, 2\mu_F), (2\mu_R, \mu_F), (\mu_R, \mu_F/2), (\mu_R/2, \mu_F)$

from hadronic jets or photon conversions while maintaining high efficiency for prompt leptons from W-boson decays. A dedicated study of the isolation variables defining the `Tight_VarRad` WP revealed that the level of agreement between data and simulation depends noticeably on the choice of Monte Carlo generator. In particular, larger data-to-MC discrepancies are observed when using the Sherpa generator compared to the Powheg+Pythia8 (PP8) reference, as illustrated in Figure 4.9. The figure shows examples of the data-to-MC ratios of the `topoetcone20` isolation variable in events with one or two tightly identified electrons (`TightLH` used for electrons, while `Medium` ID quality for muons). The Sherpa prediction clearly deviates more from the data than the PP8.

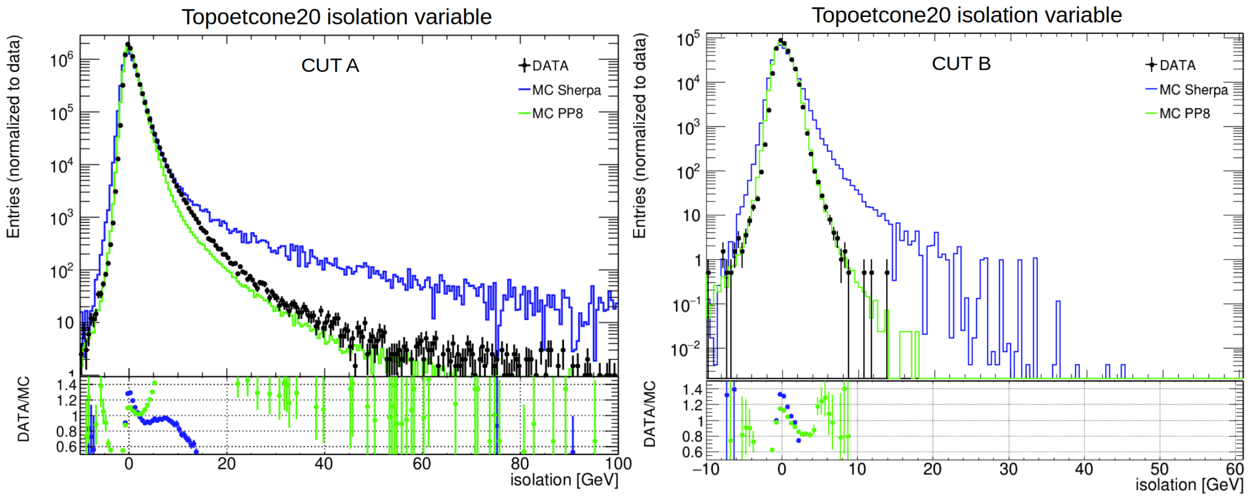

Figure 4.9: Comparison of the data-to-MC ratios of the `topoetcone20` isolation variable for two different MC generators. (Left) Events with at least one electron satisfying the *Tight* identification criteria. (Right) Events with exactly two *Tight* electrons passing the *Tight* isolation requirement, selected around the Z-boson mass window $76 < m_{ee} < 106$ GeV.

Since the isolation SFs used in the thesis are derived from the Powheg+Pythia8 sample, the corresponding systematic uncertainties do not cover the observed discrepancies when switching to Sherpa. Therefore, additional generator-dependent correction factors—referred to as *MC-to-MC SFs*—are introduced to correct the isolation efficiencies in the Sherpa simulation. MC-to-MC SFs are determined by comparing the isolation efficiencies obtained from the two MC generators. The isolation efficiency is defined as:

$$\mathrm{Eff} = \frac{N_{\mathrm{evt}}^{\mathrm{pass}}}{N_{\mathrm{evt}}^{\mathrm{total}}}, \tag{4.13}$$

where $N_{\mathrm{evt}}^{\mathrm{pass}}$ and $N_{\mathrm{evt}}^{\mathrm{total}}$ are the numbers of events passing the *Tight_VarRad* isolation selection and the total number of events considered, respectively. All standard corrections and data-to-MC SFs are applied consistently in both samples, except for the isolation SF itself, which is omitted from the denominator of Eq. (4.13) to avoid double-counting. The fractional difference between the efficiencies predicted by PP8 and Sherpa is used to compute the MC-to-MC SF. Isolation efficiencies and the resulting MC-to-MC SFs are evaluated separately for electrons and muons using $Z \to \ell\ell$ and $Z \to \mu\mu$ events. The efficiencies are parameterized as a function of the lepton transverse momentum, p_{T}, since no significant dependence on pseudorapidity (η) was observed. Figure 4.10 presents the isolation efficiencies for both generators (top panels) and the derived MC-to-MC SFs (bottom panels). For both lepton flavours, the Sherpa isolation efficiency is systematically lower than that of PP8, leading to MC-to-MC SFs slightly below unity at low p_{T}, converging to unity at higher p_{T}.

These additional scale factors ensure consistent isolation efficiency across different MC generators, thereby improving the accuracy of simulated signal and background samples. The corresponding un-

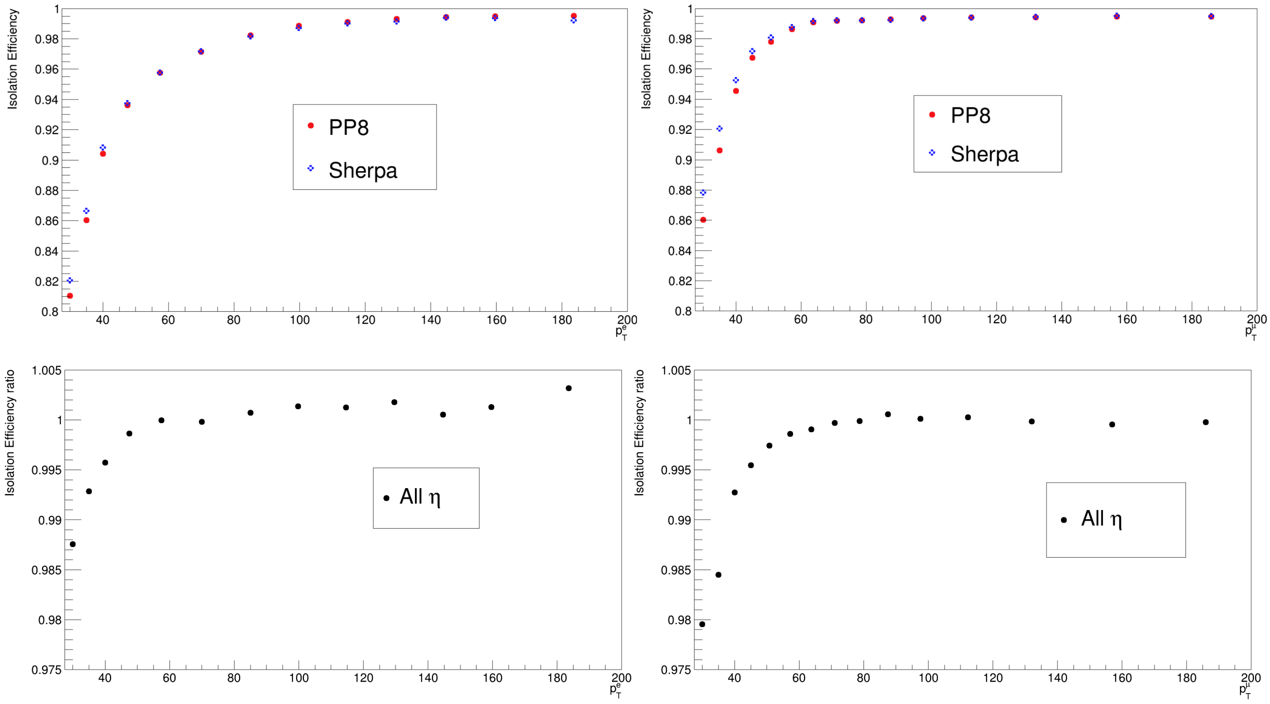

Figure 4.10: Isolation efficiencies for electrons (left) and muons (right) from $Z \to \ell\ell$ events for two MC generators (top) and the derived MC-to-MC scale factors (bottom) integrated in pseudorapidity η.

certainties are propagated through the final analysis as part of the overall lepton efficiency systematic uncertainty.

4.4.4 Control plots

Distributions of the key kinematic variables — lepton pseudorapidity (η_ℓ), transverse momentum (p_{T}^{ℓ}), missing transverse momentum ($p_{\mathrm{T}}^{\mathrm{miss}}$), and W-boson transverse mass (m_{T}^{W})— for all four $W \to \ell\nu$ decay channels are shown in Figures 4.11–4.14. Overall, good agreement is observed between the data and predictions within the total systematic uncertainties, as indicated by the hashed uncertainty bands. Multijet background shape is obtained from a template fit from the control region as described in Section 4.3.3. The flat data-to-prediction ratio in lepton η_ℓ distributions demonstrates good modeling (after applying SF as described in Section 4.4.1) of lepton reconstruction, identification, and trigger efficiencies. A slight excess at high lepton p_{T} is visible (a bit higher in the electron channel), reflecting observed theoretical miss-modeling of the boson p_{T}, which has only a marginal effect on the determination of the inclusive and fiducial cross-section. The same behaviour can be observed in $E_{\mathrm{T}}^{\mathrm{miss}}$ and transvere mass m_{T}^{W} distributions.

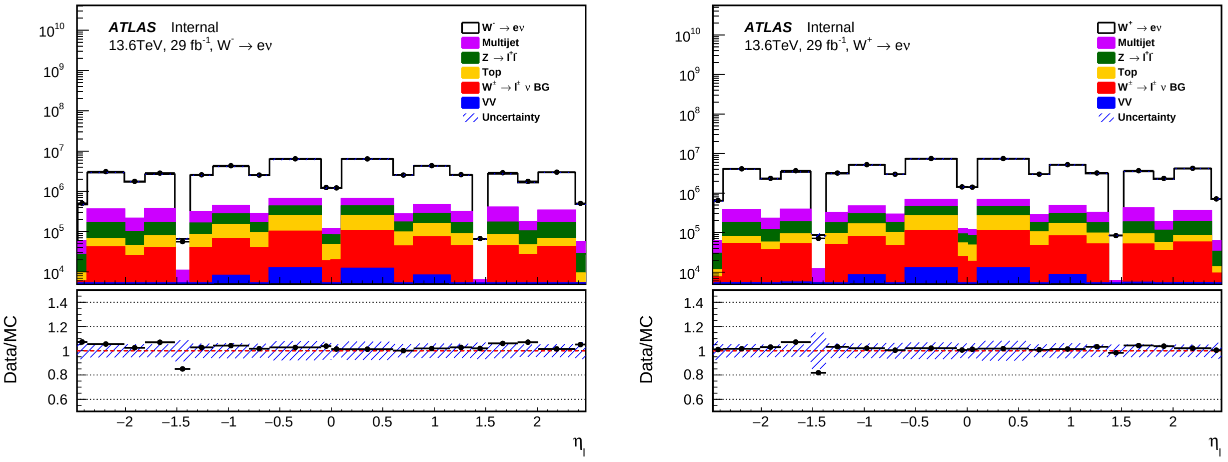

(a) $W^- \to e^- \bar{\nu}$

(b) $W^+ \to e^+ \nu$

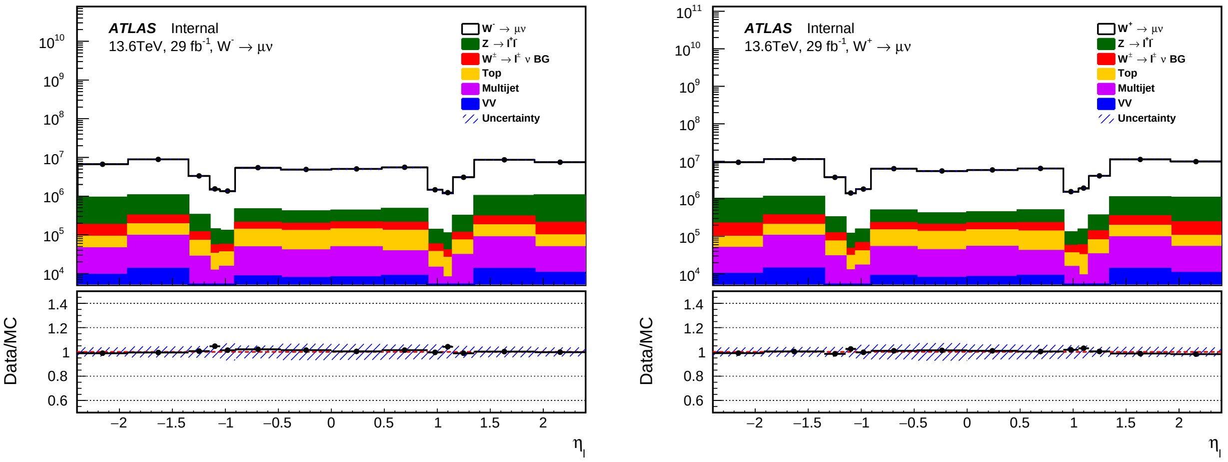

(c) $W^- \to \mu^- \bar{\nu}$

(d) $W^+ \to \mu^+ \nu$

Figure 4.11: Distributions of the lepton pseudorapidity η_ℓ for the four $W \to \ell\nu$ channels: (a) $W^- \to e^- \bar{\nu}$, (b) $W^+ \to e^+ \nu$, (c) $W^- \to \mu^- \bar{\nu}$, and (d) $W^+ \to \mu^+ \nu$. The data are compared to the predictions with bands indicating the total systematic uncertainty.

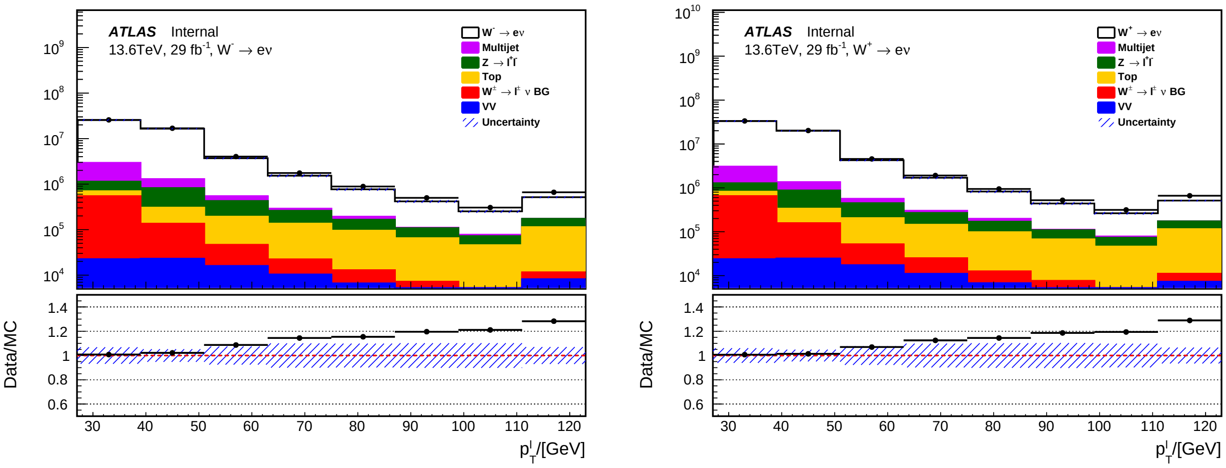

(a) $W^{-} \to e^{-}\bar{\nu}$ (b) $W^{+} \to e^{+}\nu$

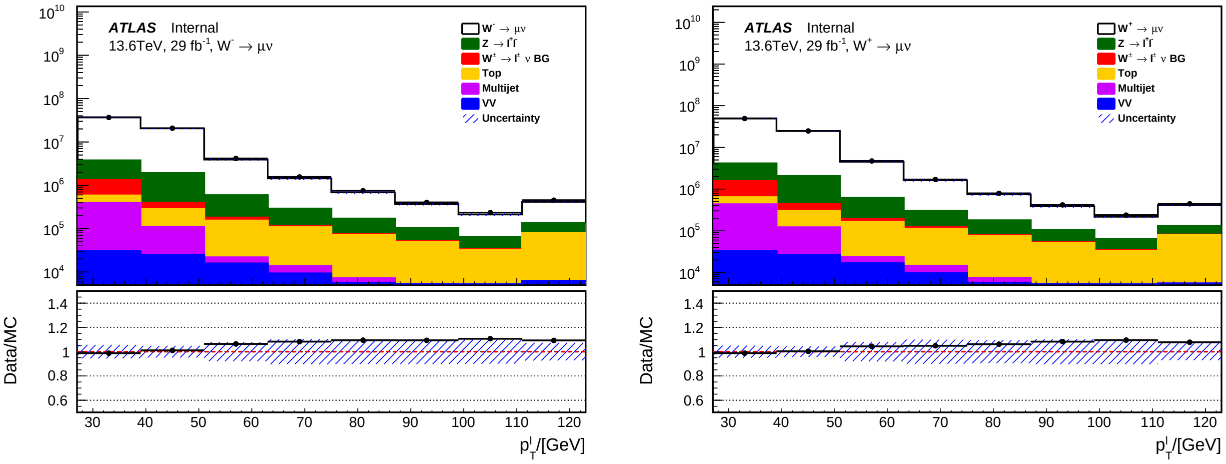

(c) $W^{-} \to \mu^{-}\bar{\nu}$ (d) $W^{+} \to \mu^{+}\nu$

Figure 4.12: Distributions of the lepton transverse momentum p_{T}^{ℓ} for the four $W \to \ell\nu$ channels: (a) $W^{-} \to e^{-}\bar{\nu}$, (b) $W^{+} \to e^{+}\nu$, (c) $W^{-} \to \mu^{-}\bar{\nu}$, and (d) $W^{+} \to \mu^{+}\nu$. The last bin includes overflow events. The data are compared to the predictions with bands indicating the total systematic uncertainty.

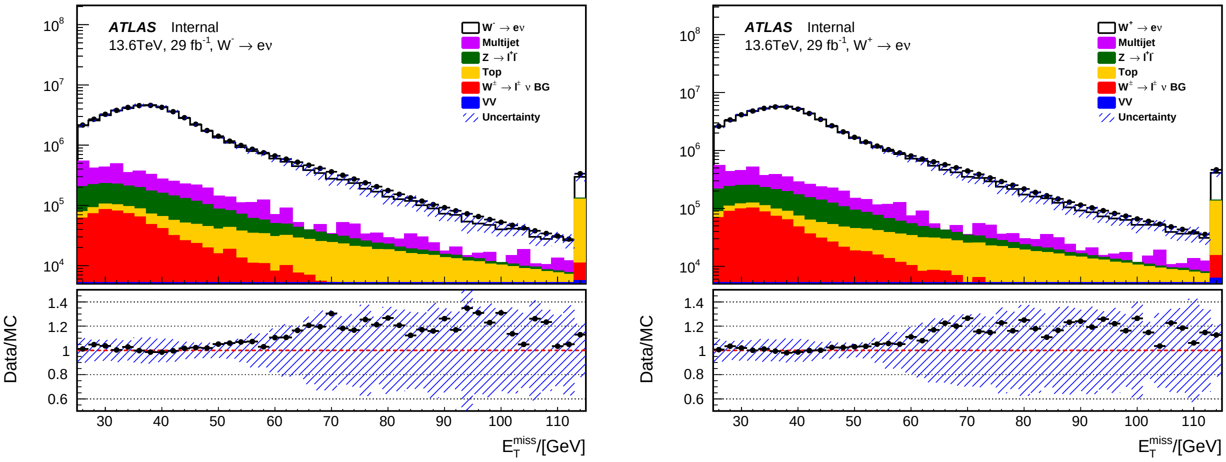

(a) $W^- \to e^- \bar{\nu}$

(b) $W^+ \to e^+ \nu$

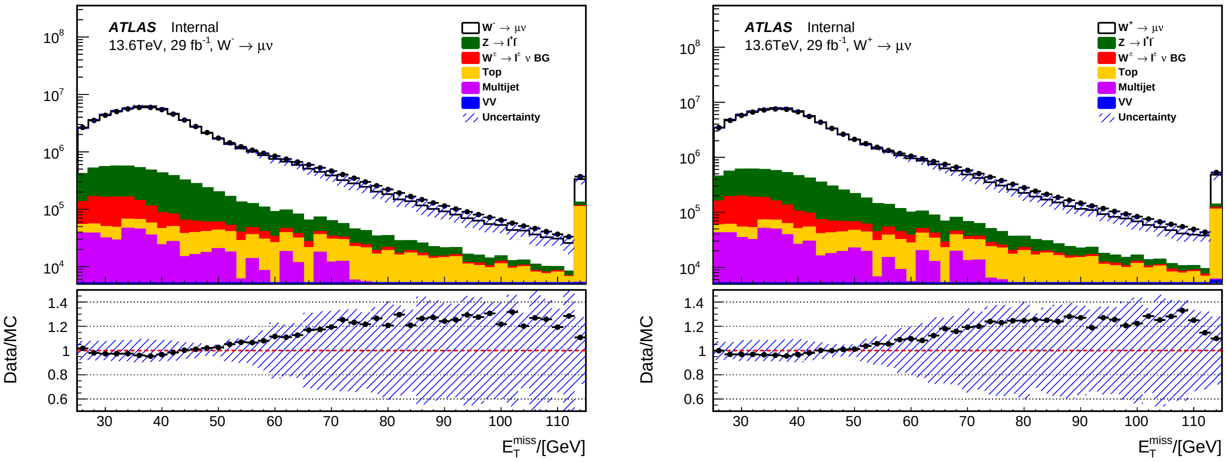

(c) $W^- \to \mu^- \bar{\nu}$

(d) $W^+ \to \mu^+ \nu$

Figure 4.13: Distributions of the missing transverse momentum $p_{\mathrm{T}}^{\mathrm{miss}}$ for the four $W \to \ell\nu$ channels: (a) $W^- \to e^- \bar{\nu}$, (b) $W^+ \to e^+ \nu$, (c) $W^- \to \mu^- \bar{\nu}$, and (d) $W^+ \to \mu^+ \nu$. The last bin includes overflow events. The data are compared to the predictions with bands indicating the total systematic uncertainty.

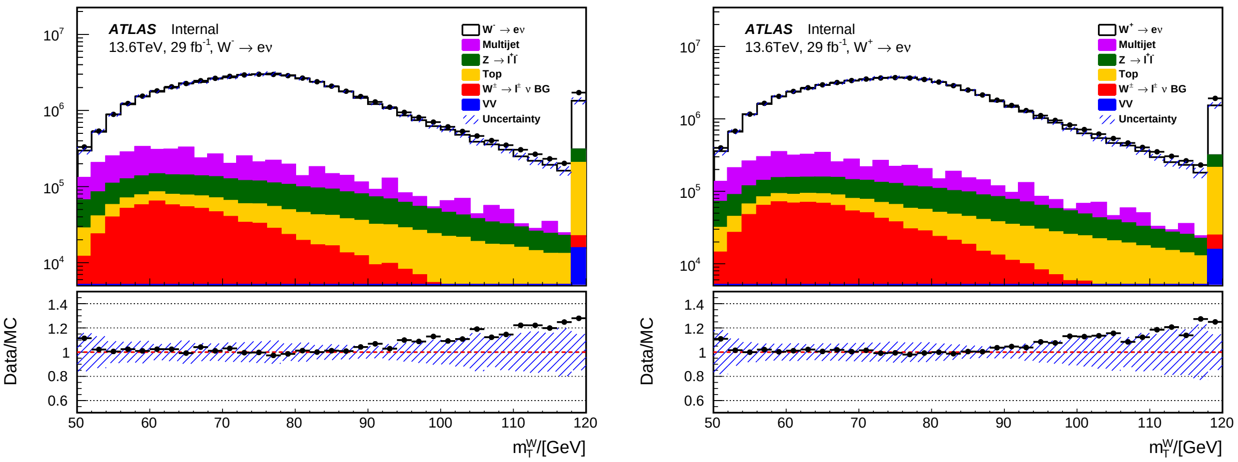

(a) $W^- \to e^-\bar{\nu}$ (b) $W^+ \to e^+\nu$

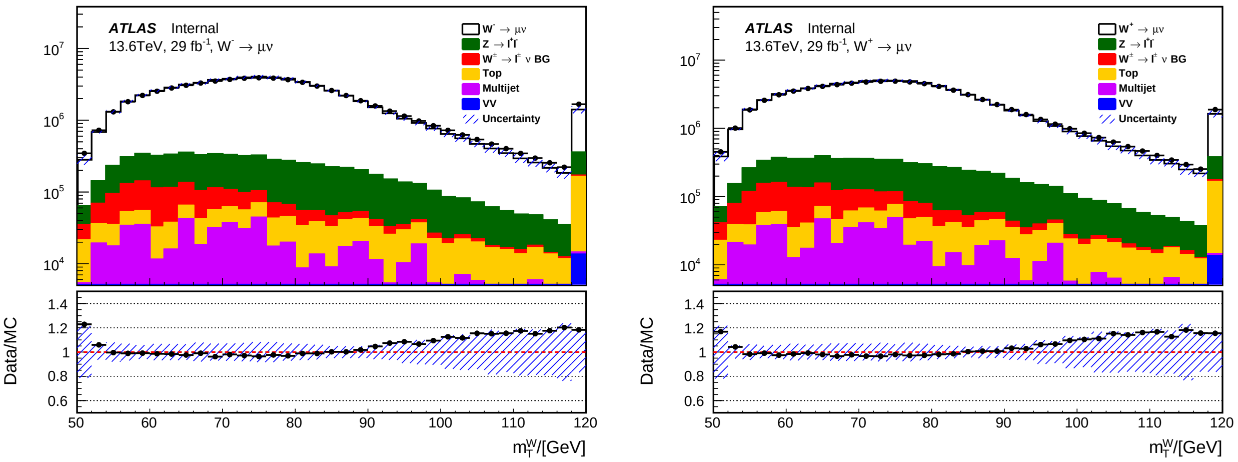

(c) $W^- \to \mu^-\bar{\nu}$ (d) $W^+ \to \mu^+\nu$

Figure 4.14: Distributions of the transverse mass m_{T}^{W} for the four $W \to \ell\nu$ channels: (a) $W^- \to e^-\bar{\nu}$, (b) $W^+ \to e^+\nu$, (c) $W^- \to \mu^-\bar{\nu}$, and (d) $W^+ \to \mu^+\nu$. The last bin includes overflow events. The data are compared to the predictions with bands indicating the total systematic uncertainty.

4.5 Results and conclusions of Chapter 4

4.5.1 Cross-section measurement from event counting

The total and fiducial cross-sections are initially evaluated using the event-counting approach, a conventional method that directly relates the number of background-subtracted signal events to the integrated luminosity through the acceptance and correction factors discussed in Section 4.1. The results will later be compared with those obtained using the *profile-likelihood* (PLH) method [260], which represents a more modern approach taken as the baseline in this thesis. Results are summarized in Table 4.8. Acceptances and C factors are obtained from fully simulated SHERPA samples. The uncertainties on the acceptance arise from PDFs, α_S variations, QCD scale variations, and parton shower variations; hence, purely theoretical. Assuming these sources are uncorrelated, overall acceptance uncertainty is $\sim 2.4\%$. The uncertainties on the cross-sections arise, apart from the acceptance, from different sources described in the previous section. The overall uncertainty is obtained by taking the quadrature sum of different sources of uncertainty. Overall uncertainty is lower in the muon channel than in the electron channel due to a lower level of multijet background (hence a lower impact of the MJ background uncertainty propagated to the final measurement) and lower lepton identification uncertainty. Statistical uncertainties are marginal in all channels, as expected.

One can observe that the results between the electron and muon channels (of the same charge) are compatible within the given uncertainties (excluding the fully correlated luminosity uncertainty). This also holds for the fiducial cross-sections. The difference in acceptance between positively and negatively charged channels stems from differences in the W-boson rapidity distributions (which reflect differences in W-boson production in a pp collider). Differences in acceptance between the electron and muon channels due to FSR are marginal. Overall, the precision achieved with the simple correlation model for the total cross-section is 5.4% and 5.1% for W^+ and W^- in the electron channel, and 4.5% and 4.4% for W^+ and W^- in the muon channel. Fiducial cross-sections are measured with precision in the range 3.6%–4.9%.

Table 4.8: The measured cross-sections using the event counting approach.

	$\sigma \pm \delta\sigma_{\text{stat}} \pm \delta\sigma_{\text{syst}} \pm \delta\sigma_{\text{lumi}}$	
	$W^- \to e^-\bar{\nu}$	$W^+ \to e^+\nu$
C	0.4445	0.4385
σ^{fid} [pb]	$3379.4 \pm 0.6 \pm 140.7 \pm 86.5$	$4346.0 \pm 0.6 \pm 156.2 \pm 108.2$
Acceptance A	0.381 ± 0.009	0.366 ± 0.009
σ^{tot} [pb]	$8875.0 \pm 1.4 \pm 423.4 \pm 227.2$	$11874.7 \pm 1.7 \pm 523.9 \pm 295.7$
	$W^- \to \mu^-\bar{\nu}$	$W^+ \to \mu^+\nu$
C	0.5872	0.5933
σ^{fid} [pb]	$3306.3 \pm 0.5 \pm 92.6 \pm 84.0$	$4240.5 \pm 0.5 \pm 112.6 \pm 105.2$
Acceptance A	0.381 ± 0.009	0.365 ± 0.010
σ^{tot} [pb]	$8684.7 \pm 1.2 \pm 316.1 \pm 220.5$	$11614.2 \pm 1.4 \pm 434.1 \pm 288.1$

4.5.2 Cross-section measurement from PLH

The profile-likelihood method is employed to extract the inclusive and fiducial cross-section results for the W-boson production. In this approach, a complete statistical model is constructed to relate the observed event yields in data to the expected signal and background contributions. The likelihood function is defined as:

$$L(\vec{n};\mu_s,\vec{\theta}) = \prod_{c\in\text{channels}} \text{Pois}(n_{\text{data}}\,|\,\mu_s S_c + B_c(\vec{\theta})) \prod_{i\in\text{NPs}} G(\theta_i)\,, \tag{4.14}$$

where the product runs over all analysis channels c and *nuisance parameters* (NP). Here, μ_s denotes the *signal strength*, which represents the *parameter of interest* (POI). It scales the expected signal yield and is directly proportional to the measured cross-section, $\sigma_{\text{meas}} = \mu_s \times \sigma^{\text{exp}}_{\text{MC}}$, with $\sigma^{\text{exp}}_{\text{MC}}$ being the nominal theoretical prediction from the simulated signal sample. The terms S_c and $B_c(\vec{\theta})$ correspond to the expected number of signal and background events in each channel c, respectively. The background normalizations are treated as free parameters that can vary within their prior uncertainties. These priors are obtained from auxiliary measurements or from theoretical predictions of the corresponding cross-sections, thereby constraining the degree to which the fit can adjust each background yield. The vector $\vec{\theta}$ represents the set of NPs that account for systematic effects, such as detector calibration, modeling uncertainties, and background normalizations. Each nuisance parameter is constrained by a Gaussian term $G(\theta_i)$ centered on its nominal value, with a width corresponding to its prior uncertainty. The overall likelihood, therefore, consists of a product of Poisson probabilities (for event yields in each bin and channel) and Gaussian constraint terms for the nuisance parameters. The PLH model is implemented using the `TRExFitter` framework, which internally relies on `HistFactory` [261] for the construction of the statistical model. The maximization of the likelihood and the estimation of confidence intervals are performed with `xRooFit` [262, 263]. Theoretical uncertainties affecting the W signal are incorporated through dedicated normalization factors applied to the signal templates. These factors are derived by comparing the correction factors C defined in Eq. (4.1) for the nominal and systematically varied MC samples, and taking their relative differences.

The same PLH framework is used to extract the ratio of the fiducial cross-sections, R_{W^+/W^-}. The likelihood in Eq. (4.14) is reformulated by expressing the W^+ signal strength in terms of the ratio R_{W^+/W^-} as follows:

$$\begin{aligned} L(\vec{n};\mu_s,\vec{\theta}) = &\prod_{c\in W^+\text{ channels}} \text{Pois}(n_{\text{data}}\,|\,R_{W^+/W^-}\,\mu_{W^-} S_c + B_c(\vec{\theta})) \\ &\times \prod_{c\in W^-\text{ channels}} \text{Pois}(n_{\text{data}}\,|\,\mu_{W^-} S_c + B_c(\vec{\theta})) \prod_{i\in\text{NPs}} G(\theta_i)\,, \end{aligned}$$

where $R_{W^+/W^-} = \mu_{W^+}/\mu_{W^-}$ is the fitted POI.

Simultaneous profile-likelihood fits are performed across the four single lepton regions, $W^+ \to e^+\nu$, $W^+ \to \mu^+\nu$, $W^- \to e^-\bar{\nu}$, $W^- \to \mu^-\bar{\nu}$. The fitted signal strengths are:

$$\begin{aligned} \mu_{W^-\to e\nu} &= 1.000^{+0.052}_{-0.049}\,, & \mu_{W^-\to\mu\nu} &= 0.976^{+0.039}_{-0.037}\,, \\ \mu_{W^+\to e\nu} &= 1.000^{+0.047}_{-0.044}\,, & \mu_{W^+\to\mu\nu} &= 0.976^{+0.037}_{-0.036}\,. \end{aligned}$$

A good agreement with unity is observed for both the electron and muon channels. The uncertainty for the electron channel is in the range 4.4%–5.2%, and 3.6%–3.9% for the muon channel. This represents an improvement of about $\sim 0.5\%$ with respect to the results obtained with the event counting method presented in the previous section. To assess agreement between the fitted value of a parameter and its expected or prior value in the PLH method, a pull plot is constructed. It represents a set of "pulls" calculated for each NP, where a pull is defined as the difference between the post-fit (estimated) value and the pre-fit (prior) value, divided by the uncertainty. Analyzing the pulls for NPs helps check whether the estimated uncertainties are reasonable and to understand constraints (to determine how much the cross-section measurement constrains the NPs relative to their original, auxiliary constraints). Figure 4.15(a) shows the nuisance-parameter pulls, and as can be observed, no significant pulls can be observed (all values are within 2 standard deviations). Another way of visualizing the contribution of the different uncertainty components to the total uncertainty can be obtained from ranking plots, as in Figure 4.16. The central value shows the pull, and the black line shows the constraint of the NP in the fit. The blue colour bands correspond to the upper axis; they show the contribution of the uncertainty to the total uncertainty of the measured observable. The empty boxes show the pre-fit contribution, while the filled boxes show the post-fit contribution. The ordering of the NPs in the ranking plot is based on the post-fit impact each NP has on the POI. If the NPs have an asymmetrical impact, the larger of the variations is taken in the ordering. Thus, the most contributing uncertainty is shown on top, and the least contributing one on the bottom. As one can observe, luminosity is the dominant uncertainty in the cross-section measurement, followed by multijet-related uncertainties (for the electron) or jet reconstruction-related uncertainties (for the muon channel). No significant pulls or constraints are observed. The post-fit NP correlations, which are obtained in the process of the likelihood minimization, are shown in Figure 4.17.

Separate combined fits for each charge, $W^+ \to \ell\nu$ and $W^- \to \ell\nu$ are also performed. In these fits, the uncertainties related to lepton reconstruction and trigger efficiencies, as well as to the energy scale and resolution calibrations, are treated as uncorrelated between the electron and muon channels. The multijet background uncertainty is likewise considered uncorrelated. Conversely, experimental uncertainties associated with jets, missing transverse momentum ($E_{\mathrm{T}}^{\mathrm{miss}}$), pile-up, and integrated luminosity are assumed to be fully correlated between channels. For background processes, the modeling uncertainties of the electroweak and top-quark contributions are treated as uncorrelated, whereas the signal-modeling uncertainties are taken to be fully correlated when combining the electron and muon channels. The resulting combined fit yields:

$$\mu_{W^-\to\ell\nu} = 0.978^{+0.037}_{-0.037}\,, \qquad \mu_{W^+\to\ell\nu} = 0.978^{+0.035}_{-0.036}\,.$$

The corresponding NP pulls are shown in Figure 4.15(b).

A single fit sharing one signal-strength parameter across all four channels, $W^\pm \to \ell\nu$, gives:

$$\mu_{W^\pm\to\ell\nu} = 0.978^{+0.035}_{-0.035}\,.$$

The NP pulls are shown in Figure 4.15(c). The combined acceptance, estimated as a weighted average of two charges, is $A = 0.372 \pm 0.009$.

The fiducial ratio, $\sigma_{W^+}/\sigma_{W^-}$, is obtained from a combined fit to the four $\ell^\pm\nu$ regions. As most of the uncertainties cancel out in the ratio, the multijet background uncertainties become the dominant sources for the W boson cross-section ratios, since the multijet uncertainties for W^+ and W^- in each lepton channel are regarded as independent sources. The result yields:

$$\mu_{W^+}/\mu_{W^-} = 1.001^{+0.016}_{-0.018}\,.$$

The signal strength parameter, μ_s, obtained from the fit, represents the ratio of the measured to the predicted yields. By scaling the theoretical prediction for the fiducial region with this parameter, $\sigma_{\mathrm{fid}}^{\mathrm{MC}}$, the fiducial cross-section σ_{fid} is determined. The uncertainty on μ_s is propagated to the uncertainty on σ_{fid} accordingly. To obtain the total cross-section, σ_{tot}, the fiducial value is extrapolated to the full phase-space using the acceptance A, which accounts for the fraction of generated events passing the fiducial selection, as described in this chapter. One can observe that the values of μ_s are compatible with unity, indicating that the fits prefer the predicted cross-sections. Table 4.9 summarizes all measured cross-section results together with their total uncertainties. One can observe that the results for the total and fiducial cross-sections in four measurement channels match those obtained with the event-counting method presented in Table 4.8. Statistical uncertainties between the two methods are also compatible. The results also show full compatibility between the electron and muon channels, as well as between the two charge states. This agreement holds for both the total and fiducial cross-sections.

Individual $W \to \ell\nu$ channels

Combined W^+ and W^- fits

Inclusive $W^\pm$ fit

Figure 4.15: Nuisance-parameter pulls from (a) the four individual $W \to \ell\nu$ fits, (b) the combined W^+/W^- fits, and (c) the inclusive $W^\pm$ fit. Points indicate post-fit NP values with uncertainties.

4.5.3 Compatibility and PDF comparison

The compatibility between the electron and muon decay channels of the W^- and W^+ measurements is evaluated by comparing the combined and individual results, as shown on the left side of Fig-

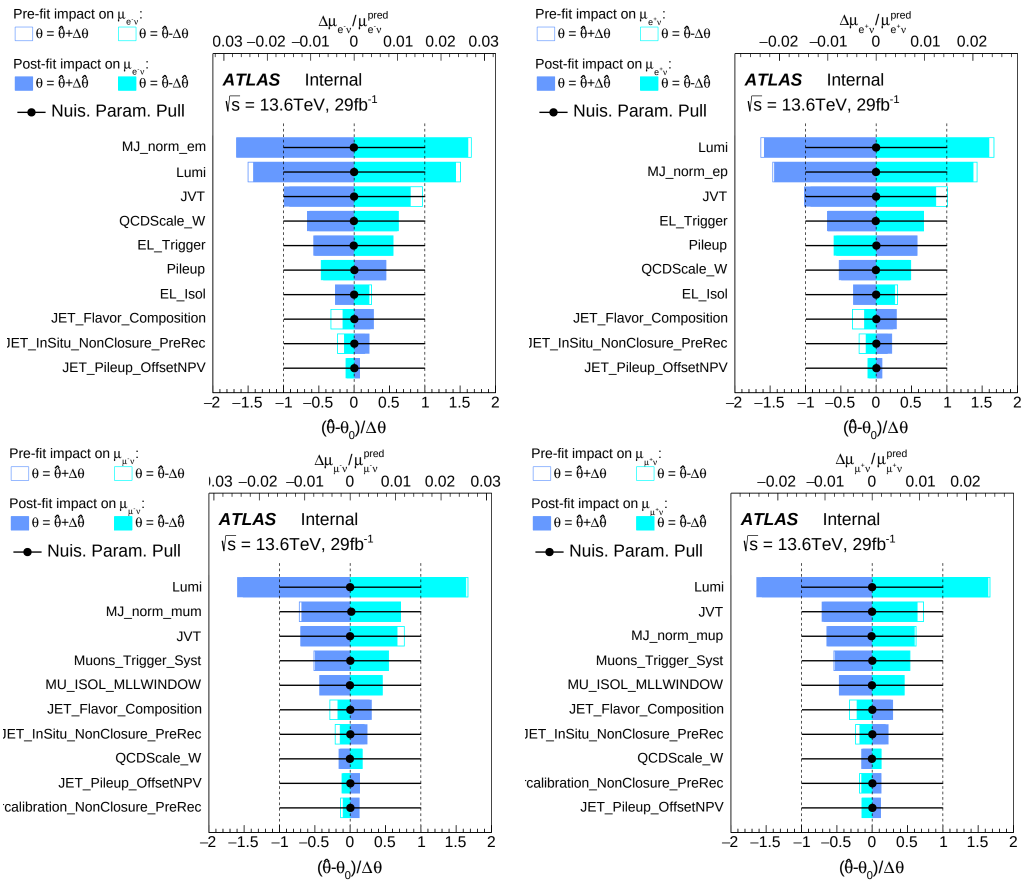

Figure 4.16: Systematic uncertainties ranked by their impact on μ for $W^- \to e^-\bar{\nu}$ (top left), $W^+ \to e^+\nu$ (top right), $W^- \to \mu^-\bar{\nu}$ (bottom left), and $W^+ \to \mu^+\nu$ (bottom right). Bars show pre-fit and post-fit impacts.

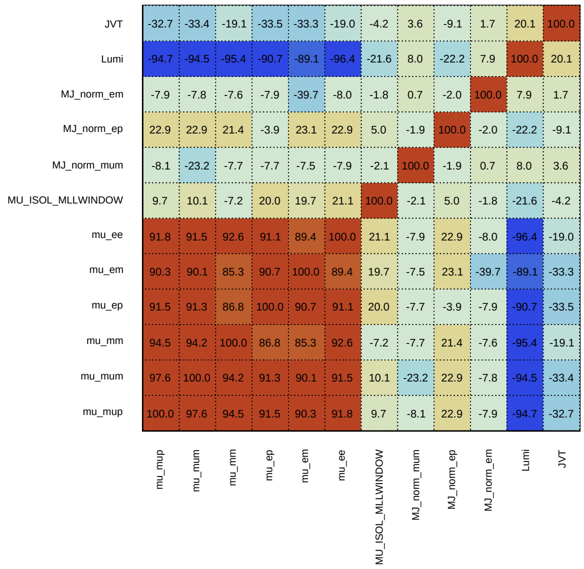

	mu_mup	mu_mum	mu_mm	mu_ep	mu_em	mu_ee	MU_ISOL_MLLWINDOW	MJ_norm_mum	MJ_norm_ep	MJ_norm_em	Lumi	JVT
JVT	-32.7	-33.4	-19.1	-33.5	-33.3	-19.0	-4.2	3.6	-9.1	1.7	20.1	100.0
Lumi	-94.7	-94.5	-95.4	-90.7	-89.1	-96.4	-21.6	8.0	-22.2	7.9	100.0	20.1
MJ_norm_em	-7.9	-7.8	-7.6	-7.9	-39.7	-8.0	-1.8	0.7	-2.0	100.0	7.9	1.7
MJ_norm_ep	22.9	22.9	21.4	-3.9	23.1	22.9	5.0	-1.9	100.0	-2.0	-22.2	-9.1
MJ_norm_mum	-8.1	-23.2	-7.7	-7.7	-7.5	-7.9	-2.1	100.0	-1.9	0.7	8.0	3.6
MU_ISOL_MLLWINDOW	9.7	10.1	-7.2	20.0	19.7	21.1	100.0	-2.1	5.0	-1.8	-21.6	-4.2
mu_ee	91.8	91.5	92.6	91.1	89.4	100.0	21.1	-7.9	22.9	-8.0	-96.4	-19.0
mu_em	90.3	90.1	85.3	90.7	100.0	89.4	19.7	-7.5	23.1	-39.7	-89.1	-33.3
mu_ep	91.5	91.3	86.8	100.0	90.7	91.1	20.0	-7.7	-3.9	-7.9	-90.7	-33.5
mu_mm	94.5	94.2	100.0	86.8	85.3	92.6	-7.2	-7.7	21.4	-7.6	-95.4	-19.1
mu_mum	97.6	100.0	94.2	91.3	90.1	91.5	10.1	-23.2	22.9	-7.8	-94.5	-33.4
mu_mup	100.0	97.6	94.5	91.5	90.3	91.8	9.7	-8.1	22.9	-7.9	-94.7	-32.7

Figure 4.17: Correlation matrix of nuisance parameters for the four individual $W \to \ell\nu$ fits. Positive correlations are shown in shades of red, and negative/anti-correlations are shown in blue. Only NPs with at least one correlation > 20% are displayed.

Table 4.9: The measured cross-sections using the profile-likelihood method. The quoted errors correspond to statistical, total experimental, and luminosity uncertainties.

	Channels	
	$W^- \to e^-\bar{\nu}$	$W^+ \to e^+\nu$
$\sigma^{\text{fid}} \pm \delta\sigma_{\text{stat}} \pm \delta\sigma_{\text{syst}} \pm \delta\sigma_{\text{lumi}}$ [pb]	$3380.5 \pm 0.6^{+149.2+90.5}_{-141.6-85.2}$	$4346.7 \pm 0.6^{+170.2+112.2}_{-161.4-106.5}$
$\sigma^{\text{tot}} \pm \delta\sigma_{\text{stat}} \pm \delta\sigma_{\text{syst}} \pm \delta\sigma_{\text{lumi}}$ [pb]	$8878.1 \pm 1.4^{+443.1+237.6}_{-425.5-223.8}$	$11876.6 \pm 1.7^{+555.5+306.6}_{-535.7-290.9}$
	$W^- \to \mu^-\bar{\nu}$	$W^+ \to \mu^+\nu$
$\sigma^{\text{fid}} \pm \delta\sigma_{\text{stat}} \pm \delta\sigma_{\text{syst}} \pm \delta\sigma_{\text{lumi}}$ [pb]	$3305.5 \pm 0.5^{+98.2+87.0}_{-93.4-81.8}$	$4240.9 \pm 0.5^{+119.1+107.8}_{-115.9-103.0}$
$\sigma^{\text{tot}} \pm \delta\sigma_{\text{stat}} \pm \delta\sigma_{\text{syst}} \pm \delta\sigma_{\text{lumi}}$ [pb]	$8682.6 \pm 1.2^{+330.5+228.5}_{-320.8-214.9}$	$11615.1 \pm 1.4^{+452.0+295.3}_{-445.8-282.1}$
	$W^- \to \ell^-\bar{\nu}$	$W^+ \to \ell^+\nu$
$\sigma^{\text{fid}} \pm \delta\sigma_{\text{stat}} \pm \delta\sigma_{\text{syst}} \pm \delta\sigma_{\text{lumi}}$ [pb]	$3307.8 \pm 0.4^{+92.4+83.9}_{-91.2-84.9}$	$4249.3 \pm 0.4^{+112.4+104.8}_{-111.8-106.4}$
$\sigma^{\text{tot}} \pm \delta\sigma_{\text{stat}} \pm \delta\sigma_{\text{syst}} \pm \delta\sigma_{\text{lumi}}$ [pb]	$8687.8 \pm 0.9^{+318.5+220.3}_{-316.1-222.9}$	$11624.3 \pm 1.1^{+435.3+286.7}_{-434.2-291.1}$
	$W^\pm \to \ell^\pm\nu$	
$\sigma^{\text{fid}} \pm \delta\sigma_{\text{stat}} \pm \delta\sigma_{\text{syst}} \pm \delta\sigma_{\text{lumi}}$ [pb]	$7557.0 \pm 0.5^{+194.5+188.3}_{-193.1-189.7}$	
$\sigma^{\text{tot}} \pm \delta\sigma_{\text{stat}} \pm \delta\sigma_{\text{syst}} \pm \delta\sigma_{\text{lumi}}$ [pb]	$20312.0 \pm 1.4^{+732.9+506.2}_{-730.3-510.0}$	
	W^+/W^-	
R$\pm\delta$R	$1.286^{+0.021}_{-0.023}$	

ure 4.18, where the combined results are obtained from simultaneous $e - \mu$ fits. The figure presents the measured ratios of the fiducial cross-sections to their respective theoretical predictions. Electron and muon decay channel results are shown with their respective lepton-flavour-specific uncertainties. The combined point is displayed with two uncertainty bars: the inner bar reflects the uncorrelated contribution (comprising the statistical uncertainty and those systematic components that are specific to a single lepton flavour), while the outer bar shows the total uncertainty, which additionally includes the systematics that are correlated between the electron and muon channels. A good overall agreement is observed: the electron and muon measurements are statistically compatible within their uncertainties. This confirms that the reconstruction, identification, and calibration procedures for electrons and muons are well understood and that any residual differences between the two channels are within the expected statistical and systematic limits. The right panel of Figure 4.18 compares the measured fiducial cross-sections with theoretical predictions obtained using different PDF sets. The ratios illustrate the level of agreement between the data and each prediction, allowing a direct assessment of which PDF set provides the best overall description of the measurement. The two uncertainty bands around the measured points represent the total uncertainty with and without the contribution from the luminosity uncertainty, respectively, highlighting the relative impact of the luminosity precision on the overall measurement accuracy. A complete set of predicted fiducial and total cross-sections for all considered PDF sets in this thesis is provided in Appendix.

The measured total cross-section is shown as a function of $\sqrt{s}$, together with the predictions based on CT14NNLO in Figure 4.19. Good agreement is observed between the data and the prediction. The largest source of theoretical uncertainties is the PDF uncertainties. Figure 4.20 presents the measured and predicted W^+/W^- cross-section ratios, compared with theoretical predictions obtained using different PDF sets. The measured ratio shows good overall consistency with all predictions, indicating that the data are well described within the current PDF uncertainties. The shaded band represents the total systematic uncertainty of the measurement. Uncertainties related to the integrated luminosity are not included, as they are fully correlated among the individual fiducial cross-sections and thus cancel

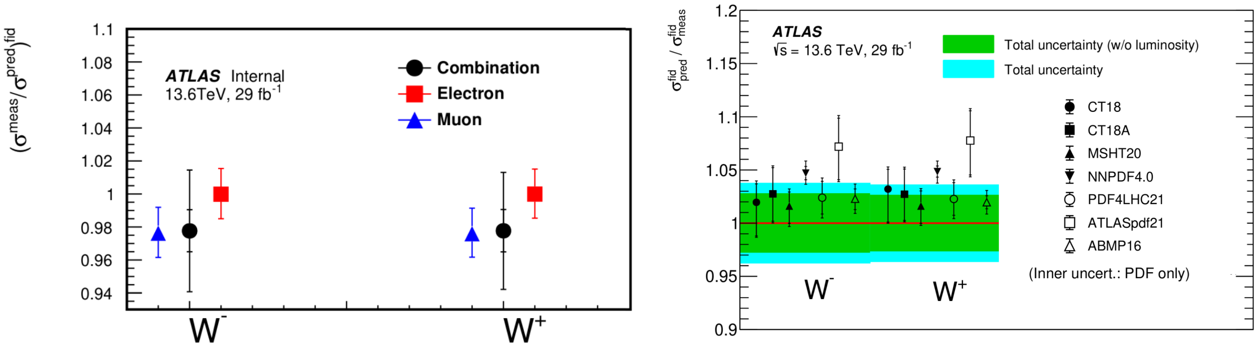

Figure 4.18: Left: Ratios of the measured fiducial cross-sections to the predicted values for electron, muon channels, and combination. The inner error bar of the combined channels is the uncorrelated systematic uncertainty, and the outer bar is the total uncertainty. Right: The ratio of the predictions obtained with different PDF sets and the measured fiducial cross-sections. The cyan-green shaded bands represent the difference in total uncertainty when the luminosity uncertainty is excluded from the calculation. The predictions are displayed with the inner (outer) error bars representing PDF (theory) uncertainty.

in the ratio.

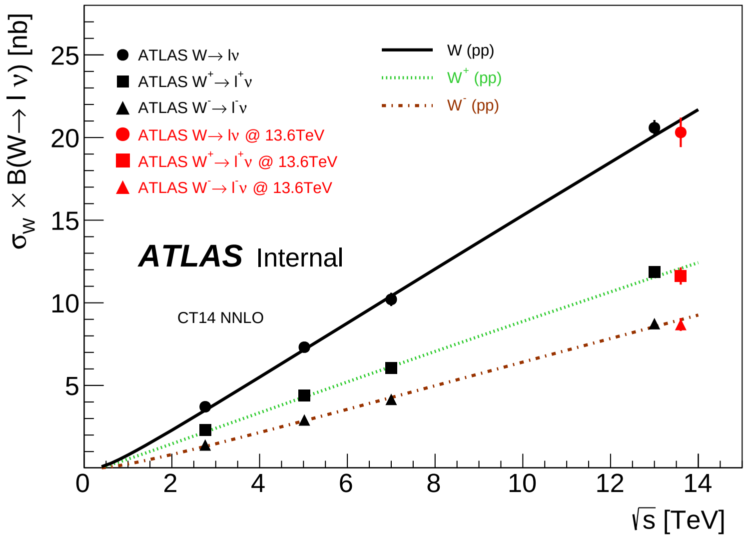

Figure 4.19: Comparison between CT14NNLO prediction and ATLAS measured cross-sections as a function of $\sqrt{s}$ for $W \rightarrow \ell\nu$, [264].

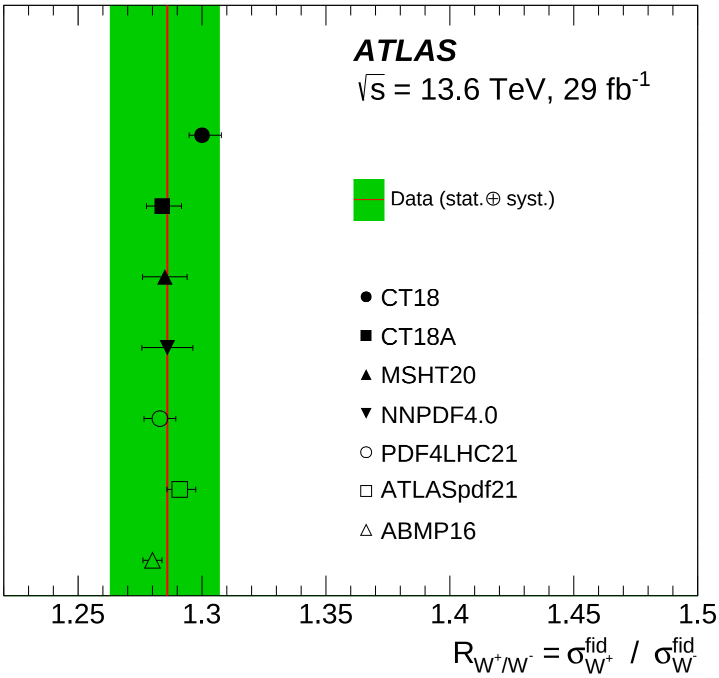

Figure 4.20: Summary of measured and predicted cross-section ratio W^+/W^-. The data is compared with theoretical predictions obtained from several modern PDF sets. The shaded band represents the total (systematic and statistical) data uncertainty. PDF results are displayed with their theory uncertainties.

Conclusion

In this thesis, studies covering two major components of the ATLAS physics programme are presented: the absolute calibration of the luminosity from the pp collisions at $\sqrt{s} = 900$ GeV and the measurement of W-boson production cross-sections using pp collision data at $\sqrt{s} = 13.6$ TeV.

The luminosity scale for the high-β^* collisions at $\sqrt{s} = 900$ GeV is determined using data collected during van der Meer scans in several fills conducted in October and November of 2018. The calibration procedure encounters several major challenges, including the selection of a robust fit model, the presence of significant ghost-charge and satellite contamination, and the evaluation of the non-factorization uncertainty. Noise sources of background and afterglow are subtracted, and the single-beam background is evaluated using the fills with comparable intensities in colliding and unpaired bunches. The absolute luminosity calibration is based mostly on the November scan session, while the October data is employed to determine the emittance growth correction and its associated uncertainty, which is propagated to the total uncertainty of the calibration. Reference specific luminosity variations and non-factorization effects are the dominant contributors to the total uncertainty across all scans. On average, the beam-beam corrections constitute the most significant single correction, though with a relatively small associated uncertainty. The total uncertainty of the calibration procedure yields 1.85%. Calibration constants (and corresponding integrated luminosities) are derived for several algorithms with sufficient statistics constructed for the LUCID detector. Consistency across luminosity algorithms is assessed using Inner Detector track counting data together with LUCID inclusive, coincidence, and hit-counting algorithms. The integrated luminosity values delivered by LHC for the 900 GeV 2018 dataset are evaluated for two configurations of β^* to be used for the elastic scattering study:

$$\mathcal{L}_{\text{int}} = 925.4 \pm 0.5_{\text{stat}} \pm 20.0_{\text{sys}}\ \mu\text{b}^{-1}, \quad (\beta^* = 50/100\ \text{m}), \tag{4.15}$$

$$\mathcal{L}_{\text{int}} = 501.0 \pm 0.4_{\text{stat}} \pm 10.6_{\text{sys}}\ \mu\text{b}^{-1}, \quad (\beta^* = 11\ \text{m}). \tag{4.16}$$

The resulting total systematic uncertainty on the integrated luminosity amounts to 2.1% and includes contributions from the calibration procedure, stability of detector response, and consistency cross-checks.

The measurement of the inclusive W-boson production cross-section is performed using pp collision data corresponding to 29 fb^{-1} collected by the ATLAS experiment at the centre-of-mass energy of $\sqrt{s} = 13.6$ TeV. The study is performed using $W \to \ell\nu$ decay channel, where ℓ corresponds to an electron or a muon. The cross-sections, as well as the corresponding charge ratio, are also measured in a fiducial region, defined by $p_{\text{T}}^{\ell} > 27$ GeV, $|\eta_\ell| < 2.5$, $p_{\text{T}}^{\text{miss}} > 25$ GeV, and $m_{\text{T}}^{W} > 50$ GeV. Signal acceptance and correction factors are estimated using the SHERPA 2.2.12 model. The background level for electroweak and top processes is estimated using simulation, while the multijet background is estimated using a data-driven technique. Experimental and modeling uncertainties are propagated to the measurement, with dominant uncertainties arising from luminosity and jet reconstruction (for the muon channel), and multijet level and luminosity (for the electron channel). Total and fiducial cross-sections for the four single-lepton channels: $W^+ \to e^+\nu$, $W^+ \to \mu^+\nu$, $W^- \to e^-\bar{\nu}$, and $W^- \to \mu^-\bar{\nu}$ are first determined using a classical event counting approach. The results are then compared to the results obtained using the Profile-likelihood method, and found to be in excellent agreement within statistical uncertainties, with an improvement in total uncertainty by about 0.5% in the PLH method. The PLH method is used as a baseline for the measurement, including combined $W \to \ell\nu$ cross-sections as well as the charge ratio. The measured fiducial cross-sections for $W^{\pm}$ and W^--boson production and corresponding ratio are:

$$\sigma_{\text{fid}}^{W^+} = 4250 \pm 150 \text{ pb}, \tag{4.17}$$

$$\sigma_{\text{fid}}^{W^-} = 3310 \pm 120 \text{ pb}, \tag{4.18}$$

$$R_{W^+/W^-} = 1.286 \pm 0.022. \tag{4.19}$$

The quoted uncertainty corresponds to the total uncertainty, including that arising from the luminosity for the fiducial cross-section, which amounts to about 2.2%. The dominant uncertainty for the charge ratio arises from uncorrelated multijet background level uncertainties. The measured W-boson cross-sections are in good agreement with the Standard Model predictions, based on Next-to-Next-to-Leading Order in α_s (plus NLO in α_{EW}) calculation. Predictions based on the most advanced PDFs are compared to the fiducial cross-sections as well as the charge ratio. All predictions are compatible with the measurements within the quoted uncertainties.

Appendix

The following Table A.10 summarizes the predicted fiducial and total production cross-sections for the W^+ and W^- bosons reported by different PDF sets [265, 266]. Each entry includes the corresponding statistical, scale, and PDF uncertainties, while the rightmost columns list the resulting W^+/W^- ratios in the fiducial phase space. Theoretical predictions are computed at NNLO+NNLL QCD and NLO EW accuracy using DYTURBO-1.3.1 [267–270] and RENESANCE-1.3.3 [271, 272]. The QCD and EW corrections are combined following an additive prescription, consistent with the procedure adopted in Ref. [182]. The associated theoretical uncertainties include variations of the renormalization and factorization scales (to estimate missing higher-order contributions), the strong coupling constant α_s, and the choice of PDFs.

Table A.10: Predicted cross-sections for different PDF sets. Two rows per set: the fiducial cross-sections σ_{fid} (in pb) and the total cross-sections σ_{tot} (in nb). The W^+/W^- ratio (rightmost column) is shown for σ_{fid} and carries PDF uncertainty only. Uncertainties on cross-sections are (statistical, scale, PDF).

PDF set	Phase space	$pp \to \ell^-\bar{\nu}_\ell$	$pp \to \ell^+\nu_\ell$	W^+/W^-
CT18	σ_{fid} [pb]	$3372.54^{+0.1\%+1.0\%+1.7\%}_{-0.1\%-0.9\%-3.1\%}$	$4385.38^{+0.1\%+0.9\%+1.8\%}_{-0.1\%-0.8\%-3.0\%}$	$1.300^{+0.6\%}_{-0.4\%}$
	σ_{tot} [nb]	$8.922^{+0.05\%+1.0\%+1.7\%}_{-0.05\%-0.9\%-3.1\%}$	$12.055^{+0.05\%+0.9\%+1.8\%}_{-0.05\%-0.8\%-3.0\%}$	
CT18A	σ_{fid} [pb]	$3398.85^{+0.1\%+0.9\%+2.4\%}_{-0.1\%-0.9\%-2.5\%}$	$4364.99^{+0.1\%+0.9\%+2.3\%}_{-0.1\%-0.8\%-2.4\%}$	$1.284^{+0.6\%}_{-0.5\%}$
	σ_{tot} [nb]	$8.962^{+0.05\%+0.9\%+2.4\%}_{-0.05\%-0.9\%-2.5\%}$	$12.087^{+0.05\%+0.9\%+2.3\%}_{-0.05\%-0.8\%-2.4\%}$	
MSHT20	σ_{fid} [pb]	$3360.94^{+0.1\%+0.9\%+1.3\%}_{-0.1\%-1.0\%-1.6\%}$	$4317.57^{+0.1\%+0.8\%+1.4\%}_{-0.1\%-0.8\%-1.6\%}$	$1.285^{+0.7\%}_{-0.7\%}$
	σ_{tot} [nb]	$8.866^{+0.05\%+0.9\%+1.3\%}_{-0.05\%-1.0\%-1.6\%}$	$11.948^{+0.05\%+0.8\%+1.4\%}_{-0.05\%-0.8\%-1.6\%}$	
NNPDF4.0	σ_{fid} [pb]	$3463.40^{+0.1\%+0.9\%+0.6\%}_{-0.1\%-0.8\%-0.6\%}$	$4455.24^{+0.1\%+0.8\%+0.5\%}_{-0.1\%-0.9\%-0.5\%}$	$1.286^{+0.8\%}_{-0.8\%}$
	σ_{tot} [nb]	$9.069^{+0.05\%+0.9\%+0.6\%}_{-0.05\%-0.8\%-0.6\%}$	$12.194^{+0.05\%+0.8\%+0.5\%}_{-0.05\%-0.9\%-0.5\%}$	
PDF4LHC21	σ_{fid} [pb]	$3387.04^{+0.1\%+1.0\%+1.5\%}_{-0.1\%-1.1\%-1.5\%}$	$4345.91^{+0.1\%+0.9\%+1.5\%}_{-0.1\%-1.0\%-1.5\%}$	$1.283^{+0.5\%}_{-0.5\%}$
	σ_{tot} [nb]	$8.911^{+0.05\%+1.0\%+1.5\%}_{-0.05\%-1.1\%-1.5\%}$	$12.012^{+0.05\%+0.9\%+1.5\%}_{-0.05\%-1.0\%-1.5\%}$	
ATLASpdf21	σ_{fid} [pb]	$3545.58^{+0.1\%+1.1\%+2.5\%}_{-0.1\%-1.0\%-2.9\%}$	$4579.11^{+0.1\%+1.0\%+2.6\%}_{-0.1\%-1.0\%-3.0\%}$	$1.291^{+0.5\%}_{-0.4\%}$
	σ_{tot} [nb]	$9.334^{+0.05\%+1.1\%+2.5\%}_{-0.05\%-1.0\%-2.9\%}$	$12.465^{+0.05\%+1.0\%+2.6\%}_{-0.05\%-1.0\%-3.0\%}$	
ABMP16	σ_{fid} [pb]	$3383.72^{+0.1\%+1.0\%+0.9\%}_{-0.1\%-0.9\%-1.0\%}$	$4332.77^{+0.1\%+0.9\%+0.6\%}_{-0.1\%-0.9\%-0.6\%}$	$1.280^{+0.3\%}_{-0.3\%}$
	σ_{tot} [nb]	$8.847^{+0.05\%+1.0\%+0.9\%}_{-0.05\%-0.9\%-1.0\%}$	$11.974^{+0.05\%+0.9\%+0.6\%}_{-0.05\%-0.9\%-0.6\%}$	

Bibliography

[1] H. Wiedemann, “Particle Accelerator Physics”, *Springer* 4th Ed. (2015) 1021 (cit. on pp. 3, 5).

[2] L. Evans and P. Bryant, “LHC Machine”, *JINST* 3 (2008) S08001 (cit. on pp. 3, 4, 28).

[3] D. Boussard et al., *The LHC superconducting cavities*, tech. rep., 1999, URL: `https://cds.cern.ch/record/386691` (cit. on p. 4).

[4] O. S. Brüning et al., “LHC Design Report”, *CERN Yellow Reports: Monographs* (2004) (cit. on pp. 4, 9, 51).

[5] S. Y. Lee, “Accelerator Physics”, *World Sscientific* (2019) (cit. on p. 4).

[6] J. Wenninger, *Operation and Configuration of the LHC in Run 2*, tech. rep., 2019, URL: `https://cds.cern.ch/record/2668326` (cit. on p. 4).

[7] H. T. H. Piaggio, “Mathematics of Non-Linear Vibrations”, *Nature* 168 (1951) 49 (cit. on p. 5).

[8] G. Floquet, “Sur les équations différentielles linéaires à coefficients périodiques”, *Annales scientifiques de l’École Normale Supérieure* 12 (1883) 47–88 (cit. on p. 5).

[9] ATLAS Collaboration, *ATLAS Data Summary — Fill 6024*, `https://atlas-datasummary.web.cern.ch/2017/fill.py?fill=6024` (cit. on p. 7).

[10] ATLAS Collaboration, *ATLAS Run-3 Luminosity Public Results*, `https://twiki.cern.ch/twiki/bin/view/AtlasPublic/LuminosityPublicResultsRun3` (cit. on p. 7).

[11] W. Herr and B. Muratori, *Concept of luminosity*, tech. rep., CERN, 2006, URL: `https://cds.cern.ch/record/941318` (cit. on p. 9).

[12] I. Efthymiopoulos et al., “Evolution of special LHC optics configurations Run 3 update”, *JACoW IPAC* 2024 (2024) MOPC16 (cit. on p. 10).

[13] ATLAS Collaboration, “The ATLAS Experiment at the CERN Large Hadron Collider”, *JINST* 3 (2008) S08003 (cit. on pp. 11, 30, 36).

[14] CMS Collaboration, “The CMS experiment at the CERN LHC”, *JINST* 3 (2008) S08004 (cit. on pp. 11, 30).

[15] LHCb Collaboration, “The LHCb Detector at the LHC”, *JINST* 3 (2008) S08005 (cit. on pp. 11, 30).

[16] S. Van der Meer, *Calibration of the effective beam height in the ISR*, tech. rep., CERN Internal Report, CERN, 1968, URL: `https://cds.cern.ch/record/296752` (cit. on pp. 11, 41).

[17] G. Aad et al., “Electroweak, QCD and flavour physics studies with ATLAS data from Run 2 of the LHC”, *Phys. Rept.* 1116 (2025) 57–126, ISSN: 0370-1573 (cit. on p. 11).

[18] ATLAS Collaboration, “Climbing to the Top of the ATLAS 13 TeV data”, *Phys. Rept.* 1116 (2025) 127–183, ISSN: 0370-1573 (cit. on p. 12).

[19] G. Aad et al., “Luminosity Determination in pp Collisions at $\sqrt{s} = 7$ TeV Using the ATLAS Detector at the LHC”, *Eur. Phys. J. C* 71 (2011) 1630 (cit. on p. 12).

[20] G. Aad et al., “Improved luminosity determination in pp collisions at sqrt(s) = 7 TeV using the ATLAS detector at the LHC”, *Eur. Phys. J. C* 73 (2013) 2518 (cit. on pp. 12, 41).

[21] M. Aaboud et al., “Luminosity determination in pp collisions at $\sqrt{s}$ = 8 TeV using the ATLAS detector at the LHC”, *Eur. Phys. J. C* 76 (2016) 653 (cit. on p. 12).

[22] G. Aad et al., “Luminosity determination in pp collisions at $\sqrt{s} = 13$ TeV using the ATLAS detector at the LHC”, *Eur. Phys. J. C* 83 (2023) 982 (cit. on pp. 12, 38, 56, 67, 68, 70).

[23] ATLAS Collaboration, *Luminosity determination for low-pileup datasets at $\sqrt{s} = 5$ and 13 TeV using the ATLAS detector at the LHC*, tech. rep., Geneva: CERN, 2020, URL: `https://cds.cern.ch/record/2725195` (cit. on p. 12).

[24] ATLAS collaboration, *Preliminary analysis of the luminosity calibration of the ATLAS 13.6 TeV data recorded in 2022*, tech. rep., Geneva: CERN, 2023, URL: `https://cds.cern.ch/record/2853525` (cit. on pp. 12, 81, 94).

[25] ATLAS collaboration, *Preliminary analysis of the luminosity calibration for the ATLAS 13.6 TeV data recorded in 2023*, tech. rep., Geneva: CERN, 2024, URL: `https://cds.cern.ch/record/2900949` (cit. on p. 12).

[26] ATLAS collaboration, *Preliminary analysis of the luminosity calibration for the ATLAS 13.6 TeV data recorded in 2024 and combination with 2022 and 2023*, tech. rep., Geneva: CERN, 2025, URL: `https://cds.cern.ch/record/2945956` (cit. on p. 12).

[27] M. E. Peskin and D. V. Schroeder, *An Introduction to Quantum Field Theory*, Addison-Wesley, 1995, ISBN: 978-0-201-50397-5 (cit. on pp. 13, 40).

[28] T.-P. Cheng and L.-F. Li, *Gauge Theory of Elementary Particle Physics*, Oxford University Press, 1984, ISBN: 978-0-19-851961-4 (cit. on p. 13).

[29] R. P. Feynman, “Space-Time Approach to Quantum Electrodynamics”, *Phys. Rev.* 76 (1949) 769–789 (cit. on p. 13).

[30] J. Schwinger, “On Quantum-Electrodynamics and the Magnetic Moment of the Electron”, *Phys. Rev.* 73 (1948) 416–417 (cit. on p. 13).

[31] S.-I. Tomonaga, “On a Relativistically Invariant Formulation of the Quantum Theory of Wave Fields”, *Prog. Theor. Phys.* 1 (1946) 27–42 (cit. on p. 13).

[32] S. L. Glashow, “Partial-Symmetries of Weak Interactions”, *Nucl. Phys.* 22 (1961) 579–588 (cit. on pp. 13, 16).

[33] S. Weinberg, “A Model of Leptons”, *Phys. Rev. Lett.* 19 (1967) 1264–1266 (cit. on pp. 13, 16).

[34] A. Salam and J. C. Ward, “Electromagnetic and weak interactions”, *Phys. Lett.* 13 (1964) 168 (cit. on pp. 13, 16, 17).

[35] D. J. Gross and F. Wilczek, “Ultraviolet Behavior of Non-Abelian Gauge Theories”, *Phys. Rev. Lett.* 30 (1973) 1343–1346 (cit. on p. 13).

[36] H. D. Politzer, “Reliable Perturbative Results for Strong Interactions?”, *Phys. Rev. Lett.* 30 (1973) 1346 (cit. on pp. 13, 16).

[37] H. Fritzsch, M. Gell-Mann, and H. Leutwyler, “Advantages of the Color Octet Gluon Picture”, *Phys. Lett. B* 47 (1973) 365–368 (cit. on p. 13).

[38] C. Jacobs, *Does Quantum Gravity Happen at the Planck Scale?*, 2025, URL: `https://arxiv.org/abs/2501.07614` (cit. on p. 13).

[39] NIST CODATA, *Planck mass energy equivalent in GeV*, `https://physics.nist.gov/cgi-bin/cuu/Value?plkmc2gev`, 2018 (cit. on p. 13).

[40] V. Faraoni, “Three new roads to the Planck scale”, *Am. J. Phys.* 85 (2017) 865–869, ISSN: 0002-9505 (cit. on p. 13).

[41] D. J. Griffiths, *Introduction to Elementary Particles*, 2nd rev. version, Wiley, 2008, URL: `https://cds.cern.ch/record/111880` (cit. on p. 13).

[42] D. H. Perkins, *Introduction to High-Energy Physics*, 4th, Cambridge University Press, 2000, URL: `https://cds.cern.ch/record/396126` (cit. on p. 13).

[43] F. Halzen and A. D. Martin, *Quarks and Leptons: An Introductory Course in Modern Particle Physics*, Wiley, 1984, URL: `https://cds.cern.ch/record/100339` (cit. on p. 13).

[44] A. Djouadi, “The Anatomy of electro-weak symmetry breaking. I: The Higgs boson in the standard model”, *Phys. Rept.* 457 (2008) 1–216 (cit. on p. 13).

[45] A. Djouadi, “The Anatomy of electro-weak symmetry breaking. II. The Higgs bosons in the minimal supersymmetric model”, *Phys. Rept.* 459 (2008) 1–241 (cit. on p. 13).

[46] S. Bilenky, *Neutrinos: Majorana or Dirac?*, 2020, URL: `https://arxiv.org/abs/2008.02110` (cit. on p. 13).

[47] A. B. Arbuzov, “Quantum Field Theory and the Electroweak Standard Model” (2017) 1–34, ed. by M. Mulders and G. Zanderighi (cit. on p. 14).

[48] E. Noether, “Invariant variation problems”, *Transport Theory and Statistical Physics* 1 (1971) 186–207, ISSN: 1532-2424 (cit. on p. 13).

[49] T. W. B. Kibble, “Symmetry breaking in non-Abelian gauge theories”, *Phys. Rev.* 155 (1967) 1554 (cit. on pp. 14, 17).

[50] S. Weinberg, *The Quantum Theory of Fields, Volume 1*, Cambridge University Press, 1995, ISBN: 9780521550017, URL: `https://books.google.rs/books?id=doeDB3_WLvwC` (cit. on p. 14).

[51] N. Cabibbo, “Unitary Symmetry and Leptonic Decays”, *Phys. Rev. Lett.* 10 (1963) 531 (cit. on p. 15).

[52] M. Kobayashi and T. Maskawa, “CP Violation in the Renormalizable Theory of Weak Interaction”, *Prog. Theor. Phys.* 49 (1973) 652 (cit. on p. 15).

[53] P. A. M. Dirac, “A Theory of Electrons and Protons”, *Proc. Roy. Soc. Lond. A* 126 (1930) 360 (cit. on p. 15).

[54] F. J. Dyson, “The Radiation Theories of Tomonaga, Schwinger, and Feynman”, *Phys. Rev.* 75 (1949) 486, URL: `http://link.aps.org/doi/10.1103/PhysRev.75.486` (cit. on p. 15).

[55] S. Navas and others (Particle Data Group), “Review of Particle Physics”, *Phys. Rev. D* 110 (2024) 030001, See the chapter "Quantum Chromodynamics", Fig. 9.5 for the running α_s summary (cit. on p. 15).

[56] C.-N. Yang and R. L. Mills, “Conservation of Isotopic Spin and Isotopic Gauge Invariance”, *Phys. Rev.* 96 (1954) 191 (cit. on p. 16).

[57] S. L. Glashow, J. Iliopoulos, and L. Maiani, “Weak Interactions with Lepton-Hadron Symmetry”, *Phys. Rev. D* 2 (1970) 1285 (cit. on p. 16).

[58] D. J. Gross and F. Wilczek, “Asymptotically Free Gauge Theories. 1”, *Phys. Rev. D* 8 (1973) 3633 (cit. on p. 16).

[59] H. D. Politzer, “Asymptotic Freedom: An Approach to Strong Interactions”, *Phys. Rept.* 14 (1974) 129 (cit. on p. 16).

[60] K. G. Wilson, “Confinement of Quarks”, *Phys. Rev. D* 10 (1974) 2445 (cit. on p. 16).

[61] P. W. Higgs, “Broken symmetries, massless particles and gauge fields”, *Phys. Lett.* 12 (1964) 132 (cit. on p. 17).

[62] F. Englert and R. Brout, “Broken Symmetry and the Mass of Gauge Vector Mesons”, *Phys. Rev. Lett.* 13 (1964) 321 (cit. on p. 17).

[63] P. W. Higgs, “Broken Symmetries and the Masses of Gauge Bosons”, *Phys. Rev. Lett.* 13 (1964) 508 (cit. on p. 17).

[64] G. ’t Hooft, “Renormalization of Massless Yang-Mills Fields”, *Nucl. Phys. B* 33 (1971) 173 (cit. on p. 17).

[65] G. ’t Hooft and M. J. G. Veltman, “Regularization and Renormalization of Gauge Fields”, *Nucl. Phys. B* 44 (1972) 189 (cit. on p. 17).

[66] G. Aad et al., “Observation of a new particle in the search for the Standard Model Higgs boson with the ATLAS detector at the LHC”, *Phys. Lett. B* 716 (2012) 1–29 (cit. on p. 18).

[67] S. Chatrchyan et al., “Observation of a New Boson at a Mass of 125 GeV with the CMS Experiment at the LHC”, *Phys. Lett. B* 716 (2012) 30–61 (cit. on p. 18).

[68] W. de Boer, “Precision Experiments at LEP”, *Advances Series on Directions in High Energy Physics* 23 (2015) 107–136 (cit. on p. 18).

[69] ALEPH and DELPHI and L3 and OPAL and LEP Electroweak Working Group, “Precision Electroweak Measurements on the Z Resonance”, *Phys. Rept.* 427 (2006) 257–454 (cit. on p. 18).

[70] H1 and ZEUS Collaborations, “Combination of Measurements of Inclusive Deep Inelastic $e^{\pm}p$ Scattering Cross Sections and QCD Analysis of HERA Data”, *Eur. Phys. J. C* 75 (2015) 580 (cit. on p. 18).

[71] C. Diaconu, “The Physics of deep-inelastic scattering at HERA”, *AIP Conf. Proc.* 972 (2008) 203–211, ed. by L. Trache and S. Stoica (cit. on p. 18).

[72] CDF and D0 Collaborations, “Combination of CDF and D0 Results on the Mass of the W Boson”, *Phys. Rev. D* 88 (2013) 052018 (cit. on p. 18).

[73] ATLAS and CMS Collaborations, “Review of the Physics Results from the LHC Run 2”, *Eur. Phys. J. C* 80 (2020) 123 (cit. on p. 18).

[74] J. Ellis, “Searching for Particle Physics Beyond the Standard Model at the LHC and Elsewhere”, *AIP Conf. Proc.* 1446 (2012) 9–28, ed. by J. Kouneiher et al. (cit. on p. 18).

[75] J. Wess and B. Zumino, “Supergauge Transformations in Four-Dimensions”, *Nucl. Phys. B* 70 (1974) 39 (cit. on p. 19).

[76] *Standard Model Summary Plots June 2024*, tech. rep., Geneva: CERN, 2024, URL: `https://cds.cern.ch/record/2903866` (cit. on p. 19).

[77] S. Drell and T. Yan, “Massive Lepton Pair Production in Hadron–Hadron Collisions at High Energies”, *Phys. Rev. Lett.* 25 (1970) 316–320 (cit. on p. 19).

[78] R. P. Feynman, "Very High-Energy Collisions of Hadrons", *Phys. Rev. Lett.* 23 (1969) 1415–1417 (cit. on p. 20).

[79] E. D. Bloom and F. J. Gilman, "Scaling, Duality, and the Behavior of Resonances in Inelastic Electron–Proton Scattering", *Phys. Rev. Lett.* 25 (1970) 1140–1144 (cit. on p. 20).

[80] M. H. Seymour and M. Marx, *Monte Carlo Event Generators*, 2013, URL: `https://arxiv.org/abs/1304.6677` (cit. on p. 21).

[81] V. N. Gribov et al., "Evolution Equations for Parton Densities in Quantum Chromodynamics", *Nucl. Phys. B* 126 (1977) 298–318 (cit. on p. 21).

[82] H1 and Z. Collaborations, *Combination and QCD Analysis of Charm Production Cross Section Measurements in Deep-Inelastic ep Scattering at HERA*, tech. rep., DESY, 2013, URL: `https://arxiv.org/abs/1310.8361` (cit. on p. 22).

[83] J. C. Collins, D. E. Soper, and G. F. Sterman, "Factorization for Short Distance Hadron–Hadron Scattering", *Nucl. Phys. B* 261 (1985) 104–142 (cit. on p. 22).

[84] J. C. Collins, D. E. Soper, and G. F. Sterman, "Factorization of Hard Processes in QCD", *Adv. Ser. Direct. High Energy Phys.* 5 (1989) 1–91 (cit. on p. 22).

[85] T.-J. Hou et al., "New CTEQ global analysis of quantum chromodynamics with high-precision data from the LHC", *Phys. Rev. D* 103 (2021) 014013 (cit. on pp. 23, 99).

[86] A. Martin et al., "Parton distributions and the LHC: W and Z production", *Eur. Phys. J. C* 14 (2000) 133–145, ISSN: 1434-6052 (cit. on pp. 23–25).

[87] S. Dittmaier, A. Huss, and C. Schwinn, "Dominant mixed QCD-electroweak O($\alpha_s\alpha$) corrections to Drell–Yan processes in the resonance region", *Nucl. Phys. B* 904 (2016) 216–252 (cit. on p. 23).

[88] S. Dittmaier and M. Krämer, "Electroweak radiative corrections to W boson production at hadron colliders", *Phys. Rev. D* 65 (2002) 073007 (cit. on p. 23).

[89] U. Baur and D. Wackeroth, "Electroweak radiative corrections to $p\bar{p} \to W^{\pm} \to \ell^{\pm}\nu$ beyond the pole approximation", *Phys. Rev. D* 70 (2004) 073015 (cit. on p. 23).

[90] G. Aad et al., "Measurement of the $W \to \tau\nu_\tau$ cross section in pp collisions at $\sqrt{s}$ =7 TeV with the ATLAS experiment", *Phys. Lett. B* 706 (2012) 276–294 (cit. on p. 25).

[91] G. Aad et al., "Test of the universality of τ and μ lepton couplings in W-boson decays with the ATLAS detector", *Nature Phys.* 17 (2021) 813–818 (cit. on p. 26).

[92] S. Navas et al., "Review of particle physics", *Phys. Rev. D* 110 (2024) 030001 (cit. on p. 26).

[93] M. Cacciari, G. P. Salam, and G. Soyez, "The anti-kt jet clustering algorithm", *JHEP* 2008 (2008) 063 (cit. on p. 28).

[94] CERN, *LHC Report: LHC reaches 2017 targets*, `https://home.cern/news/news/accelerators/lhc-report-lhc-reaches-2017-targets`, 2017 (cit. on p. 28).

[95] ATLAS Collaboration, *ATLAS takes a breath of oxygen*, `https://atlas.cern/Updates/News/First-Oxygen-Run`, July 2025 (cit. on p. 29).

[96] G. Aad et al., "Observation of a new particle in the search for the Standard Model Higgs boson with the ATLAS detector at the LHC", *Phys. Lett. B* 716 (2012) 1–29, ISSN: 0370-2693 (cit. on p. 29).

[97] ALICE Collaboration, "The ALICE experiment at the CERN LHC", *JINST* 3 (2008) S08002 (cit. on p. 30).

[98] TOTEM Collaboration, "The TOTEM experiment at the CERN Large Hadron Collider", *JINST* 3 (2008) S08007 (cit. on p. 30).

[99] LHCf Collaboration, "The LHCf detector at the CERN Large Hadron Collider", *JINST* 3 (2008) S08006 (cit. on p. 30).

[100] J. L. Pinfold, "The MoEDAL Experiment at the LHC – a New Light on the Terascale Frontier", *J. Phys. Conf. Ser.* 631 (2015) 012014 (cit. on p. 30).

[101] FASER Collaboration, "FASER: ForwArd Search ExpeRiment at the LHC", *Eur. Phys. J. C* 80 (2020) 61 (cit. on p. 30).

[102] The SND@LHC collaboration, "SND@LHC: the scattering and neutrino detector at the LHC", *JINST* 19 (2024) P05067 (cit. on p. 30).

[103] G. Aad et al., "The ATLAS experiment at the CERN Large Hadron Collider: a description of the detector configuration for Run 3", *JINST* 19 (2024) P05063, ISSN: 1748-0221 (cit. on p. 31).

[104] ATLAS Collaboration, "The ATLAS Inner Detector commissioning and calibration", *Eur. Phys. J. C* 70 (2010) 787–821, ISSN: 1434-6052 (cit. on p. 32).

[105] N. Wermes and G. Hallewel, *ATLAS pixel detector*, tech. rep., Geneva, 1998, URL: `https://cds.cern.ch/record/381263` (cit. on p. 32).

[106] A. Ahmad et al., "The Silicon microstrip sensors of the ATLAS semiconductor tracker", *Nucl. Instrum. Meth. A* 578 (2007) 98–118 (cit. on p. 32).

[107] T. Akesson et al., "Status of design and construction of the Transition Radiation Tracker (TRT) for the ATLAS experiment at the LHC", *Nucl. Instrum. Meth. A* 522 (2004) 131–145, ed. by C. Favuzzi et al. (cit. on p. 32).

[108] ATLAS Collaboration, *ATLAS calorimeter performance*, tech. rep., Geneva, 1996, URL: `https://cds.cern.ch/record/331059` (cit. on p. 33).

[109] ATLAS Collaboration, *ATLAS liquid-argon calorimeter*, tech. rep., Geneva, 1996, URL: `https://cds.cern.ch/record/331061` (cit. on p. 33).

[110] ATLAS Collaboration, *ATLAS tile calorimeter*, tech. rep., Geneva, 1996, URL: `https://cds.cern.ch/record/331062` (cit. on p. 33).

[111] ATLAS Collaboration, *ATLAS muon spectrometer*, tech. rep., Geneva, 1997, URL: `https://cds.cern.ch/record/331068` (cit. on p. 33).

[112] F. Bauer et al., "Construction and Test of MDT Chambers for the ATLAS Muon Spectrometer", *Nucl. Instrum. Meth. A* 461 (2001) 17–20, ed. by G. Batignani et al. (cit. on p. 33).

[113] T. Argyropoulos et al., "Cathode Strip Chambers in ATLAS: Installation, Commissioning and in Situ Performance", *IEEE Trans. Nucl. Sci.* 56 (2009) 1568–1574 (cit. on p. 33).

[114] ATLAS Collaboration, "ATLAS data quality operations and performance for 2015–2018 data-taking", *JINST* 15 (2020) P04003 (cit. on p. 34).

[115] ATLAS Collaboration, "The ATLAS Data Acquisition and High Level Trigger system", *JINST* 11 (2016) P06008 (cit. on p. 34).

[116] M. Wu, "FELIX: Readout upgrade for the ATLAS Trigger DAQ system in HL-LHC", *Nucl. Instrum. Meth. A* 1048 (2023) 167994, ISSN: 0168-9002 (cit. on p. 34).

[117] A. Borga et al., *The ATLAS Readout System for LHC Runs 2 and 3*, 2023, URL: `https://arxiv.org/abs/2307.11557` (cit. on p. 34).

[118] J. Andreeva, M. Litmaath, and P. Paparrigopoulos, "WLCG Operations: Evolution and Challenges on the Way to HL-LHC", *EPJ Web Conf.* 337 (2025) 01335 (cit. on p. 34).

[119] Nason, P., "A new method for combining NLO QCD with shower Monte Carlo algorithms", *JHEP* 11 (2004) 040 (cit. on pp. 34, 81).

[120] Frixione, S. and Nason, P. and Ridolfi, G., "A positive-weight next-to-leading-order Monte Carlo for heavy flavour hadroproduction", *JHEP* 09 (2007) 126 (cit. on pp. 34, 81).

[121] Alwall, J. et al., "The automated computation of tree-level and next-to-leading order differential cross sections, and their matching to parton shower simulations", *JHEP* 07 (2014) 079 (cit. on p. 34).

[122] Gleisberg, T. et al., "Event generation with SHERPA 1.1", *JHEP* 02 (2009) 007 (cit. on p. 34).

[123] Sjöstrand, T. et al., "An introduction to PYTHIA 8.2", *Comput. Phys. Commun.* 191 (2015) 159–177 (cit. on pp. 34, 81).

[124] Agostinelli, S. et al. (GEANT4 Collaboration), "GEANT4: A simulation toolkit", *Nucl. Instrum. Meth. A* 506 (2003) 250–303 (cit. on pp. 34, 82).

[125] G. Avoni et al., "The LUCID detector for luminosity monitoring at LHC", *JINST* 3 (2008) P06001 (cit. on p. 35).

[126] G. Avoni et al., "Performance of the LUCID detector at LHC", *Nucl. Instrum. Meth. A* 617 (2010) 327–330 (cit. on p. 35).

[127] G. Avoni et al., "The new LUCID-2 detector for luminosity measurement and monitoring in ATLAS", *JINST* 13 (2018) P07017 (cit. on p. 35).

[128] ATLAS Collaboration, *Upgrade of the ATLAS LUCID detector for Run 3*, tech. rep., CERN, 2022, URL: `https://cds.cern.ch/record/2800376` (cit. on p. 35).

[129] ATLAS Collaboration, *LUCID Run2*, `https://twiki.cern.ch/twiki/bin/viewauth/Atlas/LucidRun2`, 2025 (cit. on p. 35).

[130] V. Cindro et al., "The ATLAS Beam Conditions Monitor", *JINST* 3 (2008) P02004 (cit. on p. 36).

[131] ATLAS Collaboration, "Readiness of the ATLAS Tile Calorimeter for LHC collisions", *Eur. Phys. J. C* 70 (2010) 1193–1236 (cit. on p. 36).

[132] ATLAS Collaboration, "Readiness of the ATLAS Liquid Argon Calorimeter for LHC collisions", *Eur. Phys. J. C* 70 (2010) 723–753 (cit. on p. 36).

[133] S. White, "The ATLAS zero degree calorimeter", *Nucl. Instrum. Meth. A* 617 (2010) 126–128, ed. by G. Chiarelli et al. (cit. on p. 36).

[134] P. Jenni et al., *ATLAS Forward Detectors for Measurement of Elastic Scattering and Luminosity*, tech. rep., Geneva, 2008, URL: `https://cds.cern.ch/record/1095847` (cit. on p. 36).

[135] A. Sopczak et al., "Precision Luminosity of LHC Proton–Proton Collisions at 13 TeV Using Hit Counting With TPX Pixel Devices", *IEEE Trans. Nucl. Sci.* 64 (2017) 915–924, ISSN: 1558-1578 (cit. on p. 37).

[136] A. Sopczak et al., "Precision Measurements of Induced Radioactivity and Absolute Luminosity Determination with TPX Detectors in LHC Proton–Proton Collisions at 13 TeV", *IEEE Trans. Nucl. Sci.* 65 (2018) 1371–1377 (cit. on p. 37).

[137] B. Bergmann et al., "Evaluation of Timepix3 as a luminosity detector at LHC during 2018 pp collisions at $\sqrt{s} = 13$ TeV", *Eur. Phys. J. C* 85 (2025) (cit. on p. 37).

[138] J. Emery et al., "The Large Hadron Collider's beam wire scanner consolidation", *PoS JACoW IBIC* (2024) WEP29 (cit. on p. 40).

[139] H. Sullivan, *New Generation of Beam Wire Scanners for the LHC*, Presentation at 59th SY-BI Students & R&D Meeting, CERN, 29 Nov 2024, `https://indico.cern.ch/event/1483792/contributions/6252394`, 2024 (cit. on p. 40).

[140] E. Bravin et al., "First Beam Measurements with the LHC Synchrotron Light Monitors" (2010), URL: https://cds.cern.ch/record/1271742 (cit. on p. 40).

[141] D. Butti et al., "Status of the Synchrotron Radiation Telescope at the Large Hadron Collider", *Proceedings of the 14th International Beam Instrumentation Conference (IBIC 2025)*, https://meow.elettra.eu/90/pdf/TUPCO03.pdf, 2025, 624–631 (cit. on p. 40).

[142] R. Aaij et al., "Absolute luminosity measurements with the LHCb detector at the LHC", *JINST* 7 (2012) P01010 (cit. on p. 40).

[143] M. Schott, *Determination of integrated Luminosity via W/Z Boson Production at the ATLAS Detector*, tech. rep., Geneva: CERN, 2011, URL: https://cds.cern.ch/record/1341251 (cit. on p. 41).

[144] M. W. O'Keefe, "Luminosity Determination using $Z \rightarrow \ell\ell$ events at $\sqrt{s}$ = 13TeV with the ATLAS detector", *PoS* ICHEP2020 (2021) 812 (cit. on p. 41).

[145] CMS Collaboration, *Luminosity determination using Z boson production at the CMS experiment*, tech. rep., Geneva: CERN, 2023, URL: https://cds.cern.ch/record/2852905 (cit. on p. 41).

[146] *Bernoulli trial*, https://en.wikipedia.org/w/index.php?title=Bernoulli_trial&oldid=123456789, 2025 (cit. on p. 44).

[147] G. Aad et al., "Luminosity Determination in pp Collisions at $\sqrt{s} = 7$ TeV Using the ATLAS Detector at the LHC", *Eur. Phys. J. C* 71 (2011) 1630 (cit. on pp. 46, 67).

[148] S. S. Mortensen et al., *Measurement of the ρ-parameter and the total cross section from elastic scattering in pp collisions at $\sqrt{s} = 8$ TeV with the ATLAS detector*, tech. rep., Geneva: CERN, 2017, URL: https://cds.cern.ch/record/2280918 (cit. on p. 47).

[149] G. Antchev et al., "First determination of the ρ parameter at $\sqrt{s} = 13$ TeV: probing the existence of a colourless C-odd three-gluon compound state", *Eur. Phys. J. C* 79 (2019) 785 (cit. on p. 47).

[150] G. Aad et al., "Measurement of the total cross section and ρ-parameter from elastic scattering in pp collisions at $\sqrt{s} = 13$ TeV with the ATLAS detector", *Eur. Phys. J. C* 83 (2023) 441 (cit. on p. 47).

[151] V. A. Petrov and N. P. Tkachenko, "Coulomb-nuclear interference: Theory and practice for pp-scattering at 13 TeV", *Phys. Rev. D* 106 (2022) 054003 (cit. on p. 47).

[152] G. Antchev et al., "Measurement of elastic pp scattering at $\sqrt{\mathrm{s}} = 8$ TeV in the Coulomb–nuclear interference region: determination of the ρ -parameter and the total cross-section", *Eur. Phys. J. C* 76 (2016) 661 (cit. on p. 47).

[153] M. Palm, *Comparison of FBCT & BSRL bunch-by-bunch response*, 2018, URL: https://indico.cern.ch/event/775187/contributions/3221948/ (cit. on p. 48).

[154] C. Barschel et al., *Results of the LHC DCCT Calibration Studies*, tech. rep., Geneva, 2012, URL: https://cds.cern.ch/record/1425904 (cit. on p. 51).

[155] P. Odier, M. Ludwig, and S. Thoulet, *The DCCT for the LHC Beam Intensity Measurement*, tech. rep., Geneva: CERN, 2009, URL: https://cds.cern.ch/record/1183400 (cit. on p. 51).

[156] G. Anders et al., *STUDY OF THE RELATIVE LHC BUNCH POPULATIONS FOR LUMINOSITY CALIBRATION*, tech. rep., CERN, 2012, URL: https://cds.cern.ch/record/1427726 (cit. on p. 51).

[157] D. Belohrad et al., *The LHC Fast BCT system: A comparison of Design Parameters with Initial Performance*, tech. rep., Geneva: CERN, 2010, URL: https://cds.cern.ch/record/1267400 (cit. on p. 51).

[158] C. Ohm and T. Pauly, "The ATLAS beam pick-up based timing system", *Nucl. Instrum. Meth. A* 623 (2010) 558–560 (cit. on p. 51).

[159] A. Boccardi et al., *LHC Luminosity calibration using the Longitudinal Density Monitor*, 2013, URL: https://cds.cern.ch/record/1556087 (cit. on p. 54).

[160] A. Jury, M. G. Berges, and S. Mazzoni, *Longitudinal Density Monitor Error Analysis Report*, tech. rep., CERN, 2024, URL: https://edms.cern.ch/file/3324712/1/BSRL_Error_Analysis_Report.docx (cit. on p. 54).

[161] M. Centis Vignali et al., "Deep Diffused Avalanche Photodiodes for Charged Particles Timing", *Nucl. Instrum. Meth. A* 958 (2020) 162405, ed. by M. Krammer et al. (cit. on p. 54).

[162] A. Babaev et al., "Impact of beam–beam effects on absolute luminosity calibrations at the CERN Large Hadron Collider", *Eur. Phys. J. C* 84 (2024), ISSN: 1434-6052 (cit. on pp. 59, 60).

[163] M. Bassetti and G. Erskine, *Closed Expression for the Electrical Field of a Two-dimensional Gaussian Charge*, tech. rep., Geneva: CERN, 1980, URL: https://cds.cern.ch/record/122227 (cit. on p. 62).

[164] F. W. Jones, W. Herr, and T. Pieloni, *Parallel Beam-Beam Simulation Incorporating Multiple Bunches and Multiple Interaction Regions*, tech. rep., 2007, 4 p, URL: https://cds.cern.ch/record/1058519 (cit. on p. 62).

[165] V. Balagura, "Van der Meer scan luminosity measurement and beam–beam correction", *Eur. Phys. J. C* 81 (2021) 26 (cit. on p. 62).

[166] P. Forck, P. Kowina, and D. Liakin, *Beam position monitors*, tech. rep., CERN, 2009, URL: https://cds.cern.ch/record/1213277 (cit. on p. 64).

[167] M. Gąsior et al., "First Operational Experience with the LHC Diode ORbit and OScillation (DOROS) System", *PoS JACoW IBIC* (2016) MOPG07 (cit. on p. 64).

[168] D. Brandt, L. Vos, and B. Spataro, *Impedance of the LHC Arc Beam Position Monitors (BPMs)*, tech. rep., CERN, 2002, URL: https://cds.cern.ch/record/691832/files/project-note-284.pdf (cit. on p. 64).

[169] ATLAS Collaboration, "Improved luminosity determination in pp collisions at $\sqrt{s} = 7$ TeV using the ATLAS detector at the LHC", *Eur. Phys. J. C* 73 (2013) 2518 (cit. on p. 67).

[170] ATLAS Collaboration, "Luminosity determination in pp collisions at $\sqrt{s} = 8$ TeV using the ATLAS detector at the LHC", *Eur. Phys. J. C* 76 (2016) 653 (cit. on p. 67).

[171] H. Bartosik and G. Rumolo, *Production of single Gaussian bunches for Van der Meer scans in the LHC injector chain*, tech. rep., 2013, URL: https://cds.cern.ch/record/1590405 (cit. on p. 67).

[172] P. Grafström and W. Kozanecki, "Luminosity determination at proton colliders", *Prog. Part. Nucl. Phys.* 81 (2014) (cit. on p. 67).

[173] T. Barklow, *Non-factorization in vdM scans at 900 GeV in 2018*, https://indico.cern.ch/event/1213164/contributions/5102920/, 2022 (cit. on p. 68).

[174] B. Cole, L. B. Havener, and W. Kozanecki, *Luminosity calibration for November 2015* $\sqrt{s} = 5.02$ *TeV pp measurements*, tech. rep., Geneva: CERN, 2016, URL: https://cds.cern.ch/record/2199372 (cit. on p. 68).

[175] F. James and M. Roos, “Minuit: A System for Function Minimization and Analysis of the Parameter Errors and Correlations”, *Comput. Phys. Commun.* 10 (1975) 343–367, ISSN: 0010-4655 (cit. on p. 69).

[176] R. Hawkings and W. Kozanecki, *Magnetic non-linearities in Run 2 ATLAS vdM analyses*, tech. rep., Geneva: CERN, 2021, URL: `https://cds.cern.ch/record/2782532` (cit. on p. 70).

[177] F. Malek, R. Hawkings, and W. Kozanecki, *Length Scale Calibration during the November 2018 scans with pp collisions at* $\sqrt{s} = 900$ *GeV using the ATLAS detector*, tech. rep., Geneva: CERN, 2021, URL: `https://cds.cern.ch/record/2798102` (cit. on p. 70).

[178] E. Sanzani et al., *Luminosity measurement for the 900 GeV 2018 pp dataset*, tech. rep., Geneva: CERN, 2024, URL: `https://cds.cern.ch/record/2905677` (cit. on p. 76).

[179] R. K. Ellis, W. J. Stirling, and B. R. Webber, “QCD and collider physics”, *Cambridge University Press* (1996) (cit. on p. 79).

[180] A. Collaboration, “Measurement of $W^{\pm}$-boson and Z-boson production cross-sections in pp collisions at $\sqrt{s} = 2.76$ TeV with the ATLAS detector”, *Eur. Phys. J. C* 79 (2019), ISSN: 1434-6052 (cit. on p. 80).

[181] A. Collaboration, “Measurements of W and Z boson production in pp collisions at $\sqrt{s} = 5.02$ TeV with the ATLAS detector”, *Eur. Phys. J. C* 79 (2019), ISSN: 1434-6052 (cit. on p. 80).

[182] A. Collaboration, “Precision measurement and interpretation of inclusive W^+, W^- and Z/γ^* production cross sections with the ATLAS detector”, *Eur. Phys. J. C* 77 (2017), ISSN: 1434-6052 (cit. on pp. 80, 117).

[183] M. Aaboud et al., “Measurement of the Drell-Yan triple-differential cross section in pp collisions at $\sqrt{s} = 8$ TeV”, *JHEP* 12 (2017) 059 (cit. on p. 80).

[184] G. Aad et al., “Measurement of the cross-section and charge asymmetry of W bosons produced in proton–proton collisions at $\sqrt{s} = 8$ TeV with the ATLAS detector”, *Eur. Phys. J. C* 79 (2019) 760 (cit. on p. 80).

[185] G. Aad et al., “Measurement of $W^{\pm}$ and Z-boson production cross sections in pp collisions at $\sqrt{s} = 13$ TeV with the ATLAS detector”, *Phys. Lett. B* 759 (2016) 601–621 (cit. on p. 80).

[186] G. Aad et al., “Measurement of the transverse momentum distribution of Drell–Yan lepton pairs in proton–proton collisions at $\sqrt{s} = 13$ TeV with the ATLAS detector”, *Eur. Phys. J. C* 80 (2020) 616 (cit. on p. 80).

[187] S. Chatrchyan et al., “Measurement of the Inclusive W and Z Production Cross Sections in pp Collisions at $\sqrt{s} = 7$ TeV”, *JHEP* 10 (2011) 132 (cit. on p. 81).

[188] S. Chatrchyan et al., “Measurement of the Differential and Double-Differential Drell-Yan Cross Sections in Proton-Proton Collisions at $\sqrt{s} = 7$ TeV”, *JHEP* 12 (2013) 030 (cit. on p. 81).

[189] S. Chatrchyan et al., “Measurement of Inclusive W and Z Boson Production Cross Sections in pp Collisions at $\sqrt{s}$ = 8 TeV”, *Phys. Rev. Lett.* 112 (2014) 191802 (cit. on p. 81).

[190] V. Khachatryan et al., “Measurements of differential and double-differential Drell-Yan cross sections in proton-proton collisions at 8 TeV”, *Eur. Phys. J. C* 75 (2015) 147 (cit. on p. 81).

[191] A. M. Sirunyan et al., “Measurements of the W boson rapidity, helicity, double-differential cross sections, and charge asymmetry in pp collisions at $\sqrt{s}$ = 13 TeV”, *Phys. Rev. D* 102 (2020) 092012 (cit. on p. 81).

[192] R. Aaij et al., *Measurement of the $W \to \mu\nu_\mu$ cross-sections as a function of the muon transverse momentum in pp collisions at 5.02 TeV*, tech. rep., Sept. 2025, URL: `https://arxiv.org/abs/2509.18817` (cit. on p. 81).

[193] R. Aaij et al., “Measurement of the forward W boson cross-section in pp collisions at $\sqrt{s} = 7$ TeV”, *JHEP* 12 (2014) 079 (cit. on p. 81).

[194] R. Aaij et al., “Measurement of forward W and Z boson production in pp collisions at $\sqrt{s} = 8$ TeV”, *JHEP* 01 (2016) 155 (cit. on p. 81).

[195] E. Bothmann et al., “Event generation with Sherpa 2.2”, *SciPost Phys.* 7 (2019) 034 (cit. on p. 81).

[196] F. Buccioni et al., “OpenLoops 2”, *Eur. Phys. J. C* 79 (2019) 866 (cit. on p. 81).

[197] F. Cascioli, P. Maierhöfer, and S. Pozzorini, “Scattering Amplitudes with Open Loops”, *Phys. Rev. Lett.* 108 (2012) 111601 (cit. on p. 81).

[198] A. Denner, S. Dittmaier, and L. Hofer, “COLLIER: A fortran-based complex one-loop library in extended regularizations”, *Comput. Phys. Commun.* 212 (2017) 220–238 (cit. on p. 81).

[199] S. Schumann and F. Krauss, “A parton shower algorithm based on Catani–Seymour dipole factorisation”, *JHEP* 03 (2008) 038 (cit. on p. 81).

[200] S. Höche et al., “QCD matrix elements + parton showers. The NLO case”, *JHEP* 04 (2013) 027 (cit. on p. 81).

[201] R. D. Ball et al., “Parton distributions for the LHC run II”, *JHEP* 04 (2015) 040 (cit. on pp. 81, 99).

[202] C. Anastasiou et al., “High-precision QCD at hadron colliders: Electroweak gauge boson rapidity distributions at next-to-next-to leading order”, *Phys. Rev. D* 69 (2004) 094008 (cit. on p. 81).

[203] S. Alioli et al., “A general framework for implementing NLO calculations in shower Monte Carlo programs: the POWHEG BOX”, *JHEP* 06 (2010) 043 (cit. on p. 81).

[204] ATLAS Collaboration, “Measurement of the Z/γ^* boson transverse momentum distribution in pp collisions at $\sqrt{s} = 7$ TeV with the ATLAS detector”, *JHEP* 09 (2014) 145 (cit. on p. 82).

[205] H.-L. Lai et al., “New parton distributions for collider physics”, *Phys. Rev. D* 82 (2010) 074024 (cit. on p. 82).

[206] J. Pumplin et al., “New Generation of Parton Distributions with Uncertainties from Global QCD Analysis”, *JHEP* 07 (2002) 012 (cit. on p. 82).

[207] P. Golonka and Z. Was, “PHOTOS Monte Carlo: A Precision tool for QED corrections in Z and W decays”, *Eur. Phys. J. C* 45 (2006) 97–107 (cit. on pp. 82, 99).

[208] N. Davidson, T. Przedzinski, and Z. Was, “PHOTOS Interface in C++: Technical and physics documentation”, *Comput. Phys. Commun.* 199 (2016) 86–101 (cit. on p. 82).

[209] ATLAS Collaboration, *ATLAS Pythia 8 tunes to 7 TeV data*, tech. rep., Geneva: CERN, 2014, URL: `https://cds.cern.ch/record/1966419` (cit. on p. 82).

[210] M. Beneke et al., “Hadronic top-quark pair production with NNLL threshold resummation”, *Nucl. Phys. B* 855 (2012) 695–741 (cit. on p. 82).

[211] M. Cacciari et al., “Top-pair production at hadron colliders with next-to-next-to-leading logarithmic soft-gluon resummation”, *Phys. Lett. B* 710 (2012) 612–622 (cit. on p. 82).

[212] P. Bärnreuther, M. Czakon, and A. Mitov, “Percent-Level-Precision Physics at the Tevatron: Next-to-Next-to-Leading Order QCD Corrections to $q\bar{q} \to t\bar{t}+X$”, *Phys. Rev. Lett.* 109 (2012) 132001 (cit. on p. 82).

[213] M. Czakon and A. Mitov, “NNLO corrections to top-pair production at hadron colliders: the all-fermionic scattering channels”, *JHEP* 12 (2012) 054 (cit. on p. 82).

[214] M. Czakon and A. Mitov, “NNLO corrections to top pair production at hadron colliders: the quark-gluon reaction”, *JHEP* 01 (2013) 080 (cit. on p. 82).

[215] M. Czakon, P. Fiedler, and A. Mitov, “Total Top-Quark Pair-Production Cross Section at Hadron Colliders Through $O(\alpha_S^4)$”, *Phys. Rev. Lett.* 110 (2013) 252004 (cit. on p. 82).

[216] M. Czakon and A. Mitov, “Top++: A program for the calculation of the top-pair cross-section at hadron colliders”, *Comput. Phys. Commun.* 185 (2014) 2930 (cit. on p. 82).

[217] G. Aad et al., “Emulating the impact of additional proton–proton interactions in the ATLAS simulation by presampling sets of inelastic Monte Carlo events”, *Comput. Softw. Big Sci.* 6 (2022) 3 (cit. on p. 82).

[218] S. Porteboeuf, T. Pierog, and K. Werner, “Producing Hard Processes Regarding the Complete Event: The EPOS Event Generator”, *45th Rencontres de Moriond on QCD and High Energy Interactions*, Gioi Publishers, 2010, 135–140, URL: `https://arxiv.org/abs/1006.2967` (cit. on p. 82).

[219] T. Pierog et al., “EPOS LHC: Test of collective hadronization with data measured at the CERN Large Hadron Collider”, *Phys. Rev. C* 92 (2015) 034906 (cit. on p. 82).

[220] R. D. Ball et al., “Parton Distribution Benchmarking with LHC Data”, *JHEP* 04 (2013) 125 (cit. on p. 82).

[221] ATLAS Collaboration, *The Pythia 8 A3 tune description of ATLAS minimum bias and inelastic measurements incorporating the Donnachie-Landshoff diffractive model*, tech. rep., Geneva: CERN, 2016, URL: `https://cds.cern.ch/record/2206965` (cit. on p. 82).

[222] G. Aad et al., “The ATLAS Simulation Infrastructure”, *Eur. Phys. J. C* 70 (2010) 823–874 (cit. on p. 82).

[223] R. Frühwirth, “Application of Kalman filtering to track and vertex fitting”, *Nucl. Instrum. Meth. A* 262 (1987) 444–450, ISSN: 0168-9002 (cit. on p. 83).

[224] T. G. Cornelissen et al., “The global χ^2 track fitter in ATLAS”, *J. Phys. Conf. Ser.* 119 (2008) 032013 (cit. on p. 84).

[225] ATLAS Collaboration, *A neural network clustering algorithm for the ATLAS silicon pixel detector*, tech. rep., CERN, 2014, URL: `https://cds.cern.ch/record/1712337/files/PERF-2012-05-PCTF.pdf` (cit. on p. 84).

[226] M. Aaboud et al., “Reconstruction of primary vertices at the ATLAS experiment in Run 1 proton–proton collisions at the LHC”, *Eur. Phys. J. C* 77 (2017) 332 (cit. on p. 84).

[227] G. Aad et al., “Electron and photon performance measurements with the ATLAS detector using the 2015–2017 LHC proton–proton collision data”, *JINST* 14 (2019) P12006 (cit. on pp. 85, 95, 96).

[228] G. Aad et al., “Electron reconstruction and identification in the ATLAS experiment using the 2015 and 2016 LHC proton–proton collision data at $\sqrt{s} = 13$ TeV”, *Eur. Phys. J. C* 79 (2019) 639 (cit. on p. 85).

[229] ATLAS Collaboration, *Electron identification efficiency with Run3 early data*, `https://atlas.web.cern.ch/Atlas/GROUPS/PHYSICS/PLOTS/EGAM-2022-04/index.php`, 2022 (cit. on p. 86).

[230] G. Aad et al., “Muon reconstruction and identification efficiency in ATLAS using the full Run 2 *pp* collision data set at $\sqrt{s} = 13$ TeV”, *Eur. Phys. J. C* 81 (2021) 578 (cit. on pp. 86, 96, 97).

[231] ATLAS Collaboration, “Muon reconstruction performance of the ATLAS detector in proton–proton collision data at $\sqrt{s} = 13\,\text{TeV}$”, *Eur. Phys. J. C* 76 (2016) 292 (cit. on pp. 86, 96).

[232] ATLAS Collaboration, *Muon reconstruction and identification performance of the ATLAS detector using 2022 and 2023 LHC pp collision data at* $\sqrt{s} = 13.6$ *TeV*, `https://atlas.web.cern.ch/Atlas/GROUPS/PHYSICS/PLOTS/MUON-2023-02/`, ATLAS public plots (Muon), 2023 (cit. on p. 87).

[233] ATLAS Collaboration, *Muon reconstruction performance of the ATLAS detector in 2022*, `https://atlas.web.cern.ch/Atlas/GROUPS/PHYSICS/PLOTS/MUON-2023-01/index.php`, ATLAS public plots (Muon), 2023 (cit. on p. 87).

[234] M. Cacciari, G. P. Salam, and G. Soyez, “The anti-k_t jet clustering algorithm”, *JHEP* 04 (2008) 063 (cit. on p. 87).

[235] M. Cacciari, G. P. Salam, and G. Soyez, “FastJet User Manual”, *Eur. Phys. J. C* 72 (2012) 1896 (cit. on p. 87).

[236] ATLAS Collaboration, *Tagging and suppression of pileup jets with the ATLAS detector*, tech. rep., Geneva: CERN, 2014, URL: `https://cds.cern.ch/record/1700870` (cit. on p. 87).

[237] L. J. Caviedes Betancourt, C. Sandoval Usme, and M. Holzbock, “Calibration of the NN Jet Vertex Tagger using $Z \to \mu^+\mu^-$ events in the ATLAS detector”, *8th ComHEP: Colombian Meeting on High Energy Physics*, 2023, URL: `https://indico.global/event/8711/contributions/84109/attachments/38846/72323/COMHEP_2023_LauraCaviedes.pdf` (cit. on p. 87).

[238] G. Aad et al., “The performance of missing transverse momentum reconstruction and its significance with the ATLAS detector using 140 fb^{-1} of $\sqrt{s} = 13$ TeV pp collisions”, *Eur. Phys. J. C* 85 (2025) 606 (cit. on p. 87).

[239] M. Aaboud et al., “Performance of missing transverse momentum reconstruction with the ATLAS detector using proton-proton collisions at $\sqrt{s}$ = 13 TeV”, *Eur. Phys. J. C* 78 (2018) 903 (cit. on pp. 88, 97).

[240] ATLAS Collaboration, E_T^{miss} *performance in the ATLAS detector using 2015-2016 LHC p-p collisions*, tech. rep., Geneva: CERN, 2018, URL: `https://cds.cern.ch/record/2625233` (cit. on p. 88).

[241] ATLAS Collaboration, *Run-3 (2022+2023) Jet and MET Performance*, `https://atlas.web.cern.ch/Atlas/GROUPS/PHYSICS/PLOTS/JETM-2024-03/`, ATLAS public plots (Jet/MET), 2024 (cit. on p. 88).

[242] ATLAS Collaboration, “ATLAS b-jet identification performance and efficiency measurement with $t\bar{t}$ events in pp collisions at $\sqrt{s} = 13\,\text{TeV}$”, *Eur. Phys. J. C* 79 (2019) 970 (cit. on p. 89).

[243] S. Navas et al., “Review of Particle Physics”, *Phys. Rev. D* 110 (2024) 030001 (cit. on p. 95).

[244] M. Aaboud et al., “Electron efficiency measurements with the ATLAS detector using 2012 LHC proton–proton collision data”, *Eur. Phys. J. C* 77 (2017) 195 (cit. on p. 95).

[245] G. Aad et al., “Measurement of the muon reconstruction performance of the ATLAS detector using 2011 and 2012 LHC proton–proton collision data”, *Eur. Phys. J. C* 74 (2014) 3130 (cit. on p. 95).

[246] G. Aad et al., “The ATLAS Trigger System for LHC Run 3 and Trigger performance in 2022”, *JINST* 19 (2024) P06029 (cit. on p. 95).

[247] G. Aad et al., “Jet energy scale and resolution measured in proton–proton collisions at $\sqrt{s} =$ 13 TeV with the ATLAS detector”, *Eur. Phys. J. C* 81 (2021) 689 (cit. on p. 97).

[248] G. Aad et al., “Measurement of the $t\bar{t}$ cross section and its ratio to the Z production cross section using pp collisions at $\sqrt{s} = 13.6$ TeV with the ATLAS detector”, *Phys. Lett. B* 848 (2024) 138376 (cit. on pp. 97, 99).

[249] R. D. Ball et al., “The PDF4LHC21 combination of global PDF fits for the LHC Run III”, *J. Phys. G* 49 (2022) 080501 (cit. on p. 99).

[250] T. Cridge et al., “An investigation of the α_S and heavy quark mass dependence in the MSHT20 global PDF analysis”, *Eur. Phys. J. C* 81 (2021) 744 (cit. on p. 99).

[251] R. D. Ball et al., “The path to proton structure at 1% accuracy: NNPDF Collaboration”, *Eur. Phys. J. C* 82 (2022) 428 (cit. on p. 99).

[252] S. Alekhin et al., “Parton distribution functions, α_s, and heavy-quark masses for LHC Run II”, *Phys. Rev. D* 96 (2017) 014011 (cit. on p. 99).

[253] G. Aad et al., “Determination of the parton distribution functions of the proton using diverse ATLAS data from pp collisions at $\sqrt{s} = 7$, 8 and 13 TeV”, *Eur. Phys. J. C* 82 (2022) 438 (cit. on p. 99).

[254] S. Jadach et al., “Systematic Studies of Exact $\mathcal{O}(\alpha^{2L})$ CEEX EW Corrections in a Hadronic MC for Precision Z/γ^* Physics at LHC Energies”, *Phys. Rev. D* 99 (2019) 076016 (cit. on p. 99).

[255] M. Chiesa, F. Piccinini, and A. Vicini, “Direct determination of $\sin^2\theta^{\ell}_{eff}$ at hadron colliders”, *Phys. Rev. D* 100 (2019) 071302 (cit. on p. 99).

[256] A. Arbuzov et al., “Update of the MCSANC Monte Carlo integrator, v. 1.20”, *JETP Lett.* 103 (2016) 131–136 (cit. on p. 99).

[257] S. Dittmaier, A. Huss, and C. Schwinn, “Mixed QCD-electroweak $\mathcal{O}(\alpha_s\alpha)$ corrections to Drell-Yan processes in the resonance region: pole approximation and non-factorizable corrections”, *Nucl. Phys. B* 885 (2014) 318–372 (cit. on p. 99).

[258] E. Richter-Was and Z. Was, “Adequacy of Effective Born for electroweak effects and TauSpinner algorithms for high energy physics simulated samples”, *Eur. Phys. J. Plus* 137 (2022) 95 (cit. on p. 99).

[259] J. Kretzschmar et al., *Samples and Physics modelling for low pile-up runs taken in 2017 and 2018*, tech. rep., Geneva: CERN, 2019, URL: `https://cds.cern.ch/record/2657141` (cit. on p. 99).

[260] G. Cowan et al., “Asymptotic formulae for likelihood-based tests of new physics”, *Eur. Phys. J. C* 71 (2011) 1554 (cit. on p. 106).

[261] K. Cranmer et al., *HistFactory: A tool for creating statistical models for use with RooFit and RooStats*, tech. rep., New York: New York U., 2012, URL: `https://cds.cern.ch/record/1456844` (cit. on p. 107).

[262] S. Hageböck et al., “A Faster, More Intuitive RooFit”, *EPJ Web Conf.* 245 (2020) 06007 (cit. on p. 107).

[263] ROOT development team, *RooFit — ROOT Data Analysis Framework*, `https://root.cern/manual/roofit/`, CERN, 2025 (cit. on p. 107).

[264] S. Dulat et al., “New parton distribution functions from a global analysis of quantum chromodynamics”, *Phys. Rev. D* 93 (2016) 033006 (cit. on p. 112).

[265] ATLAS Collaboration, *Measurement of the vector boson production cross sections and their ratios using the LHC Run 3 pp collision data at 13.6 TeV*, tech. rep., Geneva: CERN, 2022, URL: `https://cds.cern.ch/record/2841234` (cit. on p. 117).

[266] G. Aad et al., “Measurement of vector boson production cross sections and their ratios using pp collisions at $\sqrt{s} = 13.6$ TeV with the ATLAS detector”, *Phys. Lett. B* 854 (2024) 138725 (cit. on p. 117).

[267] S. Camarda et al., “DYTurbo: Fast predictions for Drell-Yan processes”, *Eur. Phys. J. C* 80 (2020) 251 (cit. on p. 117).

[268] S. Camarda, L. Cieri, and G. Ferrera, “Drell–Yan lepton-pair production: qT resummation at N3LL accuracy and fiducial cross sections at N3LO”, *Phys. Rev. D* 104 (2021) L111503 (cit. on p. 117).

[269] S. Camarda, L. Cieri, and G. Ferrera, “Fiducial perturbative power corrections within the $\mathbf{q}_T$ subtraction formalism”, *Eur. Phys. J. C* 82 (2022) 575 (cit. on p. 117).

[270] S. Camarda, L. Cieri, and G. Ferrera, “Drell–Yan lepton-pair production: qT resummation at N4LL accuracy”, *Phys. Lett. B* 845 (2023) 138125 (cit. on p. 117).

[271] R. Sadykov and V. Yermolchyk, “Polarized NLO EW e^+e^- cross section calculations with ReneSANCe-v1.0.0”, *Comput. Phys. Commun.* 256 (2020) 107445 (cit. on p. 117).

[272] S. Bondarenko et al., “Hadron-hadron collision mode in ReneSANCe-v1.3.0”, *Comput. Phys. Commun.* 285 (2023) 108646 (cit. on p. 117).

Biography of the author

Veljko Maksimović was born on October 9, 1993, in Novi Pazar. He completed the Gymnasium in Novi Pazar in 2012 with excellent success (grade point average 5.0). In the same year, he enrolled at the Faculty of Physics, University of Belgrade. After successfully completing his undergraduate studies (grade point average 9.21), he continued to the Master's program at the same faculty, which he completed in 2019 with an average grade of 10.0. He defended his Master's thesis entitled "Possibilities for Improving the Measurement of the W-Boson Mass in the ATLAS Experiment" with a grade of 10. The supervisor of his Master's thesis was Dr. Nenad Vranješ, Research Professor at the Institute of Physics in Belgrade. During his Master's studies, Veljko Maksimović joined the ATLAS experiment at CERN. His research focused on reducing the measurement uncertainty in the determination of the W-boson mass through momentum-scale calibration using ATLAS data collected in 2011 and 2012. In September 2019, he contributed to the organization of the first *Standard Model Workshop* in Belgrade, which gathered researchers from the ATLAS Collaboration at CERN.

Since October 2019, Veljko Maksimović has been a doctoral student at the Faculty of Physics, University of Belgrade, specializing in High Energy Physics and Nuclear Physics. He was engaged in the fundamental research project OI 171004 of the Ministry of Education, Science and Technological Development of the Republic of Serbia, within the High Energy Physics Laboratory of the Institute of Physics in Belgrade. During his PhD studies, he worked on luminosity calibration using the *van der Meer* method for the special low-energy proton–proton run of the Large Hadron Collider in 2018. The results of this work were summarized in an internal note of the ATLAS Collaboration. In collaboration with colleagues from the ATLAS experiment, he is in the final stages of preparing a publication entitled "Determination of the luminosity in pp collisions for elastic scattering measurements at $\sqrt{s} = 900$ GeV using the ATLAS detector at the LHC", with the goal of submitting the manuscript to the *European Physical Journal C*. In June 2021, he became a signatory on the ATLAS authorship list after successfully completing his qualification task. At the beginning of the current ATLAS Run 3, he joined the analysis team working on measurements of fiducial and total production cross-sections of the W and Z bosons, which resulted in two publications in the journal *Physics Letters B*. These publications represent the first results of this kind at a center-of-mass energy of $\sqrt{s} = 13.6$ TeV.

The candidate delivered a presentation entitled "Absolute Luminosity Calibration in pp Collisions at $\sqrt{s} = 900$ GeV in the ATLAS Experiment" at the 11th regional conference of the *Balkan Physical Union (BPU11 Congress)*, held in Belgrade from August 28 to September 1, 2022. On a related topic, titled "Van der Meer Analysis of 2018 pp Data Collected at 900 GeV", he presented a poster at the *ATLAS Week* organized at CERN from February 13 to 17, 2023. In 2025, he was selected to represent the ATLAS Collaboration with a talk at the *Workshop on Quantum Entanglement at the Energy Frontier*, held from April 25 to 28 at the School of Physics, Peking University. The topic of his presentation was "Quantum Entanglement from the LHC ATLAS Experiment". In addition, the candidate attended the *CERN Accelerator School* (2022), the *MCnet Summer School* (June 10–14, 2024) focused on Monte Carlo generator techniques, and the *CERN–Fermilab HCP Summer School*, intended for final-year PhD students, held at CERN from August 22 to 31, 2023. The candidate is fluent in Serbian and English.

Author‘s publications :

- G. Aad, ..., **V. Maksimovic**, *et al.*, "Measurement of vector boson production cross sections and their ratios using pp collisions at $\sqrt{s}$ =13.6 TeV with the ATLAS detector", *Physics Letters B* **854** (2024) 138725.
- G. Aad, ..., **V. Maksimovic**, *et al.*, "Measurement of the $t\bar{t}$ cross section and its ration to the Z production cross section using pp collisions at $\sqrt{s}$ = 13.6 TeV with ATLAS detector", *Physics Letters B* **848** (2024) 138376.
- R. Hawkings, W. Kozanecki, J. Kuechler, **V. Maksimovic**, K. Monig, N. Vranjes, "Absolute luminosity calibration for the 900 GeV 2018 pp dataset with the ATLAS detector", ATL-COM-DAPR-2024-020 (2024).
- G. Aad, ..., **V. Maksimovic**, *et al.*, "Determination of the luminosity in pp collisions for elastic scattering measurements at $\sqrt{s}$ = 900 GeV using the ATLAS detector at the LHC", Target journal: *European Physical Journal C (EPJC)*. Manuscript in preparation.

Изјава о ауторству

Име и презиме аутора – Вељко Максимовић

Број индекса – 8003/2019

Изјављујем

да је докторска дисертација под насловом

W Boson Physics and Luminosity Calibration at the ATLAS Experiment

(Физика W бозона и калибрација луминозности на експерименту АТЛАС)

- резултат сопственог истраживачког рада;
- да дисертација у целини ни у деловима није била предложена за стицање друге дипломе према студијским програмима других високошколских установа;
- да су резултати коректно наведени и
- да нисам кршио ауторска права и користио интелектуалну својину других лица.

У Београду, 2022

Потпис аутора

____

Изјава о истоветности штампане и електронске верзије докторског рада

Име и презиме аутора – Вељко Максимовић

Број индекса – 8003/2019

Студијски програм – Физика високих енергија и нуклеарна физика

Наслов рада – **W Boson Physics and Luminosity Calibration at the ATLAS Experiment**

(Физика W бозона и калибрација луминозности на експерименту АТЛАС)

Ментор – др Ненад Врањеш

Изјављујем да је штампана верзија мог докторског рада истоветна електронској верзији коју сам предала ради похрањивања у Дигиталном репозиторијуму Универзитета у Београду.

Дозвољавам да се објаве моји лични подаци везани за добијање академског назива доктора наука, као што су име и презиме, година и место рођења и датум одбране рада.

Ови лични подаци могу се објавити на мрежним страницама дигиталне библиотеке, у електронском каталогу и у публикацијама Универзитета у Београду.

У Београду, 2022

Потпис аутора

____

Изјава о коришћењу

Овлашћујем Универзитетску библиотеку „Светозар Марковић“ да у Дигитални репозиторијум Универзитета у Београду унесе моју докторску дисертацију под насловом:

W Boson Physics and Luminosity Calibration at the ATLAS Experiment

(Физика W бозона и калибрација луминозности на експерименту АТЛАС)

која је моје ауторско дело.

Дисертацију са свим прилозима предала сам у електронском формату погодном за трајно архивирање.

Моју докторску дисертацију похрањену у Дигиталном репозиторијуму Универзитета у Београду и доступну у отвореном приступу могу да користе сви који поштују одредбе садржане у одабраном типу лиценце Креативне заједнице (Creative Commons) за коју сам се одлучила.

1. Ауторство (CC BY)
2. Ауторство – некомерцијално (CC BY-NC)
3. Ауторство – некомерцијално – без прерада (CC BY-NC-ND)
4. Ауторство – некомерцијално – делити под истим условима (CC BY-NC-SA)
5. Ауторство – без прерада (CC BY-ND)
6. Ауторство – делити под истим условима (CC BY-SA)

(Молимо да заокружите само једну од шест понуђених лиценци.
Кратак опис лиценци је саставни део ове изјаве).

У Београду, 2022

Потпис аутора

____

1. Ауторство. Дозвољавате умножавање, дистрибуцију и јавно саопштавање дела, и прераде, ако се наведе име аутора на начин одређен од стране аутора или даваоца лиценце, чак и у комерцијалне сврхе. Ово је најслободнија од свих лиценци.

2. Ауторство – некомерцијално. Дозвољавате умножавање, дистрибуцију и јавно саопштавање дела, и прераде, ако се наведе име аутора на начин одређен од стране аутора или даваоца лиценце. Ова лиценца не дозвољава комерцијалну употребу дела.

3. Ауторство – некомерцијално – без прерада. Дозвољавате умножавање, дистрибуцију и јавно саопштавање дела, без промена, преобликовања или употребе дела у свом делу, ако се наведе име аутора на начин одређен од стране аутора или даваоца лиценце. Ова лиценца не дозвољава комерцијалну употребу дела. У односу на све остале лиценце, овом лиценцом се ограничава највећи обим права коришћења дела.

4. Ауторство – некомерцијално – делити под истим условима. Дозвољавате умножавање, дистрибуцију и јавно саопштавање дела, и прераде, ако се наведе име аутора на начин одређен од стране аутора или даваоца лиценце и ако се прерада дистрибуира под истом или сличном лиценцом. Ова лиценца не дозвољава комерцијалну употребу дела и прерада.

5. Ауторство – без прерада. Дозвољавате умножавање, дистрибуцију и јавно саопштавање дела, без промена, преобликовања или употребе дела у свом делу, ако се наведе име аутора на начин одређен од стране аутора или даваоца лиценце. Ова лиценца дозвољава комерцијалну употребу дела.

6. Ауторство – делити под истим условима. Дозвољавате умножавање, дистрибуцију и јавно саопштавање дела, и прераде, ако се наведе име аутора на начин одређен од стране аутора или даваоца лиценце и ако се прерада дистрибуира под истом или сличном лиценцом. Ова лиценца дозвољава комерцијалну употребу дела и прерада. Слична је софтверским лиценцама, односно лиценцама отвореног кода.